CDF/PHYS/EXOTIC/CDFR/10561
June 29, 2011
Version 1.0

Search for H → WW Production Using 8.2 fb^{-1}

Doug Benjamin, Mark Kruse, Seig Oh, Geumbong Yu

Duke University

Sebastian Carron, Massimo Casarsa, Pedro Movilla Fernandez, Eric James, Sergo Jindariani, Thomas Junk

Fermilab

Roman Lysak

IEP SAS, Slovakia

Maria d'Errico, Matteo Bauce, Antonio Limosani, Donatella Lucchesi

INFN and University of Padova

Anadi Canepa

TRIUMF

Aidan Robson, Rick St. Denis, Peter Bussey

University of Glasgow

Matthew Herndon

University of Wisconsin, Madison

Jason Nett

Texas A&M University

Satyajit Behari

Johns Hopkins University

Ben Carls
University of Illinois, Urbana Champaign

Abstract

We present a search for Standard Model (SM) Higgs to WW^* production in dilepton plus $\not\!\!E_T$ channels using approximately 8.2 fb^{-1} of integrated luminosity. The analysis described here relies on almost the same techniques described in CDF Note 9863. The primary differences in the two searches are: the addition of new data (from 7.1 fb^{-1} to 8.2 fb^{-1}); the addition of trilepton search channels; a loosened criteria for likelihood-based electron selection which improves acceptance while doubling the electron fake rate from that of the previous analysis. We utilize multivariate discriminants separately optimized for events containing zero, one, and two or more jets in the opposite-sign dilepton final states. For all jet multiplicites, we take into account four possible Higgs boson production mechanisms: gluon fusion, associated production with a W boson, associated production with a Z boson, and vector boson fusion. We also include an analysis of an opposite-sign dilepton event sample with zero or one jets with a dilepton mass of less than 16 GeV/c^2 and considers only potential signal from gluon fusion. We also include an analysis of a same-sign dilepton event sample which can potentially contain additional signal events originating from the associated Higgs boson production mechanisms. In this update, we also include an analysis of a trilepton event sample which may also potentially contain additional signal events originating from the associated Higgs boson production mechanisms. Based on the dilepton opposite-sign selection criteria defined in CDF Note 9195 and a data sample of about 8.2 fb^{-1}, we observe (summing over all jet bins) a total of 2471 candidate events compared with an expectation of 2528 ± 174 background events and 42.7 ± 5.1 signal events for a Standard Model Higgs boson with a mass of 165 GeV/c^2. In our low-dilepton mass opposite-sign event candidate sample we observe 134 candidate events compared with an expectation of 127 ± 10 background events and 1.2 ± 0.2 signal events for a Standard Model Higgs boson with a mass of 165 GeV/c^2. In our same-sign dilepton event candidate sample we observe 91 candidate events compared with an expectation of 90 ± 15 background events and 2.1 ± 0.3 signal events for a Standard Model Higgs boson with a mass of 165 GeV/c^2. In our trilepton event candidate sample we observe 55 candidate events compared with an expectation of 50 ± 4 background events and 1.8 ± 0.2 signal events for a Standard Model Higgs boson with a mass of 165 GeV/c^2. Based on these samples, we determine an observed 95% C.L. upper cross section limit of 0.9 times the SM prediction at NNLL for a Higgs mass of 165 GeV/c^2 to be compared with the value for the median of the expected limit (0.97). Results for eighteen other Higgs mass hypotheses ranging from 110 GeV/c^2 to 200 GeV/c^2 are also presented.

Contents

1 Introduction

In this note, we present a search for Standard Model $H \to WW^* \to l\nu l\nu$ production using approximately 7.1 fb^{-1} of integrated luminosity. This search builds on CDF Note 9863 [1], from which it inherits the most recent improvements of the analysis, most notably the likelihood-based selection of central electrons, and the addition of events containing low-dilepton mass pairs (< 16 GeV$/c^2$) as a separate search region (CDF Note 9864 [2]).

Another set of improvements were incorporated into the 5.9 fb^{-1} version of the analysis [3], which are summarized below for the reader's convenience:

- A loosened cut on the likelihood-based central electron selection, which improves electron acceptance while approximately doubling the fake rate. This modification is described in detail in Section 3.
- Separation of the TCE and likelihood-based central electron categories. Previously, since most TCE pass the likelihood-based selection, the TCE had been dropped as a separate electron category. It has now been reinstated, and the likelihood-based central electron category is defined as electron candidates which pass the likelihood selection but do not pass TCE selection. This was done for the benefit of the same-sign dilepton search, as the likelihood-based electrons have a higher rate of charge mismeasurement than the TCE.
- The addition of periods 24, 25, 26, and 27 data, which corresponds to approximately 1100 pb^{-1}, or a luminosity increase of $\sim$23%.
- Inclusion of the reprocessed period 18 data; approximately 100 pb^{-1} of period 18 data which was previously marked bad for silicon data due to a bad silicon calibration has been recovered and is now considered good for silicon.
- Reweighting of the gluon fusion ($gg \to H$) Pythia Monte Carlo samples to match the resummed Higgs p_T spectrum from theoretical calculations.
- Fill in the missing Higgs signal samples on the mass grid, so that a limit is determined for every 5 GeV interval (this involved adding samples for $m_H = 115$, 125, 135, 185, and 195).
- Incorporate the signal contributions from vector boson fusion and associated production with a W or Z boson in the event sample with opposite-sign dileptons and zero reconstructed jets. Previously this event sample considered only signal contributions from gluon fusion; adding the additional signal production modes corresponds to an increase in expected signal of 16% for a Higgs boson of $m_H = 115$, 6.2% for $m_H = 160$, and 6% for $m_H = 200$ GeV.

- Inclusion of trilepton searches for the signatures $WH \to WWW^* \to l\nu l\nu l\nu$ and $ZH \to ZWW^* \to lll\nu + X$. These searches were separately blessed with 4.8 fb^{-1} as described in CDF Note 10020 [4], and are here updated with the same improvements (where applicable) as the dilepton analyses.

- Improved treatment of many systematic uncertainties, including further investigation of potential shape systematics, described in detail in Section 16.

Another improvement implemented in the 5.9 fb^{-1} version of the analysis is the extension of the $W\gamma$ Monte Carlo samples to include modeling of the later run periods. Previously, the $W\gamma$ samples consisted of one fully run-dependent sample which went through period 13. We now use an additional Monte Carlo sample generated with a higher luminosity profile (based on a specific set of runs from periods 10 to 12) to model data collected from period 14 onward (periods 14 to 27 for the case of 5.9 fb^{-1}).

A similar improvement was made for the WW Monte Carlo sample, which previously consisted of one fully run-dependent sample generated with MC@NLO which only went through period 7. We have now updated our version of MC@NLO to the latest release, 3.41, and generated two new samples to replace the older fully run-dependent sample. One new sample is also fully run-dependent, from periods 0 to 13. The second sample is generated with a higher luminosity profile, as described above for the $W\gamma$ sample, to model data from period 14 onward.

In order to avoid complications in data-to-Monte-Carlo comparisons, we treat periods 14 to 27 as a single data period with a unique set of scale factors, trigger efficiencies, etc. Monte Carlo events in the higher luminosity samples are each assigned to a specific run number contained within period 15 and a unique event number to ensure that events are not accidentally removed as duplicates. All of the signal samples and most of the other background samples were already updated this way in [5].

2 New Categories and Improved Isolation

In order to increase acceptance, we added two new categories to the analysis. Firstly, we implemented a category called IsoCrkTrk in an effort to recover electrons passing through calorimeter cracks. For these, the calorimeter isolation is recalculated, removing E_{em} from calorimeter towers adjacent to the track. Secondly, a likelihood based plug electron category was implemented called PLBE. These two categories did not replace existing categories. They were only added to increase acceptance and were made orthogonal to the existing categories. Both IsoCrkTrk and PLBE were previously used in search for $ZZ \rightarrow llll$ and are more thoroughly described in [6].

In decays of $H \rightarrow WW$, the charged leptons from the $W \rightarrow l\nu$ will oftentimes be within a ΔR_{ll} of 0.4. In this instance, the two high p_T would normally spoil each others track and colorimeter isolations and veto the event. To prevent this from occuring and increase acceptance, we determined new calorimeter and track isolations for candidate leptons.

To recalculate the isolations, we created lists of high quality muon and electron candidates. To appear on the list, muons must have $E_{em} < 2 + Max(0, 0.0115 \times p - 100)$, $E_{had} < 6 + Max(0, 0.0280 \times p - 100)$, $z_0 < 60$ cm, $p_T > 10$ GeV/c, $d_0 < 0.02$ cm (if track had SVX hits), and $d_0 < 0.20 <$ cm (if track had no SVX hits). To appear on the list, electrons must have have a track, $E_{had}/E_{em} < 0.055 + 0.0045 \times (E_{em} + E_{had})$, $z_0 < 60$ cm, and $E_T > 10$ GeV.

After making the lists, we recalculated the standard isolations using the standard method:

$$CalIso = \frac{E_T^{cone} - E_T^{electron}}{E_T^{electron}},$$

with the track isolation defined as above, using tracks instead of calorimeter energies. In the case that a tower of track on the list was found within the 0.4 ΔR_{ll} cone, the towers and tracks corresponding to the other, high quality muon or electron, were vetoed from the calculation. This then greatly reduces lepton candidates mutually spoiling each others isolation.

We used the new isolations described here for all categories with the exceptions of CrkTrk, IsoCrkTrk, CMIOPES, BMU, PHX, and PLBE. These categories proved susceptible to duplicate tracks, resulting in artificially low isolations.

3 Updated Lepton Identification

The current Higgs searches are mainly statistically limited; for this reason it's important to maximize the acceptance of the analysis. Since we're looking at both Ws decaying leptonically, one of the key points in maximizing the acceptance is the lepton identification for electrons and muons[1].

Previous $H \to WW$ analyses rely on the lepton identification described in CDF Note 8538 [7], which aims to exploit every region of the CDF detector where an energy measurement can be made to define a set of unique (non-overlapping) categories for electron and muon identification. The muon selections were updated in the most recent $H \to WW$ analysis, described in CDF Note 9697 [5]. The analysis presented in 9697 used the following categories:

- Electrons: TCE, PHX
- Muons: CMUP, CMP, CMU, CMX, CMXMsKs, BMU, CMIOCES, CMIOPES, CrkTrk

The triggers used to collect the data sample for this analysis are based on leptons, and are deeply connected with the lepton definitions. Trigger paths exploited by the analysis in Note 9402 can be summarized in 4 categories (present in the CDF trigger tables in various versions):

- MUON_CMUP18
- MUON_CMP18_PHI_GAP
- MUON_CMX18
- ELECTRON_CENTRAL_18
- MET_PEM

The CMU muons triggered by the MUON_CMU18_ETA_GAP path will be included in a later version of the analysis, as this trigger has only been working properly since period 21 data-taking.

The aim of the study described in this CDF Note is to improve electron identification using a likelihood method. In Section 3.1 we describe in detail this likelihood method. Sections 3.2 and 3.3 describe the lepton ID scale factor and fake rate calculations for each of the categories. Finally, we perform the strongest check of the new electrons' behavior in Section 3.4, measuring the cross section of the Drell-Yan ($p\bar{p} \to Z/\gamma^{\star} \to l^{+}l^{-}$, $l = e, \mu$) process separately for each dilepton type.

---

[1] τ's are currently considered only if decaying to an electron or muon. Studies are ongoing to include hadronically decaying τ's in the same framework, but they will not be discussed in this note.

3.1 Likelihood Method for Lepton Identification

The standard method for lepton identification uses cuts on many different identification variables (see TCE definition in Tab. 1). Each cut decreases reconstruction efficiency, and candidates which fail even one cut by a small margin are removed from the sample. Finding each possible lepton candidate is extremely important in such low-statistics searches as looking for the Higgs boson at the Tevatron.

Therefore we developed a method which tries to exploit the identification variables in better way. Instead of cutting on each individual variable, we combine identification variables into one discriminant and cut only on the value of this final discriminant. It is expected that this should increase the efficiency of reconstruction (while keeping the same fake rate). The method we use is a likelihood method, which calculates the probability of a candidate to be a real or "fake" lepton and computes the likelihood discriminant.

Currently we apply the method only on central electron candidates. In the previous analysis described in CDF Note 9863 [1], these newly identified central electrons (Likelihood-Based Electrons, LBE) replaced the TCE category, as nearly all TCE passed the LBE criteria. However, it was found that the Monte Carlo did not model well the charge fake rate of LBE. Thus using LBE instead of TCE caused an increase in observed background over the expectations for the same-sign dilepton search. For this updated analysis, we have separated TCE and LBE categories. TCE are defined identically to Tab. 1. The LBE are now defined as electron candidates which do not satisfy TCE criteria but do pass the likelihood selection. The only disadvantage to this separation is that the statistics for LBE dilepton categories are limited in some channels. The statistics are sufficient to determine efficiencies and measure Drell-Yan cross sections, but these have larger uncertainties than in the TCE categories.

3.1.1 Likelihood definition for central electrons

For our likelihood method, we choose most of the identification, non-kinematic variables which were used in identification of TCE (for definition of TCE, see Tab. 1). Specifically, these are

- E_{HAD}/E_{EM} – the ratio of the hadronic calorimeter energy to the electromagnetic calorimeter energy associated with the candidate
- E/P – the ratio of the EM cluster transverse energy to the COT track transverse momentum
- $Lshr$ – the lateral shower profile in the transverse plane to the electron direction
- $CalIso$ – The energy E_T in a cone of radius $\Delta R = \sqrt{(\Delta\eta)^2 + (\Delta\phi)^2} \leq 0.4$ around the electron cluster excluding the electron cluster divided by the energy in the

electron cluster:

$$CalIso = \frac{E_T^{cone} - E_T^{electron}}{E_T^{electron}}$$

- $TrkIso$ – the same variable as above $CalIso$ but measured using tracks instead of calorimeter
- $Q \times \Delta x_{CES}$ – The distance in the r-ϕ plane between the extrapolated, COT beam constrained track and the best matching CES cluster, times the charge Q of the track.
- Δz_{CES} – The distance in the r-z plane between the extrapolated, COT beam constrained track and the best matching CES cluster.
- $NCotHitsAx$ – number of COT hits on axial layers belonging to track associated to the candidate electron
- $NCotHitsSt$ – number of COT hits on stereo layers belonging to track associated to the candidate electron
- χ^2_{COT} – χ^2 associated with the COT hits belonging to track
- $NSvxHits$ – number of SVX hits belonging to track associated to the candidate electron

These variables are then used in calculation of the likelihood which has the following form:

$$\mathcal{L}(\vec{x}) = \frac{L_{sig}}{L_{sig} + L_{bckg}} = \frac{\prod_{i=1}^{N} P_i^{sig}(x_i)}{\prod_{i=1}^{N} P_i^{sig}(x_i) + \prod_{i=1}^{N} P_i^{bckg}(x_i)} \tag{1}$$

where

- x_i – means the i-th identification variable used in the likelihood. These are the 11 variables described above.
- N - the number of ID variables, in our case 11.
- $P_i^{sig}(x_i), P_i^{bckg}(x_i)$ - these are the functions which give the probability to obtain a certain value x_i for the i-th ID variable. These are obtained using signal and background (“fakes”) templates.

By definition, the value of $\mathcal{L}$ is restricted within the range $(0.0, 1.0)$. As can be seen, the essential feature of this method is to obtain templates for ID variables for real electrons and “fakes”.

	TCE
Region	central
Fiducial	track fiducial to CES
Track p_T	≥ 10 $(5 if E_T < 20)$
Track $\|z_0\|$	≤ 60 cm
# Ax SL (5hits)	≥ 3
# St SL (5hits)	≥ 2
Conversion	$\neq 1$
E_{HAD}/E_{EM}	$\leq 0.055 + 0.00045 * E$
Iso/E_T	≤ 0.1
Lshr	≤ 0.2
E/P	$< 2.5 + 0.015 * E_T$
signed CES ΔX	$-3 \leq q * \Delta X \leq 1.5$ cm
CES $\|\Delta Z\|$	< 3 cm
Track	Beam constrained

Table 1: Definition of TCE.

Central electron probe
Track or SMX fiducial to CES
Track $p_T \geq 5$ GeV
Track $Z_0 \leq 60$ cm

Table 2: Definition of central electron probe object.

Central fakeable electron
Track fiducial to CES
$E_{HAD}/E_{EM} <= 0.125 + 0.00045 * E$
$CalIso < 0.3$
not a conversion

Table 3: Definition of central electron fakeable object.

3.1.2 Building of signal and background templates

We use data to build the signal and background templates. This is done by selecting samples dominated by real high p_T electrons (Z boson candidates) for signal templates and dominated by fake electrons (dijet data) for background templates.

Building of the signal templates is done as follows (very similar selection to one use for efficiency calculation, see [7]). We select Z candidates (76 GeV < $\mathrm{M}_{\ell\ell}$ < 106 GeV) from high p_T electron data (bhelbj dataset) where one electron is a fully identified central electron (TCE) while the second electron candidate must pass just basic central electron object criteria (must pass "CEM probe" criteria, see definition in Tab. 2). We also require opposite charge between identified electron and "Probe" object ("probe" should also not be a conversion) where both have $E_T > 10$ GeV. Such a sample is completely dominated by Drell-Yan events. The ID variables of these probes are used to make the signal templates. In the case where both legs are identified as TCE, they are both used for template creation.

Building of the templates for "fakes" is done the following way (very similar selection to one used in fake rate calculation, see [7]). We select candidates from jet data (JET20 dataset - gjt1bk) where there is one identified jet ($E_T > 20$ GeV) and another fakeable object ("CEM Fakeable" object, see definition in Tab. 3). We also require

- the "fakeable" object must pass basic kinematic criteria: $E_T > 10\ GeV$, track $p_T > 5\ GeV$, $|z_0| < 60\ cm$.
- the combination of jet and fakeable object fall out of the Z mass peak $(76\ GeV, 106\ GeV)$ to remove contribution from Z events
- fakeable electron is not in the leading E_T jet in order to remove trigger bias (also leading jet must have $E_T^{raw} > 20$ GeV).
- leading jet $|z_0| < 60$ cm and $|\Delta z_0(``fakeable'' \ object\ and\ leading\ jet)| < 4$ cm.
- reject cosmic events

Since we obtained our templates using data samples, our templates contain background events. In the case of signal, this means "fake" electrons, in case of the templates for "fakes", this means real electrons. Therefore we perform background subtraction to the templates. The background subtraction is done the following way:

- For signal: We plot the distribution of likelihood variables for the probes. As can be seen in Fig. 1, the histogram has a very sharp peak at 1.0 while having a small bump at 0.0 (for the background case, this is opposite). We normalize the likelihood distribution for the "fakes" in such way that it has the same value in the first bin as the value in the 1st bin of the signal likelihood distribution. By obtaining the integral over whole range (0.0,1.0), we get an estimate of the number of "fake"

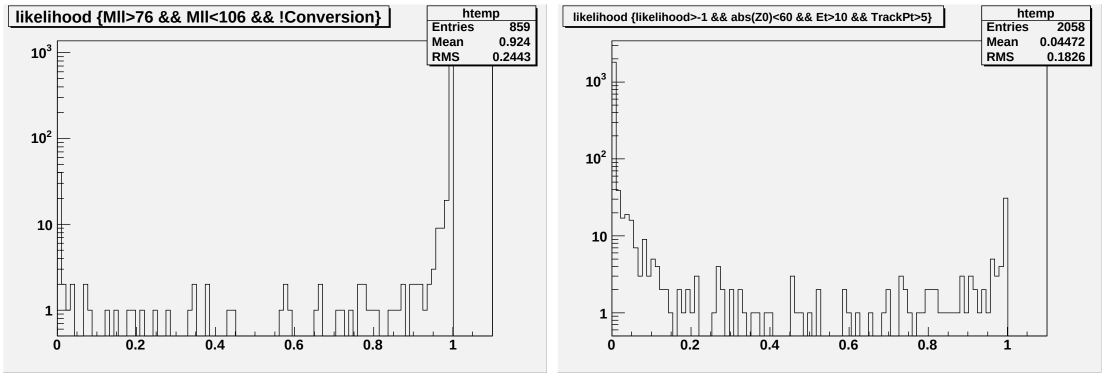

Figure 1: Likelihood distribution for signal probes (left) and fakeable objects (right).

electrons in the signal templates. This turns out to be small ($\sim 3\%$). We then subtract such fraction of background templates from signal templates.

- For fakes: we estimate the expected contribution of "signal" events (real electrons) in the background templates using $W \to \ell\nu$ and $Z \to ee$ MC samples. This turns out to be an even smaller effect ($\sim 1\%$), but we again subtract the signal templates (appropriately scaled to 1%) from the background templates.

The signal and background templates for all used electron ID variables are shown in Figs. 2 through 5. Just for comparison, there are shown distributions of variables for data and MC ($Z \to ee$) in signal case and JET20 and JET100 samples in case of background templates. For signal, the data and MC distributions agree quite well for most of the variables. For background, JET20 and JET100 do not agree very well due to the fact that some of the variables are E_T dependent, and the E_T spectrum of these two datasets is quite different. Since the JET20 E_T distribution is closer to what we expect for our signal sample, we use the templates obtained from the JET20 sample.

3.1.3 Likelihood based electron (LBE)

We define a new central electron category, the likelihood based electron (LBE), which we will use in addition to TCE electrons. We first apply basic identification and kinematic criteria on electron candidates and then make a cut on the likelihood value at the end. All the requirements used for LBEs are listed below:

- have CEM fiducial track
- $Z_0(track) < 60$ cm
- electron candidate is not a conversion
- $E_{HAD}/E_{EM} < 0.125$ to satisfy the trigger requirement

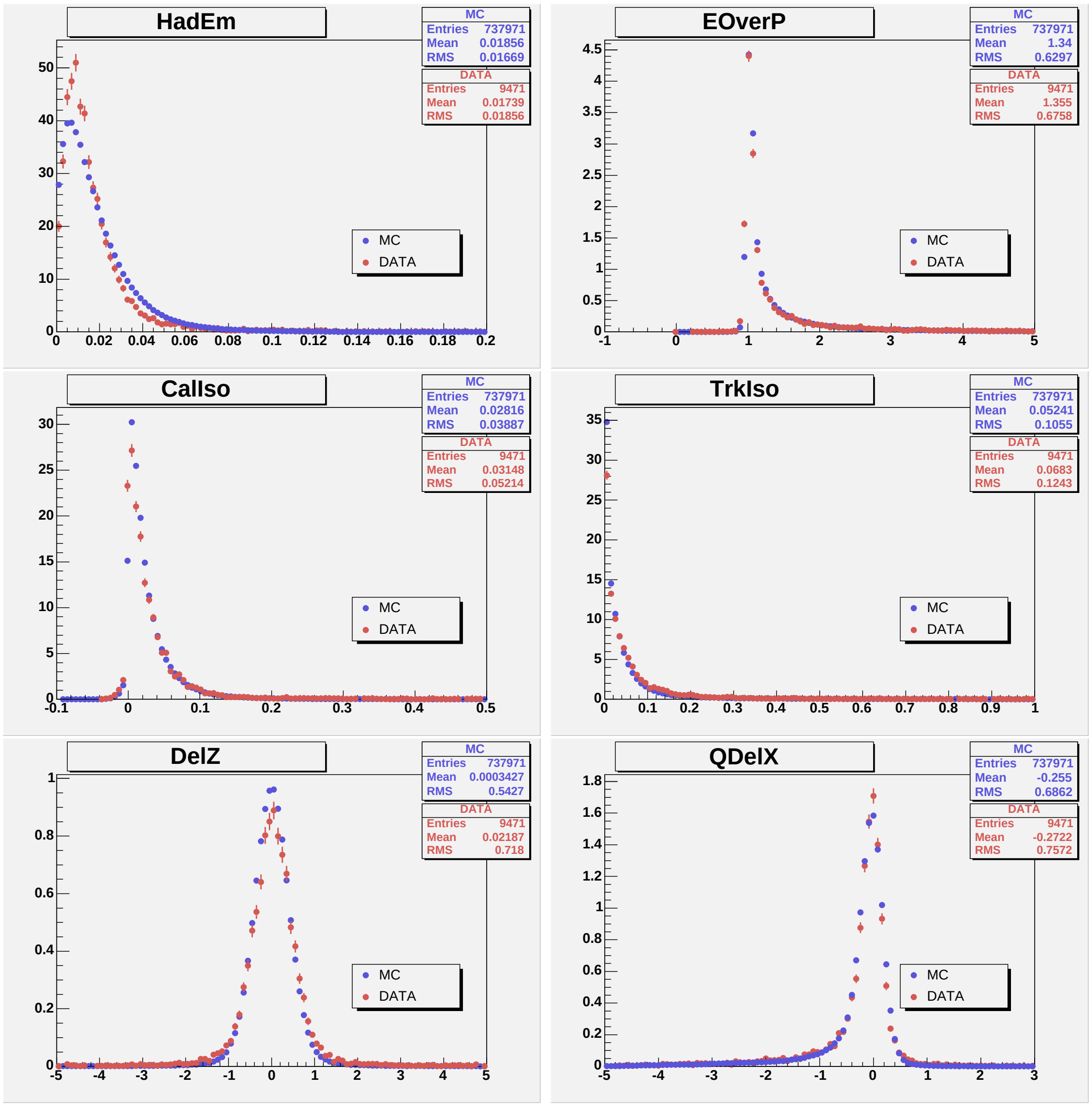

Figure 2: Signal templates for the likelihood method.

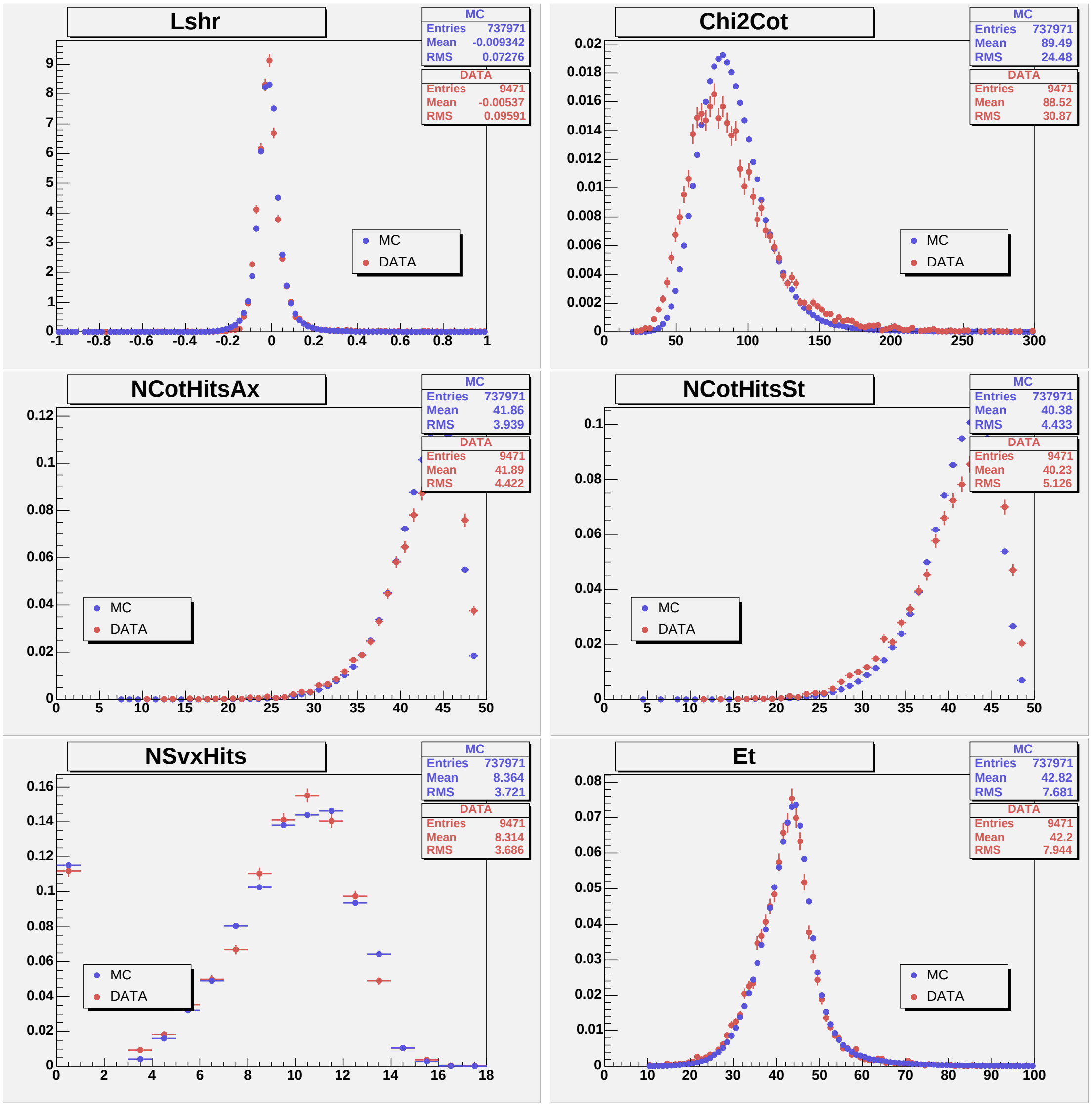

Figure 3: Signal templates for the likelihood method.

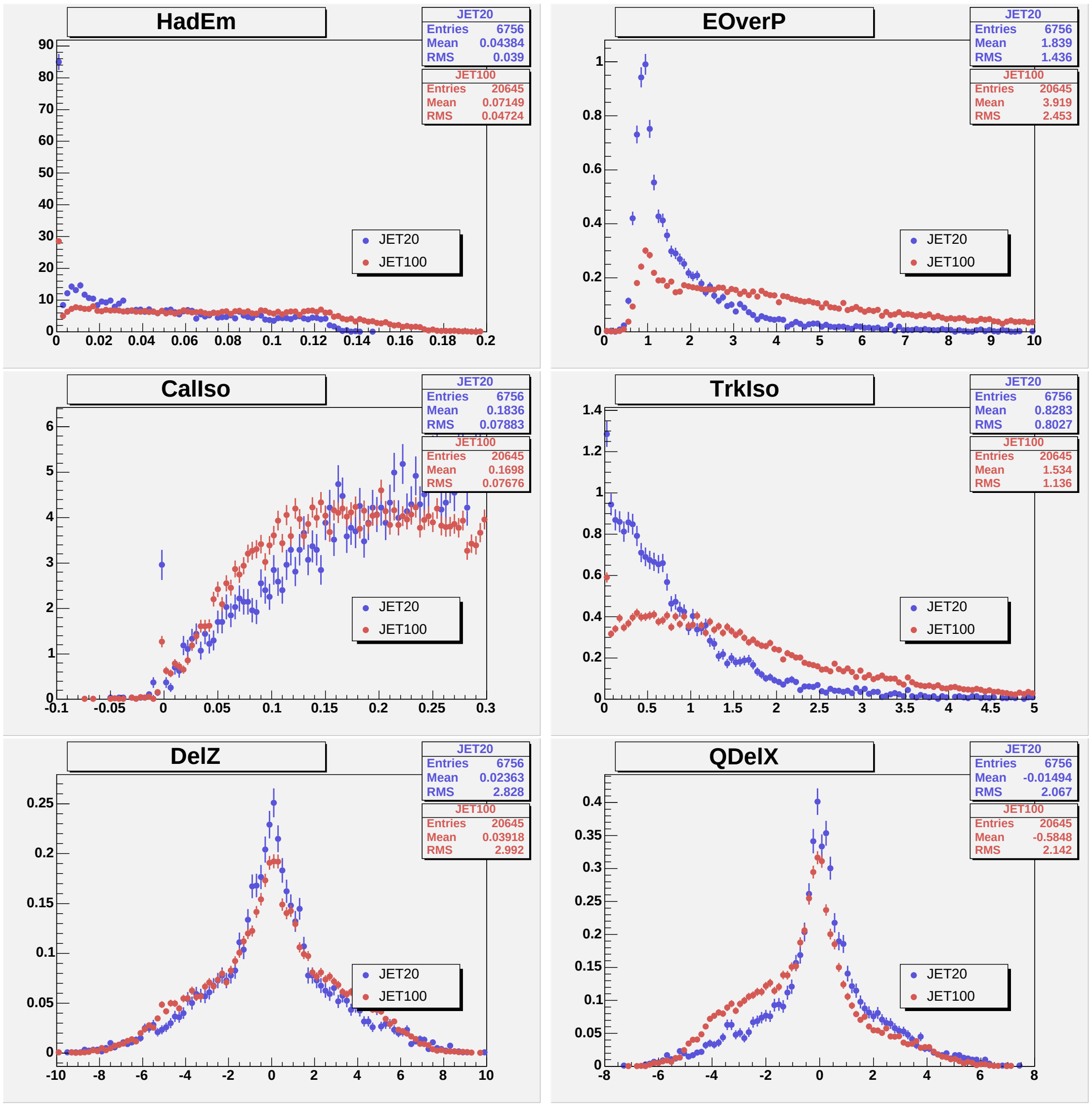

Figure 4: Background templates for the likelihood method.

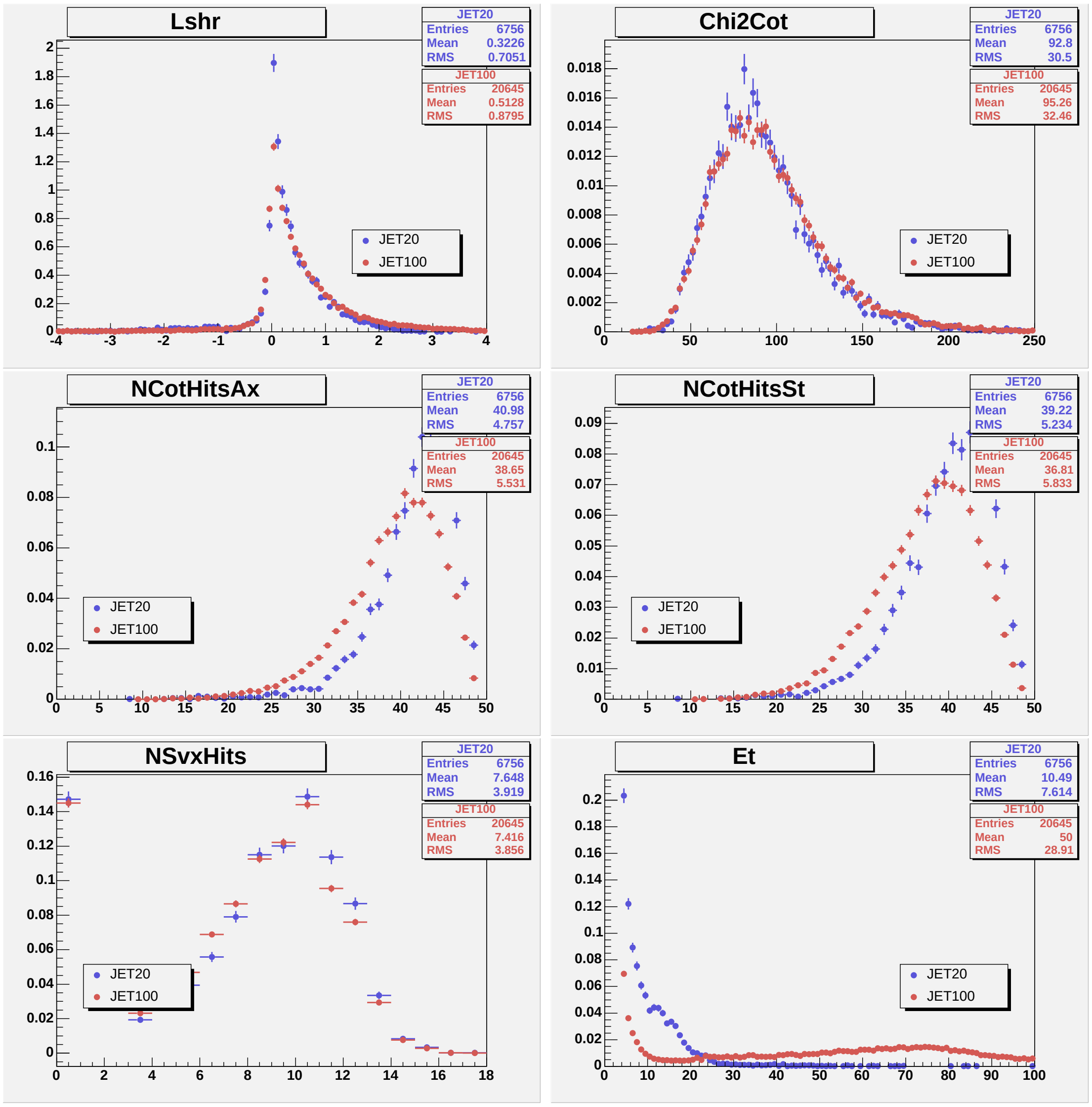

Figure 5: Background templates for the likelihood method.

- $CalIso < 0.3$ - weak cut on the calorimeter isolation to satisfy the requirement on fakeable objects used in the template building procedure
- $p_T(track) > 10$ GeV ($p_T(track) > 5$ GeV if $E_T < 20$ GeV)
- $\mathcal{L} > \mathcal{L}_{cut}$ - value of likelihood must be greater than a cut value, which we set to $\mathcal{L}_{cut} = 0.90$ according to the optimization described in the next section, Sec. 3.1.4. The value of this cut was changed from $\mathcal{L}_{cut} = 0.99$ as compared to the previous version of this analysis described in CDF Note 9863 [1].

One assumption which we use for LBE is that it has the same trigger efficiency as TCE. We checked this assumption by selecting $e - \mu$ events from our signal region with 0 jets, with a requirement that the μ fires the trigger. By checking how often TCE and LBE pass the trigger requirement, we obtained the following trigger efficiency for TCE ($78/83 = 0.94$) and for LBE ($84/88 = 0.95$). Within our limited statistics, we conclude that the trigger efficiency is the same for LBE and TCE. However, for the future we plan to make more a detailed study of this assumption.

3.1.4 Optimization of LBE likelihood cut

We optimized the cut on the likelihood ratio by calculating the reconstruction efficiency and LBE fake rates for different possible cuts. The reconstruction efficiency is calculated for the Drell-Yan control region using both the data and the Drell-Yan MC samples. The fake rates are calculated from jet-triggered data samples as described in Sec. 3.3. Looking at these dependencies (see Fig. 6), we conclude that moving the cut from 0.99 down to 0.9 will get us most of the available efficiency gain ($\sim 5\%$ in data) while still keeping the fake rates about the same (within systematic and statistical uncertainties) except for very low E_T jets. Thus we decide to use a cut of 0.90 for LBEs in this updated analysis.

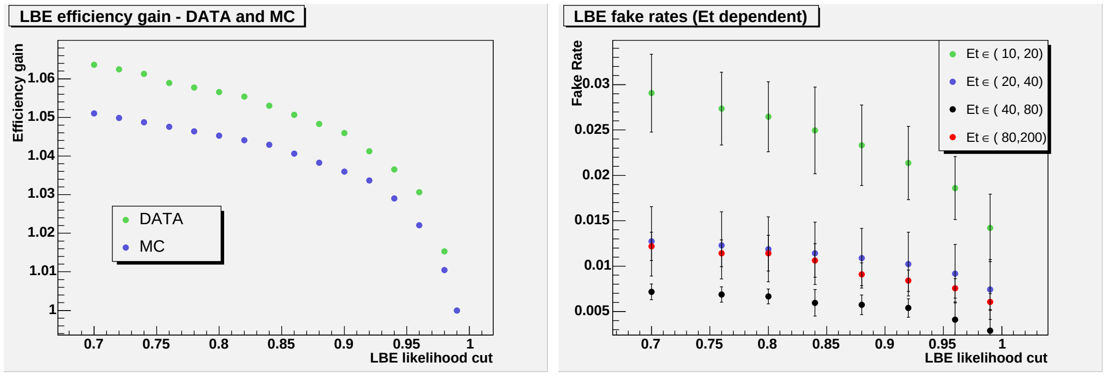

Figure 6: The likelihood ratio cut dependence of reconstruction efficiency (left) and fake rates for LBEs (right). The reconstruction efficiency is shown as a ratio with the efficiency for a LBE > 0.99 cut; the value of 1.05 for LBE > 0.90 indicates a 5% gain over a cut of LBE > 0.99. The fake rates are shown summed over bins of jet E_T; by relaxing the LBE cut from 0.99 to 0.90, the fake rate increases for low E_T jets, but stays nearly the same (within systematic and statistical uncertainties) for jets with $E_T > 20$ GeV.

3.2 Lepton ID Scale Factors

To measure lepton ID scale factors, we measure the lepton efficiencies in both data and MC simulation and divide the two result to apply a per-event SF to our MC simulations. We again use the *tag & probe* method, selecting Z candidates in the $76 < m(ll) < 106$ GeV dilepton invariant mass window, as described in the CDF Note 8538 [7]. As explained in detail in this reference, we use probe objects for which we assume MC simulation well describes the efficiency, and calculate only the efficiency on top of these requirements. Generic probes are defined for Central and Forward muons and then used with the fiduciality requirement to define the actual probe to be used in the efficiency calculation. Background subtraction is also performed using data from the Z-mass sidebands.

Results are shown in Tables 5-18, grouped by run period ranges as defined in the official webpage [8]. The only exception is what we call period 0k, which groups also data acquired in the 0m dataset, since these data are pretty homogenous. Efficiencies, as well as scale factors, are calculated for both track isolated (which are the ones actually used in the analysis, except for PHX and LBE) and non-track isolated leptons. For LBE categories, since track isolation is an input to the likelihood, we use LBE without the track isolation cut. To qualify as an LBE-only, an electron candidate must not satisfy the TCE with track isolation criteria. For other candidates, track isolation (< 0.1) is required in a cone of 0.4 around the leptons. We also calculate the electron efficiencies that will be used in the analysis with exactly the same method described in [7]. As also in this reference, we calculate efficiencies for stubless categories as the difference of the one removing vetos and the veto efficiency, in order to properly account for stubbed muon SFs using the same formulas described in that note. For CMIOPES and BMU categories, we apply the PES tracking efficiency scale factor to account for forward tracking reconstruction scale factors between data and MC. This scale factor is evaluated using electrons, since that is the only way to measure it in data, but should also model well what happens for muons.

We observe an excess of central tracks in MC reconstructed near the bottom 90° of the COT. Figure 7 shows the ϕ distribution for central tracks with $\rho_{COT} > 140$ cm in Z events selected with a CMUP tag leg and requiring $86 < m(ll) < 106$ GeV for different run periods (p0-p9, p10-p13, and p14-p23). Data and Monte Carlo distributions are normalized in the region $0° < \phi < 225°$ and $315° < \phi < 360°$. Since the effect is clearly dependent on the run period, we apply a scale factor to all central muon types which point in the $225° < \phi < 315°$ region depending on the run period as shown in Table 4. This ϕ-dependent excess of tracks is not observed for central electron types.

Period	SF
0-9	1.001
10-13	0.945
14-27	0.870

Table 4: Scale Factor evaluated for muons pointing to the bottom 90° of the detector.

Run Range: 0d

	data	MC	Scale Fac
CMUP	0.879 ± 0.011	0.903 ± 0.001	0.973 ± 0.012
CMU	0.000 ± 1.000	0.000 ± 1.000	0.000 ± 1.000
CMP	0.000 ± 1.000	0.000 ± 1.000	0.000 ± 1.000
CMX	0.947 ± 0.014	0.922 ± 0.003	1.028 ± 0.016
CMXMsKs	0.000 ± 1.000	0.000 ± 1.000	0.000 ± 1.000
BMU	0.826 ± 0.023	0.733 ± 0.004	1.127 ± 0.033
CMIOCES	0.367 ± 0.005	0.350 ± 0.002	1.049 ± 0.017
CMIOPES	0.689 ± 0.012	0.689 ± 0.002	1.000 ± 0.018
CrkTrk μ	0.733 ± 0.011	0.765 ± 0.002	0.958 ± 0.015
CMUP Trk Iso	0.869 ± 0.011	0.896 ± 0.001	0.970 ± 0.012
CMU Trk Iso	0.000 ± 1.000	0.000 ± 1.000	0.000 ± 1.000
CMP Trk Iso	0.000 ± 1.000	0.000 ± 1.000	0.000 ± 1.000
CMX Trk Iso	0.927 ± 0.014	0.912 ± 0.003	1.016 ± 0.016
CMXMsKs Trk Iso	0.000 ± 1.000	0.000 ± 1.000	0.000 ± 1.000
BMU Trk Iso	0.816 ± 0.024	0.725 ± 0.004	1.126 ± 0.033
CMIOCES Trk Iso	0.363 ± 0.005	0.347 ± 0.002	1.048 ± 0.017
CMIOPES Trk Iso	0.667 ± 0.012	0.683 ± 0.002	0.977 ± 0.018
CrkTrk μ Trk Iso	0.719 ± 0.011	0.756 ± 0.002	0.951 ± 0.015

Table 5: Muon efficiencies for dataset 0d (period 0) with and without track isolation cut.

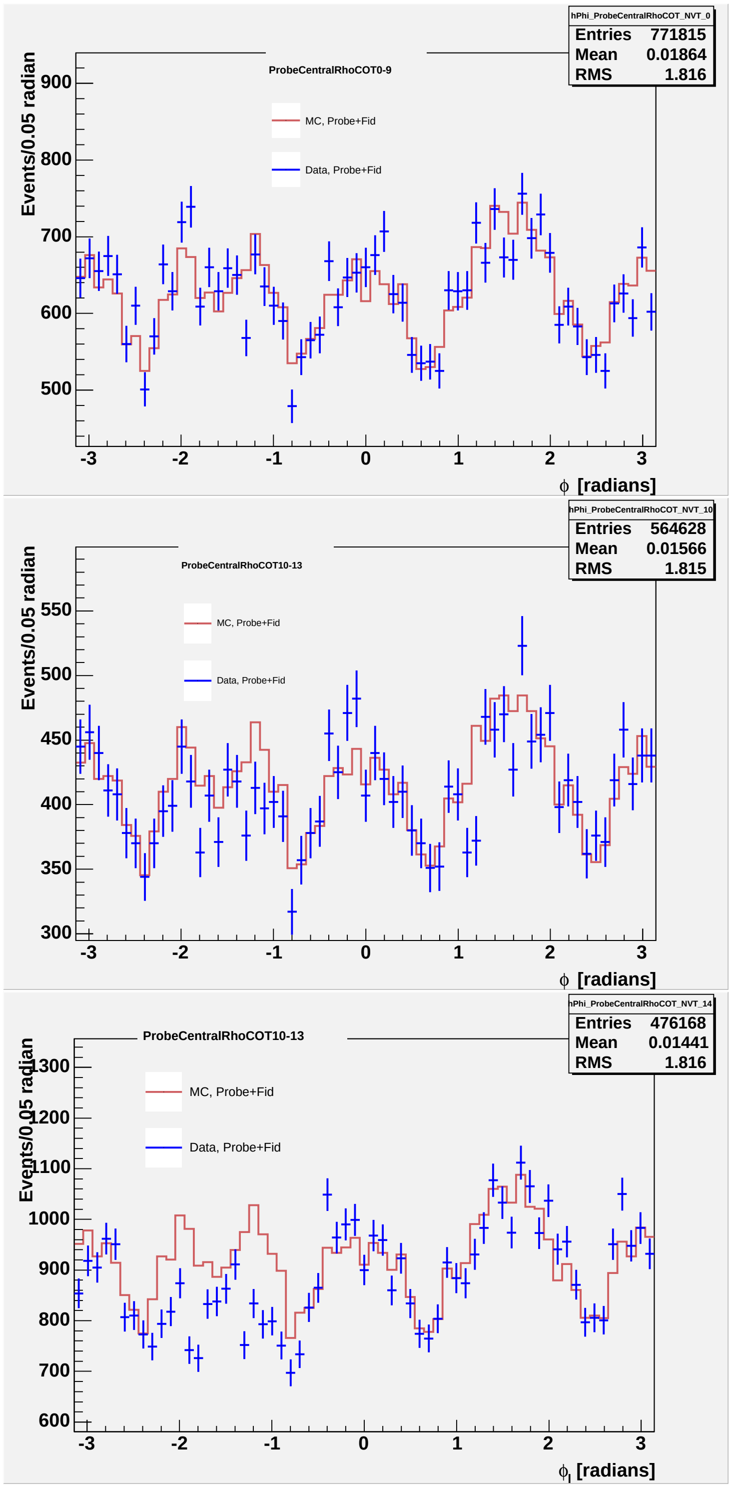

Figure 7: ϕ distribution for central tracks in Z events selected with a CMUP tag. Data periods 0 to 9 shown on top, periods 10 to 13 in the middle, and periods 14 to 23 on the bottom.

Run Range: 0h

	data	MC	Scale Fac
CMUP	0.847 ± 0.008	0.903 ± 0.001	0.938 ± 0.009
CMU	0.000 ± 0.500	0.000 ± 0.500	0.000 ± 0.500
CMP	0.000 ± 0.500	0.000 ± 0.500	0.000 ± 0.500
CMX	0.938 ± 0.015	0.920 ± 0.002	1.019 ± 0.017
CMXMsKs	0.000 ± 0.500	0.000 ± 0.500	0.000 ± 0.500
BMU	0.797 ± 0.018	0.720 ± 0.003	1.107 ± 0.025
CMIOCES	0.363 ± 0.005	0.343 ± 0.001	1.060 ± 0.014
CMIOPES	0.609 ± 0.012	0.606 ± 0.002	1.005 ± 0.020
CrkTrk μ	0.777 ± 0.009	0.795 ± 0.002	0.977 ± 0.012
CMUP Trk Iso	0.834 ± 0.008	0.895 ± 0.001	0.932 ± 0.010
CMU Trk Iso	0.000 ± 0.500	0.000 ± 0.500	0.000 ± 0.500
CMP Trk Iso	0.000 ± 0.500	0.000 ± 0.500	0.000 ± 0.500
CMX Trk Iso	0.906 ± 0.016	0.908 ± 0.002	0.998 ± 0.018
CMXMsKs Trk Iso	0.000 ± 0.500	0.000 ± 0.500	0.000 ± 0.500
BMU Trk Iso	0.767 ± 0.018	0.714 ± 0.003	1.075 ± 0.026
CMIOCES Trk Iso	0.354 ± 0.005	0.339 ± 0.001	1.043 ± 0.015
CMIOPES Trk Iso	0.588 ± 0.012	0.601 ± 0.002	0.979 ± 0.020
CrkTrk μ Trk Iso	0.760 ± 0.009	0.785 ± 0.002	0.967 ± 0.012

Table 6: Muon efficiencies for dataset 0h (periods 1-4) with and without track isolation cut.

Run Range: 0i1

	data	MC	Scale Fac
CMUP	0.840 ± 0.011	0.902 ± 0.001	0.931 ± 0.012
CMU	0.000 ± 0.577	0.000 ± 0.577	0.000 ± 0.577
CMP	0.000 ± 0.577	0.000 ± 0.577	0.000 ± 0.577
CMX	0.942 ± 0.017	0.919 ± 0.003	1.026 ± 0.019
CMXMsKs	0.000 ± 0.577	0.000 ± 0.577	0.000 ± 0.577
BMU	0.775 ± 0.023	0.721 ± 0.004	1.075 ± 0.032
CMIOCES	0.369 ± 0.006	0.340 ± 0.002	1.085 ± 0.018
CMIOPES	0.617 ± 0.015	0.599 ± 0.003	1.029 ± 0.025
CrkTrk μ	0.774 ± 0.012	0.793 ± 0.002	0.976 ± 0.015
CMUP Trk Iso	0.830 ± 0.011	0.892 ± 0.002	0.931 ± 0.013
CMU Trk Iso	0.000 ± 0.577	0.000 ± 0.577	0.000 ± 0.577
CMP Trk Iso	0.000 ± 0.577	0.000 ± 0.577	0.000 ± 0.577
CMX Trk Iso	0.903 ± 0.018	0.905 ± 0.003	0.997 ± 0.020
CMXMsKs Trk Iso	0.000 ± 0.577	0.000 ± 0.577	0.000 ± 0.577
BMU Trk Iso	0.752 ± 0.023	0.715 ± 0.004	1.051 ± 0.033
CMIOCES Trk Iso	0.362 ± 0.006	0.336 ± 0.002	1.077 ± 0.019
CMIOPES Trk Iso	0.600 ± 0.015	0.594 ± 0.003	1.009 ± 0.025
CrkTrk μ Trk Iso	0.758 ± 0.012	0.783 ± 0.002	0.968 ± 0.015

Table 7: Muon efficiencies for dataset 0i1 (periods 5-7) with and without track isolation cut.

Run Range: 0i2

	data	MC	Scale Fac
CMUP	0.857 ± 0.007	0.897 ± 0.001	0.955 ± 0.008
CMU	0.000 ± 0.577	0.000 ± 0.577	0.000 ± 0.577
CMP	0.888 ± 0.029	0.919 ± 0.003	0.966 ± 0.032
CMX	0.920 ± 0.013	0.914 ± 0.002	1.007 ± 0.014
CMXMsKs	0.842 ± 0.033	0.908 ± 0.003	0.929 ± 0.036
BMU	0.799 ± 0.015	0.725 ± 0.003	1.100 ± 0.021
CMIOCES	0.328 ± 0.004	0.299 ± 0.001	1.092 ± 0.013
CMIOPES	0.586 ± 0.011	0.598 ± 0.002	0.980 ± 0.018
CrkTrk μ	0.709 ± 0.009	0.731 ± 0.001	0.971 ± 0.012
CMUP Trk Iso	0.837 ± 0.007	0.886 ± 0.001	0.944 ± 0.009
CMU Trk Iso	0.000 ± 0.577	0.000 ± 0.577	0.000 ± 0.577
CMP Trk Iso	0.852 ± 0.029	0.907 ± 0.003	0.939 ± 0.032
CMX Trk Iso	0.906 ± 0.013	0.900 ± 0.002	1.007 ± 0.014
CMXMsKs Trk Iso	0.791 ± 0.032	0.895 ± 0.004	0.885 ± 0.036
BMU Trk Iso	0.759 ± 0.015	0.719 ± 0.003	1.055 ± 0.022
CMIOCES Trk Iso	0.318 ± 0.004	0.295 ± 0.001	1.072 ± 0.014
CMIOPES Trk Iso	0.560 ± 0.011	0.591 ± 0.002	0.947 ± 0.018
CrkTrk μ Trk Iso	0.681 ± 0.009	0.719 ± 0.001	0.948 ± 0.012

Table 8: Muon efficiencies for dataset 0i2 (periods 8-10) with and without track isolation cut.

Run Range: 0j

	data	MC	Scale Fac
CMUP	0.825 ± 0.009	0.894 ± 0.001	0.924 ± 0.011
CMU	0.000 ± 0.707	0.000 ± 0.707	0.000 ± 0.707
CMP	0.817 ± 0.020	0.916 ± 0.002	0.892 ± 0.022
CMX	0.898 ± 0.016	0.915 ± 0.002	0.981 ± 0.018
CMXMsKs	0.852 ± 0.028	0.911 ± 0.003	0.936 ± 0.031
BMU	0.773 ± 0.020	0.727 ± 0.003	1.064 ± 0.028
CMIOCES	0.303 ± 0.004	0.252 ± 0.001	1.202 ± 0.019
CMIOPES	0.560 ± 0.013	0.586 ± 0.002	0.956 ± 0.023
CrkTrk μ	0.576 ± 0.011	0.582 ± 0.002	0.990 ± 0.020
CMUP Trk Iso	0.796 ± 0.009	0.882 ± 0.001	0.903 ± 0.011
CMU Trk Iso	0.000 ± 0.707	0.000 ± 0.707	0.000 ± 0.707
CMP Trk Iso	0.795 ± 0.020	0.904 ± 0.002	0.881 ± 0.022
CMX Trk Iso	0.867 ± 0.016	0.896 ± 0.002	0.967 ± 0.018
CMXMsKs Trk Iso	0.840 ± 0.028	0.896 ± 0.003	0.938 ± 0.031
BMU Trk Iso	0.748 ± 0.020	0.720 ± 0.004	1.039 ± 0.029
CMIOCES Trk Iso	0.287 ± 0.004	0.248 ± 0.001	1.159 ± 0.019
CMIOPES Trk Iso	0.533 ± 0.013	0.580 ± 0.002	0.920 ± 0.023
CrkTrk μ Trk Iso	0.549 ± 0.011	0.571 ± 0.002	0.962 ± 0.020

Table 9: Muon efficiencies for dataset 0j (period 11-12) with and without track isolation cut.

Run Range: 0j13

	data	MC	Scale Fac
CMUP	0.839 ± 0.010	0.895 ± 0.001	0.937 ± 0.012
CMU	0.000 ± 1.000	0.000 ± 1.000	0.000 ± 1.000
CMP	0.819 ± 0.020	0.913 ± 0.003	0.897 ± 0.023
CMX	0.900 ± 0.018	0.913 ± 0.003	0.986 ± 0.020
CMXMsKs	0.815 ± 0.030	0.916 ± 0.003	0.890 ± 0.032
BMU	0.795 ± 0.025	0.696 ± 0.004	1.142 ± 0.037
CMIOCES	0.300 ± 0.006	0.253 ± 0.002	1.184 ± 0.024
CMIOPES	0.520 ± 0.019	0.521 ± 0.003	0.999 ± 0.036
CrkTrk μ	0.560 ± 0.012	0.588 ± 0.002	0.952 ± 0.021
CMUP Trk Iso	0.815 ± 0.010	0.884 ± 0.001	0.922 ± 0.012
CMU Trk Iso	0.000 ± 1.000	0.000 ± 1.000	0.000 ± 1.000
CMP Trk Iso	0.804 ± 0.020	0.901 ± 0.003	0.893 ± 0.023
CMX Trk Iso	0.886 ± 0.018	0.898 ± 0.003	0.986 ± 0.020
CMXMsKs Trk Iso	0.794 ± 0.029	0.904 ± 0.003	0.879 ± 0.032
BMU Trk Iso	0.773 ± 0.025	0.692 ± 0.004	1.118 ± 0.037
CMIOCES Trk Iso	0.290 ± 0.006	0.249 ± 0.002	1.165 ± 0.024
CMIOPES Trk Iso	0.496 ± 0.018	0.517 ± 0.003	0.959 ± 0.036
CrkTrk μ Trk Iso	0.542 ± 0.012	0.578 ± 0.002	0.937 ± 0.021

Table 10: Muon efficiencies for dataset 0j13 (period 13) with and without track isolation cut.

Run Range: 0k

	data	MC	Scale Fac
CMUP	0.787 ± 0.003	0.889 ± 0.001	0.885 ± 0.004
CMU	0.000 ± 1.000	0.000 ± 1.000	0.000 ± 1.000
CMP	0.792 ± 0.007	0.911 ± 0.002	0.869 ± 0.008
CMX	0.887 ± 0.006	0.906 ± 0.002	0.979 ± 0.007
CMXMsKs	0.821 ± 0.009	0.907 ± 0.002	0.905 ± 0.010
BMU	0.771 ± 0.008	0.705 ± 0.003	1.094 ± 0.012
CMIOCES	0.300 ± 0.002	0.252 ± 0.001	1.188 ± 0.011
CMIOPES	0.562 ± 0.005	0.582 ± 0.002	0.966 ± 0.009
CrkTrk μ	0.563 ± 0.004	0.589 ± 0.001	0.955 ± 0.007
CMUP Trk Iso	0.766 ± 0.003	0.875 ± 0.001	0.875 ± 0.004
CMU Trk Iso	0.000 ± 1.000	0.000 ± 1.000	0.000 ± 1.000
CMP Trk Iso	0.768 ± 0.007	0.897 ± 0.002	0.856 ± 0.008
CMX Trk Iso	0.857 ± 0.006	0.887 ± 0.002	0.967 ± 0.007
CMXMsKs Trk Iso	0.789 ± 0.009	0.891 ± 0.002	0.886 ± 0.010
BMU Trk Iso	0.758 ± 0.008	0.696 ± 0.003	1.089 ± 0.012
CMIOCES Trk Iso	0.290 ± 0.002	0.248 ± 0.001	1.168 ± 0.011
CMIOPES Trk Iso	0.557 ± 0.005	0.574 ± 0.002	0.970 ± 0.010
CrkTrk μ Trk Iso	0.545 ± 0.004	0.577 ± 0.001	0.945 ± 0.007

Table 11: Muon efficiencies for dataset 0k (periods 14-27) with and without track isolation cut.

Run Range: 0d

	data	MC	Scale Fac
LBE ($L > 0.9$)	0.911 ± 0.003	0.900 ± 0.001	1.013 ± 0.003
LBE ($L > 0.9$)only	0.093 ± 0.003	0.090 ± 0.001	1.044 ± 0.030
TCE	0.876 ± 0.004	0.861 ± 0.001	1.018 ± 0.005
LCE	0.042 ± 0.002	0.045 ± 0.001	0.915 ± 0.059
PHXTrk	0.863 ± 0.004	0.865 ± 0.001	0.998 ± 0.005
PHXPEM	0.850 ± 0.005	0.894 ± 0.001	0.951 ± 0.005
PEM	0.808 ± 0.009	0.857 ± 0.001	0.943 ± 0.010
CrkTrk e	0.792 ± 0.013	0.834 ± 0.002	0.949 ± 0.015
PESTrk	0.369 ± 0.005	0.404 ± 0.001	0.914 ± 0.014
TCE Trk Iso	0.820 ± 0.004	0.813 ± 0.001	1.009 ± 0.006
LCE Trk Iso	0.032 ± 0.002	0.037 ± 0.001	0.868 ± 0.073
CrkTrk e Trk Iso	0.766 ± 0.012	0.821 ± 0.002	0.934 ± 0.014
PESTrk Trk Iso	0.369 ± 0.005	0.404 ± 0.001	0.914 ± 0.014
PHXTrk Trk Iso	0.863 ± 0.004	0.865 ± 0.001	0.998 ± 0.005
PHXPEM Trk Iso	0.850 ± 0.005	0.894 ± 0.001	0.951 ± 0.005
PEM Trk Iso	0.808 ± 0.009	0.857 ± 0.001	0.943 ± 0.010

Table 12: Electron efficiencies for dataset 0d (period 0) with and without track isolation cut. No track isolation cut is applied to the PHX and LBE categories; the LBE-only category is used in the analysis.

Run Range: 0h

	data	MC	Scale Fac
LBE ($L > 0.9$)	0.901 ± 0.003	0.901 ± 0.001	1.000 ± 0.003
LBE ($L > 0.9$)only	0.097 ± 0.002	0.092 ± 0.001	1.044 ± 0.027
TCE	0.869 ± 0.004	0.862 ± 0.001	1.008 ± 0.004
LCE	0.040 ± 0.002	0.042 ± 0.001	0.955 ± 0.048
PHXTrk	0.880 ± 0.004	0.874 ± 0.001	1.007 ± 0.004
PHXPEM	0.839 ± 0.004	0.881 ± 0.001	0.953 ± 0.005
PEM	0.762 ± 0.008	0.832 ± 0.001	0.916 ± 0.009
CrkTrk e	0.855 ± 0.013	0.864 ± 0.002	0.989 ± 0.016
PESTrk	0.361 ± 0.005	0.379 ± 0.001	0.951 ± 0.013
TCE Trk Iso	0.807 ± 0.004	0.811 ± 0.001	0.995 ± 0.005
LCE Trk Iso	0.027 ± 0.002	0.033 ± 0.001	0.826 ± 0.059
CrkTrk e Trk Iso	0.816 ± 0.012	0.847 ± 0.002	0.963 ± 0.014
PESTrk Trk Iso	0.361 ± 0.005	0.379 ± 0.001	0.951 ± 0.013
PHXTrk Trk Iso	0.880 ± 0.004	0.874 ± 0.001	1.007 ± 0.004
PHXPEM Trk Iso	0.839 ± 0.004	0.881 ± 0.001	0.953 ± 0.005
PEM Trk Iso	0.762 ± 0.008	0.832 ± 0.001	0.916 ± 0.009

Table 13: Electron efficiencies for dataset 0h (periods 1-4) with and without track isolation cut. No track isolation cut is applied to the PHX and LBE categories; the LBE-only category is used in the analysis.

Run Range: 0i1

	data	MC	Scale Fac
LBE ($L > 0.9$)	0.894 ± 0.004	0.897 ± 0.001	0.996 ± 0.004
LBE ($L > 0.9$)only	0.102 ± 0.003	0.095 ± 0.001	1.075 ± 0.034
TCE	0.861 ± 0.005	0.857 ± 0.001	1.006 ± 0.006
LCE	0.041 ± 0.002	0.043 ± 0.001	0.959 ± 0.059
PHXTrk	0.885 ± 0.004	0.869 ± 0.001	1.018 ± 0.005
PHXPEM	0.825 ± 0.005	0.875 ± 0.001	0.943 ± 0.006
PEM	0.742 ± 0.012	0.813 ± 0.002	0.912 ± 0.015
CrkTrk e	0.821 ± 0.016	0.858 ± 0.002	0.957 ± 0.019
PESTrk	0.364 ± 0.006	0.374 ± 0.001	0.973 ± 0.017
TCE Trk Iso	0.794 ± 0.005	0.804 ± 0.001	0.987 ± 0.006
LCE Trk Iso	0.030 ± 0.002	0.033 ± 0.001	0.895 ± 0.074
CrkTrk e Trk Iso	0.787 ± 0.015	0.841 ± 0.003	0.935 ± 0.017
PESTrk Trk Iso	0.364 ± 0.006	0.374 ± 0.001	0.973 ± 0.017
PHXTrk Trk Iso	0.885 ± 0.004	0.869 ± 0.001	1.018 ± 0.005
PHXPEM Trk Iso	0.825 ± 0.005	0.875 ± 0.001	0.943 ± 0.006
PEM Trk Iso	0.742 ± 0.012	0.813 ± 0.002	0.912 ± 0.015

Table 14: Electron efficiencies for dataset 0i1 (periods 5-7) with and without track isolation cut. No track isolation cut is applied to the PHX and LBE categories; the LBE-only category is used in the analysis.

Run Range: 0i2

	data	MC	Scale Fac
LBE ($L > 0.9$)	0.889 ± 0.003	0.896 ± 0.000	0.992 ± 0.003
LBE ($L > 0.9$)only	0.112 ± 0.002	0.096 ± 0.000	1.166 ± 0.024
TCE	0.858 ± 0.003	0.857 ± 0.001	1.001 ± 0.004
LCE	0.042 ± 0.002	0.043 ± 0.001	0.977 ± 0.045
PHXTrk	0.878 ± 0.003	0.878 ± 0.001	1.000 ± 0.003
PHXPEM	0.812 ± 0.004	0.872 ± 0.001	0.931 ± 0.004
PEM	0.699 ± 0.008	0.799 ± 0.001	0.875 ± 0.010
CrkTrk e	0.809 ± 0.012	0.852 ± 0.002	0.948 ± 0.014
PESTrk	0.351 ± 0.004	0.371 ± 0.001	0.947 ± 0.012
TCE Trk Iso	0.782 ± 0.004	0.803 ± 0.001	0.974 ± 0.005
LCE Trk Iso	0.028 ± 0.002	0.033 ± 0.001	0.855 ± 0.057
CrkTrk e Trk Iso	0.761 ± 0.010	0.835 ± 0.002	0.911 ± 0.012
PESTrk Trk Iso	0.351 ± 0.004	0.371 ± 0.001	0.947 ± 0.012
PHXTrk Trk Iso	0.878 ± 0.003	0.878 ± 0.001	1.000 ± 0.003
PHXPEM Trk Iso	0.812 ± 0.004	0.872 ± 0.001	0.931 ± 0.004
PEM Trk Iso	0.699 ± 0.008	0.799 ± 0.001	0.875 ± 0.010

Table 15: Electron efficiencies for dataset 0i2 (periods 8-10) with and without track isolation cut. No track isolation cut is applied to the PHX and LBE categories; the LBE-only category is used in the analysis.

Run Range: 0j

	data	MC	Scale Fac
LBE ($L > 0.9$)	0.882 ± 0.003	0.887 ± 0.001	0.994 ± 0.004
LBE ($L > 0.9$)only	0.123 ± 0.003	0.100 ± 0.001	1.230 ± 0.030
TCE	0.848 ± 0.004	0.850 ± 0.001	0.997 ± 0.005
LCE	0.045 ± 0.002	0.043 ± 0.001	1.044 ± 0.057
PHXTrk	0.878 ± 0.004	0.879 ± 0.001	0.999 ± 0.004
PHXPEM	0.805 ± 0.005	0.857 ± 0.001	0.939 ± 0.005
PEM	0.660 ± 0.010	0.758 ± 0.002	0.871 ± 0.013
CrkTrk e	0.848 ± 0.017	0.846 ± 0.002	1.002 ± 0.021
PESTrk	0.351 ± 0.005	0.363 ± 0.001	0.967 ± 0.014
TCE Trk Iso	0.763 ± 0.005	0.791 ± 0.001	0.964 ± 0.006
LCE Trk Iso	0.029 ± 0.002	0.031 ± 0.001	0.938 ± 0.076
CrkTrk e Trk Iso	0.788 ± 0.014	0.826 ± 0.002	0.954 ± 0.017
PESTrk Trk Iso	0.351 ± 0.005	0.363 ± 0.001	0.967 ± 0.014
PHXTrk Trk Iso	0.878 ± 0.004	0.879 ± 0.001	0.999 ± 0.004
PHXPEM Trk Iso	0.805 ± 0.005	0.857 ± 0.001	0.939 ± 0.005
PEM Trk Iso	0.660 ± 0.010	0.758 ± 0.002	0.871 ± 0.013

Table 16: Electron efficiencies for dataset 0j (period 11-12) with and without track isolation cut. No track isolation cut is applied to the PHX and LBE categories; the LBE-only category is used in the analysis.

Run Range: 0j13

	data	MC	Scale Fac
LBE ($L > 0.9$)	0.886 ± 0.004	0.891 ± 0.001	0.994 ± 0.004
LBE ($L > 0.9$)only	0.112 ± 0.003	0.096 ± 0.001	1.168 ± 0.035
TCE	0.851 ± 0.005	0.855 ± 0.001	0.995 ± 0.006
LCE	0.047 ± 0.003	0.042 ± 0.001	1.109 ± 0.072
PHXTrk	0.860 ± 0.005	0.857 ± 0.001	1.004 ± 0.005
PHXPEM	0.808 ± 0.006	0.863 ± 0.001	0.935 ± 0.006
PEM	0.688 ± 0.010	0.790 ± 0.002	0.872 ± 0.012
CrkTrk e	0.817 ± 0.018	0.846 ± 0.002	0.965 ± 0.021
PESTrk	0.261 ± 0.006	0.283 ± 0.001	0.925 ± 0.020
TCE Trk Iso	0.776 ± 0.005	0.799 ± 0.001	0.972 ± 0.007
LCE Trk Iso	0.033 ± 0.003	0.032 ± 0.001	1.052 ± 0.095
CrkTrk e Trk Iso	0.771 ± 0.015	0.830 ± 0.002	0.930 ± 0.019
PESTrk Trk Iso	0.261 ± 0.006	0.283 ± 0.001	0.925 ± 0.020
PHXTrk Trk Iso	0.860 ± 0.005	0.857 ± 0.001	1.004 ± 0.005
PHXPEM Trk Iso	0.808 ± 0.006	0.863 ± 0.001	0.935 ± 0.006
PEM Trk Iso	0.688 ± 0.010	0.790 ± 0.002	0.872 ± 0.012

Table 17: Electron efficiencies for dataset 0j13 (period 13) with and without track isolation cut. No track isolation cut is applied to the PHX and LBE categories; the LBE-only category is used in the analysis.

Run Range: 0k

	data	MC	Scale Fac
LBE ($L > 0.9$)	0.876 ± 0.001	0.883 ± 0.000	0.992 ± 0.001
LBE ($L > 0.9$)only	0.120 ± 0.001	0.102 ± 0.000	1.172 ± 0.011
TCE	0.845 ± 0.002	0.847 ± 0.001	0.997 ± 0.002
LCE	0.046 ± 0.001	0.043 ± 0.001	1.064 ± 0.039
PHXTrk	0.888 ± 0.001	0.866 ± 0.001	1.025 ± 0.002
PHXPEM	0.771 ± 0.002	0.847 ± 0.001	0.910 ± 0.002
PEM	0.611 ± 0.003	0.733 ± 0.001	0.834 ± 0.005
CrkTrk e	0.801 ± 0.005	0.834 ± 0.001	0.960 ± 0.007
PESTrk	0.319 ± 0.002	0.352 ± 0.001	0.906 ± 0.006
TCE Trk Iso	0.762 ± 0.002	0.786 ± 0.001	0.970 ± 0.003
LCE Trk Iso	0.028 ± 0.001	0.031 ± 0.001	0.915 ± 0.053
CrkTrk e Trk Iso	0.756 ± 0.005	0.814 ± 0.002	0.929 ± 0.006
PESTrk Trk Iso	0.319 ± 0.002	0.352 ± 0.001	0.906 ± 0.006
PHXTrk Trk Iso	0.888 ± 0.001	0.866 ± 0.001	1.025 ± 0.002
PHXPEM Trk Iso	0.771 ± 0.002	0.847 ± 0.001	0.910 ± 0.002
PEM Trk Iso	0.611 ± 0.003	0.733 ± 0.001	0.834 ± 0.005

Table 18: Electron efficiencies for dataset 0k (periods 14-27) with and without track isolation cut. No track isolation cut is applied to the PHX and LBE categories; the LBE-only category is used in the analysis.

3.3 Fake Rate Measurements

The lepton fake rates (*ie.* the probability for jets to fake a lepton) are measured in the jet samples and corrected for the small contribution of real isolated leptons from electroweak processes, as described in detail in [7]. This probability is measured as a function of the p_T of the object and results are used to derive a data-driven modeling of the W+jets background as described in Section 5.3.

As a brief reminder we repeat here the master formula for the calculation of such fake rates for a generic category i:

$$f_i = \frac{N_i(\text{IdentifiedLeptons}) - \sum_{j \in \text{EWK}} N_{ij}(\text{IdentifiedLeptons})}{N_i(\text{DenominatorObjects}) - \sum_{j \in \text{EWK}} N_{ij}(\text{DenominatorObjects})} \tag{2}$$

As with the scale factor calculation, the procedure relies on generic Central/Forward muon *Denominator Objects* which are then made category specific by applying the fiduciality requirements. In order to perform the electroweak subtraction we normalize the MC simulation to the data effectively analyzed in each of the jet 20, 50, 70, and 100 triggered samples. Table 19 reports the effective (*ie.* corrected for trigger prescale factors) luminosities of such samples.

Sample	Effective Luminosity (nb)
Jet 20	$3301 \cdot 1.019$
Jet 50	$80127 \cdot 1.019$
Jet 70	$723584 \cdot 1.019$
Jet 100	$5788635 \cdot 1.019$

Table 19: Effective luminosity for each of the samples after trigger prescale correction for em_nosi goodrun list. These are used for the electroweak subtraction.

Results of the fake rate calculations are shown in Figures 8 to 9. Fake rate calculations are averaged over all the data available to maximize the statistics available. We assign a systematic based on the scatter of the results between the jet samples: an uncorrelated systematic, α, is added to each jet sample measurement until all the points are consistent within 1σ of the new mean, where the mean and the σ from the mean are calculated using $\sqrt{\text{stat err} + \alpha}$ as the uncertainty on each point. This result is shown as a light gray band in the figures, while the dark band is the result of the statistical error only.

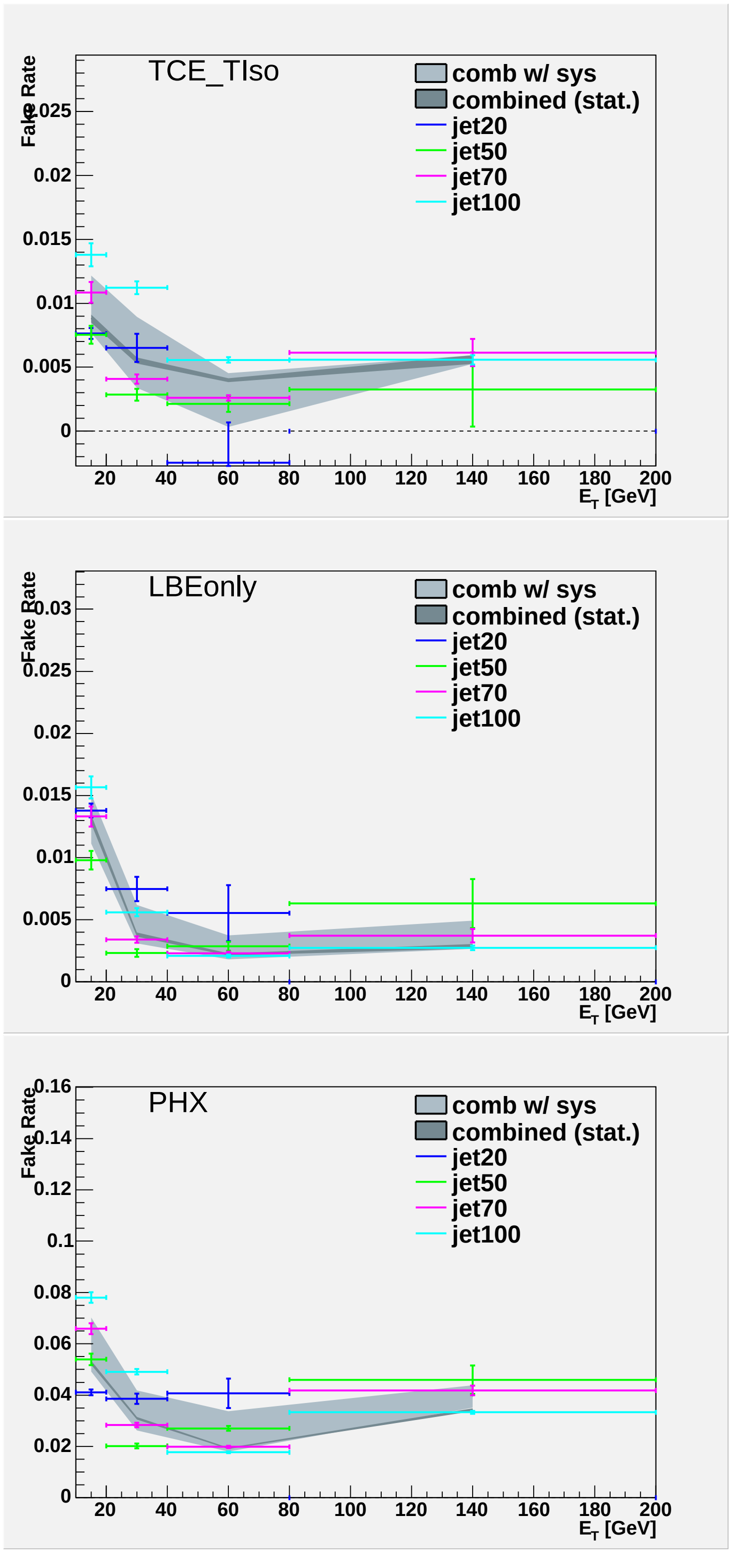

Figure 8: Fake rates for electrons. PHX and LBE have no track isolation requirement.

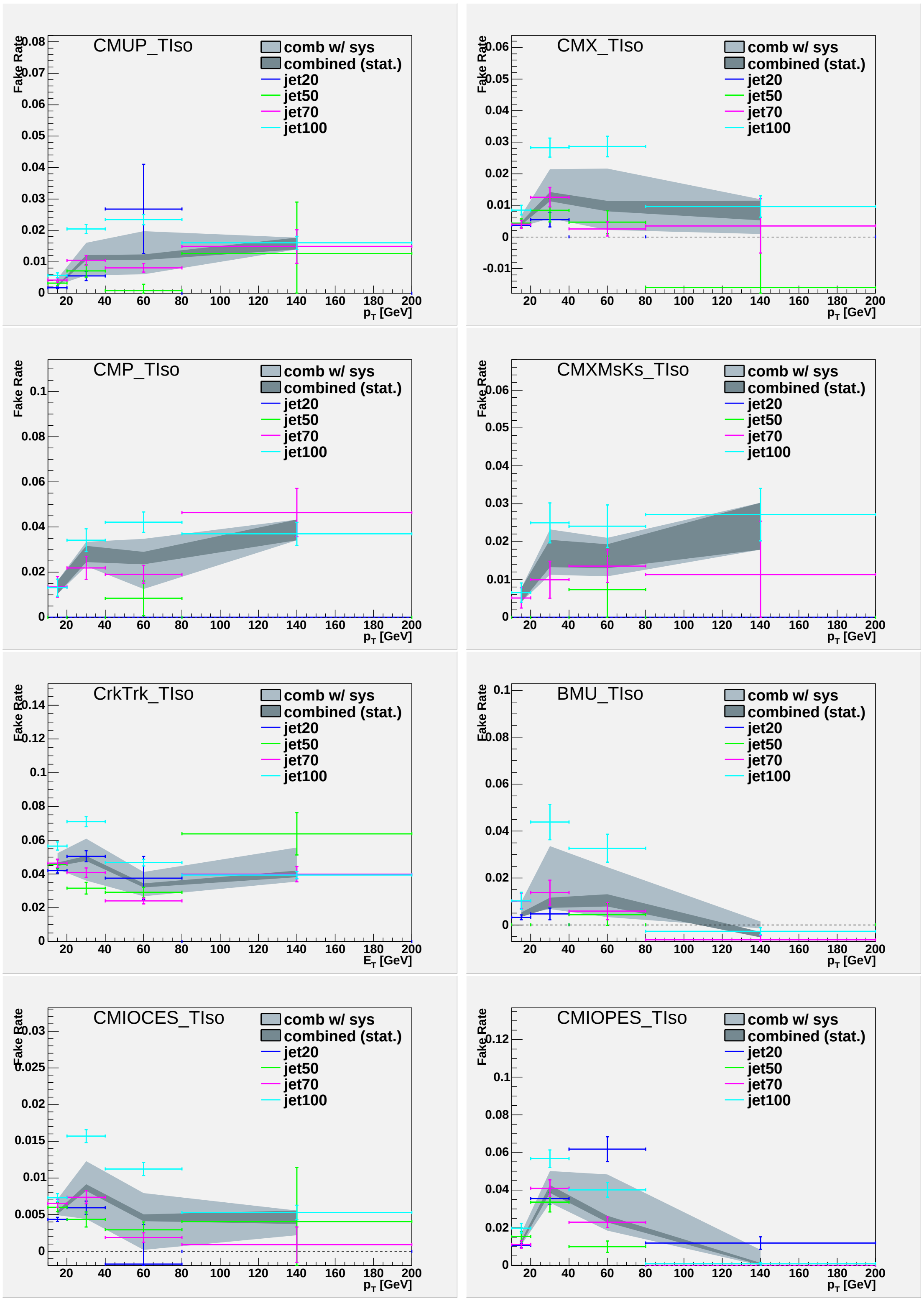

Figure 9: Fake rates for muons.

3.4 DY Cross Section Measurements

In this section we measure the DY cross-section by comparing reconstructed $p\bar{p} \to Z \to l^+l^-(l = e, \mu)$ events in data with Pythia MC simulations. This provides a sensible measurement of the luminosity of the data sample, and is also probably the strongest check of the definition of new categories. Agreement on the cross section value among different dilepton categories tells us that we're correctly modeling their behaviour in our simulation, and the average cross section value of all dilepton categories tells us if the observed yields are in agreement with the luminosity measurement. We select Z candidates requiring two opposite sign leptons (e or μ, belonging to the defined categories) with invariant mass $76 < m(ll) < 106$ GeV, and require $\not\!\!E_T < 15$ GeV for $e\mu$ events and $\not\!\!E_T < 25$ GeV for all other combinations. All base analysis requirements are also applied: good run list selection, $\Delta z_0(ll) < 4$ cm, cosmic veto, and requiring a trigger lepton coherent with trigger bits (for data).

In previous versions of the analysis, the results for categories with a CMP muon showed more events observed in data than predicted by MC. However, the statistics for CMP are not large, and the effect was consistent within statistical uncertainties. With the data sample updated to 5.9 fb^{-1}, the effect persisted at the 10% level for those categories where CMP was the trigger lepton (CMP-CMP, CMP-forward muon, and CMP-CrkTrk). Based on this evidence, we decided to scale the CMP trigger efficiencies up by 10% for the MC. The following results are calculated after applying this scaling.

In Table 20 we show the following results for each dilepton category: the number of events predicted and observed, their ratio, the resulting DY cross section with its statistical error, and the residual between the measured value and the weighted average of all the categories (systematic uncertainties are not accounted for).

After applying the CMP trigger efficiency scale factor, results show a reasonable agreement for all categories within few percent. The only visible shift is for CMXMsKs, for which the statistics are still quite low. Considering that systematic uncertainties (such as trigger efficiencies, SF errors, etc.) are not accounted for in these errors, we think this effect is not worrisome. The PHX category is known to have a lower measurement (and for this reason it's excluded in the calculation of the weighted mean) since in this low $\not\!\!E_T$ region we do not model correctly the turn-on of the MET_PEM trigger (by which these events are triggered); this effect is not present in the signal region since the $\not\!\!E_T$ cut puts events in the plateau of the turn-on curve.

Category	DY MC	Data	Data/MC	DY x-sec (pb) ± stat.	Residual [σ]
LBE LBE	111738.0	110392	0.99	248.28 ± 0.78	3.8
LBE PHX	104597.5	101760	0.97	244.49 ± 0.79	-1.1
PHX PHX	2634.5	1010	0.38	96.34 ± 3.04	-49.1
LBE CMUP	36.9	29	0.79	197.33 ± 37.65	-1.3
LBE CMP	4.9	5	1.03	257.88 ± 121.31	0.1
LBE CMX	15.6	28	1.79	450.35 ± 90.60	2.3
LBE CMXMsKs	3.4	1	0.29	73.44 ± 74.66	-2.3
LBE BMU	5.1	4	0.78	196.86 ± 101.24	-0.5
LBE CMIOCES	29.9	27	0.90	226.84 ± 45.22	-0.4
LBE CMIOPES	12.9	12	0.93	232.98 ± 69.48	-0.2
PHX CMUP	30.2	34	1.13	283.14 ± 50.38	0.8
PHX CMP	5.6	5	0.89	224.74 ± 104.90	-0.2
PHX CMX	13.7	15	1.10	275.31 ± 73.78	0.4
PHX CMXMsKs	2.6	2	0.76	191.45 ± 139.08	-0.4
PHX BMU	4.1	6	1.47	369.31 ± 158.25	0.8
PHX CMIOCES	19.6	31	1.58	396.75 ± 75.14	2.0
PHX CMIOPES	8.9	7	0.79	197.33 ± 76.27	-0.6
CMUP CMUP	21664.8	21283	0.98	246.88 ± 1.74	0.9
CMUP CMP	6092.4	6266	1.03	258.47 ± 3.39	3.9
CMUP CMX	21580.5	21182	0.98	246.66 ± 1.75	0.8
CMUP CMXMsKs	4166.0	3839	0.92	231.58 ± 3.86	-3.6
CMUP BMU	7093.3	6820	0.96	241.62 ± 3.01	-1.2
CMUP CMIOCES	31772.4	32528	1.02	257.28 ± 1.48	8.1
CMUP CMIOPES	14571.4	14061	0.96	242.50 ± 2.10	-1.3
CMX CMP	3087.4	3111	1.01	253.23 ± 4.73	1.7
CMX CMX	6252.9	5947	0.95	239.01 ± 3.21	-2.0
CMX CMXMsKs	1543.9	1394	0.90	226.90 ± 6.29	-2.9
CMX BMU	3628.3	3239	0.89	224.34 ± 4.06	-5.2
CMX CMIOCES	16420.5	15825	0.96	242.19 ± 2.00	-1.6
CMX CMIOPES	7212.5	6762	0.94	235.61 ± 2.95	-3.3
CMXMsKs CMP	906.5	818	0.90	226.77 ± 8.17	-2.3
CMXMsKs CMXMsKs	356.3	376	1.06	265.18 ± 14.18	1.4
CMXMsKs BMU	618.5	597	0.97	242.59 ± 10.22	-0.3
CMXMsKs CMIOCES	2337.2	2850	1.22	306.44 ± 6.01	10.2
CMXMsKs CMIOPES	983.8	999	1.02	255.20 ± 8.30	1.2
CMP CMP	694.8	739	1.06	267.30 ± 10.16	2.2
CMP BMU	757.0	770	1.02	255.61 ± 9.47	1.1
CMP CMIOCES	3241.5	3583	1.11	277.78 ± 4.82	6.7
CMP CMIOPES	1530.1	1588	1.04	260.81 ± 6.72	2.3
LBE CrkTrk	50127.4	46984	0.94	235.55 ± 1.12	-8.7
PHX CrkTrk	11337.4	9402	0.83	208.41 ± 2.18	-17.0
CMUP CrkTrk	26224.7	25162	0.96	241.12 ± 1.56	-2.7
CMP CrkTrk	2698.8	2916	1.08	271.53 ± 5.18	5.1
CMX CrkTrk	13343.7	12259	0.92	230.88 ± 2.15	-6.7
CMXMsKs CrkTrk	1971.0	2037	1.03	259.72 ± 5.94	2.4

Table 20: Drell-Yan cross section measurement for each dilepton category. See text for detailed explanation.

4 Event Selection

In this section, we describe our candidate selection. This includes the triggers, reconstruction of low-level objects, and our high-level cuts. The general strategy is to use cuts to supress the Drell-Yan background and then rely on matrix element calculations and neural networks to discriminate against the other backgrounds.

4.1 Datasets

We use the following trigger paths:

- ELECTRON_CENTRAL_18
- MUON_CMUP18
- MUON_CMX18
- MET_PEM
- MUON_CMP18_PHI_GAP

The corresponding datasets are bhel0d/0h/0i/0j/0k/0m (electrons), bhmu0d/0h/0i/0j/0k/0m (muons), and bpel0d/0h/0i/0j/0k/0m (MET+PEM). We use the following v33 good run lists slightly modified to recover portions of runs that contain bad beamline data (see CDF Note 9195):

- EM_NOSI
- EM_CMUP_NOSI
- EM_MU_NOSI_CMXIGNORED
- EM_SI
- EM_CMUP_SI
- EM_MU_SI_CMXIGNORED
- EM_MU_SI_BMU

We also use separate good run lists for 0n dataset, which consists of the reprocessed silicon data for runs 262865-263615 (from period 18) as documented on
http://www-cdf.fnal.gov/internal/dqm/goodrun/p18Sirecovered/goodp18Si.html.
The luminosity of each good run list is shown in Table 4.1.

Good run list	$\mathcal{L}$ (pb^{-1})
EM_NOSI	5898.6
EM_CMUP_NOSI	5830.1
EM_MU_NOSI_CMXIGNORED	5683.4
EM_SI	5684.5
EM_CMUP_SI	5624.1
EM_MU_SI_CMXIGNORED	5481.4

Table 21: Luminosity for each of the good run lists (v33) used in this analysis. These have been scaled by the factor of 1.019.

4.2 Low-level Objects

The muon categories introduced in the previous version of this analysis (CMP, CMU, CMXMsKs, and BMU) are described in CDF 9697 [5]. All previous lepton categories are identically defined as in CDF 8719, except for the changes mentioned in CDF 9697. For the CMIOPES category, there are also several additional requirements to those in CDF 8719, designed to veto events with a CMIOPES muon with poorly measured curvature. These cuts were also made in previous versions of the analysis (CDF 9685) and are as follows:

- Number of SVX hits > 3
- Curvature significance > 12 based on error from the covariance matrix

4.3 High-level Cuts

Except for the requirement on the dilepton invariant mass, m_{ll}, we use the same high-level cuts as in CDF 8719 to define a "base region". The m_{ll} cut was lowered from 25 GeV to 16 GeV as in CDF 8700.

5 Sample Modeling

In this section we describe how we model the selected sample. Section 5.1 describes the Monte Carlo samples used, Section 5.2 describes the data based corrections made to the Monte Carlo, and Section 5.3 describes the modeling of the W+jets background.

5.1 Monte Carlo Samples

The acceptance and several of the backgrounds are estimated using Monte Carlo samples. Table 22 lists all the samples used. Here we provide some brief notes on the samples.

WW

As WW is by far the dominant background to this analysis, we take special care using a NLO Monte Carlo generator, MC@NLO. In previous versions of this analysis, we used an NLO WW run-dependent sample which was generated with run ranges only through period 7. As mentioned in the introduction of this note, we generated a new sample with the most recent version of MC@NLO (3.41). This sample consists of one fully run-dependent part, covering run ranges from periods 0 to 13. The second part is generated with a higher luminosity profile, in the same manner as all of our other MC samples, to model data from period 14 onward. In the sample, both W bosons are required to decay into either an electron, muon, or tau. Because of the way MC@NLO is implemented, in order to have the correct spin information for the W bosons we had to generate a separate sample for each of the 9 possible final states:

$$\begin{array}{lll} W^+W^- \to e^+\nu e^-\bar{\nu} & W^+W^- \to e^+\nu\mu^-\bar{\nu} & W^+W^- \to e^+\nu\tau^-\bar{\nu} \\ W^+W^- \to \mu^+\nu e^-\bar{\nu} & W^+W^- \to \mu^+\nu\mu^-\bar{\nu} & W^+W^- \to \mu^+\nu\tau^-\bar{\nu} \\ W^+W^- \to \tau^+\nu e^-\bar{\nu} & W^+W^- \to \tau^+\nu\mu^-\bar{\nu} & W^+W^- \to \tau^+\nu\tau^-\bar{\nu} \end{array}$$

Thus, a total of 18 separate MC samples was produced (for 9 final states, either run-dependent or run-independent luminosity profile). There is also a WW sample generated with Pythia which is used to check the kinematic differences between LO and NLO.

Heavy dibosons: WZ, ZZ

The WZ and ZZ samples used are all Pythia based. The WZ samples are generated with a forced decay of the Z into a lepton pair (electrons, muons, or taus) while the W is allowed to decay inclusively. The events are filtered using the generator-level information, requiring two leptons with p_T greater than 1 GeV. The ZZ sample is generated having both Z's decay inclusively and then filtering for two leptons with p_T greater than 1 GeV. The ZZ Monte Carlo includes γ^* component with M_{ll} >15 GeV/c^2.

$W\gamma$

The $W\gamma$ Monte Carlo used for this analysis uses the Baur matrix element generator [9] which is passed to Pythia via the LesHouchesModule. Because of indecision over the proper settings for the Pythia QED radiation settings the Gen5 sample has the QED turned off and the Gen6 sample has it turned on. The two settings correspond to slightly over estimating the lepton id efficiency and double counting at order α_{EM} the hard radiation, respectively. Neither of these effects should be significant for this analysis, relative to the conversion finding efficiency and K-factor uncertainties. It should also be noted that the $W\gamma$ cross-section has been measured at CDF [10, 11] and DØ.

$Z\gamma$

The $Z\gamma$ Monte Carlo, which is used only for the trilepton searches, uses the Baur matrix element generator [9] which is passed to Pythia via the LesHouchesModule. The $Z\gamma$ samples are generated with the QED turned on. The $Z\gamma$ cross-section has also been measured at CDF [10, 12] and DØ.

$t\bar{t}$

The $t\bar{t}$ sample is also Pythia based, and is generated for a top-quark mass of 175 GeV.

$Z \to \tau\tau$

The $Z \to \tau\tau$ sample is generated with a 10 GeV/c^2 minimum dilepton mass, uses Gen5 for the full run range and has no minbias in the events.

$Z \to ee$ and $Z \to \mu\mu$

The $Z \to ee$ and $Z \to \mu\mu$ samples are generated with a 20 GeV/c^2 minimum dilepton mass. They use Gen5 for the 0d run range and Gen6 for the 0h/0i/0j/0k/0m run ranges. They have a full luminosity dependent addition of minbias in the events.

5.2 Corrections to the Monte Carlo

Luminosity scaling, data-base corrections, and measured trigger efficiencies are applied to the Monte Carlo samples separately for each of the lepton pair categories. The master formula used is:

$$\frac{\sigma \times \mathcal{B} \times \epsilon_{\mathrm{filter}} \times \epsilon_i^{\mathrm{trg}} \times s_i^{\mathrm{lep}} \times \epsilon_{\mathrm{vtx}} \times \mathcal{L}_i}{N_i^{\mathrm{gen}}(|Z_0| < 60 \text{ cm})} \tag{3}$$

where

mode	Period	Stntuple	$\sigma \times \mathcal{B}$ (pb)	K-factor[a]	Filter Eff
$W\gamma \rightarrow e\nu\gamma$	0-27	re0s6d,re0s6h re0s6e,re0s6i	32.38×0.5	1.36	1.0
$W\gamma \rightarrow \mu\nu\gamma$	0-27	re0s6f,re0s6j re0s6g,re0s6k	32.38×0.5	1.36	1.0
$W\gamma \rightarrow \tau\nu\gamma$	0-11	re0s6a	13.6	1.36	1.0
WW Pythia	0-27	we0s5d,we0sbd,we0sgd we0skd,we0snd,we0saf we0sgf	11.66×0.1027	1.0	1.0
WW MC@NLO	0-27	we0sen,we0seo,we0sep we0smn,we0smo,we0smp we0stn,we0sto,we0stp we0seq,we0ser,we0ses we0smq,we0smr,we0sms we0stq,we0str,we0sts	11.66×0.1027	1.0	1.0
WZ	0-27	we0s6d,we0scd,we0shd we0sld,we0sod,we0sbf we0shf	3.46×0.101	1.0	0.754
ZZ	0-27	we0s7d,we0sdd,we0sid we0smd,we0spd,we0scf we0sif	1.511	1.0	0.233
$t\bar{t}$	0-11	te0s2z	7.04×0.1027	1.0	1.0
$Z \rightarrow ee$	0-27	ze1s6d[b],ze1sad,ze0scd ze0sdd,ze0sed,ze0see ze0seh,ze0sej,ze0sei	355[c]	1.38	1.0
$Z \rightarrow \mu\mu$	0-27	ze1s6m[b],ze1s9m,ze0sbm ze0scm,ze0sdm,ze0sem ze0sfm,ze0sgm,ze0sim	355[c]	1.38	1.0
$Z \rightarrow \tau\tau$	0-27	ze0s8t,ze0sat[d] ze0sbt,ze0sct	355[c]	1.38	1.0
$Z \rightarrow ee$	0-11	zx0see	920[e]	1.38	0.0156
$Z \rightarrow \mu\mu$	0-11	zx0sem	920[e]	1.38	0.0156
$Z \rightarrow \tau\tau$	0-11	zx0set	1272[f]	1.38	0.00713
$Z\gamma \rightarrow ee\gamma$	0-11	re0s33	10.33	1.36	1.0
$Z\gamma \rightarrow \mu\mu\gamma$	0-11	re0s34	10.33	1.36	1.0
$Z\gamma \rightarrow \tau\tau\gamma$	0-11	re0s37	10.33	1.36	1.0

[a] If cross section is NLO, then K-factor is one.

[b] Gen5 tarball for period 0.

[c] $\mathrm{m}_{ll} > 20$.

[d] $\mathrm{m}_{ll} > 30$ ($\sigma = 237$) for this sample only.

[e] $10 < \mathrm{m}_{ll} < 20$.

[f] $\mathrm{m}_{ll} > 10$.

Table 22: Monte Carlo samples used in this analysis.

$M_H(GeV^2)$	Period	Stntuple	σ (pb)	BR ($H \to WW$)	BR($WW \to \ell\nu\ell\nu$)
110	0-27	dhgs4a,dhgs6a	1.413	0.0459	0.1027
115	0-27	dhgs4l,dhgs6l	1.240	0.0827	0.1027
120	0-27	dhgs4b,dhgs6b	1.093	0.1364	0.1027
125	0-27	dhgs4m,dhgs6m	0.967	0.2078	0.1027
130	0-27	dhgs4c,dhgs6c	0.858	0.2943	0.1027
135	0-27	dhgs4n,dhgs6n	0.764	0.3910	0.1027
140	0-27	dhgs4d,dhgs6d	0.682	0.4916	0.1027
145	0-27	dhgs4o,dhgs6o	0.611	0.5915	0.1027
150	0-27	dhgs4e,dhgs6e	0.548	0.6891	0.1027
155	0-27	dhgs4p,dhgs6p	0.492	0.7892	0.1027
160	0-27	dhgs4f,dhgs6f	0.439	0.9048	0.1027
165	0-27	dhgs4q,dhgs6q	0.389	0.9591	0.1027
170	0-27	dhgs4g,dhgs6g	0.349	0.9639	0.1027
175	0-27	dhgs4r,dhgs6r	0.314	0.9581	0.1027
180	0-27	dhgs4h,dhgs6h	0.283	0.9325	0.1027
185	0-27	dhgs4s,dhgs6s	0.255	0.8450	0.1027
190	0-27	dhgs4i,dhgs6i	0.231	0.7870	0.1027
195	0-27	dhgs4t,dhgs6t	0.210	0.7588	0.1027
200	0-27	dhgs4j,dhgs6j	0.192	0.7426	0.1027

Table 23: Higgs production via gluon fusion. The production cross section is taken from a NNLL calculation [13] while the BR($H \to WW$) is from version 3.53 of HDECAY.

$M_H(GeV^2)$	Period	Stntuple	σ (pb)	BR ($H \rightarrow WW$)	BR($WW \rightarrow \ell\nu\ell\nu$)
110	0-27	vhgs1a,vhgs3a,vhgs6a	0.0871	0.0459	0.1027
115	0-27	vhgs2l,vhgs3l,vhgs6l	0.0791	0.0827	0.1027
120	0-27	vhgs1b,vhgs3b,vhgs6b	0.0717	0.1364	0.1027
125	0-27	vhgs2m,vhgs3m,vhgs6m	0.0674	0.2078	0.1027
130	0-27	vhgs1c,vhgs3c,vhgs6c	0.0625	0.2943	0.1027
135	0-27	vhgs2n,vhgs3n,vhgs6n	0.0577	0.3910	0.1027
140	0-27	vhgs1d,vhgs3d,vhgs6d	0.0526	0.4916	0.1027
145	0-27	vhgs2o,vhgs3o,vhgs6o	0.0492	0.5915	0.1027
150	0-27	vhgs1e,vhgs3e,vhgs6e	0.0457	0.6891	0.1027
155	0-27	vhgs2p,vhgs3p,vhgs6p	0.0422	0.7892	0.1027
160	0-27	vhgs1f,vhgs3f,vhgs6f	0.0386	0.9048	0.1027
165	0-27	vhgs2q,vhgs3q,vhgs6q	0.0361	0.9591	0.1027
170	0-27	vhgs1g,vhgs3g,vhgs6g	0.0336	0.9639	0.1027
175	0-27	vhgs2r,vhgs3r,vhgs6r	0.0311	0.9581	0.1027
180	0-27	vhgs1h,vhgs3h,vhgs6h	0.0286	0.9325	0.1027
185	0-27	vhgs2s,vhgs3s,vhgs6s	0.0268	0.8450	0.1027
190	0-27	vhgs1i,vhgs3i,vhgs6i	0.0249	0.7870	0.1027
195	0-27	vhgs2t,vhgs3t,vhgs6t	0.0230	0.7588	0.1027
200	0-27	vhgs1j,vhgs3j,vhgs6j	0.0212	0.7426	0.1027

Table 24: Higgs production via vector boson fusion. The BR($H \rightarrow WW$) is from version 3.53 of HDECAY.

$M_H(GeV^2)$	Period	Stntuple	σ (pb)	BR ($H \to WW$)	Filter Efficiency
110	0-27	fhgs4a,fhgs6a	0.2092	0.0459	0.6880
115	0-27	fhgs4l,fhgs6l	0.1788	0.0827	0.6932
120	0-27	fhgs4b,fhgs6b	0.1529	0.1364	0.6978
125	0-27	fhgs4m,fhgs6m	0.1324	0.2078	0.7004
130	0-27	fhgs4c,fhgs6c	0.1147	0.2943	0.7032
135	0-27	fhgs4n,fhgs6n	0.0993	0.3910	0.7045
140	0-27	fhgs4d,fhgs6d	0.0860	0.4916	0.7065
145	0-27	fhgs4o,fhgs6o	0.0753	0.5915	0.7075
150	0-27	fhgs4e,fhgs6e	0.0660	0.6891	0.7085
155	0-27	fhgs4p,fhgs6p	0.0578	0.7892	0.7098
160	0-27	fhgs4f,fhgs6f	0.0507	0.9048	0.7108
165	0-27	fhgs4q,fhgs6q	0.0444	0.9591	0.7114
170	0-27	fhgs4g,fhgs6g	0.0389	0.9639	0.7125
175	0-27	fhgs4r,fhgs6r	0.0346	0.9581	0.7130
180	0-27	fhgs4h,fhgs6h	0.0307	0.9325	0.7141
185	0-27	fhgs4s,fhgs6s	0.0273	0.8450	0.7149
190	0-27	fhgs4i,fhgs6i	0.0243	0.7870	0.7151
195	0-27	fhgs4t,fhgs6t	0.0217	0.7588	0.7158
200	0-27	fhgs4j,fhgs6j	0.0193	0.7426	0.7165

Table 25: Associated Higgs production with a W boson. The BR($H \to WW$) is from version 3.53 of HDECAY.

$M_H(GeV^2)$	Period	Stntuple	σ (pb)	BR ($H \rightarrow WW$)	Filter Efficiency
110	0-27	uhgs4a,uhgs6a	0.1243	0.0459	0.6930
115	0-27	uhgs4l,uhgs6l	0.1074	0.0827	0.6994
120	0-27	uhgs4b,uhgs6b	0.0927	0.1364	0.7031
125	0-27	uhgs4m,uhgs6m	0.0811	0.2078	0.7061
130	0-27	uhgs4c,uhgs6c	0.0709	0.2943	0.7087
135	0-27	uhgs4n,uhgs6n	0.0620	0.3910	0.7106
140	0-27	uhgs4d,uhgs6d	0.0542	0.4916	0.7122
145	0-27	uhgs4o,uhgs6o	0.0480	0.5915	0.7135
150	0-27	uhgs4e,uhgs6e	0.0425	0.6891	0.7151
155	0-27	uhgs4p,uhgs6p	0.0376	0.7892	0.7155
160	0-27	uhgs4f,uhgs6f	0.0333	0.9048	0.7172
165	0-27	uhgs4q,uhgs6q	0.0295	0.9591	0.7183
170	0-27	uhgs4g,uhgs6g	0.0261	0.9639	0.7184
175	0-27	uhgs4r,uhgs6r	0.0233	0.9581	0.7196
180	0-27	uhgs4h,uhgs6h	0.0208	0.9325	0.7204
185	0-27	uhgs4s,uhgs6s	0.0186	0.8450	0.7212
190	0-27	uhgs4i,uhgs6i	0.0166	0.7870	0.7220
195	0-27	uhgs4t,uhgs6t	0.0150	0.7588	0.7229
200	0-27	uhgs4j,uhgs6j	0.0135	0.7426	0.7239

Table 26: Associated Higgs production with a Z boson. The BR($H \rightarrow WW$) is from version 3.53 of HDECAY.

σ	is the cross-section for the Monte Carlo process (as listed in Tables 22-26)
$\mathcal{B}$	is any branching fraction for the Monte Carlo process (as listed in Tables 22-26)
ϵ_{filter}	is the filter efficiency applied for any filter used in the generation process (as listed in Tables 22-26)
ϵ_i^{trg}	is the effective trigger efficiency for the category (see below)
s_i^{lep}	is the effective lepton id scale factor (see below)
ϵ_{vtx}	is the run dependent efficiency of the z-vertex position requirement ($\lvert z_0\rvert < 60$ cm)
$\mathcal{L}_i$	is the luminosity of the dataset in good run list in which the lepton category falls (see Table 4.1)

The trigger efficiencies and livetimes are the same as described in CDF Note 9697 [5], with the exception of the 10% scale factor applied to CMP trigger efficiencies as explained in Section 3.4. The lepton ID scale factors for this analysis were described in Section 3.2 and summarized in Tables 5-18.

5.3 W+jets Background

We use a data-driven fake rate proceedure to estimate the backgrounds from fake leptons. The procedure for extracting the fake rates is described in CDF Note 8538. In the dilepton plus MET final state we use both calorimeter and track isolation in our selection criteria for leptons.

Fake rates determined from generic jet samples are applied to a sample of lepton plus denominator object events where the deminator object is treated in the exact same manner as a fully identified lepton. These events are scaled by the rate at which the denominator object "fakes" a specific lepton type (as measured from the generic jet data). For each data event only the highest E_T denominator object is considered, although multiple events can be created in cases where the denominator object has the ability to "fake" more than one lepton type. Both possibilities are considered separately and each generated event is scaled by the appropriate measured fake rate.

A further correction is applied for non-triggerable fake leptons. Such a correction is necessary because events with a single real lepton corresponding to any of our non-triggerable lepton types will not appear in the single lepton samples from which our fake events are generated. The non-triggerable fake rate correction is obtained from our inclusive W Monte Carlo samples. For each dilepton category, we determine a weighted ratio of $W \to \ell\nu$ events with a second lepton originating from a promoted denominator object. The ratio is the weighted number of events in which the triggerable lepton originates from the promoted denominator divided by the weighted number of events in which the real lepton from the W decay is in fact the triggerable lepton ($N^{MC}_{\text{nontrig}}/N^{MC}_{\text{triggerable}}$). The weight of each generated fake event is the simply scaled up by $1 + N^{MC}_{\text{nontrig}}/\, N^{MC}_{\text{triggerable}}$, so that

$$N^{data}_{\text{total}} = N^{data}_{\text{triggerable}} + N^{data}_{\text{triggerable}} \frac{N^{MC}_{\text{nontrig}}}{N^{MC}_{\text{triggerable}}}. \tag{4}$$

The measured ratios of W+jet events with nontriggerable versus triggerable leptons originating from the W decay are shown in Tables 27 and 28 for each dilepton category. Dilepton categories with two trigger lepton types (e.g. CMUP-CMUP) can have a small non-triggerable correction factor due to the fact that one of the two leptons can have a E_T between 10 and 20 GeV/c and hence be non-triggerable by our definition. Non-triggerable fake rate corrections are now obtained separately for each of the different candidate samples.

	Opp-sign(0 jets)	Opp-sign(1 jet)	Opp-sign(2+ jets)	Opp-sign(Low M_{ll})	Same-sign(1+ jets)
e e:					
TCE TCE	0.033	0.039	0.060	0.136	0.000
TCE LBE	0.033	0.034	0.048	0.113	0.000
TCE PHX	0.041	0.037	0.038	0.216	0.000
LBE LBE	0.086	0.058	0.049	0.139	0.000
LBE PHX	0.045	0.078	0.005	0.304	0.000
PHX PHX	0.036	0.016	0.049	0.079	0.000
e μ:					
TCE CMUP	0.042	0.060	0.056	0.166	0.000
TCE CMP	0.063	0.019	0.000	0.508	0.000
TCE CMX	0.052	0.064	0.136	0.196	0.000
TCE CMXMsKs	0.042	0.011	0.000	0.198	0.000
TCE BMU	0.215	0.231	0.297	0.371	0.383
TCE CMIOCES	0.087	0.119	0.128	0.013	0.247
TCE CMIOPES	0.101	0.100	0.113	0.052	0.149
LBE CMUP	0.045	0.059	0.034	0.160	0.000
LBE CMP	0.061	0.007	0.000	0.106	0.000
LBE CMX	0.047	0.072	0.034	0.180	0.000
LBE CMXMsKs	0.026	0.065	0.000	0.036	0.000
LBE BMU	1.307	2.336	6.609	2.441	0.000
LBE CMIOCES	0.544	0.760	0.724	0.042	0.000
LBE CMIOPES	0.697	1.074	0.832	0.125	0.000
PHX CMUP	0.048	0.049	0.028	0.000	0.000
PHX CMP	0.053	0.020	0.000	0.000	0.000
PHX CMX	0.031	0.066	0.121	0.244	0.000
PHX CMXMsKs	0.026	0.052	0.000	0.229	0.000
PHX BMU	0.454	1.060	0.000	0.188	0.000
PHX CMIOCES	0.201	0.576	0.719	0.307	0.000
PHX CMIOPES	0.243	0.471	0.275	0.252	0.000
μ μ:					
CMUP CMUP	0.067	0.084	0.141	0.233	0.000
CMUP CMP	0.104	0.068	0.000	1.003	0.000
CMUP CMX	0.057	0.049	0.097	0.250	0.000
CMUP CMXMsKs	0.079	0.000	0.000	0.354	0.000
CMUP BMU	0.698	0.958	0.787	0.000	0.757
CMUP CMIOCES	0.239	0.318	0.434	0.134	0.613
CMUP CMIOPES	0.300	0.252	0.890	0.000	0.418
CMX CMP	0.055	0.000	0.000	0.000	0.000
CMX CMX	0.049	0.104	0.000	0.164	0.000
CMX CMXMsKs	0.068	0.000	0.000	0.332	0.000
CMX BMU	0.446	0.657	0.000	0.000	1.363
CMX CMIOCES	0.205	0.359	0.311	0.154	0.456
CMX CMIOPES	0.272	0.187	0.789	0.111	0.348
CMXMsKs CMP	0.143	0.000	0.000	0.000	0.000
CMXMsKs CMXMsKs	0.000	0.000	0.000	2.579	0.000
CMXMsKs BMU	0.492	0.000	0.000	0.000	2.491
CMXMsKs CMIOCES	0.223	0.226	0.990	0.000	0.684
CMXMsKs CMIOPES	0.077	1.150	0.000	0.000	0.648
CMP CMP	0.000	0.000	0.000	0.000	0.000
CMP BMU	0.879	1.010	4.023	0.000	1.970
CMP CMIOCES	0.699	0.728	1.122	0.000	1.600
CMP CMIOPES	0.459	0.773	1.771	0.000	0.883
e Trk:					
TCE CrkTrk	0.052	0.068	0.099	0.013	0.180
LBE CrkTrk	0.353	0.354	0.419	0.042	0.000
PHX CrkTrk	0.154	0.256	0.528	0.082	0.000
μ Trk:					
CMUP CrkTrk	0.174	0.185	0.396	0.052	0.504
CMP CrkTrk	0.320	0.287	0.314	0.342	0.712
CMX CrkTrk	0.128	0.188	0.084	0.068	0.521
CMXMsKs CrkTrk	0.139	0.218	0.322	0.144	0.328

Table 27: Ratio of non-triggerable to triggerable fakes by dilepton category and signal region. Note that the ratio for dilepton categories with two trigger lepton types is expected to be zero in the same-sign region since both leptons are required to have $p_T > 20$ GeV/c.

	Same-sign(Low M_{ll})	Opp-sign LowMetSpec(Low M_{ll})	Same-sign(0 jets)
e e:			
TCE TCE	0.100	0.000	0.000
TCE LBE	0.100	0.000	0.000
TCE PHX	0.106	0.000	0.000
LBE LBE	0.191	0.000	0.000
LBE PHX	0.039	0.000	0.000
PHX PHX	0.114	3.145	0.000
e μ:			
TCE CMUP	0.195	0.167	0.000
TCE CMP	0.000	0.000	0.000
TCE CMX	0.414	0.000	0.000
TCE CMXMsKs	0.294	0.000	0.000
TCE BMU	0.152	0.000	0.420
TCE CMIOCES	0.026	0.000	0.218
TCE CMIOPES	0.000	0.000	0.182
LBE CMUP	0.100	0.149	0.000
LBE CMP	0.282	0.000	0.000
LBE CMX	0.414	0.000	0.000
LBE CMXMsKs	0.000	0.000	0.000
LBE BMU	0.000	0.000	0.000
LBE CMIOCES	0.082	0.000	0.000
LBE CMIOPES	0.000	0.000	0.000
PHX CMUP	0.000	0.000	0.000
PHX CMP	0.000	0.000	0.000
PHX CMX	0.073	0.000	0.000
PHX CMXMsKs	0.000	0.000	0.000
PHX BMU	0.587	0.000	0.000
PHX CMIOCES	0.278	0.000	0.000
PHX CMIOPES	0.115	0.000	0.000
μ μ:			
CMUP CMUP	0.243	1.728	0.000
CMUP CMP	0.208	0.000	0.000
CMUP CMX	0.161	0.000	0.000
CMUP CMXMsKs	0.000	0.000	0.000
CMUP BMU	0.000	0.000	1.440
CMUP CMIOCES	0.168	0.000	0.564
CMUP CMIOPES	0.000	0.000	0.551
CMX CMP	0.000	0.000	0.000
CMX CMX	0.000	0.000	0.000
CMX CMXMsKs	0.000	0.000	0.000
CMX BMU	0.000	0.000	0.899
CMX CMIOCES	0.088	0.000	0.489
CMX CMIOPES	0.000	0.000	0.450
CMXMsKs CMP	0.000	0.000	0.000
CMXMsKs CMXMsKs	0.000	0.000	0.000
CMXMsKs BMU	0.000	0.000	0.464
CMXMsKs CMIOCES	0.000	0.000	0.686
CMXMsKs CMIOPES	1.331	0.000	0.091
CMP CMP	0.000	0.000	0.000
CMP BMU	0.000	0.000	1.511
CMP CMIOCES	0.000	0.000	1.388
CMP CMIOPES	0.000	0.000	0.922
e Trk:			
TCE CrkTrk	0.025	0.000	0.172
LBE CrkTrk	0.053	0.000	0.000
PHX CrkTrk	0.093	0.000	0.000
μ Trk:			
CMUP CrkTrk	0.097	0.000	0.472
CMP CrkTrk	0.000	0.000	0.815
CMX CrkTrk	0.038	0.000	0.442
CMXMsKs CrkTrk	0.076	0.000	0.300

Table 28: Ratio of non-triggerable to triggerable fakes by dilepton category and control region. Note that the ratio for dilepton categories with two trigger lepton types is expected to be zero in the same-sign region since both leptons are required to have $p_T > 20$ GeV/c.

Category	WW	WZ	ZZ	$t\bar{t}$	DY	$W\gamma$	W+jets	Total	Data
$e\ e$	9.8	7.5	7.6	5.4	4175.4	3.2	47.5	4256.4	4436.0
$e\ \mu$	0.0	0.0	0.0	0.0	0.0	0.0	0.0	0.0	0.0
$\mu\ \mu$	7.9	4.9	5.4	4.3	2173.6	0.0	22.4	2218.4	2407.0
e trk	7.4	2.4	2.4	3.9	1165.9	0.5	32.3	1214.8	1109.0
μ trk	4.2	1.4	1.4	2.3	575.4	0.1	13.0	597.8	596.0
Total:	29.3	16.1	16.8	15.9	8090.2	3.8	115.2	8287.4	8548.0

Table 29: Predicted and observed yields in the same-flavor Drell-Yan Region after moving the DY $\not\!\!E_T$ cut and renormalizing as a function of $M_{\ell\ell}$.

6 Control Regions

In this section, we present the control regions in which we have tested our data model. Each control region attempts to isolate or enhance effects that must be modeled. Control regions are generally events obtained using the standard opposite-sign selection criteria from Section 4 but with the cuts on one particular selection requirement reversed. The control regions considered are:

- Events in a Drell-Yan (DY) control region are required to have $15 < \not\!\!E_{Tspec} < 25$ GeV and a dilepton invariant mass in the Z mass region $76 < M_{\ell\ell} < 106$ GeV. Only ee, $\mu\mu$, and e/μ+track events are accepted. This event sample is used to tune the $\not\!\!E_T$ cut in our Drell-Yan MC.
- Events in another Drell-Yan (DY) control region are required to have $\not\!\!E_T < 25$ GeV ($\not\!\!E_T < 15$ GeV for $e\mu$ candidates) and a dilepton invariant mass in the Z mass region $76 < M_{\ell\ell} < 106$ GeV. This event sample tests our modeling of lepton ID scale factors and trigger efficiencies over all the different lepton categories as well as the luminosity accounting based on our good run lists.
- Events in the same-sign region satisfy an equivalent set of selection criteria to the opposite-sign events contained within our signal regions. These events test our modeling of contributions from photons and jets misidentified as leptons

More detail regarding each of the control regions is given below.

6.1 Same-flavor Drell-Yan Control Region

Put here a description of the DY3 Met scaling

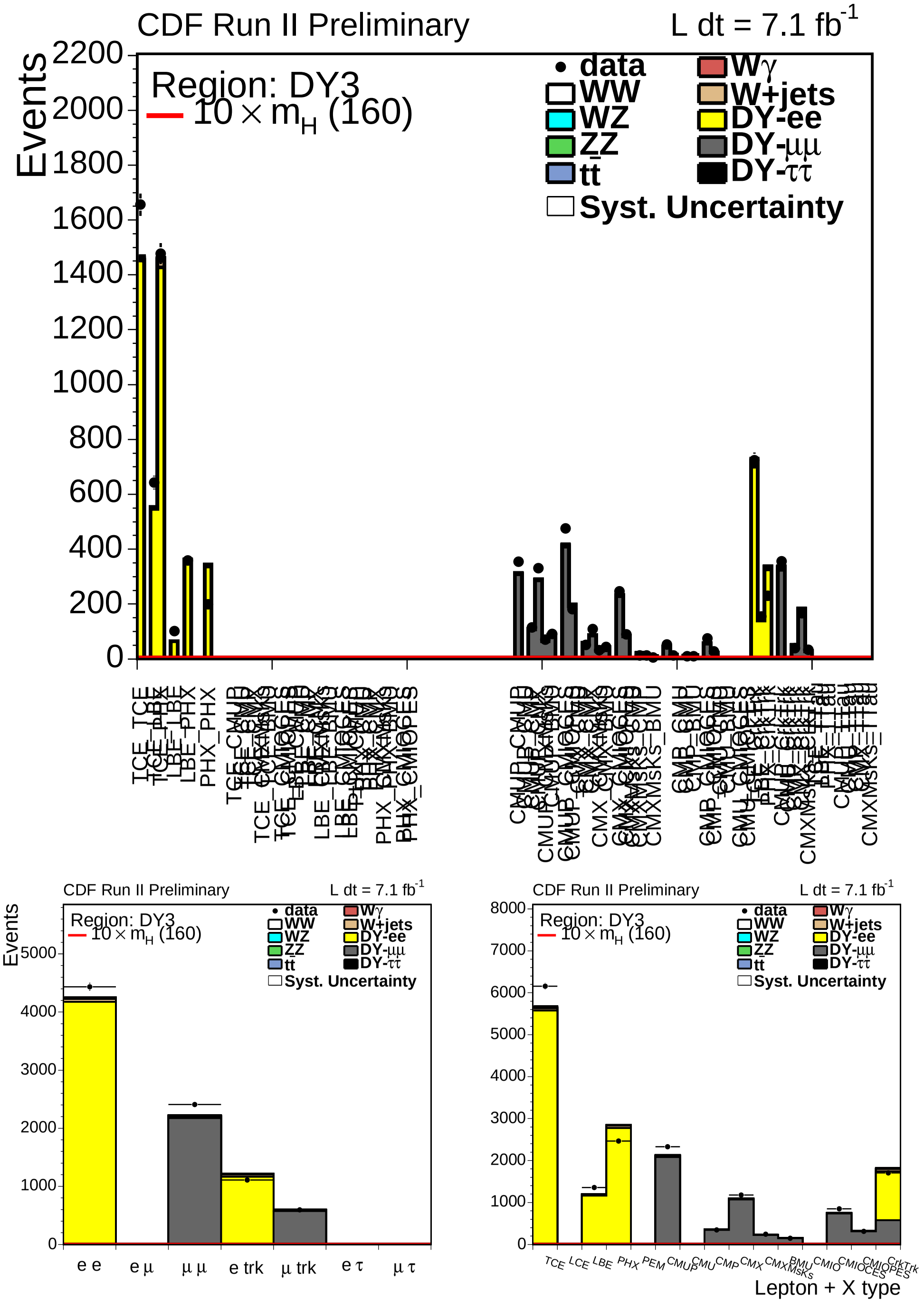

Figure 10: Same-flavor Drell-Yan control region after $\not\!\!E_T$ tuning.

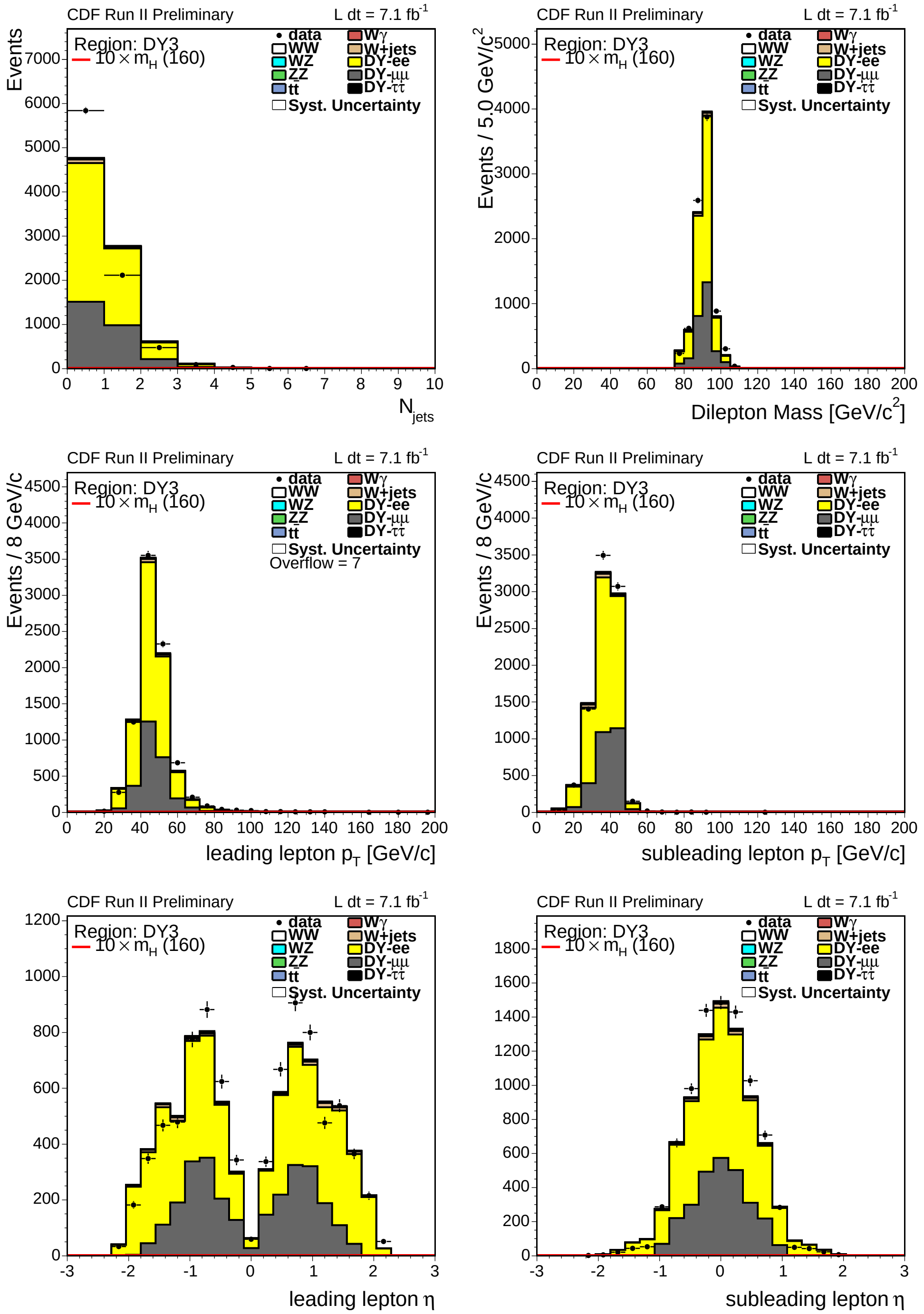

Figure 11: Same-flavor Drell-Yan control region after $\not\!\!E_T$ tuning.

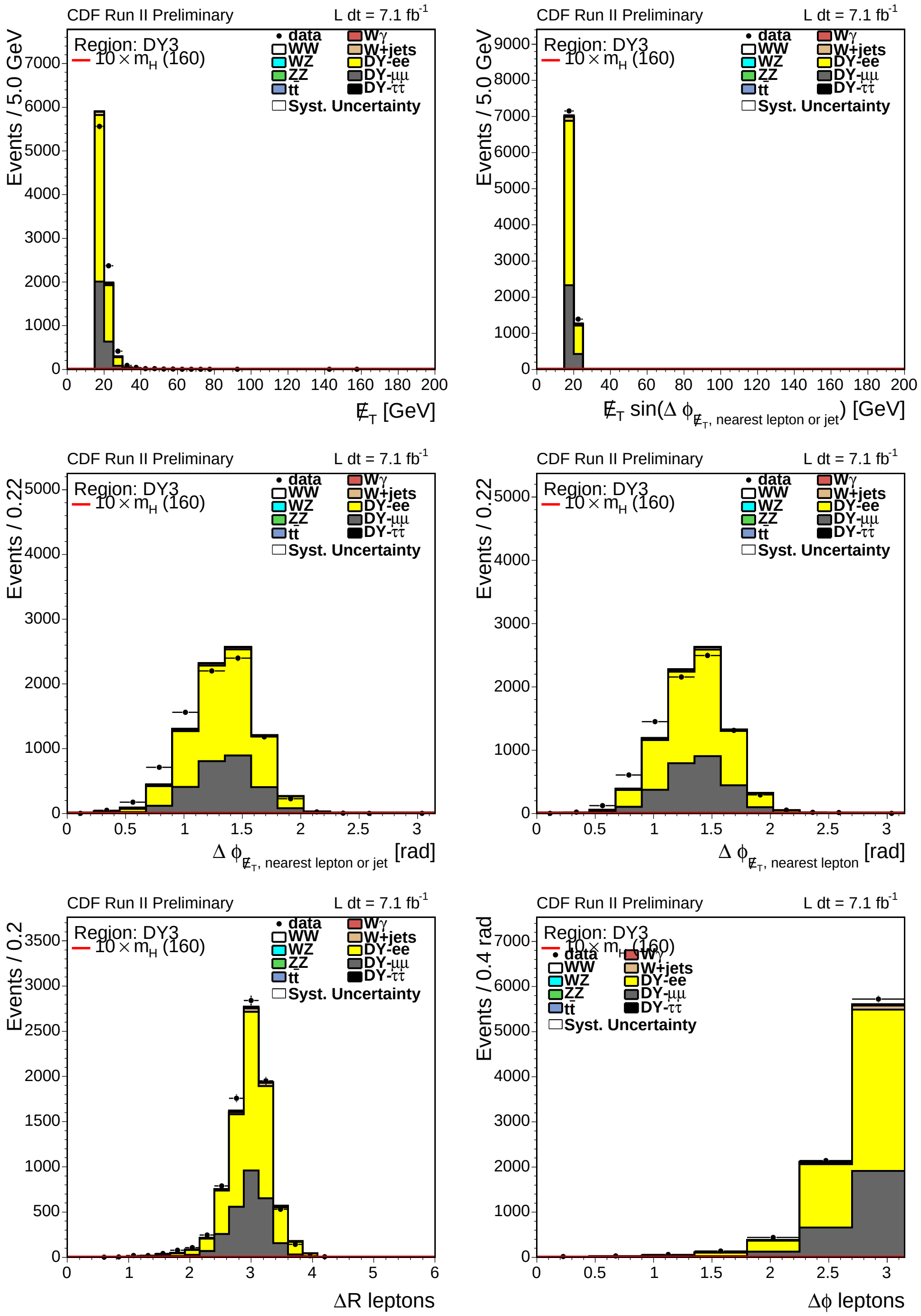

Figure 12: Same-flavor Drell-Yan control region after $\not\!\!E_T$ tuning.

Category	WW	WZ	ZZ	$t\bar{t}$	DY	$W\gamma$	W+jets	Total	Data
$e\ e$	17.0	107.3	101.3	4.6	293309.6	4.4	1592.1	295136.2	284153.0
$e\ \mu$	15.4	0.4	0.2	3.3	269.1	1.2	416.4	706.0	274.0
$\mu\ \mu$	14.7	76.8	75.7	3.6	206689.7	0.0	1119.0	207979.5	205711.0
e trk	12.8	30.3	29.4	3.2	80914.4	0.8	1563.7	82554.5	74527.0
μ trk	7.7	21.2	20.4	1.9	57466.0	0.1	749.0	58266.5	54915.0
Total:	67.6	235.9	227.0	16.6	638648.8	6.6	5440.2	644642.6	619580.0

Table 30: Predicted and observed yields in the Drell-Yan Region.

Category	WW	WZ	ZZ	$t\bar{t}$	DY	$W\gamma$	W+jets	Total	Data
$e\ e$	10.5	7.3	1.8	4.6	19.1	95.3	95.9	234.4	244.0
$e\ \mu$	12.0	12.7	1.1	5.0	65.8	82.0	114.0	292.8	256.0
$\mu\ \mu$	0.0	4.0	0.5	0.0	0.5	0.0	11.2	16.1	13.0
e trk	3.7	3.7	0.5	1.4	6.3	19.0	26.4	60.9	76.0
μ trk	0.0	2.0	0.2	0.0	1.3	2.8	11.7	18.0	13.0
Total:	26.2	29.7	4.1	11.1	93.0	199.1	259.1	622.2	602.0

Table 31: Expected and observed yields in the Same-Sign region.

6.2 Dilepton Z-mass (DY) Control Region

Here we consider opposite-sign dileptons in the Z mass region $76 < M_{\ell\ell} < 106$ GeV which is completely dominated by the Drell-Yan process. We require one trigger lepton and a second lepton with $E_T > 10$ GeV. We also require $\not\!\!E_T < 25$ GeV (< 15 GeV for $e\mu$ pairs) in this region, and include events with any number of jets. Because this region requires an inverse $\not\!\!E_T$ cut, we do not apply the DY $\not\!\!E_T$ scaling here.

Table 30 and Figures 13-15 show the agreement between the expected number of events and the observed yield for each dilepton catagory, and for lepton categories combined into ee and $\mu\mu$. We generally find good agreement in the shapes and normalizaton.

6.3 Base Same Sign Control Region

To check modeling of the W+jets and $W\gamma$ fake backgrounds, we look at events that satisfy all signal selection criteria with the exception of the opposite sign requirement which is reversed. We now also include events with any number of jets; previously this control region was limited to events with only zero or one jets. This region is dominated by fake leptons originating either from jets or photons. The PHX categories also have significant contributions from charge mis-identification. The results are shown in Table 31. In this region we observe excellent agreement in the observed and predicted numbers of events as well as in the predicted and observed kinematic distributions as shown in Figures 16-18.

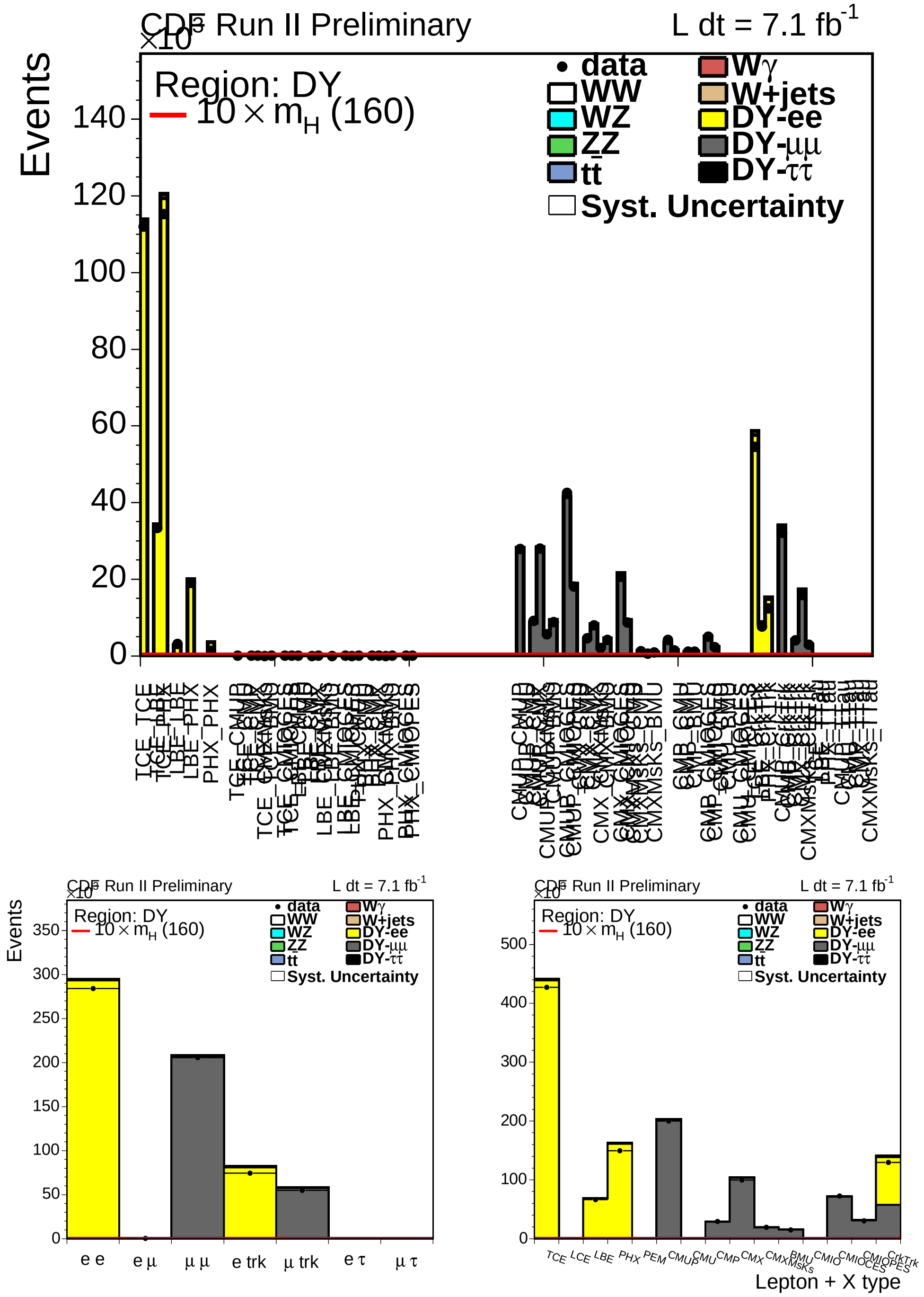

Figure 13: Drell-Yan ($Z \rightarrow l^{+}l^{-}$) control region.

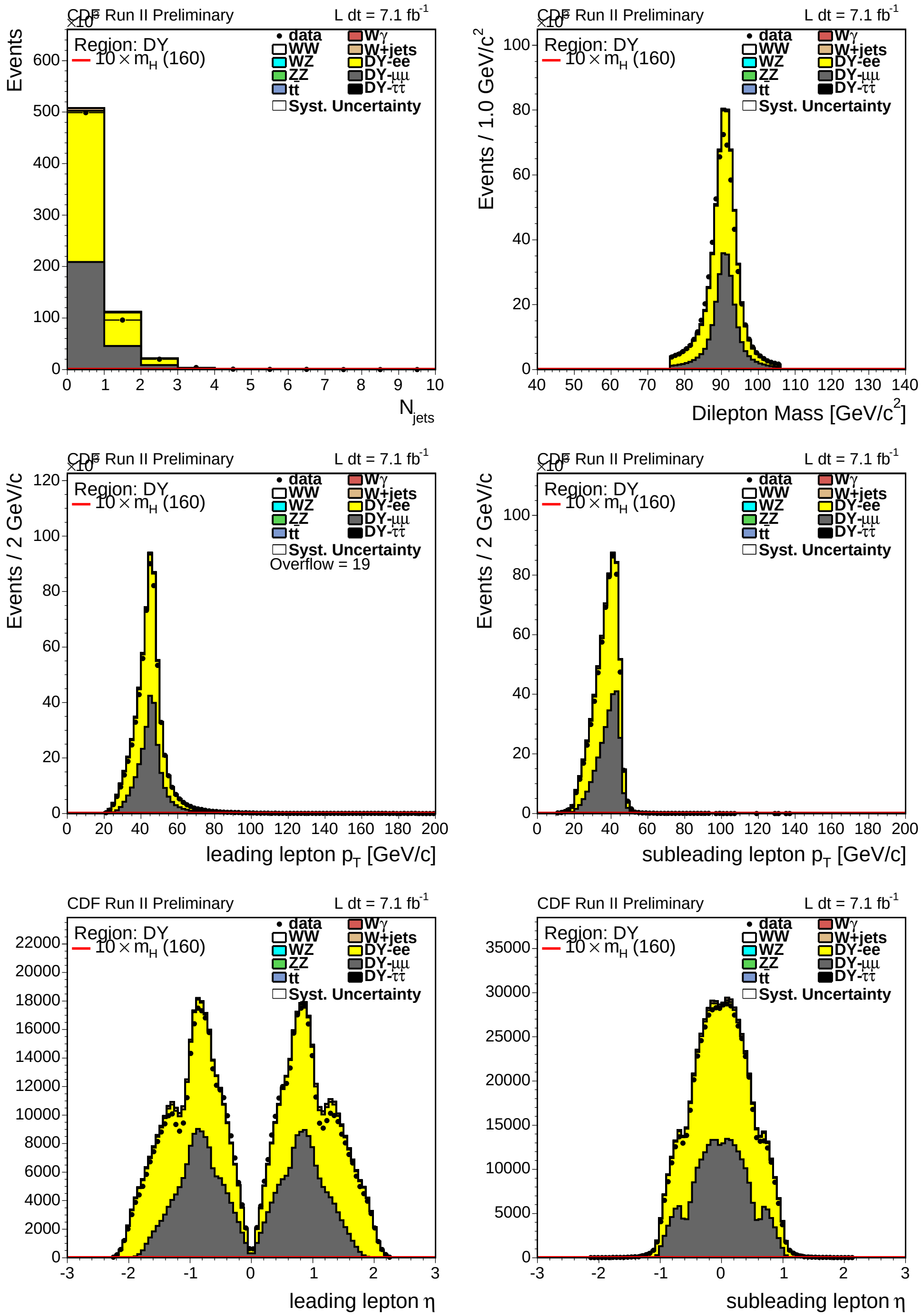

Figure 14: Drell-Yan ($Z \to l^+l^-$) control region.

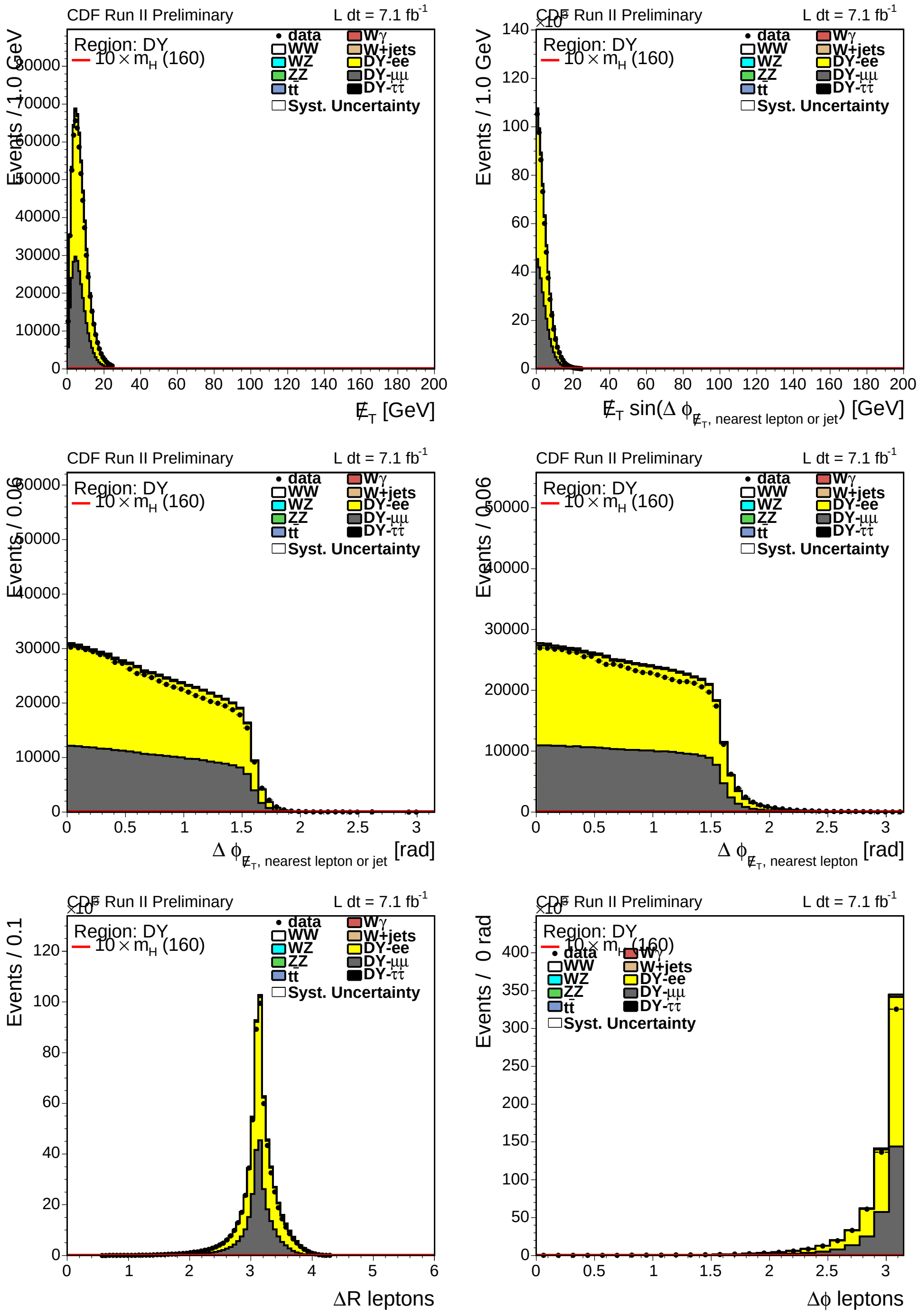

Figure 15: Drell-Yan ($Z \to l^+ l^-$) control region.

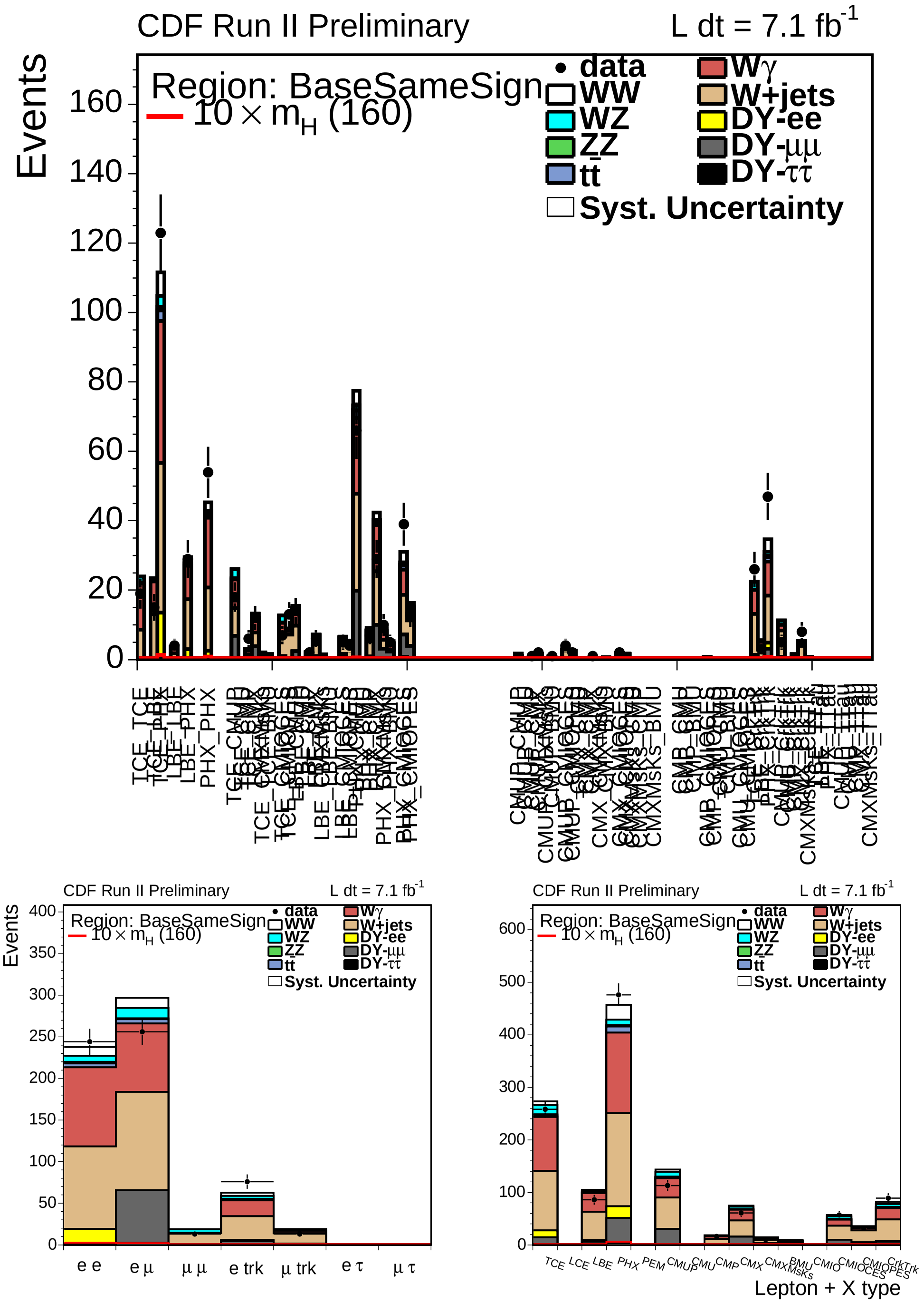

Figure 16: Base Same Sign control region.

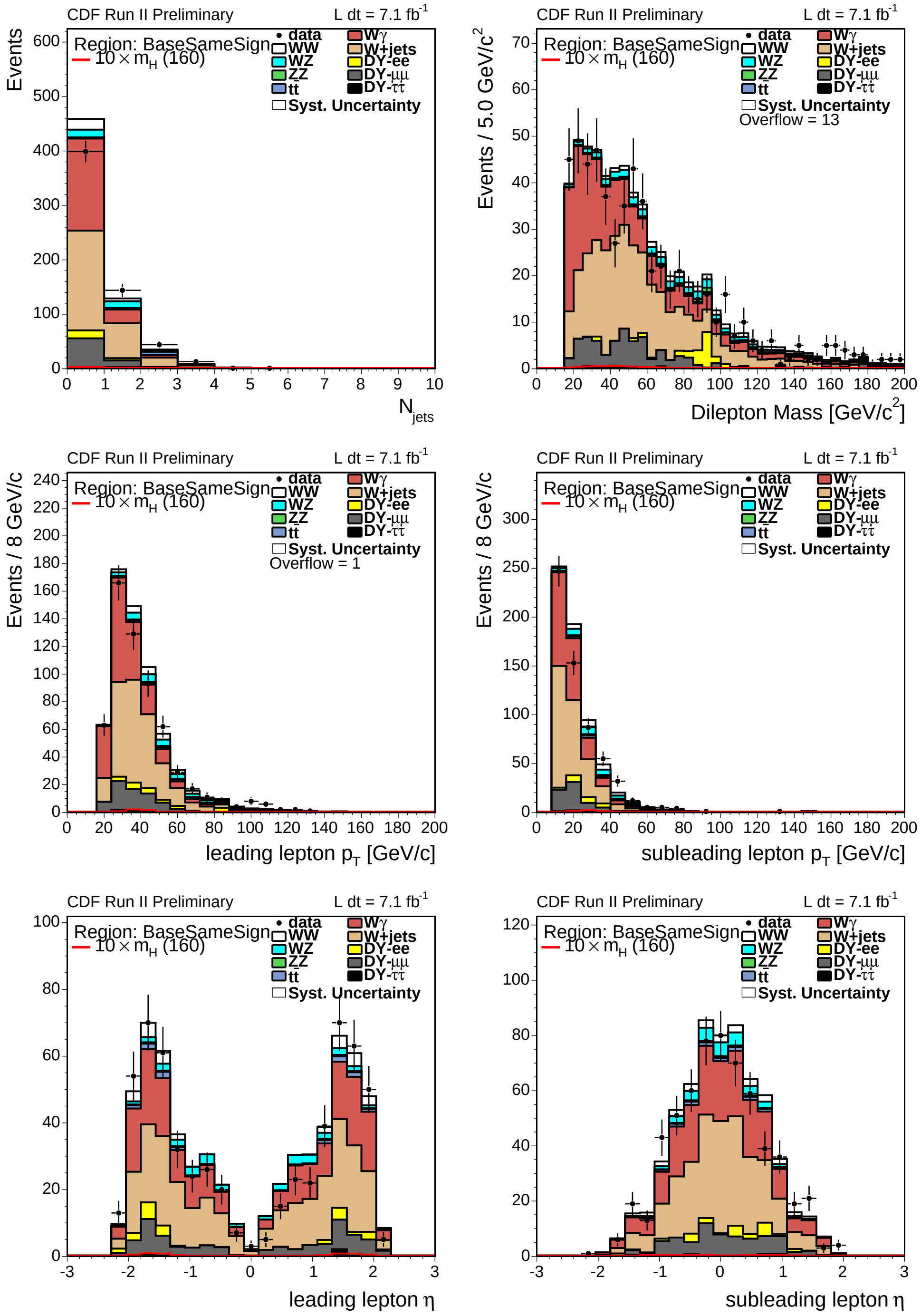

Figure 17: Base Same Sign control region.

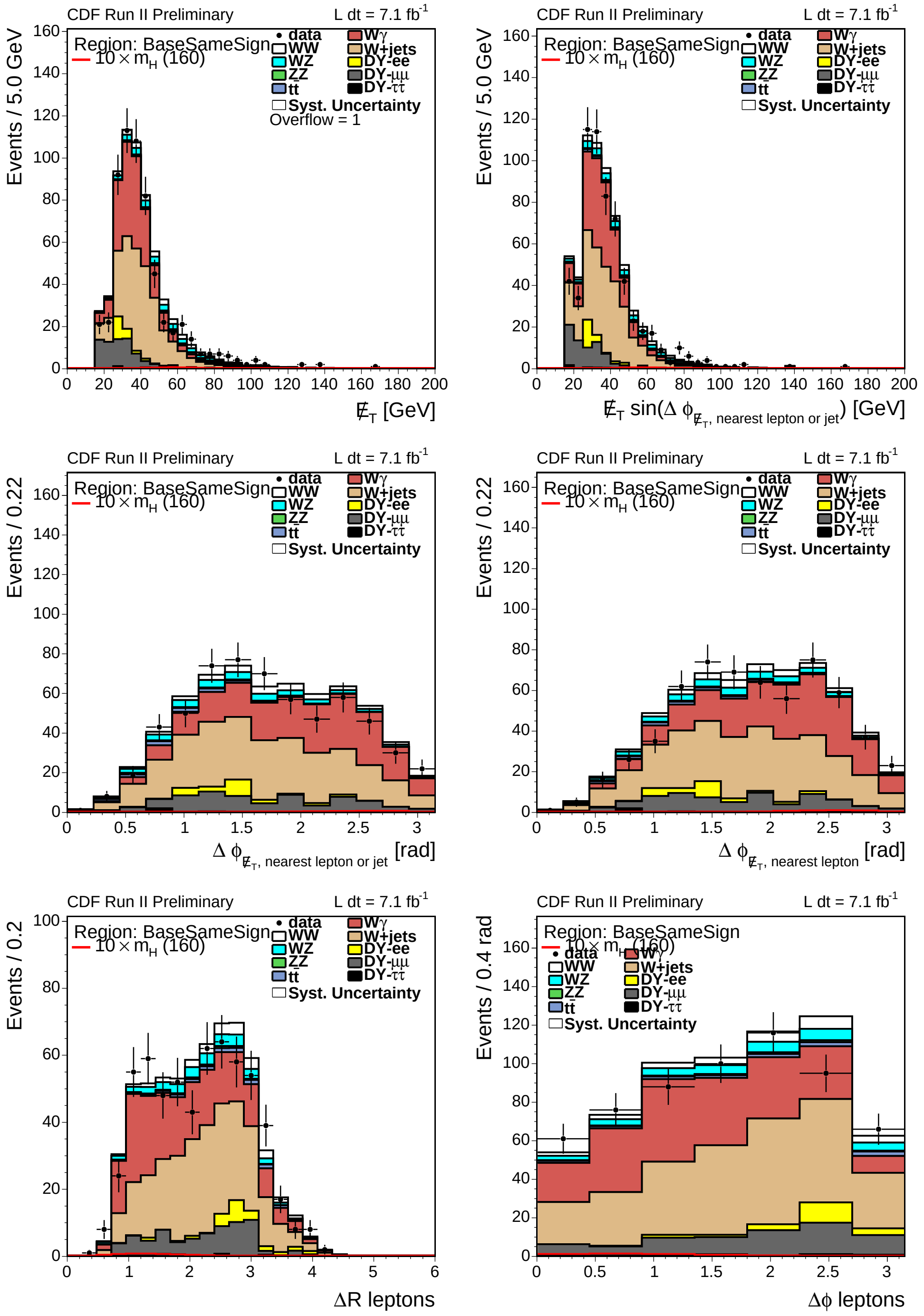

Figure 18: Base Same Sign control region.

7 Systematics

Sources of systematic uncertainty for this analysis are similar to those for the previous analysis using 4.8 fb^{-1} [1]. The $W\gamma$ uncertainties are derived in part from the studies of the $M_{ll} < 16$ GeV same-sign events as described in Section 11.2.1. The fake rate systematic uncertainties have been re-evaluated for all channels, and jet energy scale systematics have been evaluated for all channels for the first time. These are described in Sections 7.2.1 and 7.2.2.

Systematic uncertainties may effect both the normalization (or "rate") and the shape of the templates used in the limit calculation. As propagating the effects of shape uncertainties is CPU intensive, we only consider shape uncertainties for those expected to be significant. At this time the shape uncertainties considered in order of expected significance are the jet energy scale (JES) and initial state radiation (ISR). These studies are described below in Section 7.6. After evaluating the shapes, we decided not to apply any shape uncertainties at this point.

The rate systematics are determined separately for each search channel included in the analysis. The summary of all systematics are presented in Tables 44-45 for the 0 jet channel, Tables 49-50 for the 1 jet channel, Tables 54-55 for the 2 or more jets channel, Table 62 for the low-$M_{\ell\ell}$ channel, Table 67 for the same-sign channel, and Table **??** for the trilepton channels.

7.1 Cross Section Systematics

For the background processes, we take the theoretical uncertainties on the cross sections, which are calculated to either next-to-next-to-leading order ($t\bar{t}$ with $m_{top} = 172.4$ GeV [14]), next-to-leading order (WW [15], WZ and ZZ [16]), or leading order with estimated higher order corrections ($W\gamma$ [17], $Z\gamma$, and Drell-Yan). Of the signal processes, VH and VBF are electroweak processes. VH are known to NNLO, so the theoretical uncertainty on these cross sections is small, less than 5% [18]. VBF is known only to NLO, but the residual theoretical uncertainty is still estimated to be less than 10% [18].

Gluon fusion is a QCD process, so even though it is known to NNLO, the theoretical uncertainty is larger. Also important, since we divide our events by jet multiplicity, the theoretical uncertainty on the higher multiplicity jet bins is larger than the uncertainty on the inclusive cross section calculation. There exist several programs which compute the theoretical cross section for $gg \rightarrow H$ production at the Tevatron to NNLO. The previous zero and one jets version of this analysis used the FEHiP program [19]. For these studies we use the HNNLO program [20, 21, 22], which has the advantage that it makes user-specified histograms of kinematic variables. Because the Higgs is a pseudo-scalar, we expect the effects on its kinematic variables to be limited to p_{T} and rapidity. HNNLO also allows the user to define analysis selection cuts. For the studies in this section, we required the jets to have a parton-level $p_T > 20$ GeV/c and $|\eta| < 2.5$. For the leptons, we

$\mu_R = \mu_F$	0 Jet	1 Jet	2 Jet
320	1.809	0.555	0.061
160	1.992	0.716	0.103
80	2.111	0.896	0.185
40	2.079	0.185	0.355

Table 32: Value of the cross section (in *pb*) divided into jet bins, calculated by HNNLO for variations of the renormalization and factorization scales μ_R and μ_F for a Higgs of mass 160 GeV. The exact value of the cross sections depend on cuts made before calculations, and these values are not used elsewhere in the analysis. The uncertainty is determined by the percentage change around the central value $\mu_R = \mu_F = M_H$.

required one have $p_T > 20$ GeV/c and the other have $p_T > 10$ GeV/c; both were required to have $|\eta| < 2$.

There are two main independent sources of theoretical uncertainty; other sources were found to be negligible [23]. The two main sources are the uncalculated higher-order QCD radiative corrections and knowledge of the parton distributions. To estimate the size of the QCD corrections, we use a method commonly used in perturbative QCD calculations, which is to vary the renormalization and factorization scales (μ_R and μ_F respectively). This was recently done in [24] using the new MSTW2008 NNLO PDFs [25] dividing the theoretical cross section uncertainties by jet bins as done in this analysis. We cross-check these results using the HNNLO program with the MSTW2008 NNLO PDFs. Comparing NNLO calculations from FEHiP to recent N^{3}LO calculations [26, 27] shows the best value for NNLO predictions is to set $\mu_R = M_H/2$. Another reasonable choice is to set the factorization and normalization scales to be equal. However, the default scale setting used in [24] is $\mu_R = \mu_F = M_H$, so we calculate results around this central point instead.

To determine the uncertainty on the $gg \to H$ cross section due to higher order QCD corrections, we used $M_H = 160$. The resulting change in the NNLO Higgs p_{T} distribution is shown in Fig. 19. The cross section divided by jet bin is also shown in Fig. 19. The change in the cross section by jet bin is given in Tab. 32. Using $\mu_R = M_H$ as the central value, we see similar uncertainties by jet bin to those calculated in [24]. Thus we take the average of the increasing and decreasing scale variations in [24] and apply them by jet bin as the systematic uncertainty on the $gg \to H$ cross section due to scale uncertainty.

The second uncertainty on the cross section is due to our knowledge of the parton distributions. A detailed study including $gg \to H$ electroweak corrections was done in Ref. [13] and found an expected PDF uncertainty of 7.7%. However, this study did not attempt to determine the uncertainty for different jet bins. The study also does not account for the effect of varying $\alpha_s(M_Z)$. We completed our own study, using HNNLO and the MSTW2008 NNLO PDF standard error eigenvectors for a range of α_s values [28]. We used the ±90% C.L. variations of α_s and the PDF error sets, for a total of 80 PDF sets to consider. With HNNLO, we calculated the cross section in each jet bin for each

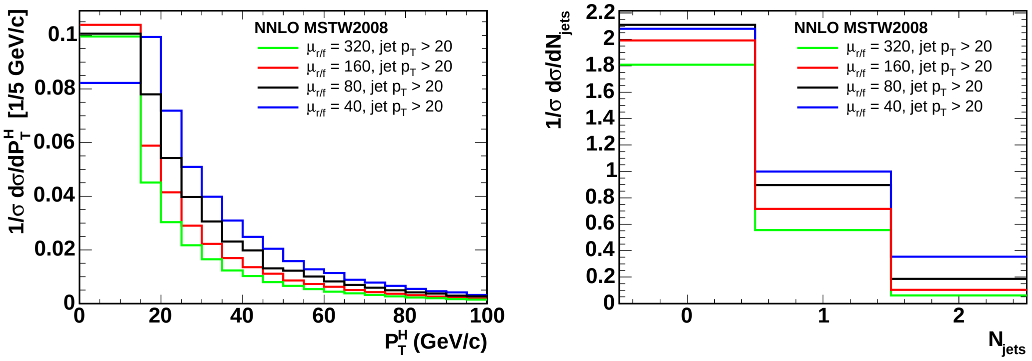

Figure 19: Changes calculated by the HNNLO program when the scales μ_R and μ_F are varied. On the left is the NNLO Higgs p_{T} distribution, while on the right is the cross section divided by jet bins.

Channel:	0 Jet	1 Jet	2 Jet
-90% C.L. α_s + PDF	-9.6%	-15.0%	-19.4%
$+90\%$ C.L. α_s + PDF	+5.6%	+19.5%	+40.0%
Cross section PDF Uncertainty	7.6%	17.3%	29.7%

Table 33: Systematic changes in the cross section, divided into jet bins and calculated using HNNLO, when considering the MSTW2008 standard error eigenvectors evaluated at the $\pm 90\%$ C.L. α_s values. We found that the -90% C.L. variations always decreased the cross section, while the $+90\%$ C.L. variations always increased the cross section; this is why they have opposite signs in the table. We take the average uncertainty as a systematic on the $gg \rightarrow H$ cross section.

PDF variation using $\mu_R = \mu_F = M_H = 160$. We found that the -90% C.L. variations always decreased the cross section, while the $+90\%$ C.L. variations always increased the cross section. We followed the standard CDF Joint Physics prescription for evaluating PDF errors and took the sum in quadrature of the change due to each PDF, separately for the -90% and $+90\%$ C.L. variations, as our uncertainty. The results are shown in Table 33. We take the average of the -90% and $+90\%$ C.L. variations as our systematic uncertainty on the cross section due to our knowledge of the PDFs.

7.2 Acceptance Systematics

The standard luminosity uncertainty of 5.9% is assigned to all processes except for W+jets, which is determined from data. As previously, the lepton ID and trigger efficiencies are varied coherently up and down to determine their affect on the acceptance. Both uncertainties have a small effect, for the most part around 2%, on the signal and background processes. Because these three effects are small and uncorrelated for every process, we combine them in quadrature.

We also consider the effect of the differences between LO and higher order calculations on the acceptance. We determine the size of higher order effects by comparing a LO Pythia WW sample to the WW MC@NLO sample. We assign the full difference (10%) to the processes simulated only by LO Pythia. The $W\gamma$ process has an additional 10% systematic uncertainty on the MC modeling of conversions, based upon the studies in Sec. 11.2.1. PDF model uncertainties were determined to be small using the standard CTEQ6M error eigenvectors in previous versions of the analysis. For all processes except WW and the $gg \rightarrow H$ signal process, the PDF model uncertainties are assumed to be covered by the 10% higher order effects uncertainty. The $gg \rightarrow H$ and WW PDF model uncertainty determinations are discussed in Sections 7.2.3 and 7.2.4.

The uncertainties on the modeling of $\not{E}_T$ has been shown in previous versions of this analysis to be very small for processes with real $\not{E}_T$. For the DY process which has no real $\not{E}_T$, we showed in Section 6.2 that we could achieve good MC modeling by shifting the $\not{E}_T$ down by 4 GeV. To determine a systematic uncertainty on this tuning, we look at the acceptance when the $\not{E}_T$ is shifted by either 2 GeV or 6 GeV. With these variations we assign a DY $\not{E}_T$ modeling systematic of between 19-25% for each jet channel.

7.2.1 W+jets Acceptance Systematics

The only uncertainty on the W+jets process, which is determined from data, is the uncertainty on the rate at which jets will fake leptons. We estimate the effect of this uncertainty on the acceptance by varying the fake rates within their assigned uncertainties (shown by the solid light grey bands in Figures 8-9). These variations have different effects in each analysis channel and thus are calculated separately for each channel. The final assigned systematic is the average change in acceptance from varying the fake rate up by 1σ and down by 1σ, as the changes are very symmetric for all channels.

7.2.2 Jet Energy Scale Acceptance Systematics

In previous versions of this analysis involving only opposite-sign jet bins, the jet energy scale systematic was found to be a small contribution and thus not included. However, now that more channels are using cuts on the number of jets or even using N_{jets} in the neural networks, we decided to evaluate the jet energy scale systematics for all channels. This was done by varying the jet energy scale within its assigned uncertainty (up and down by 1σ) for all processes modeled by Monte Carlo, and calculating the change in acceptance for each process. This systematic also has different effects in each analysis channel and are calculated separately for each channel. In jet-inclusive channels (such as the trilepton WH channel) the effect is nearly negligible. In the opposite-sign jet bin channels, the effects are anti-correlated (changing the JES moves events between jet bins but does not change overall acceptance).

7.2.3 $gg \to H$ Acceptance Systematics

The $gg \to H$ acceptance also depends on the cross section. In the previous zero and one jet analysis, the Higgs acceptance systematic was estimated by reweighting the Higgs p_{T} spectrum in Pythia to match an NLO calculation from FEHiP, with $\mu_R = \mu_F = 82.5$. This reweighting led to acceptance changes of less than 10%. In this analysis, we now reweight our Pythia samples to the p_T spectrum given by the HqT program [29, 30], as described in Section 8.3. We then use the same renormalization and factorization scale and PDF variations discussed in Section 7.1 to determine acceptance uncertainties. We reweight in the Higgs p_{T} and also, separately, the Higgs rapidity distribution.

The effect of the Higgs p_{T} reweighting depends on how many jets are in the final state. By reweighting the Higgs p_{T} spectrum, we are reweighting the vector sum of the p_{T} of the two jets which are recoiling against the Higgs. Thus, events which previously had one or more jets passing selection cuts could move into a lower jet bin, and vice versa. Because this reweighting is effectively moving events back and forth between the 0, 1, and 2+ jet bins, these acceptance systematics (referred to as "Scale (jets)" and "PDF Model (jets)" in the systematics tables) are anticorrelated between the jet bins. The effect of the Higgs rapidity distribution reweighting does not move events between different jet bins. Instead, when we reweight events by Higgs rapidity, we move the leptons into or outside of our forward acceptance. These acceptance systematics, referred to as "Scale (leptons)" and "PDF Model (leptons)" in the systematics tables, are correlated between the jet bins.

To determine an acceptance systematic from the choice of scale, we consider the scale variations $\mu_R = \mu_F = M_H/2$ and $\mu_R = \mu_F = 2 \cdot M_H$, using the MSTW2008 NNLO PDFs. We evaluate the Higgs p_T spectrum with HqT and the Higgs rapidity spectrum with HNNLO and no pre-selection cuts. To see if the acceptance changed varied as a function of Higgs mass, we considered three Higgs mass points: 135, 165, and 195. All three were found to have about the same change in acceptance, so the values for $M_H = 165$ are used for all Higgs masses. The Higgs p_T and rapidity histograms for $m_H = 165$ are shown in Fig. 20, and the changes in acceptance after reweighting are given in Tab. 34. For the rapidity reweighting, the systematic uncertainty is taken between the default acceptance, and the acceptance after reweighting to HNNLO with $\mu_R = \mu_F = M_H$. The change in acceptance between $\mu_R = \mu_F = M_H, M_H/2$, and $2 \cdot M_H$ was found to be negligible ($\sim 0.1\%$). As expected, systematic uncertainties between jet bins are anti-correlated for Higgs p_T reweighting and correlated for Higgs rapiditiy reweighting.

To determine an acceptance systematic from the knowledge of the PDFs, we again use the MSTW2008 NNLO ±90% C.L. variations of α_s and PDF standard error eigenvectors. Again, we evaluate the Higgs p_T spectrum with HqT and the Higgs rapidity spectrum with HNNLO and no pre-selection cuts, using $\mu_R = \mu_F = M_H = 165$. The standard PDF error eigenvectors were used to calculate the change for Higgs masses of 135, 165, and 195, and all three mass points showed the same change in acceptance. Therefore, for the study with variations of both α_s and PDF we only consider $M_H = 165$. Several

Higgs p_T reweighting	0 Jet	1 Jet	2 Jet	Low $M_{\ell\ell}$
$\mu_R = \mu_F = M_H/2$	-1.7%	+2.3%	+8.6%	-0.8%
$\mu_R = \mu_F = 2 \cdot M_H$	+1.3%	-1.6%	-5.0%	+1.5%
Scale (jets) Uncertainty	+1.5%	-1.9%	-6.8%	+1.2%
Higgs rapidity reweighting	0 Jets	1 Jet	2 Jet	Low $M_{\ell\ell}$
Scale (leptons) Uncertainty	1.7%	2.2%	3.1%	0.6%

Table 34: Systematic uncertainties on the $gg \to H$ acceptance due to scale variations, divided into jet bins and for the Low $M_{\ell\ell}$ search region (which uses events with zero and one jets). The Higgs p_T spectra are calculated with HqT, while the Higgs rapidity spectra are calculated with HNNLO. As expected, systematic uncertainties between jet bins are anti-correlated for Higgs p_T reweighting (indicated by the positive and negative signs). For the Higgs rapidity reweighting, the systematic uncertainty is taken between the default acceptance and the acceptance after reweighting to HNNLO with $\mu_R = \mu_F = M_H$.

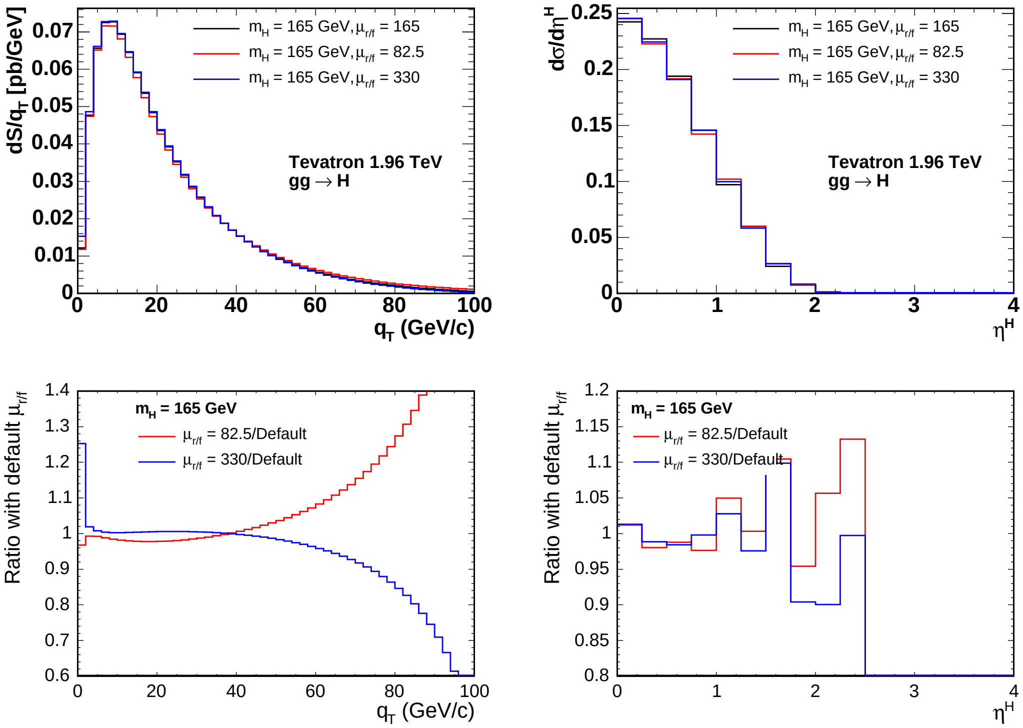

Figure 20: Effect of scale variations on the $gg \to H$ p_T spectrum (left, calculated with HqT) and the rapidity distribution (right, calculated with HNNLO) for $M_H = 165$. On top are the distributions while on the bottom are the ratios of the two scale variations ($M_H/2$ and $2 \cdot M_H$) with the default scale (M_H) distribution.

Higgs p_T reweighting	0 Jets	1 Jet	2 Jet	Low $M_{\ell\ell}$
-90% C.L. α_s + PDF	-4.5%	+5.0%	+8.7%	-1.7%
$+90\%$ C.L. α_s + PDF	+6.5%	-7.5%	-15.9%	+2.5%
PDF (jets) Uncertainty	+5.5%	-6.3%	-12.3%	+2.1%
Higgs rapidity reweighting	**0 Jets**	**1 Jet**	**2 Jet**	**Low $M_{\ell\ell}$**
-90% C.L. α_s + PDF	+1.1%	+1.6%	+2.1%	+0.2%
$+90\%$ C.L. α_s + PDF	-4.2%	-5.7%	-7.4%	-1.7%
PDF (leptons) Uncertainty	2.7%	3.6%	4.8%	1.0%

Table 35: Systematic uncertainties on the $gg \to H$ acceptance due to $\pm 90\%$ C.L. α_s and PDF variations, divided into jet bins and for the Low $M_{\ell\ell}$ search region (which uses events with zero and one jets). The Higgs p_T spectra are calculated with HqT, while the Higgs rapidity spectra are calculated with HNNLO. As expected, systematic uncertainties between jet bins are anti-correlated for Higgs p_T reweighting (indicated by the positive and negative signs) and correlated for Higgs rapidity reweighting.

examples of the Higgs p_T and rapidity histograms are shown in Fig. 21. The changes in acceptance are again added in quadrature for each of the -90% C.L. and $+90\%$ C.L. eigenvectors, as described in Section 7.1, and the results are given in Table 35. For the Higgs rapidity reweighting, the acceptance changes are calculated from the systematic varied Higgs rapidity distributions to the default MSTW2008 NNLO Higgs rapidity.

7.2.4 *WW* Acceptance Systematics

Direct WW production is the largest background for the most sensitive search channel, the opposite-sign dilepton with large missing energy and zero jets signature. This is why WW is modeled by a next-to-leading order Monte Carlo, MC@NLO. With MC@NLO, we also have the option of repeating some of the studies on scale and PDF variations performed for $gg \to H$. Instead of reweighting the Higgs p_T and rapidity, we reweight the WW sample by the p_T and rapidity of the WW system, determined from the HEPG bank by adding the four-vectors of the two leptons and two neutrinos from the W decays.

In MC@NLO, the default scale is $\mu_R = \mu_F = 1$. We generated one million WW events each with $\mu_R = \mu_F = 0.5$ and $\mu_R = \mu_F = 2$, then used these samples to reweight our much larger WW sample. The WW p_T and rapidity distributions are shown in Figure 22. Reweighting by the rapidity of the WW system had a negligible effect on the acceptance ($< 0.1\%$). Reweighting by the p_T, however, did have some effect, particularly in the high-multiplicity jet bins, as shown in Table 36.

To determine an acceptance systematic from the knowledge of the PDFs, we used the 40 CTEQ6 error eigenvectors. As our default sample is generated with CTEQ5M, there is some difference due to the newer PDF. We tested the difference by running one sample of 1 million events using the default CTEQ6M PDF, and found the change in acceptance

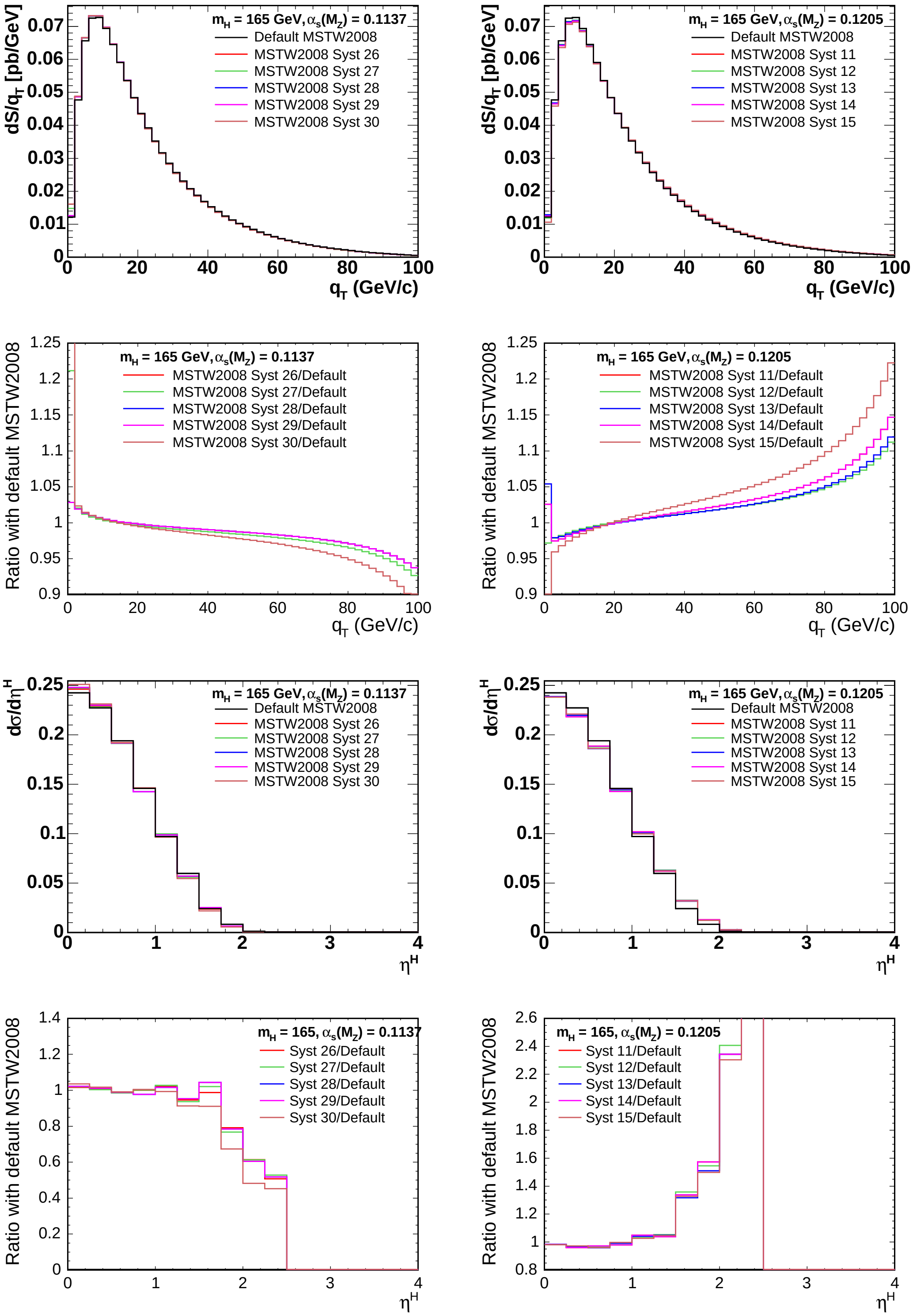

Figure 21: Top two rows show the Higgs p_T distributions for five different PDF eigenvectors, with $\alpha_s = 0.1137$ (-90% C.L. value) or $\alpha_s = 0.1205$ ($+90\%$ C.L. value). The ratios with the default Higgs p_T distribution are also shown. The bottom two rows show the Higgs rapidity distributions for the same eigenvectors. The eigenvector with the largest shape variation (30 for -90% C.L. and 15 for $+90\%$ C.L.) will be used to determine the effect of shape systematics, as discussed in Section 7.6.

WW p_T reweighting	0 Jet	1 Jet	2 Jet	Low $M_{\ell\ell}$	Same-sign
$\mu_R = \mu_F = 0.5$	-0.4%	+4.6%	+10.0%	+0.5%	+7.05%
$\mu_R = \mu_F = 2$	+0.2%	-3.4%	-6.4%	-0.4%	-5.13%
Scale (jets) Uncertainty	+0.3%	-4.0%	-8.2%	-0.4%	-6.09%

Table 36: Systematic uncertainties on the WW acceptance due to scale variations, divided into jet bins and for the Low $M_{\ell\ell}$ search region (which uses events with zero and one jets) and the same-sign search region (which uses events with one or more jets). As for scale variations in $gg \to H$, acceptance changes are anti-correlated between the jet bins, although here the Low $M_{\ell\ell}$ channel follows the sign of the 1-jet bin instead of the 0-jet bin.

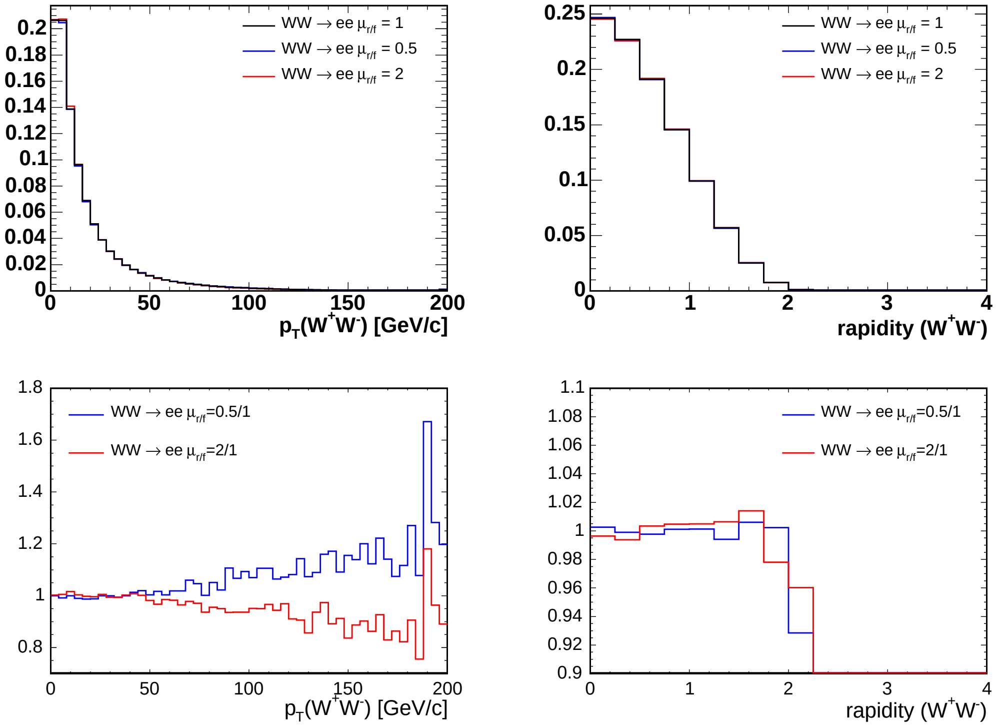

Figure 22: Effect of scale variations on the WW p_T spectrum (left) and the rapidity distribution (right), all calculated with MC@NLO. On top are the distributions while on the bottom are the ratios of the two scale variations (0.5 and 2) with the default scale (1) distribution.

WW p_T reweighting	0 Jet	1 Jet	2 Jet	Low $M_{\ell\ell}$	Same-sign
PDF, positive change	0	0.32%	2.95%	0	1.21%
PDF, negative change	1.09%	4.67%	4.23%	1.58%	5.70%
PDF (jets) Uncertainty	1.1%	4.7%	4.2%	1.6%	5.7%

Table 37: Systematic uncertainties on the WW acceptance due to PDF uncertainties, divided into jet bins and for the Low $M_{\ell\ell}$ search region (which uses events with zero and one jets) and the same-sign search region (which uses events with one or more jets). The zero entries indicate there were no PDFs which caused an increase in acceptance.

to be less than 0.5% for all channels. Thus, we calculate the PDF errors by reweighting the WW p_T distribution to each of the error eigenvectors, then add in quadrature the changes in acceptance for each channel. The changes are added separately by whether they increase or decrease the acceptance. The results, shown in Table 37, are about the same size as the scale uncertainties. We take the negative changes as our symmetric uncertainties to be conservative. Changes in shape for individual PDFs are small and we do not consider them as a shape systematic.

7.3 2 or More Jets Systematics

As explained in Section 10, the signal region with two or more reconstructed jets employs b-tagging to reduce $t\bar{t}$ background. When we apply b-tagging to our $t\bar{t}$ background model, we use the standard Data/MC efficiency scale factor correction for b-tagging which we take to be 0.94 ± 0.03. This uncertainty is taken as an additional systematic, under the heading b-tag Veto as shown in Table 54.

There is another systematic uncertainty to consider. We do not require data events to be in the silicon good run list. The only issue with this that could arise is that our Data/MC scale factor may not be properly scaling for events which fail b-tag requirements because they do not have silicon hits; the MC assumes there is always good silicon. To account for this, we look at the number of events in the data sample which come in on each good run list, as shown in Table 38. There are only 2 events not in the silicon good run list which have a b-tagged jet as found by SecVtx.

We then look only at the events in the silicon good run list. In this sample, the ratio of anti-b-tagged events to b-tagged events is 290:206. If the same ratio held true for events not in the silicon good run list (as the MC scale factor assumes it does), we would expect of the 19 events not in the silicon good run list that the ratio of anti-b-tagged events to b-tagged events should be 11.1:7.9. The observed ratio is actually 17:2, as shown in Table 38. Continuing with the thought, if we had only good Si runs we would expect $290 + 11.1 = 301.1$ events in the anti-b-tagged region, while our data show 307 events. In the same way, we expect $206 + 7.9 = 213.9$ events in the b-tagged region but see only 206 events.

2+ Jets Region	Number of Events
Total	515
Total b-tagged	206
Total anti-b-tagged	290
Total not in EM_SI	19
Total b-tagged not in EM_SI	2
Total anti-b-tagged not in EM_SI	17

Table 38: Summary of events with and without a b-tagged jet in the 2 or more jets signal region and which good run list they are selected in.

We therefore correct our MC prediction in the 2 or more jets signal region by scaling it up by the ratio $307/301.1 = 1.020$, and in the b-tagged $t\bar{t}$ control region by scaling it down by $206/213.9 = 0.972$. We take about half of the change in the signal region as an additional systematic to be added in quadrature with the b-tag Veto uncertainty. Note that this scale factor was reduced by including the reprocessed period 18 data, which is now included on the silicon good run list.

7.4 Same-Sign Systematics

Most of the systematics for the same-sign channel are the same as those in the opposite sign channels. Because we do not make a $\not{E}_{\mathrm{T}}$ cut in the same-sign channel, there is no systematic due to $\not{E}_{\mathrm{T}}$ modeling. One additional systematic is assessed based on the ability of Monte Carlo to model charge mismeasurement. The backgrounds WW, Drell-Yan, and $t\bar{t}$ contribute to the same-sign analysis only when the charge of a lepton is mismeasured[2]. These backgrounds are estimated using Monte Carlo samples; this assumes that the MC accurately models how often lepton charges are mismeasured in the data. To test this assumption, we measure the dilepton charge fake rates in the MC and in the data and compare the results.

To measure a charge fake rate for dilepton types in MC, we use the $Z \rightarrow ee$, $Z \rightarrow \mu\mu$, and WW MC@NLO samples. To maximize the statistics, we use only very basic selection cuts: lepton ID, trigger lepton requirements, good run list applied, and a ΔZ cut between the two leptons. Using the MC truth information, we compare the reconstructed charge of both leptons to the generated charge of the two leptons. We then count the number of lepton pairs with both charges correctly measured, and the pairs with the charge of one lepton mismeasured. The ratio of these two numbers is the charge fake rate. Table 39 shows the charge fake rate for all possible dilepton types. Although we do not use PHX electrons, those CFR are included for completeness.

---

[2] The case of $t\bar{t}$ where one lepton is missed and one of the b-jets fakes a lepton is included in the W+jets background.

Dilepton type	Opposite-sign events	Same-sign events	Charge fake rate
TCE-TCE	1705183	495	2.90e-4
TCE-Central μ	1304808	264	2.02e-4
TCE-Forward μ	201271	54	2.68e-4
TCE-CrkTrk	1329071	370	2.78e-4
Central μ-Central μ	2723457	1	3.67e-7
Central μ-Forward μ	917464	73	7.96e-5
Central μ-CrkTrk	1348902	47	3.48e-5
PHX-PHX	446200	118177	0.265
PHX-Central μ	492225	60755	0.123
PHX-Forward μ	78549	10505	0.134
PHX-CrkTrk	639173	84281	0.132
TCE-PHX	1732992	215982	0.125

Table 39: Calculated charge fake rates (CFR) for all dilepton types, using WW, $Z \rightarrow ee$, and $Z \rightarrow \mu\mu$ Pythia MC samples. The lepton selection is described in the text. "Central μ" includes CMUP, CMP, CMX, CMXMsKs, CMIOCES, and CMP muons, while "Forward μ" includes CMIOPES and BMU muons.

We then attempt to measure a charge fake rate directly from the data. We select events in the Drell-Yan control region, described in Sec. 6.2, which should have minimal contamination from other backgrounds such as W+jets, where same-sign events come from QCD rather than charge mismeasurement. We then repeat the procecure of counting the number of opposite-sign events and same-sign events. The resulting CFR are shown in Table 40. Unfortunately the statistics are not large enough to reliably measure a CFR for muon categories.

To determine the uncertainty on MC modeling of the charge fake rate, we compare the TCE-TCE and TCE-CrkTrk charge fake rates measured in data to those measured in MC. We subtract the MC CFR from the data CFR, and take half of that difference as the systematic. For TCE-TCE, this gives a systematic uncertainty of 19%, while for TCE-CrkTrk the systematic uncertainty would be 23%. We take an uncertainty of 19% and apply it to the WW, $t\bar{t}$, and DY backgrounds as shown in Table 67.

7.5 Trilepton Systematics

Many of the systematics discussed here are also applicable to the trilepton search. However, because there are several different backgrounds in the trilepton search, there are some systematics which apply only to those analyses. In particular, $Z\gamma$ replaces the dilepton Drell-Yan sample. Many of the systematics on $Z\gamma$ are taken from the $W\gamma$ systematics, since they are similar process and both simulated with Baur MC. The $Z\gamma$ cross-section uncertainty is set to 10%, and the uncertainty due to higher-older diagrams is also set to

Dilepton type	Opposite-sign events	Same-sign events	Charge fake rate
TCE-TCE	93635	44	4.70e-4
TCE-Central μ	57	2	0.0351
TCE-Forward μ	16	0	–
TCE-CrkTrk	45938	24	5.22e-4
Central μ-Central μ	133738	0	–
Central μ-Forward μ	38756	5	1.29e-4
Central μ-CrkTrk	46696	2	0.43e-4
PHX-PHX	1107	336	0.304
PHX-Central μ	97	67	0.691
PHX-Forward μ	13	12	0.923
PHX-CrkTrk	10404	1424	0.137
TCE-PHX	97401	12201	0.125

Table 40: Calculated charge fake rates (CFR) for all dilepton types in data, using the Drell-Yan control region. The lepton selection is described in the text. “Central μ” includes CMUP, CMP, CMX, CMXMsKs, CMIOCES, and CMP muons, while “Forward μ” includes CMIOPES and BMU muons.

10% as it is for $W\gamma$. The $Z\gamma$ sample must also have a run-dependence systematic applied, as it has only been simulated through p11.

An additional systematic on the $t\bar{t}$ sample is taken for the MC modeling of how often a b-jet will fake the third lepton. As explained in Section **??**, the MC sample is used to estimate this contribution because the fake rate for a b-jet is probably higher than the fake rate measured for light-quark jets in the jet-triggered samples. A systematic uncertainty is assigned on the increase in expected $t\bar{t}$ contribution from allowing generator-level b-quarks to be matched with reconstructed leptons. The size of this systematic is half of the observed difference, or 27.3% for the WH analysis, 42.0% for the ZH 1-jet analysis, and 22.2% for the ZH 2+ jets analysis.

7.6 Shape Systematics

At this time we consider two sources of systematics which would change the shape of the output NN distribution: the fake rate and the jet energy scale (JES) variations. The only channel in which W+jets is the dominant background contribution is in the same-sign channel. In this channel, the rate uncertainty from varying the fake rates by $\pm 1\sigma$ is 33%. However, as shown in Figure 23, when the neural network output tempates are normalized to the same area, there is no change in shape from varying the fake rate.

The jet energy scale systematic described in Sec. 7.2.2 may also be considered as a shape systematic. The effect is small, as seen when these shape systematics were considered for the trilepton ZH channels (CDF Note 10020 [4]). At this time, for technical

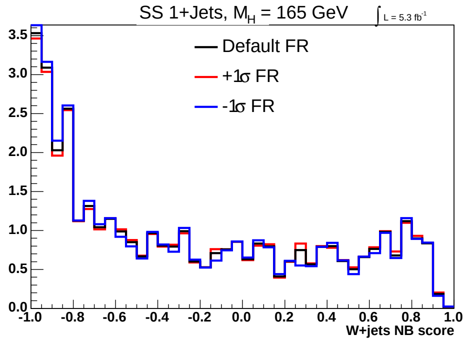

Figure 23: Effect of ±1 σ variations in the fake rates in the same-sign channel. The default shape is shown in black, while the higher fake rate is shown in red and the lower fake rate in blue. All three templates have been normalized to the area of the default template, which shows there is no visible shape change from modifying the fake rate.

reasons the JES variations have not been computed for all signal samples. Thus we do not consider the JES as a shape systematic in this updated analysis, but will consider it for the next version.

8 Opposite-sign Dilepton Signal Region with 0 Jets

The background expectation and observed yield for the opposite-sign dilepton signal region for events containing no reconstructed jets with $E_T > 15$ GeV are shown in Table 41. The expected and observed kinematic distributions for these events are shown in Figures 24-26. We stack the backgrounds on top of each other, and then for comparison we overlay the contribution from a 160 GeV/c^2 Higgs boson with yields scaled up by a factor of 10. In addition, we calculate a confidence level for data versus background expectations on each plot. The confidence levels shown are for Poisson fluctuations and the KS test.

8.1 Understanding Drell-Yan yield increase

Comparing the yields in Table 41 with the previous version of the analysis in the opposite-sign signal region with 0 jets [1], we see a higher increase in Drell-Yan yields than we expected from adding new data and relaxing the LBE cut to 0.90. We expected to see $\sim 10\%$ increase due to luminosity and another $\sim 5\%$ due to the lower cut on the likelihood value for LBE (ie. $\sim 10\%$ increase for LBE-LBE category). So overall we expected to see an increase of 20% for the LBE-LBE category and 15% for the LBE-PHX category. However, we actually see yield increases of about 36% in the LBE-LBE category and about 20% in the LBE-PHX category.

We tried to understand the reason behind this. The LBE efficiency is measured in a DY dominated region where most of the electrons are pretty well isolated, as shown in see Fig. 27. Looking at the the yield increase from the previous version to the current version of the analysis (i.e. from 4.8 fb^{-1} to 5.3 fb^{-1} analysis) as a function of TrkIso for LBEs in Fig. 28, we see that by relaxing the likelihood LBE cut we gain mostly LBE electrons with larger value of isolation (i.e. less isolated electrons), which is expected.

When we go to the signal region, the DY events are different. Since here we require $\not{E}_{T spec} > 15$ or 25 GeV, DY events pass the selection only by having jets in the final state (reconstructed or not). The isolation of electrons is worse, see Fig. 29. Using this distribution and the expected gain per TrkIso bin as seen in DY region (Fig. 28), we can estimate the expected yield increase of Drell-Yan events in the opposite sign signal region with zero jets. This gives us 10% (12%) efficiency increase for LBE using TrkIso (CalIso) dependence. Overall, we then expect $10\% + 2 * 10(12) = 30(34)\%$ yield increase for LBE-LBE category (20%(22%) for LBE-PHX category) in OS 0Jets signal region which is in very good agreement to what we actually observe.

8.2 Incorporating Additional Signal in the 0 Jet Channel

In CDF Note 9163 it was shown that using Matrix Element (ME) calculations as additional inputs to a NeuroBayes® (NB) neural network improved the overall sensitivity of the analysis. Since the ME calculations provide a model for each process based on the Leading

Category	WW	WZ	ZZ	$t\bar{t}$	DY	$W\gamma$	W+jets	Total	Data
TCE TCE	0.0	0.0	0.0	0.0	0.0	0.0	0.0	0.0	0.0
TCE LBE	0.0	0.0	0.0	0.0	0.0	0.0	0.0	0.0	0.0
TCE PHX	0.0	0.0	0.0	0.0	0.0	0.0	0.0	0.0	0.0
TCE PLBE	0.0	0.0	0.0	0.0	0.0	0.0	0.0	0.0	0.0
LBE LBE	0.0	0.0	0.0	0.0	0.0	0.0	0.0	0.0	0.0
LBE PHX	0.0	0.0	0.0	0.0	0.0	0.0	0.0	0.0	0.0
LBE PLBE	0.0	0.0	0.0	0.0	0.0	0.0	0.0	0.0	0.0
PHX PHX	9.0	0.7	1.1	0.0	7.9	18.6	15.1	52.4	62.0
PHX PLBE	2.3	0.2	0.3	0.0	2.9	7.8	7.3	20.8	23.0
PLBE PLBE	0.2	0.0	0.0	0.0	0.0	0.9	0.9	2.0	3.0
TCEni TCEni	68.0	4.3	9.9	0.3	50.1	11.6	8.2	152.3	142.0
TCEni LBEni	20.2	1.5	3.1	0.1	27.7	8.5	12.6	73.7	63.0
TCEni PHXni	0.0	0.0	0.0	0.0	0.0	0.0	0.0	0.0	0.0
TCEni PLBEni	0.0	0.0	0.0	0.0	0.0	0.0	0.0	0.0	0.0
LBEni LBEni	1.8	0.1	0.2	0.0	4.8	1.3	2.2	10.5	7.0
LBEni PHXni	0.0	0.0	0.0	0.0	0.0	0.0	0.0	0.0	0.0
LBEni PLBEni	0.0	0.0	0.0	0.0	0.0	0.0	0.0	0.0	0.0
PHXni PHXni	0.0	0.0	0.0	0.0	0.0	0.0	0.0	0.0	0.0
PHXni PLBEni	0.0	0.0	0.0	0.0	0.0	0.0	0.0	0.0	0.0
PLBEni PLBEni	0.0	0.0	0.0	0.0	0.0	0.0	0.0	0.0	0.0
TCEni PHX	50.5	3.8	6.7	0.2	40.6	33.5	33.4	168.6	216.0
TCEni PLBE	7.1	0.6	1.0	0.0	14.5	7.9	8.7	39.8	43.0
LBEni PHX	7.4	0.7	1.1	0.0	12.7	9.2	13.0	44.2	53.0
LBEni PLBE	1.2	0.1	0.2	0.0	2.3	1.9	2.6	8.3	15.0
TCE CMUP	0.0	0.0	0.0	0.0	0.0	0.0	0.0	0.0	0.0
TCE CMU	0.0	0.0	0.0	0.0	0.0	0.0	0.0	0.0	0.0
TCE CMP	0.0	0.0	0.0	0.0	0.0	0.0	0.0	0.0	0.0
TCE CMX	0.0	0.0	0.0	0.0	0.0	0.0	0.0	0.0	0.0
TCE CMXMsKs	0.0	0.0	0.0	0.0	0.0	0.0	0.0	0.0	0.0
TCE BMU	0.0	0.0	0.0	0.0	0.0	0.0	0.0	0.0	0.0
TCE CMIOCES	0.0	0.0	0.0	0.0	0.0	0.0	0.0	0.0	0.0
TCE CMIOPES	0.0	0.0	0.0	0.0	0.0	0.0	0.0	0.0	0.0
LBE CMUP	0.0	0.0	0.0	0.0	0.0	0.0	0.0	0.0	0.0
LBE CMU	0.0	0.0	0.0	0.0	0.0	0.0	0.0	0.0	0.0
LBE CMP	0.0	0.0	0.0	0.0	0.0	0.0	0.0	0.0	0.0
LBE CMX	0.0	0.0	0.0	0.0	0.0	0.0	0.0	0.0	0.0
LBE CMXMsKs	0.0	0.0	0.0	0.0	0.0	0.0	0.0	0.0	0.0
LBE BMU	0.0	0.0	0.0	0.0	0.0	0.0	0.0	0.0	0.0
LBE CMIOCES	0.0	0.0	0.0	0.0	0.0	0.0	0.0	0.0	0.0
LBE CMIOPES	0.0	0.0	0.0	0.0	0.0	0.0	0.0	0.0	0.0
PHX CMUP	0.0	0.0	0.0	0.0	0.0	0.0	0.0	0.0	0.0
PHX CMU	0.0	0.0	0.0	0.0	0.0	0.0	0.0	0.0	0.0
PHX CMP	0.0	0.0	0.0	0.0	0.0	0.0	0.0	0.0	0.0
PHX CMX	0.0	0.0	0.0	0.0	0.0	0.0	0.0	0.0	0.0
PHX CMXMsKs	0.0	0.0	0.0	0.0	0.0	0.0	0.0	0.0	0.0
PHX BMU	3.5	0.1	0.0	0.0	1.9	1.6	0.8	7.9	11.0
PHX CMIOCES	0.0	0.0	0.0	0.0	0.0	0.0	0.0	0.0	0.0
PHX CMIOPES	5.9	0.1	0.0	0.0	0.5	3.0	4.7	14.1	19.0
PLBE CMUP	0.0	0.0	0.0	0.0	0.0	0.0	0.0	0.0	0.0
PLBE CMU	0.0	0.0	0.0	0.0	0.0	0.0	0.0	0.0	0.0
PLBE CMP	0.0	0.0	0.0	0.0	0.0	0.0	0.0	0.0	0.0
PLBE CMX	0.0	0.0	0.0	0.0	0.0	0.0	0.0	0.0	0.0

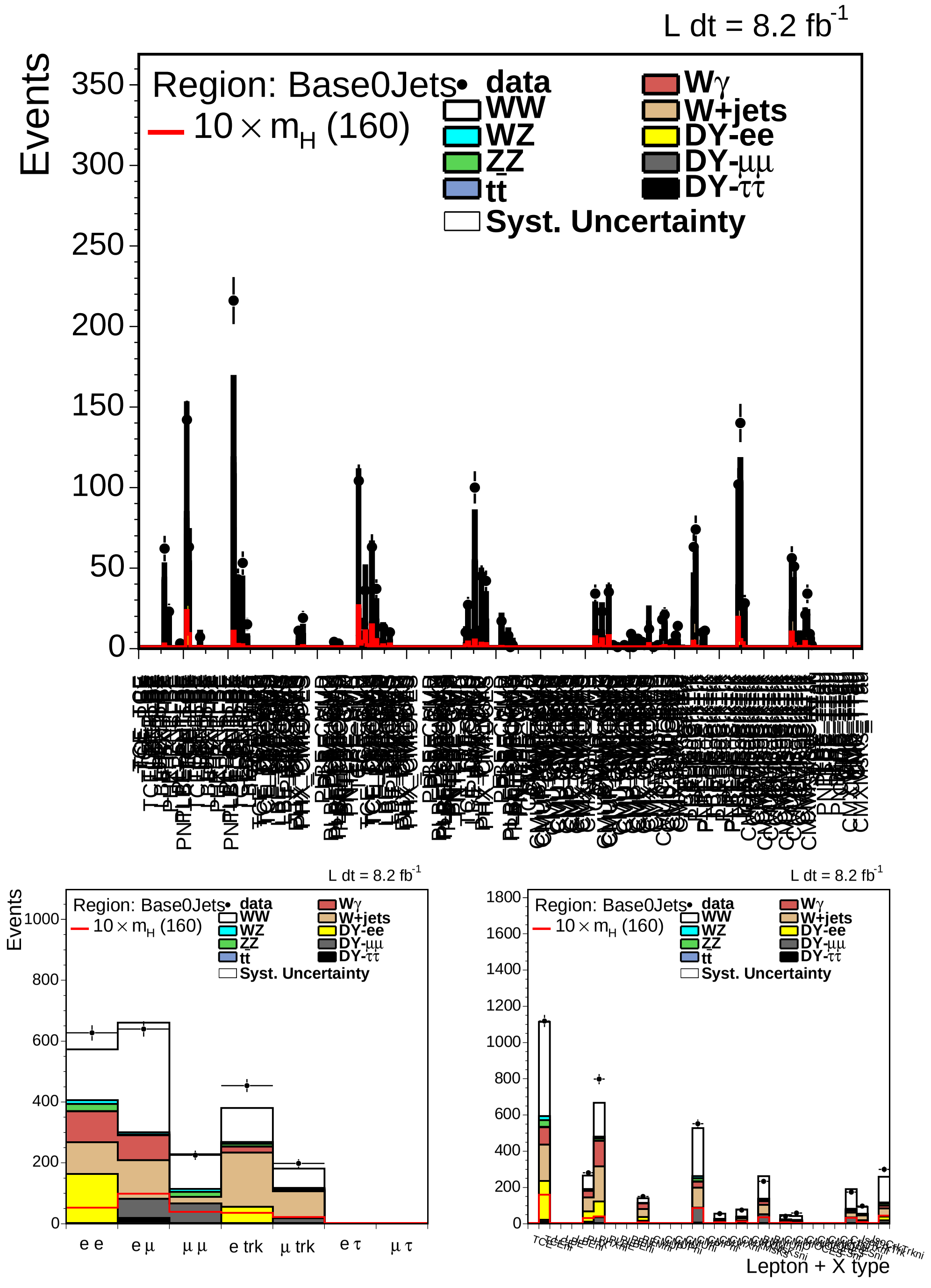

Figure 24: Signal and background in the opposite-sign signal region for events containing no reconstructed jets with $E_T > 15$ GeV.

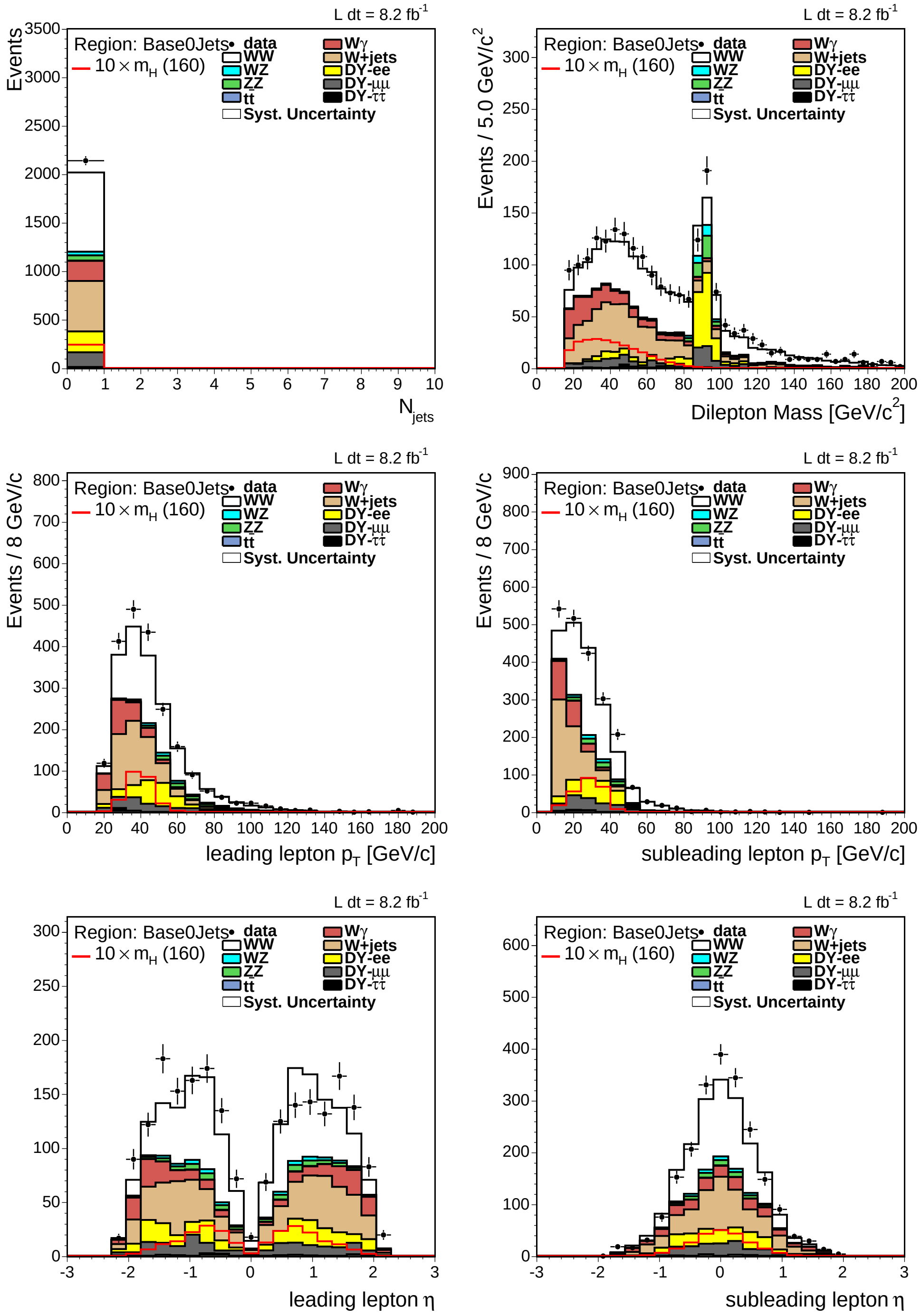

Figure 25: Signal and background in the opposite-sign signal region for events containing no reconstructed jets with $E_T > 15$ GeV.

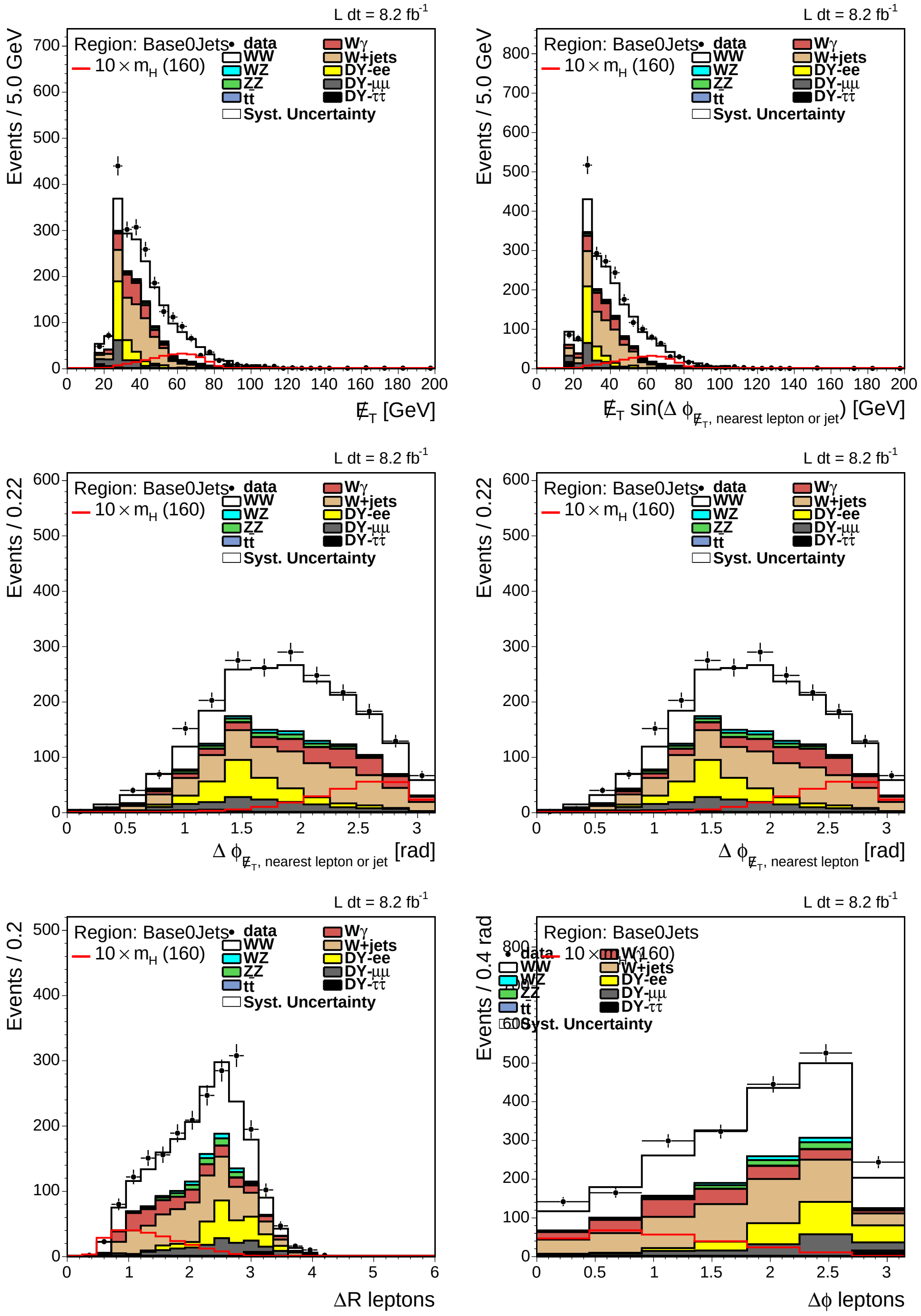

Figure 26: Signal and background in the opposite-sign signal region for events containing no reconstructed jets with $E_T > 15$ GeV.

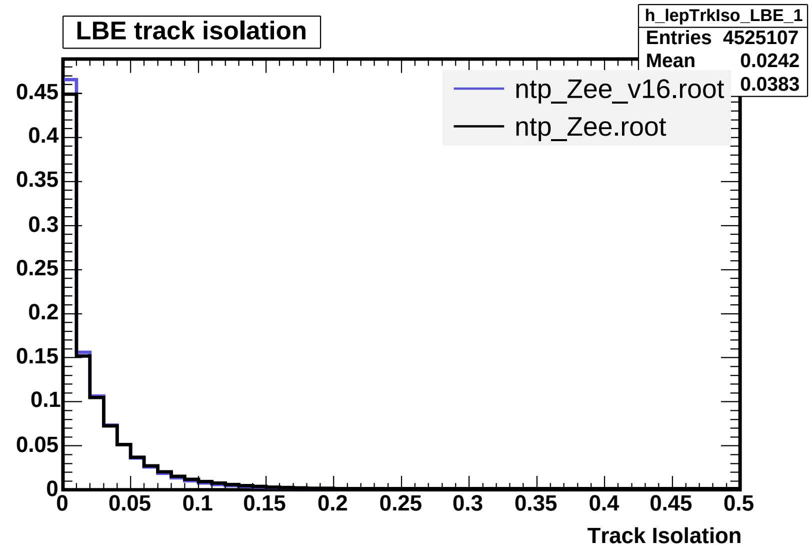

Figure 27: The track isolation distribution for LBE electrons from $Z \rightarrow ee$ sample for events passing DY region selection (blue histogram from the v16 or 4.8 fb^{-1} analysis, black histogram from the v17 or 5.3 fb^{-1} analysis).

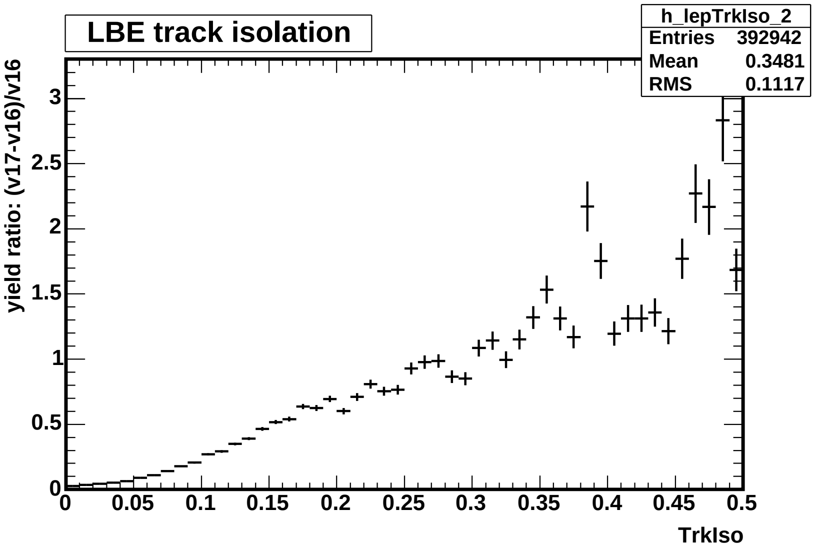

Figure 28: The fractional gain (i.e. ratio = (Yield(v17) - Yield(v16))/Yield(v16)) in yield between v16 and v17 version of analysis shown as dependence on TrkIso value of LBEs (again for LBE electrons from $Z \rightarrow ee$ sample for events passing DY region selection).

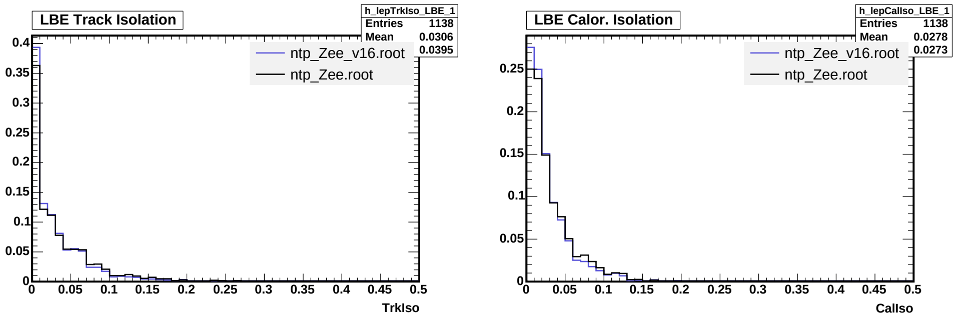

Figure 29: The track (left) and calorimeter (right) isolation distribution for LBE electrons from $Z \rightarrow ee$ sample for events passing opposite sign with zero jets signal region selection.

Order (LO) behavior of the differential cross section, we expect that using this information in the neural network works well in cases where the events are LO-like, i.e. when no additional jets are present. We therefore use, for events with 0 jets (0J), ME-based Likelihood Ratios as inputs for a NB neural network in analogy of what has been done previously and described in detail in CDF Note 9163.

In all previous versions of the analysis, the only signal contribution considered was that from gluon fusion production. The primary reason behind this was the considerable time it takes to the run the ME calculations. Incorporating the WH, ZH, and VBF signals at each mass point means running an extra 57 ME calculations. However, the benefit from the extra signal is not negligible, particularly for low Higgs boson mass. At $m_H = 115$ GeV, the associated production and VBF together contribute 16% to the total expected signal. At higher masses the gain is less (6.2% for $m_H = 160$ and 6% for $m_H = 200$ GeV) but still not inconsiderable.

For this update, we have run the default ME calculations for the additional signal production modes. At this time, we have not introduced ME calculations specifically for the new modes (WH, ZH, and VBF), although that could be instituted as an update in the future. We again use the ME-based Likelihood Ratios for WW and $gg \rightarrow H \rightarrow WW$ as neural network input variables. The neural network training is done on a weighted combination of the four signal production modes; to help discriminate the new signal contributions from the backgrounds, we introduce several additional kinematic variables to the neural network. Previously, the only kinematic variable inputs to the neural network were the ΔR and $\Delta \phi$ between the leptons and the transverse mass H_T. The neural network is now trained including the variables: dilepton mass, the transverse momentum of the leading and subleading leptons, and the transverse mass of the sum of the leptons' 4-momentums and the $\not\!\!E_T$.

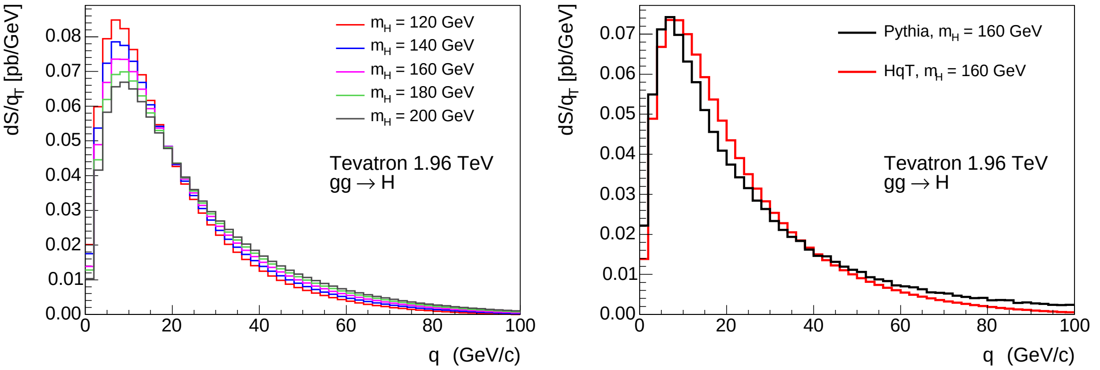

Figure 30: Left: Distributions of $gg \to H$ p_T using the HqT program, plotted for Higgs masses of 120, 140, 160, 180, and 200 GeV. Right: Comparison of the Pythia and HqT distributions of $gg \to H$ p_T for $m_H = 160$ GeV. Each Pythia MC sample is reweighted to the appropriate mass-dependent spectrum.

8.3 Reweighting of the Gluon Fusion Signal

Particularly for events with zero reconstructed jets, where the dominant background is direct WW production, the most important discriminating variables is the $\Delta\phi$ between the leptons. In order to predict the $\Delta\phi$ distribution for a given Higgs mass, it is important to correctly model the Higgs boost. Previous versions of this analysis made no corrections to the Higgs p_T spectrum from Pythia, although the HNNLO program was used to derive acceptance uncertainties as described in Section 7.2.3.

Recent theoretical progress has brought us the HqT program [29, 30]. The HNNLO program computes the cross-section for $gg \to$ Higgs production at NNLO in QCD perturbation theory. The HqT program, written by most of the same authors as HNNLO, computes the transverse momentum distribution for $gg \to$ Higgs production at NNLL+NLO accuracy, with the normalization fixed to the total NNLO cross-section. For this version of the analysis, we use HqT to produce transverse momentum distributions for each Higgs mass we consider, and then reweight the Pythia $gg \to H$ transverse momentum distributions.

Several HqT distributions at different Higgs masses are shown in Figure 30. In general, the HqT spectrum peaks at a higher p_T value than the default Pythia spectrum, but HqT also has fewer events at $p_T > 60$ GeV. The net effect of the reweighting is to slightly increase the Higgs acceptance (due to the higher peak value) and to have fewer of the Higgs events with jets (due to having fewer events at high Higgs p_T). Thus the reweighting has the effect of increasing the expected Higgs signal in the 0 jet channel, while slightly reducing the expected Higgs signal in the 1 and 2 or more jet channels.

8.4 Analysis of Opposite-Sign 0 Jet events

To optimize the choice of variables to be used as input to the neural network we begin from a large set of what we think can be discriminant variables; we then evaluate a *ranking* associated to each of them using a NB pre-training functionality [31], which gives an estimation of the discrimination power between signal and background that this variable carries. We then train a set of neural networks starting from the full list of input variables and removing one variable at time, starting from the less significant. We calculate the expected limits for each output template obtained by these networks and finally choose the set of variables which minimize the expected limit; for this study a signal with $m_H = 160$ GeV was used.

The training method used for the neural network is mostly the same as described in CDF Note 9136. We train the net to distinguish the Higgs MC sample from an admixture of each background (both MC-derived and data-driven backgrounds); each background event has a weight according to its relative expectation, which is a function of the cross section, multiple scale factors, trigger efficiencies, and MC statistics. Only for the training, we then reweight all events so that the sum of the weights is equal to the number of signal events. The only significant differences with respect to the previous trainings is the use of a newer version of the NB package (v2.1) and the use of the BFGS algorithm in the minimization. The input variables used for the 0-jet NN are shown in Table 8.4 along with a brief explanation of their meaning; for the 0J net we use 9 input nodes, 11 hidden nodes and 1 output node. The observed distributions of each 0J neural network input parameter compared with the distributions predicted by our background model are shown in Figure 31. For reference, we also include a hypothetical signal component for a Higgs boson with $m_H = 160$ GeV.

Variable	Meaning
	0J Neural Network
LRHWW	Likelihood ratio - $H \to WW$
dRLeptons	ΔR between the leptons
LRWW	Likelihood ratio - WW production
dPhiLeptons	$\Delta\phi$ between the leptons
Ht	Scalar sum of leptons E_T and $\not{E}_T$ (no jets in the event)
Mt_H	Transverse mass of the sum of lepton's 4-momenta and ($\not{E}_T$, MetX, MetY, 0) where MetX/Y are the X/Y components of the $\vec{\not{E}}_T$
dimass	Dilepton invariant mass
lep1_Pt	Transverse momentum of the first lepton
lep2_Pt	Transverse momentum of the second lepton

Table 42: Summary of inputs to 0J neural networks.

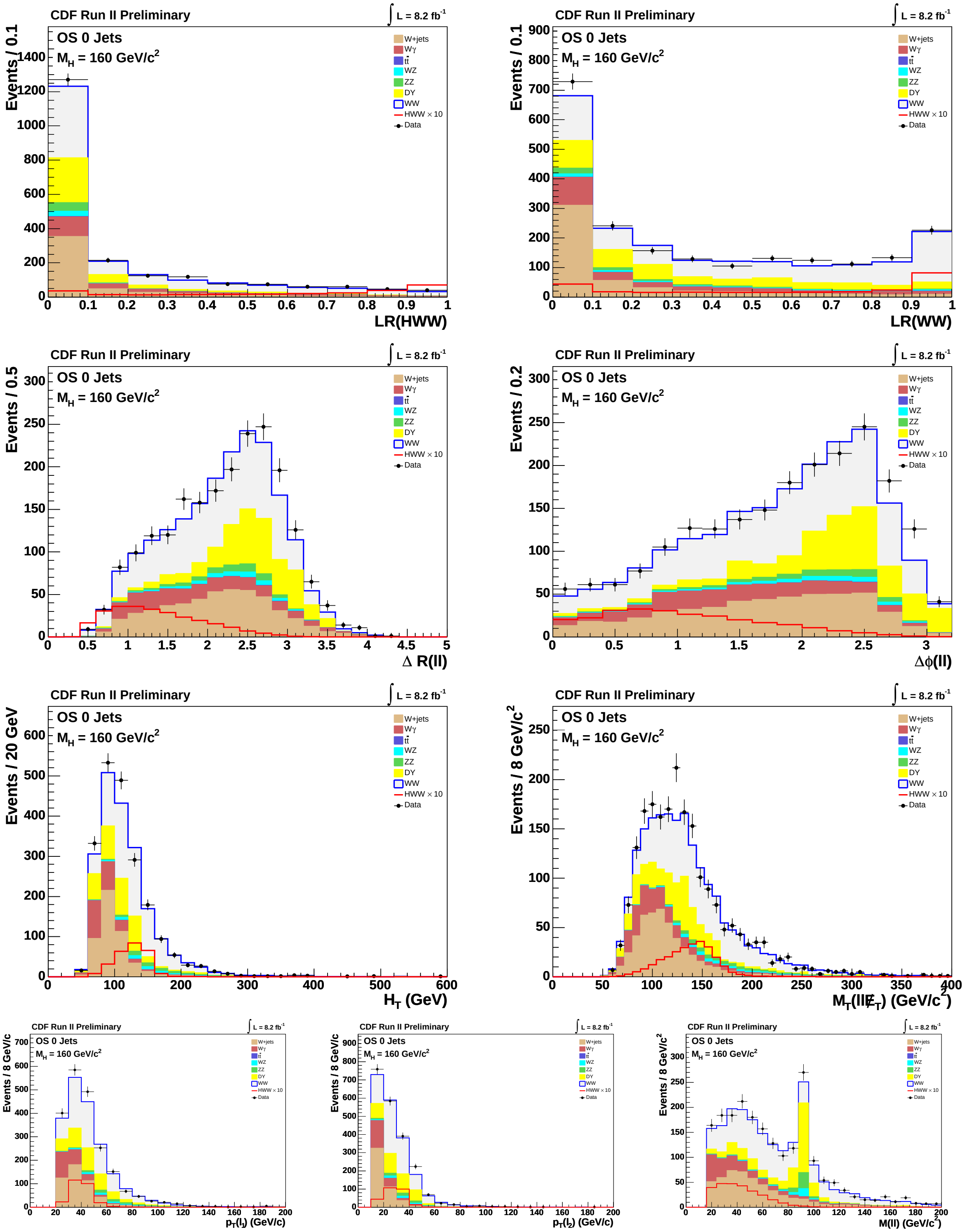

Figure 31: Neural Network input variables for 0J NN (signal for $M_H = 160$ GeV/c^2).

Mass (GeV/c^2)	gg→H	WH	ZH	VBF
110	1 (0.83/0.19)	0.14 (0.11/0.031)	0.055 (0.046/0.0096)	0.0051 (0.0042/0.00095)
115	2 (1.6/0.37)	0.2 (0.15/0.044)	0.089 (0.076/0.013)	0.01 (0.009/0.0012)
120	3.4 (2.8/0.64)	0.26 (0.2/0.062)	0.13 (0.11/0.019)	0.018 (0.015/0.0035)
125	5.3 (4.3/0.99)	0.32 (0.26/0.055)	0.19 (0.16/0.029)	0.03 (0.025/0.0043)
130	7.3 (5.9/1.3)	0.38 (0.3/0.08)	0.24 (0.2/0.044)	0.044 (0.038/0.0059)
135	9.4 (7.7/1.7)	0.42 (0.34/0.081)	0.29 (0.25/0.045)	0.059 (0.046/0.013)
140	11 (9.3/2.2)	0.44 (0.34/0.098)	0.34 (0.29/0.054)	0.075 (0.064/0.011)
145	13 (11/2.4)	0.45 (0.38/0.078)	0.37 (0.32/0.057)	0.091 (0.076/0.015)
150	15 (12/2.7)	0.45 (0.36/0.088)	0.41 (0.35/0.057)	0.1 (0.085/0.019)
155	16 (13/2.9)	0.45 (0.36/0.096)	0.42 (0.36/0.067)	0.12 (0.098/0.021)
160	17 (14/3)	0.44 (0.36/0.078)	0.44 (0.38/0.057)	0.14 (0.11/0.025)
165	17 (14/2.9)	0.41 (0.34/0.071)	0.42 (0.35/0.07)	0.14 (0.12/0.023)
170	15 (13/2.7)	0.36 (0.29/0.068)	0.39 (0.33/0.057)	0.14 (0.11/0.022)
175	14 (11/2.5)	0.32 (0.27/0.059)	0.35 (0.3/0.052)	0.13 (0.11/0.02)
180	12 (9.9/2.2)	0.28 (0.22/0.058)	0.31 (0.26/0.047)	0.12 (0.095/0.023)
185	9.9 (8.1/1.8)	0.23 (0.19/0.034)	0.25 (0.21/0.035)	0.1 (0.088/0.012)
190	8.3 (6.8/1.5)	0.18 (0.15/0.03)	0.21 (0.18/0.031)	0.088 (0.068/0.02)
195	7.2 (5.9/1.4)	0.16 (0.12/0.034)	0.18 (0.15/0.034)	0.08 (0.067/0.013)
200	6.5 (5.3/1.2)	0.14 (0.11/0.025)	0.16 (0.13/0.029)	0.072 (0.062/0.01)

Table 43: Expected Higgs Signal yields as a function of the Higgs boson mass in the 0J region for each of the contributing production processes. The numbers inside the parentheses are the expected relative contributions in the High S/B and Low S/B regions.

Templates are created for each neural network and used for calculating 95% CL limits with the MCLimit program [32]. Events are separated into Low S/B and High S/B channels based on the dilepton types and a separate set of templates is created for each of the channels. MCLimit combines the two channels to produce a single set of limits for the 0J region. Output templates for the trained 0J neural network, divided into Low S/B and High S/B, are shown in Figures 32−36.

In the 0J region we now consider potential signal contributions from four Higgs production channels: gluon fusion ($gg \to H \to WW \to ll\nu\nu$), Vector Boson Fusion (VBF), and associated production VH ($q\bar{q} \to ZH \to ZWW$ and $q\bar{q} \to WH \to WWW$). We evaluate the number of events expected from each production process as a function of the mass of the Higgs. These numbers are shown in Table 43.

In calculating the final limits, we take into account systematic uncertainties on both the signal and background models we use to train our neural networks. Systematic uncertainties for the 0J region are summarized in Tables 44 and 45. Figure 37 shows the expected (based on 10000 pseudo-experiments) and observed limits obtained from the 0J region.

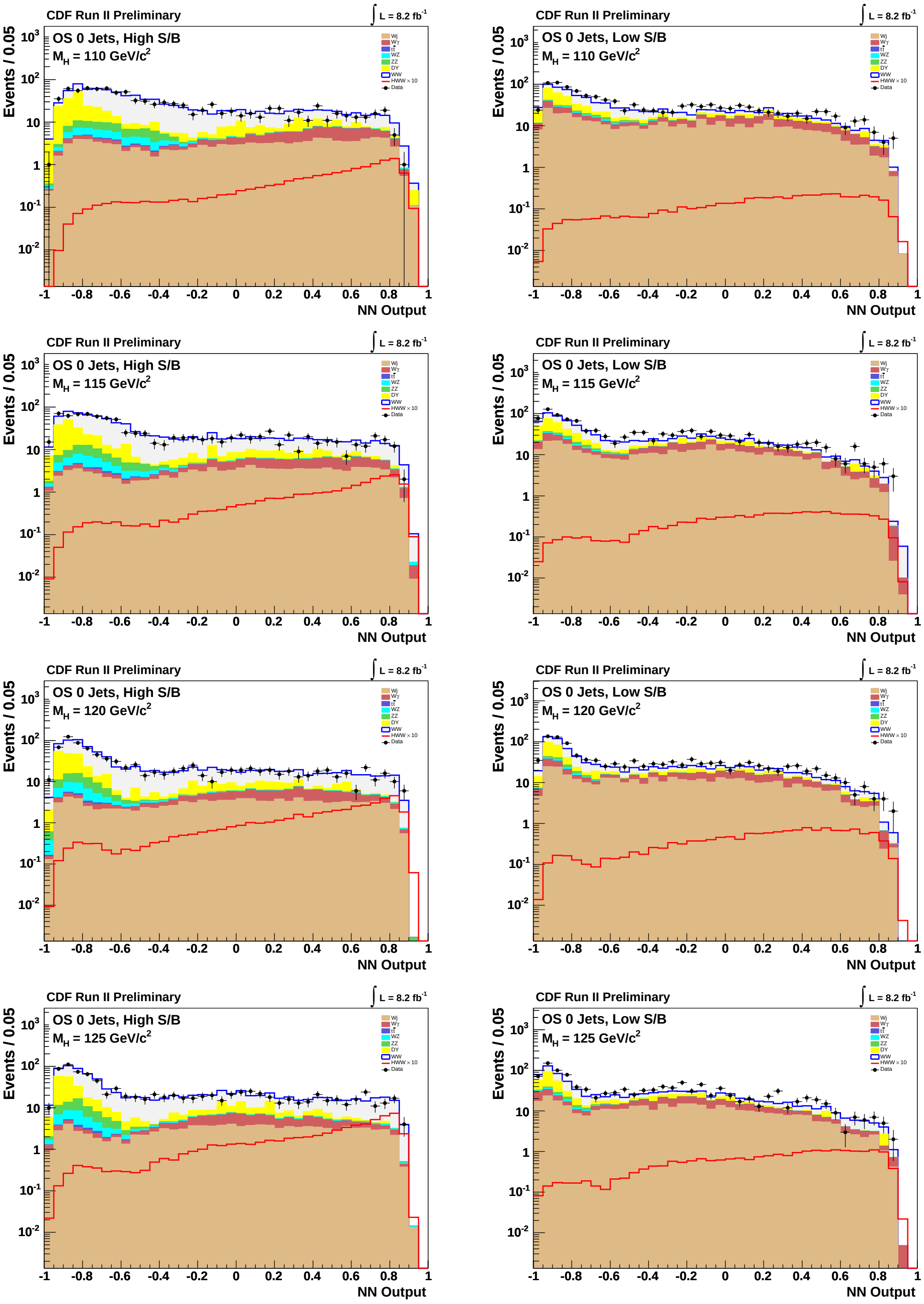

Figure 32: 0J Neural Network output templates for several Higgs masses. On the left for High S/B events and on the right for Low S/B. From the top to bottom: 110 GeV, 115 GeV, 120 GeV, and 125 GeV.

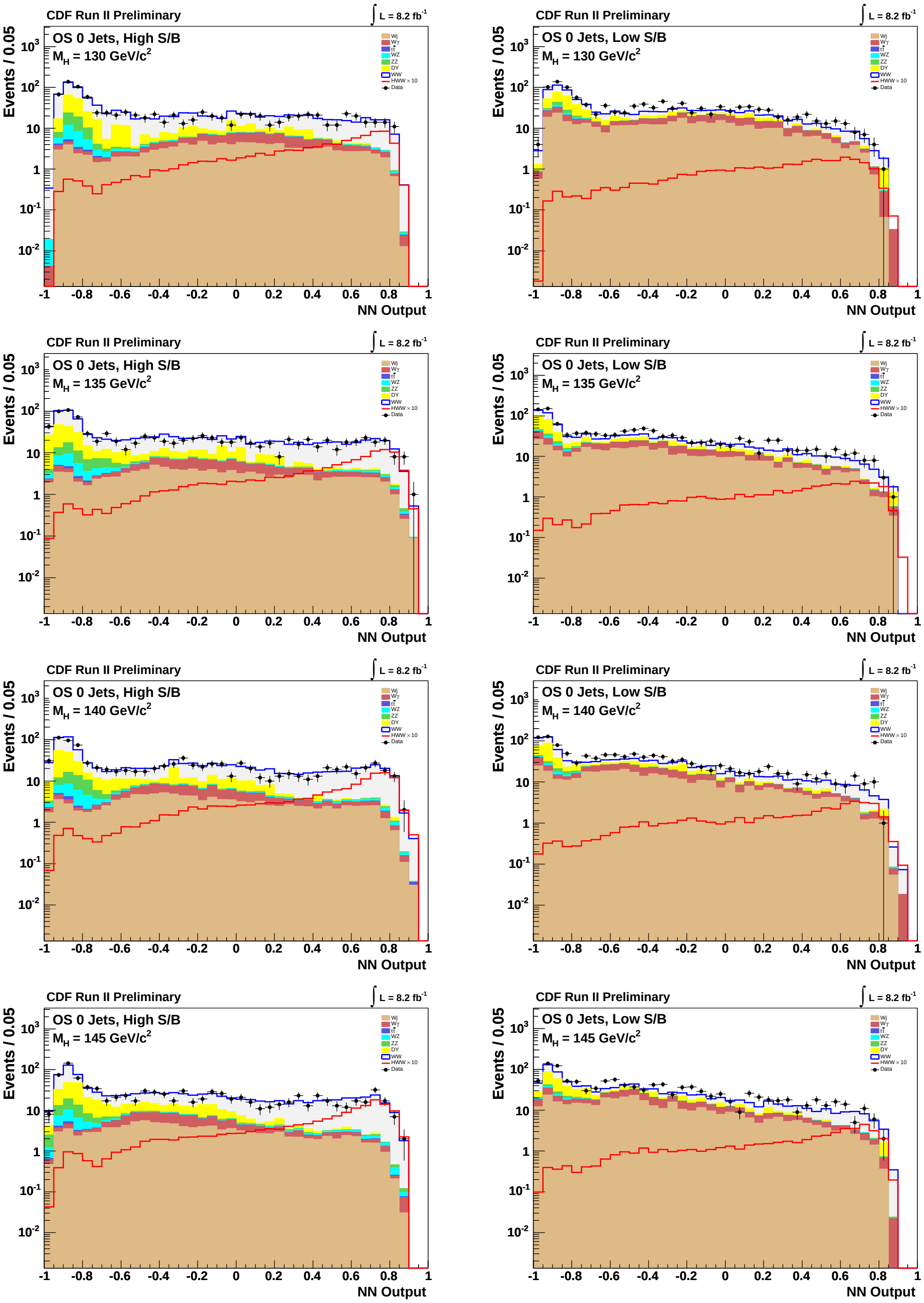

Figure 33: 0J Neural Network output templates for several Higgs masses. On the left for High S/B events and on the right for Low S/B. From the top to bottom: 130 GeV, 135 GeV, 140 GeV, and 145 GeV.

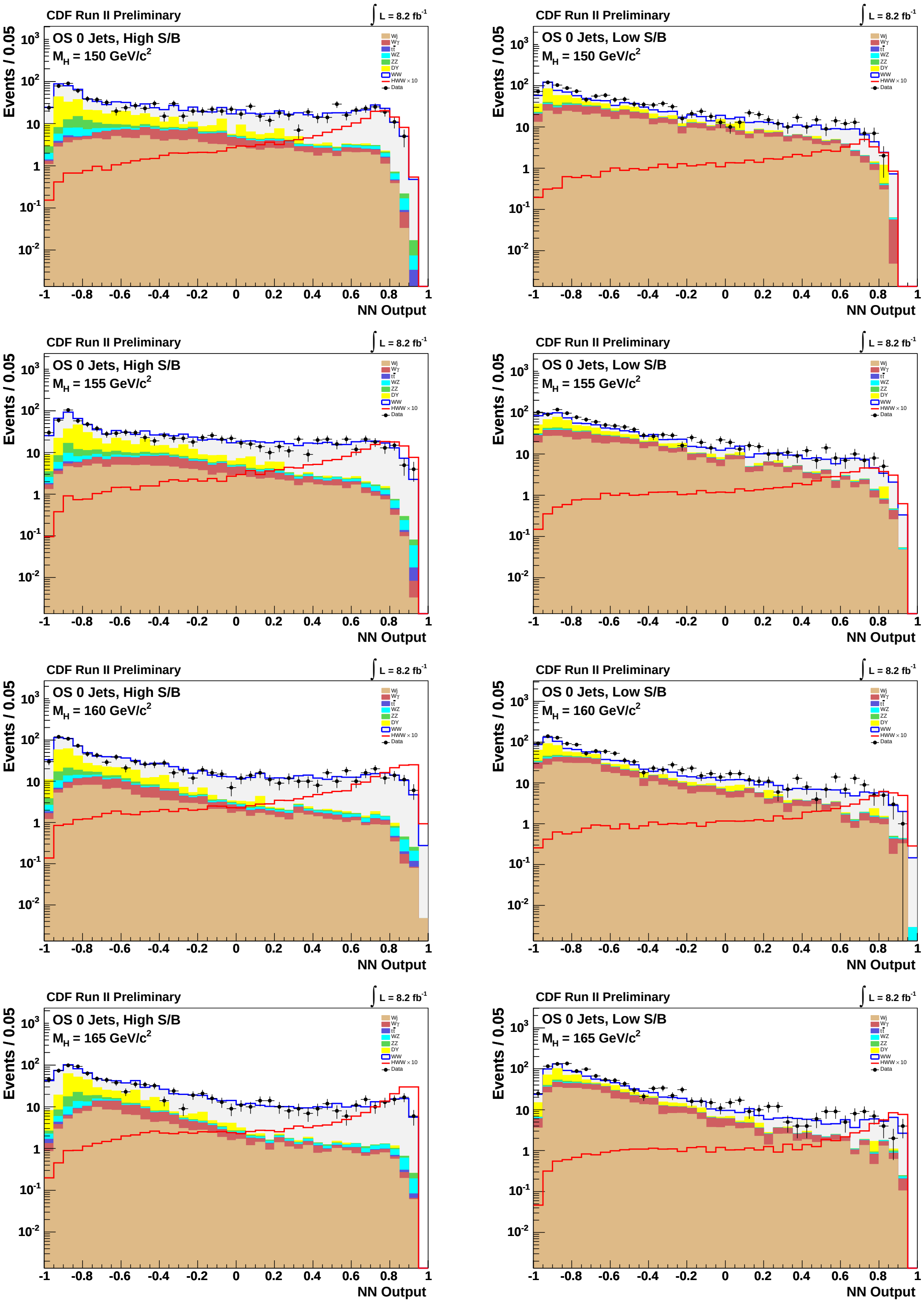

Figure 34: 0J Neural Network output templates for several Higgs masses. On the left for High S/B events and on the right for Low S/B. From the top to bottom: 150 GeV, 155 GeV, 160 GeV, and 165 GeV.

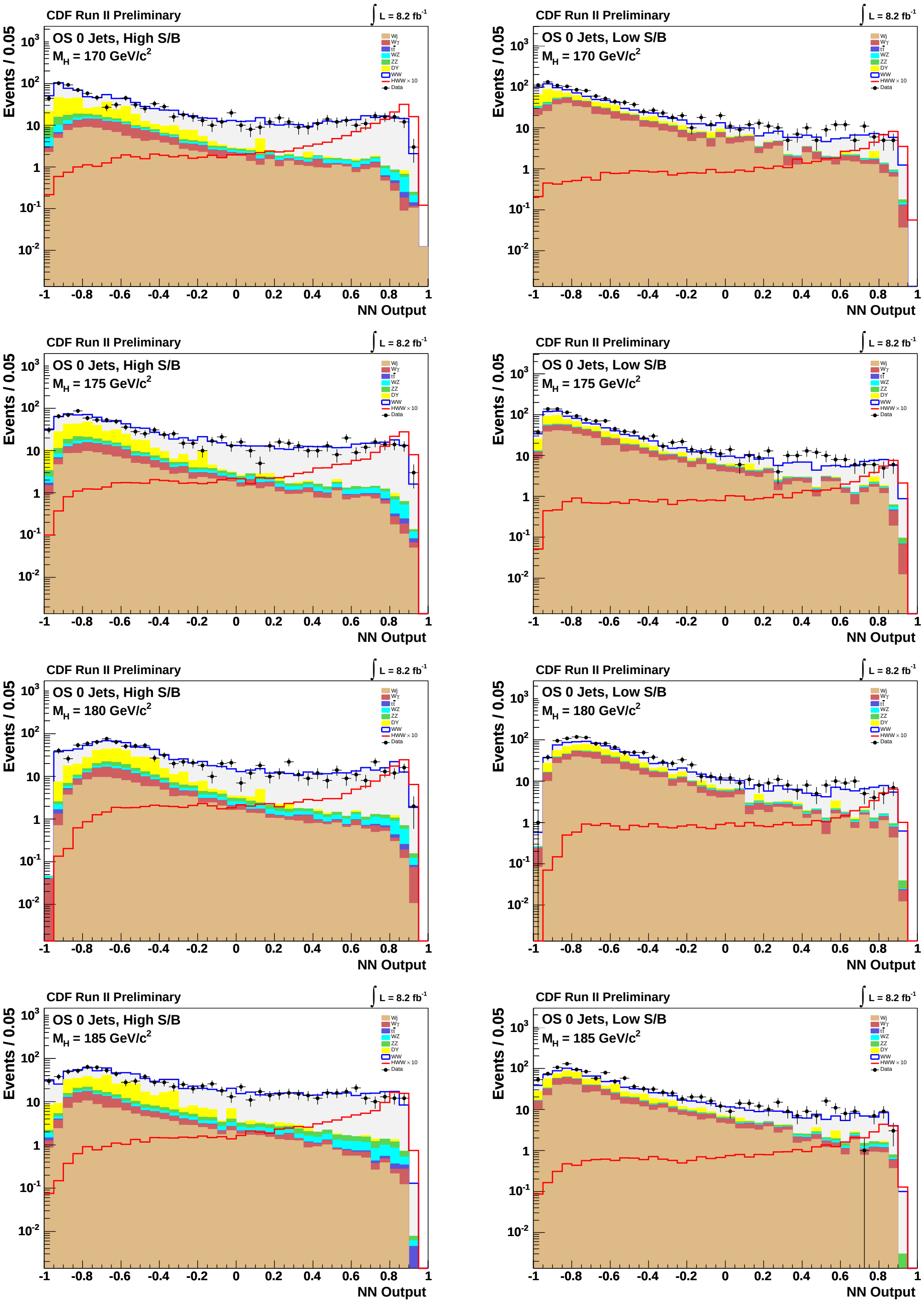

Figure 35: 0J Neural Network output templates for several Higgs masses. On the left for High S/B events and on the right for Low S/B. From the top to bottom: 170 GeV, 175 GeV, 180 GeV, 185 GeV.

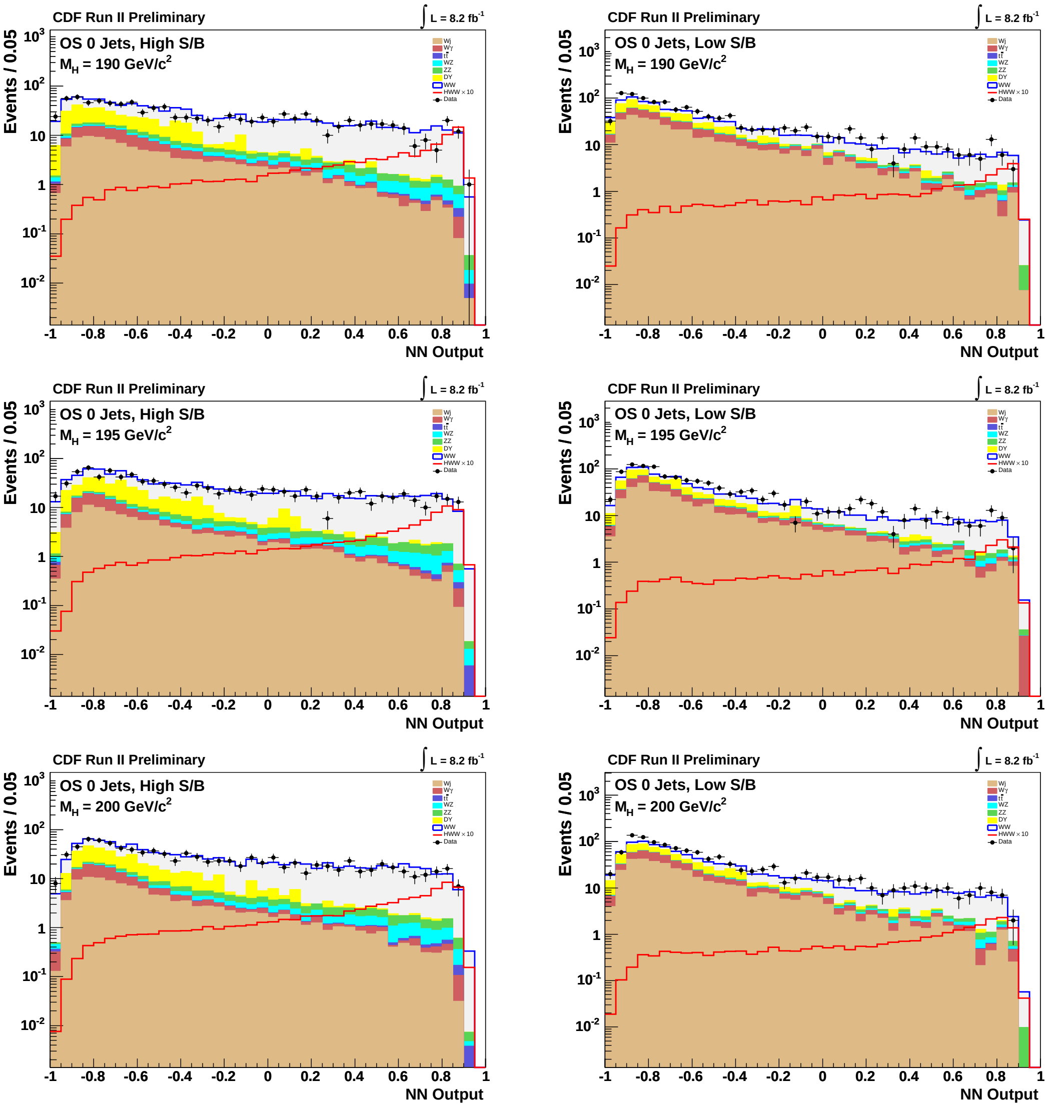

Figure 36: 0J Neural Network output templates for several Higgs masses. On the left for High S/B events and on the right for Low S/B. From the top to bottom: 190 GeV, 195 GeV, and 200 GeV.

Uncertainty Source	WW	WZ	ZZ	$t\bar{t}$	DY	$W\gamma$	W+jet
Cross Section							
Total	*6.0%*	*6.0%*	*6.0%*	10.0%			
Acceptance							
Scale (jets)	0.3%						
PDF Model (jets)	1.1%						
Higher-order Diagrams		*10.0%*	*10.0%*	10.0%		10.0%	
Jet Energy Scale	*2.6%*	*6.1%*	*3.4%*	*26.0%*	*17.5%*	*3.1%*	
Missing E_T Modeling					19.5%		
$W\gamma$ Modeling						10.0%	
Jet Fake Rates							
(Low S/B)							22.0%
(High S/B)							25.0%
Luminosity	*7.3%*	*7.3%*	*7.3%*	*7.3%*	*7.3%*		

Table 44: Systematics table for 0J analysis background processes. Cross section systematics are correlated for the diboson processes (shown in italic font) but uncorrelated between all other processes. Scale (jets), PDF Model (jets), and Jet Energy Scale systematics are anticorrelated between the 0, 1, and 2+ jet bins, as these systematics cause events to fluctuate between jet bins.

Uncertainty Source	$gg \to H$	WH	ZH	VBF
Cross Section				
Scale	7.0%			
PDF Model	7.6%			
Total		*5.0%*	*5.0%*	10.0%
Acceptance				
Scale (leptons)	1.7%			
Scale (jets)	1.5%			
PDF Model (leptons)	2.7%			
PDF Model (jets)	5.5%			
EWK Higher-order Diagrams		*10.0%*	*10.0%*	*10.0%*
Jet Energy Scale	*5.0%*	*10.5%*	*5.0%*	*11.5%*
Luminosity	*7.3%*	*7.3%*	*7.3%*	*7.3%*

Table 45: Systematics table for 0J analysis signal processes. Cross section systematics are uncorrelated between the signal processes. Higher-order diagrams for the VH and VBF processes, shown in italic font, are correlated among each other but uncorrelated from background processes. The Scale (jets) and PDF Model (jets) systematics for $gg \to H$ are anticorrelated between the 0, 1, and 2+ jet bins, as these systematics cause events to fluctuate between jet bins.

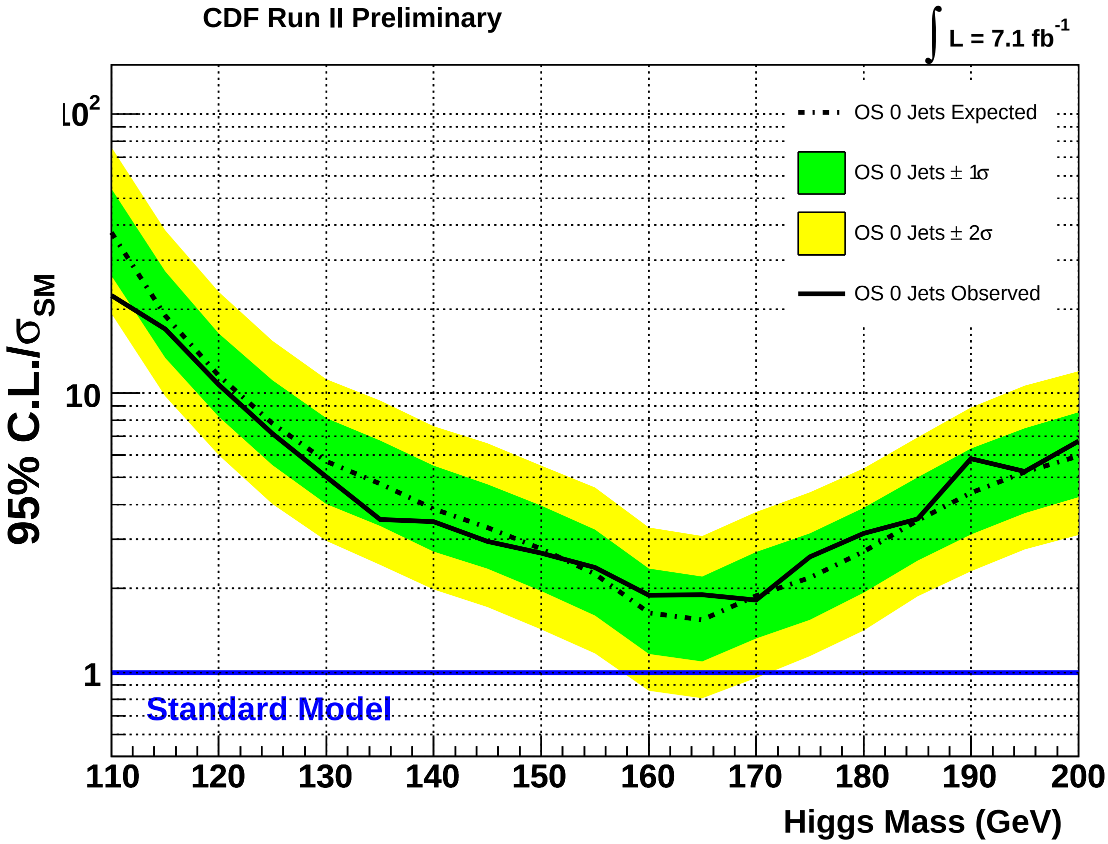

OS 0 Jets	110	115	120	125	130	135	140	145	150	155	160	165	170	175	180	185	190	195	200
$-2\sigma/\sigma_{SM}$	19.30	9.75	6.00	4.00	2.95	2.43	1.98	1.72	1.43	1.17	0.86	0.81	0.96	1.14	1.42	1.87	2.30	2.76	3.11
$-1\sigma/\sigma_{SM}$	26.41	13.42	8.27	5.53	4.01	3.35	2.71	2.35	1.95	1.60	1.17	1.10	1.33	1.54	1.93	2.51	3.12	3.72	4.25
Median/σ_{SM}	**37.62**	**19.00**	**11.57**	**7.79**	**5.71**	**4.74**	**3.86**	**3.30**	**2.77**	**2.26**	**1.63**	**1.54**	**1.88**	**2.18**	**2.71**	**3.51**	**4.40**	**5.22**	**5.95**
$+1\sigma/\sigma_{SM}$	53.96	27.29	16.37	11.14	8.13	6.78	5.51	4.72	3.96	3.24	2.36	2.20	2.70	3.15	3.89	4.99	6.35	7.51	8.55
$+2\sigma/\sigma_{SM}$	76.13	38.34	23.12	15.40	11.22	9.41	7.63	6.61	5.52	4.60	3.31	3.08	3.75	4.42	5.40	6.95	8.89	10.67	12.02
Observed/σ_{SM}	**22.38**	**16.97**	**10.74**	**7.16**	**5.03**	**3.54**	**3.47**	**2.95**	**2.67**	**2.38**	**1.89**	**1.90**	**1.81**	**2.59**	**3.15**	**3.55**	**5.84**	**5.24**	**6.75**

Figure 37: $H \rightarrow WW$ sensitivity normalized to NNLL σ_{SM} calculation from the combination of the High S/B and Low S/B channels in the 0J region. In this region we consider potential signal contributions from gluon fusion, vector boson fusion, and associated production with either a W or Z boson.

9 Opposite-sign Dilepton Signal Region with 1 Jet

The background expectation and observed yield for the opposite-sign dilepton signal region for events containing one reconstructed jet with $E_T > 15$ GeV are shown in Table 46. The expected and observed kinematic distributions for these events are shown in Figures 38-40. We stack the backgrounds on top of each other, and then for comparison we overlay the contribution from a 160 GeV/c^2 Higgs boson with yields scaled up by a factor of 10. In addition, we calculate a confidence level for data versus background expectations on each plot. The confidence levels shown are for Poisson fluctuations and the KS test.

For events with one jet (1J) we train a separate set of NB neural networks, one for each Higgs mass, and do not incorporate any inputs based on the Matrix Element calculations. As discussed previously, the ME calculations are done at LO and therefore are not as reliable for events with an extra jet which presumably originates from an extra quark or gluon radiated within the hard scattering process. Optimization and training of the neural network are done in the same manner as for the 0J case described in Section 8. For the 1J region our neural network uses 8 inputs, 10 hidden nodes and 1 output node. The input variables used for the 1J NN are shown in Table 9. The observed distributions of each 1J neural network input parameter compared with the distributions predicted by our background model are shown in Figure 41. For reference, we also include a hypothetical signal component for a Higgs boson with $m_H = 160$ GeV/c^2.

Templates are created for each neural network and used for calculating 95% CL limits with the MCLimit program [32]. Events are separated into Low S/B and High S/B channels based on the dilepton types and a separate set of templates is created for each of the channels. MCLimit combines the two channels to produce a single set of limits for the 1J region. Output templates for the trained 1J neural network, divided into Low S/B and High S/B, are shown in Figures 42−46.

In the 1J region we consider potential signal contributions from all four Higgs production processes that contribute significantly at high masses: gluon fusion ($gg \to H \to WW \to ll\nu\nu$), Vector Boson Fusion (VBF), and associated production VH ($q\bar{q} \to ZH \to ZWW$ and $q\bar{q} \to WH \to WWW$). The additional processes contribute significantly to the event regions with one or more jets and incorporating their contributions is fairly straight-forward since we do not attempt to use neural network inputs based on Matrix Element calculations in these regions. We evaluate the number of events expected from each production process as a function of the mass of the Higgs. These numbers are shown in Table 48.

In calculating the final limits, we take into account systematic uncertainties on both the signal and background models we use to train our neural networks. Systematic uncertainties for the 1J region are summarized in Tables 49 and 50. Figure 47 shows the expected (based on 10000 pseudo-experiments) and observed limits obtained from the 1J region.

Category	WW	WZ	ZZ	$t\bar{t}$	DY	$W\gamma$	W+jets	Total	Data
TCE TCE	0.0	0.0	0.0	0.0	0.0	0.0	0.0	0.0	0.0
TCE LBE	0.0	0.0	0.0	0.0	0.0	0.0	0.0	0.0	0.0
TCE PHX	0.0	0.0	0.0	0.0	0.0	0.0	0.0	0.0	0.0
TCE PLBE	0.0	0.0	0.0	0.0	0.0	0.0	0.0	0.0	0.0
LBE LBE	0.0	0.0	0.0	0.0	0.0	0.0	0.0	0.0	0.0
LBE PHX	0.0	0.0	0.0	0.0	0.0	0.0	0.0	0.0	0.0
LBE PLBE	0.0	0.0	0.0	0.0	0.0	0.0	0.0	0.0	0.0
PHX PHX	2.4	0.8	0.3	0.5	14.0	2.4	5.3	25.8	17.0
PHX PLBE	0.7	0.2	0.1	0.2	5.9	1.2	2.5	10.9	14.0
PLBE PLBE	0.1	0.0	0.0	0.0	2.8	0.3	0.3	3.5	0.0
TCEni TCEni	18.2	5.0	2.5	7.9	30.1	1.2	2.8	67.8	63.0
TCEni LBEni	6.2	1.8	0.9	3.2	18.7	0.9	4.3	35.9	43.0
TCEni PHXni	0.0	0.0	0.0	0.0	0.0	0.0	0.0	0.0	0.0
TCEni PLBEni	0.0	0.0	0.0	0.0	0.0	0.0	0.0	0.0	0.0
LBEni LBEni	0.6	0.2	0.1	0.3	3.2	0.2	0.8	5.4	5.0
LBEni PHXni	0.0	0.0	0.0	0.0	0.0	0.0	0.0	0.0	0.0
LBEni PLBEni	0.0	0.0	0.0	0.0	0.0	0.0	0.0	0.0	0.0
PHXni PHXni	0.0	0.0	0.0	0.0	0.0	0.0	0.0	0.0	0.0
PHXni PLBEni	0.0	0.0	0.0	0.0	0.0	0.0	0.0	0.0	0.0
PLBEni PLBEni	0.0	0.0	0.0	0.0	0.0	0.0	0.0	0.0	0.0
TCEni PHX	12.6	4.3	1.6	3.7	24.7	6.2	11.4	64.5	65.0
TCEni PLBE	2.0	0.7	0.3	0.7	4.4	1.1	3.1	12.2	21.0
LBEni PHX	2.1	0.8	0.3	0.9	8.4	1.0	4.6	18.1	18.0
LBEni PLBE	0.4	0.1	0.0	0.2	2.8	0.5	1.1	5.1	10.0
TCE CMUP	0.0	0.0	0.0	0.0	0.0	0.0	0.0	0.0	0.0
TCE CMU	0.0	0.0	0.0	0.0	0.0	0.0	0.0	0.0	0.0
TCE CMP	0.0	0.0	0.0	0.0	0.0	0.0	0.0	0.0	0.0
TCE CMX	0.0	0.0	0.0	0.0	0.0	0.0	0.0	0.0	0.0
TCE CMXMsKs	0.0	0.0	0.0	0.0	0.0	0.0	0.0	0.0	0.0
TCE BMU	0.0	0.0	0.0	0.0	0.0	0.0	0.0	0.0	0.0
TCE CMIOCES	0.0	0.0	0.0	0.0	0.0	0.0	0.0	0.0	0.0
TCE CMIOPES	0.0	0.0	0.0	0.0	0.0	0.0	0.0	0.0	0.0
LBE CMUP	0.0	0.0	0.0	0.0	0.0	0.0	0.0	0.0	0.0
LBE CMU	0.0	0.0	0.0	0.0	0.0	0.0	0.0	0.0	0.0
LBE CMP	0.0	0.0	0.0	0.0	0.0	0.0	0.0	0.0	0.0
LBE CMX	0.0	0.0	0.0	0.0	0.0	0.0	0.0	0.0	0.0
LBE CMXMsKs	0.0	0.0	0.0	0.0	0.0	0.0	0.0	0.0	0.0
LBE BMU	0.0	0.0	0.0	0.0	0.0	0.0	0.0	0.0	0.0
LBE CMIOCES	0.0	0.0	0.0	0.0	0.0	0.0	0.0	0.0	0.0
LBE CMIOPES	0.0	0.0	0.0	0.0	0.0	0.0	0.0	0.0	0.0
PHX CMUP	0.0	0.0	0.0	0.0	0.0	0.0	0.0	0.0	0.0
PHX CMU	0.0	0.0	0.0	0.0	0.0	0.0	0.0	0.0	0.0
PHX CMP	0.0	0.0	0.0	0.0	0.0	0.0	0.0	0.0	0.0
PHX CMX	0.0	0.0	0.0	0.0	0.0	0.0	0.0	0.0	0.0
PHX CMXMsKs	0.0	0.0	0.0	0.0	0.0	0.0	0.0	0.0	0.0
PHX BMU	0.9	0.1	0.0	0.1	1.4	0.2	0.4	3.1	3.0
PHX CMIOCES	0.0	0.0	0.0	0.0	0.0	0.0	0.0	0.0	0.0
PHX CMIOPES	1.5	0.1	0.0	0.2	2.6	0.4	3.1	8.0	8.0
PLBE CMUP	0.0	0.0	0.0	0.0	0.0	0.0	0.0	0.0	0.0
PLBE CMU	0.0	0.0	0.0	0.0	0.0	0.0	0.0	0.0	0.0
PLBE CMP	0.0	0.0	0.0	0.0	0.0	0.0	0.0	0.0	0.0
PLBE CMX	0.0	0.0	0.0	0.0	0.0	0.0	0.0	0.0	0.0

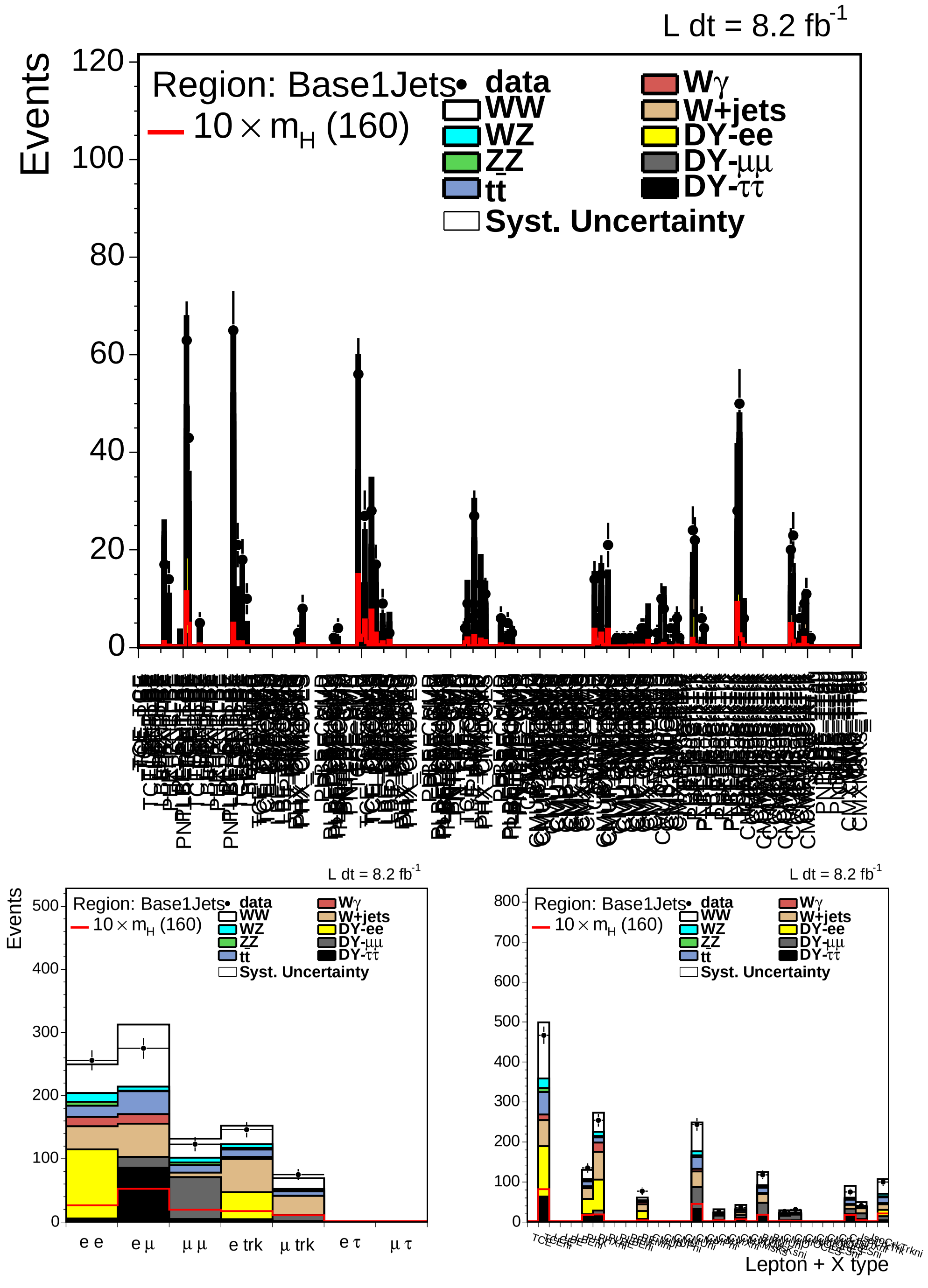

Figure 38: Signal and background in the opposite-sign signal region for events containing one reconstructed jet with $E_T > 15$ GeV.

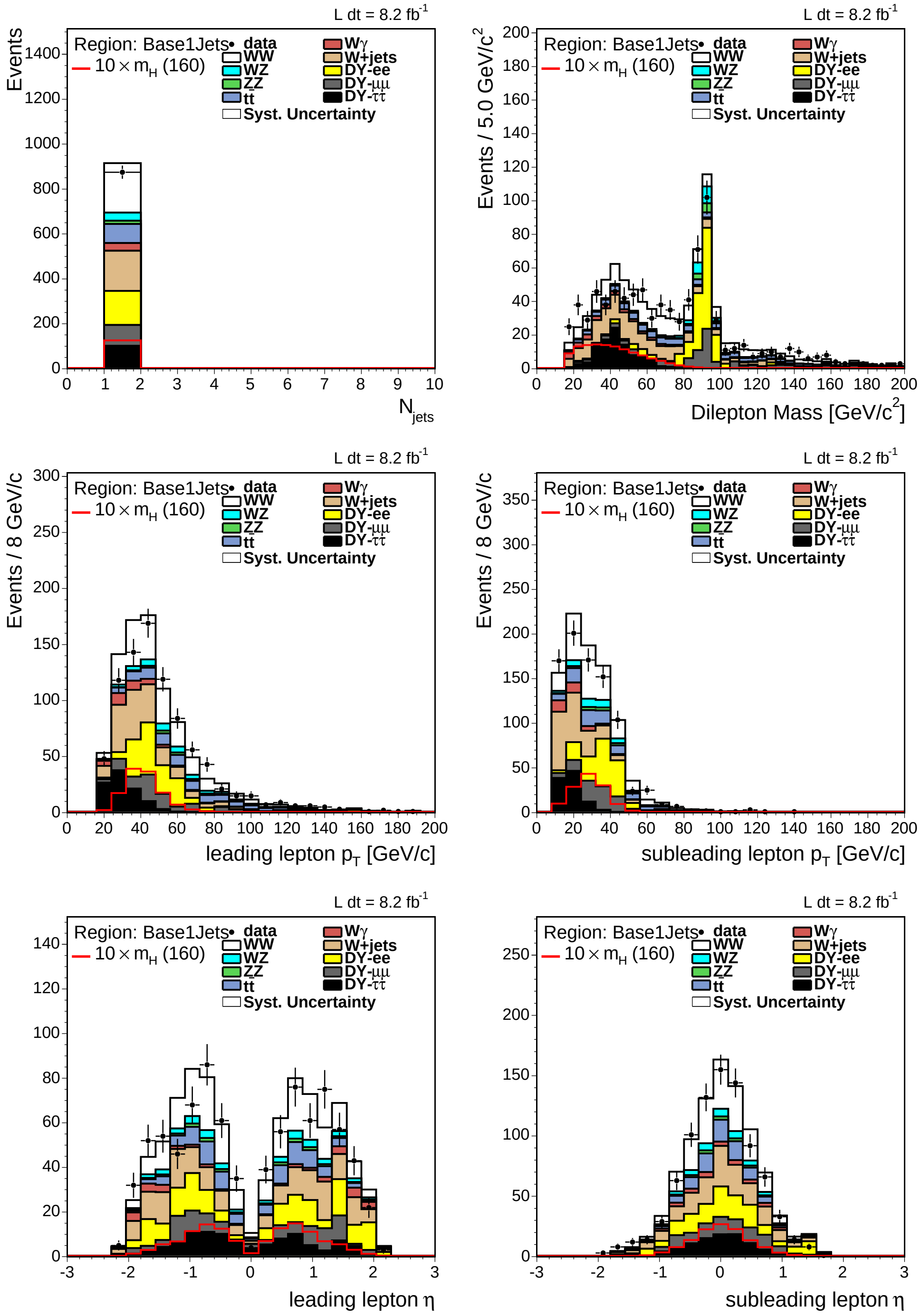

Figure 39: Signal and background in the opposite-sign signal region for events containing one reconstructed jet with $E_T > 15$ GeV.

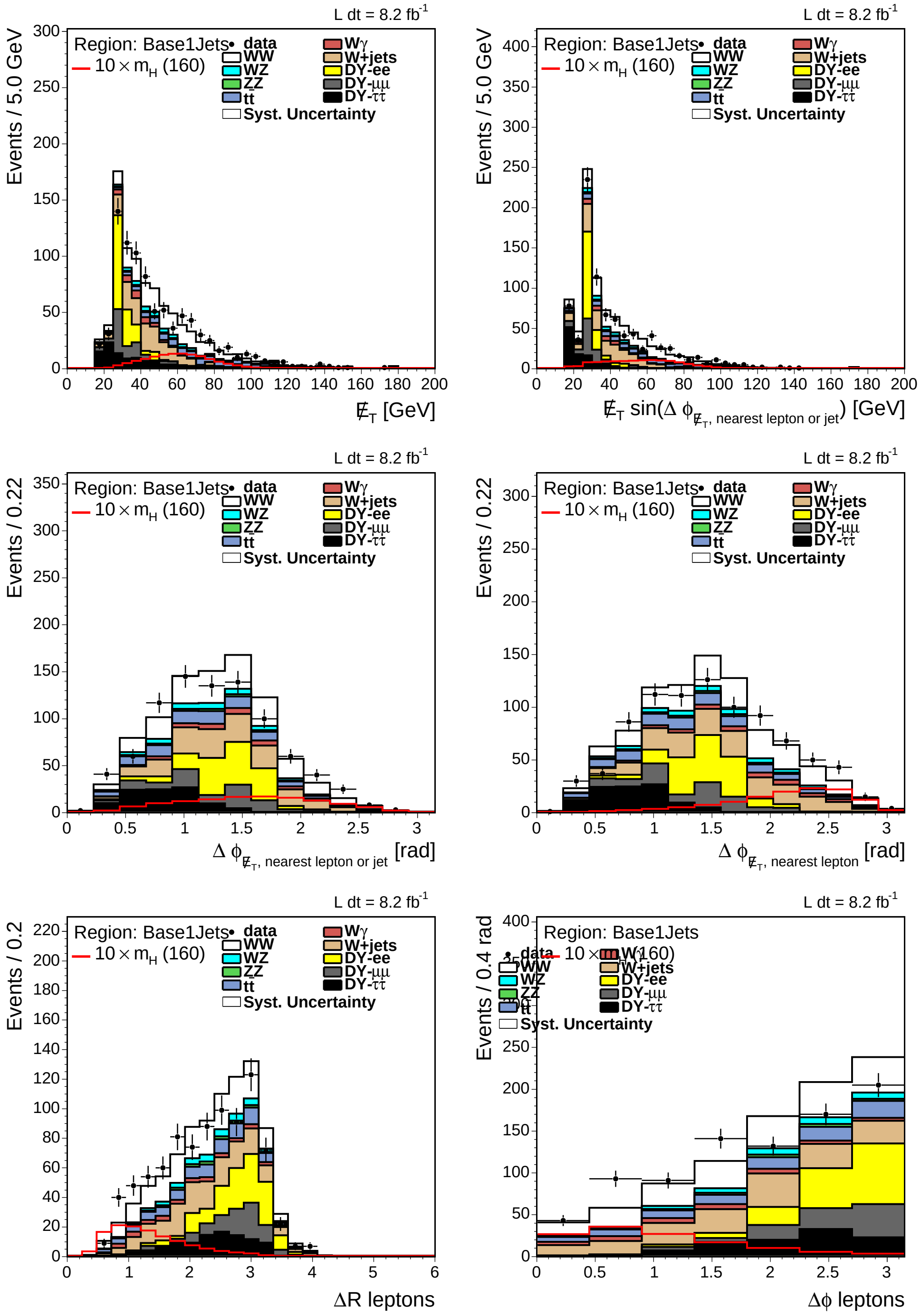

Figure 40: Signal and background in the opposite-sign signal region for events containing one reconstructed jet with $E_T > 15$ GeV.

Variable	Meaning
	1J neural networks
dRLeptons	ΔR between the leptons
Mt_H	Transverse mass of the sum of lepton's 4-momenta and ($\not\!\!E_T$, MetX, MetY, 0) where MetX/Y are the X/Y components of the $\vec{\not\!\!E}_T$
dimass	Dilepton invariant mass
MetSpec	$\not\!\!E_{Tspec} = \not\!\!E_T$ if $\Delta\phi$ ($\vec{\not\!\!E}_T$, l or j) $> \frac{\pi}{2}$ $\not\!\!E_{Tspec} = \not\!\!E_T$ sin($\Delta\phi$ ($\vec{\not\!\!E}_T$, l or j)) if $\Delta\phi$ ($\vec{\not\!\!E}_T$, l or j) $< \frac{\pi}{2}$
lep1_E	Energy of the leading (most energetic) lepton (for muons this is the lepton 3-momentum module)
lep1_Pt	Transverse momentum of the first lepton
lep2_Pt	Transverse momentum of the second lepton
Ht	Scalar sum of Leptons E_T, Jet E_T and $\not\!\!E_T$

Table 47: Summary of inputs to 1J neural networks.

Mass (GeV/c^2)	gg→H	WH	ZH	VBF
110	0.37 (0.31/0.062)	0.19 (0.15/0.036)	0.063 (0.05/0.013)	0.028 (0.024/0.0044)
115	0.74 (0.62/0.12)	0.32 (0.25/0.061)	0.1 (0.083/0.021)	0.056 (0.047/0.0085)
120	1.2 (1/0.22)	0.48 (0.39/0.091)	0.15 (0.12/0.03)	0.097 (0.082/0.015)
125	2 (1.6/0.33)	0.66 (0.54/0.12)	0.21 (0.17/0.043)	0.16 (0.13/0.025)
130	2.9 (2.4/0.5)	0.85 (0.69/0.16)	0.28 (0.23/0.052)	0.23 (0.19/0.038)
135	3.8 (3.1/0.67)	1 (0.82/0.18)	0.34 (0.27/0.064)	0.31 (0.26/0.051)
140	4.7 (3.9/0.81)	1.1 (0.91/0.2)	0.37 (0.31/0.069)	0.39 (0.33/0.062)
145	5.5 (4.6/0.98)	1.2 (0.97/0.22)	0.41 (0.34/0.075)	0.48 (0.4/0.079)
150	6.4 (5.3/1.1)	1.2 (0.99/0.22)	0.43 (0.35/0.08)	0.55 (0.47/0.088)
155	7.1 (5.9/1.2)	1.2 (1/0.22)	0.44 (0.36/0.076)	0.63 (0.53/0.1)
160	8 (6.6/1.3)	1.2 (1/0.2)	0.46 (0.38/0.078)	0.71 (0.6/0.11)
165	8 (6.6/1.3)	1.1 (0.94/0.19)	0.44 (0.37/0.069)	0.74 (0.63/0.11)
170	7.4 (6.2/1.3)	1 (0.84/0.17)	0.39 (0.33/0.069)	0.71 (0.6/0.11)
175	6.8 (5.6/1.2)	0.92 (0.76/0.15)	0.36 (0.3/0.06)	0.67 (0.56/0.11)
180	6.1 (5/1.1)	0.8 (0.66/0.14)	0.31 (0.26/0.05)	0.61 (0.51/0.096)
185	5 (4.1/0.88)	0.65 (0.54/0.11)	0.26 (0.21/0.042)	0.53 (0.44/0.088)
190	4.4 (3.6/0.78)	0.55 (0.46/0.091)	0.21 (0.18/0.035)	0.46 (0.39/0.074)
195	3.9 (3.2/0.7)	0.48 (0.39/0.082)	0.19 (0.16/0.031)	0.42 (0.34/0.072)
200	3.5 (2.9/0.64)	0.42 (0.35/0.07)	0.17 (0.14/0.027)	0.38 (0.32/0.066)

Table 48: Expected Higgs Signal yields as a function of the Higgs boson mass in the 1J region for each of the contributing production processes. The numbers inside the parentheses are the expected relative contributions in the High S/B and Low S/B regions.

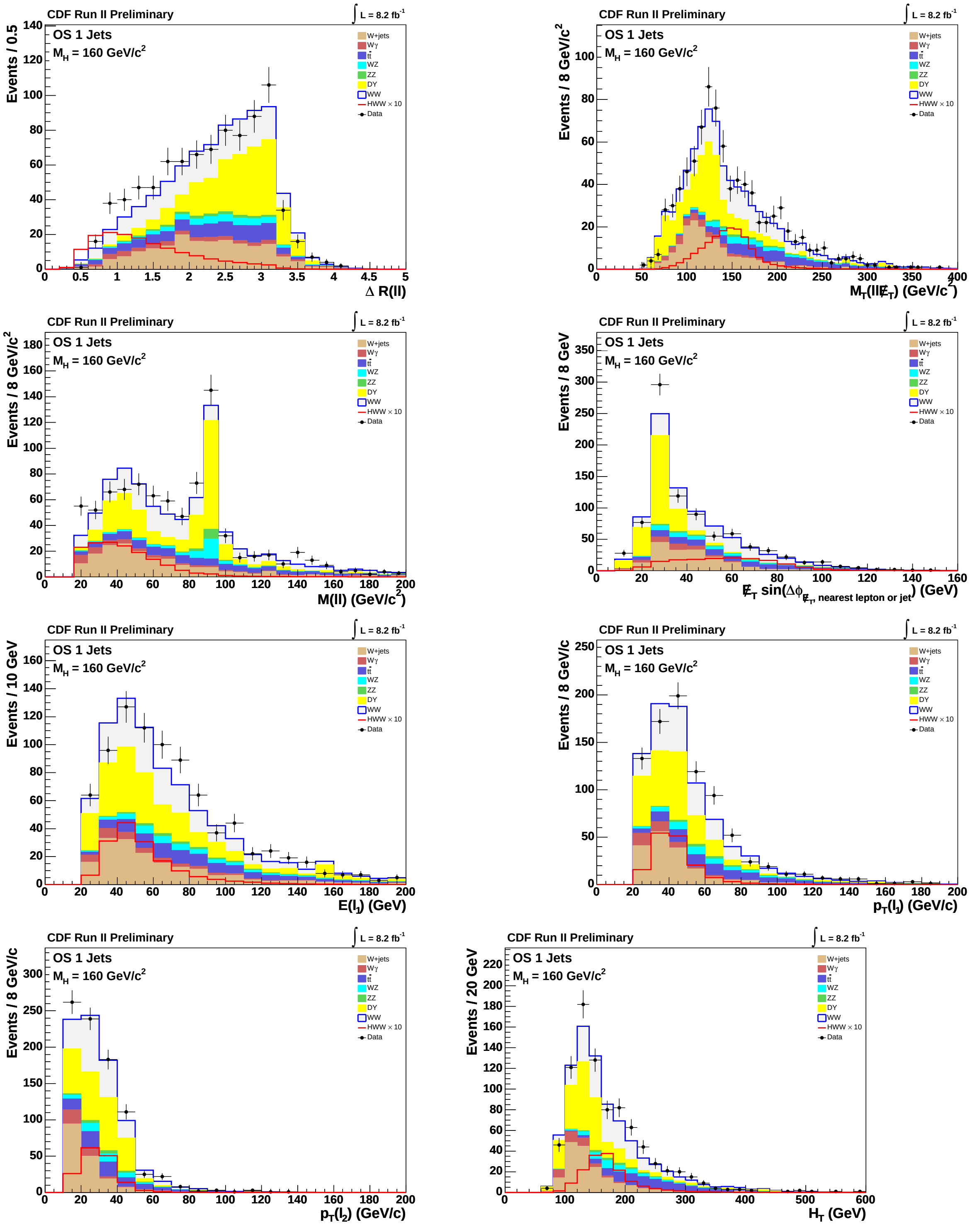

Figure 41: Neural Network input variables for 1J NN (signal for $M_H = 160$ GeV/c^2).

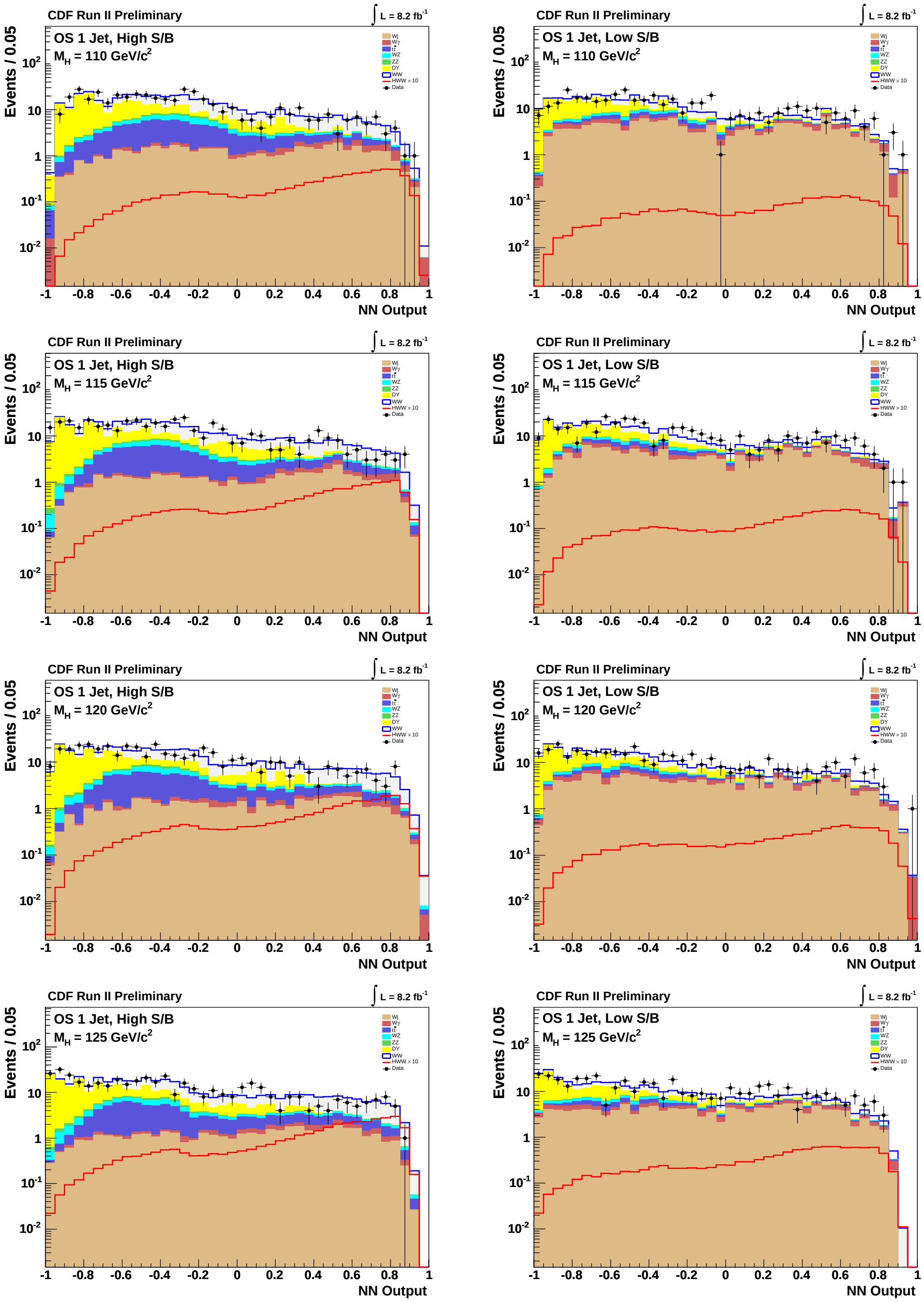

Figure 42: 1J Neural Network output templates for several Higgs masses. On the left for High S/B events and on the right for Low S/B. From the top to bottom: 110 GeV, 115 GeV, 120 GeV, and 125 GeV.

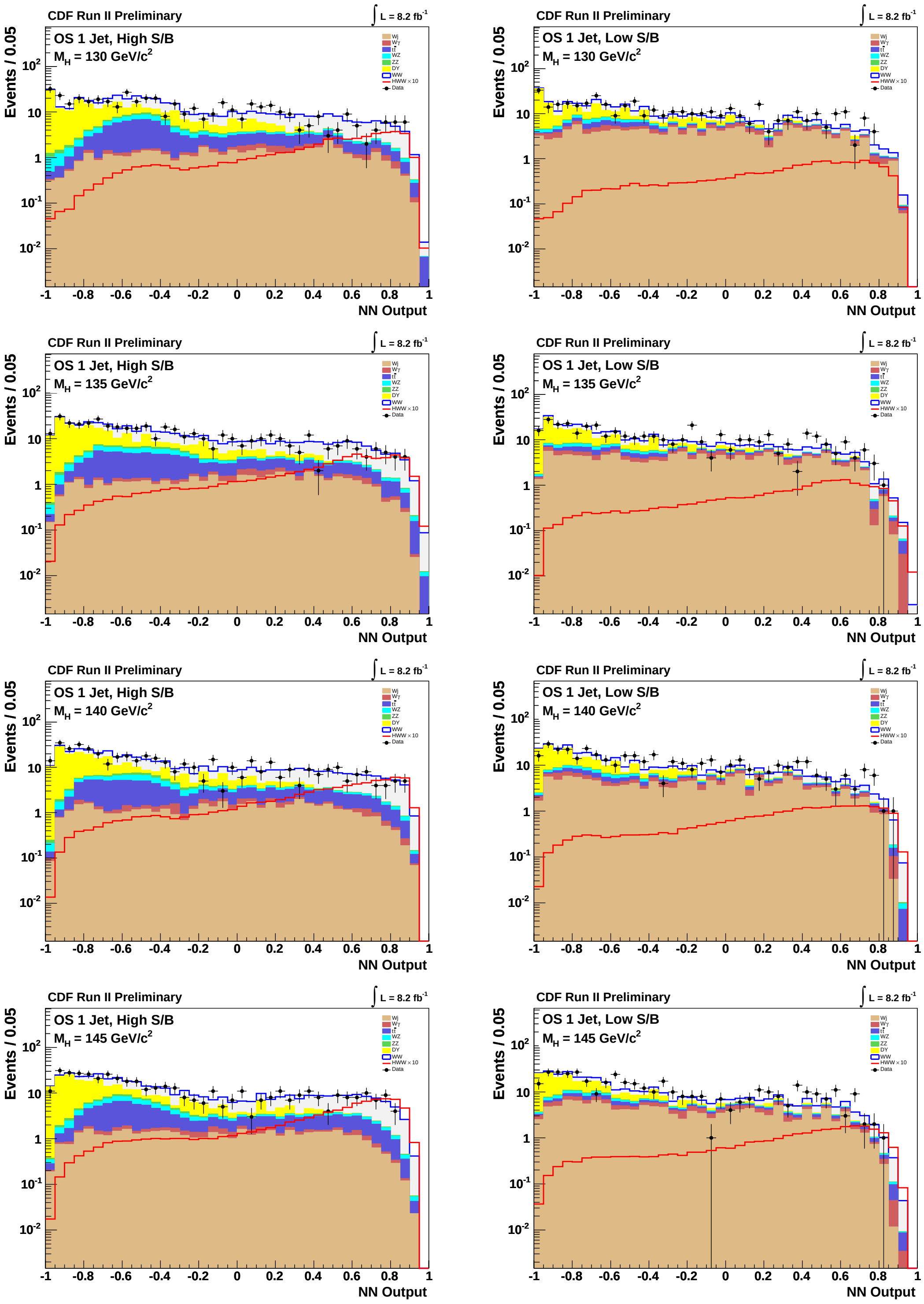

Figure 43: 1J Neural Network output templates for several Higgs masses. On the left for High S/B events and on the right for Low S/B. From the top to bottom: 130 GeV, 135 GeV, 140 GeV, and 145 GeV.

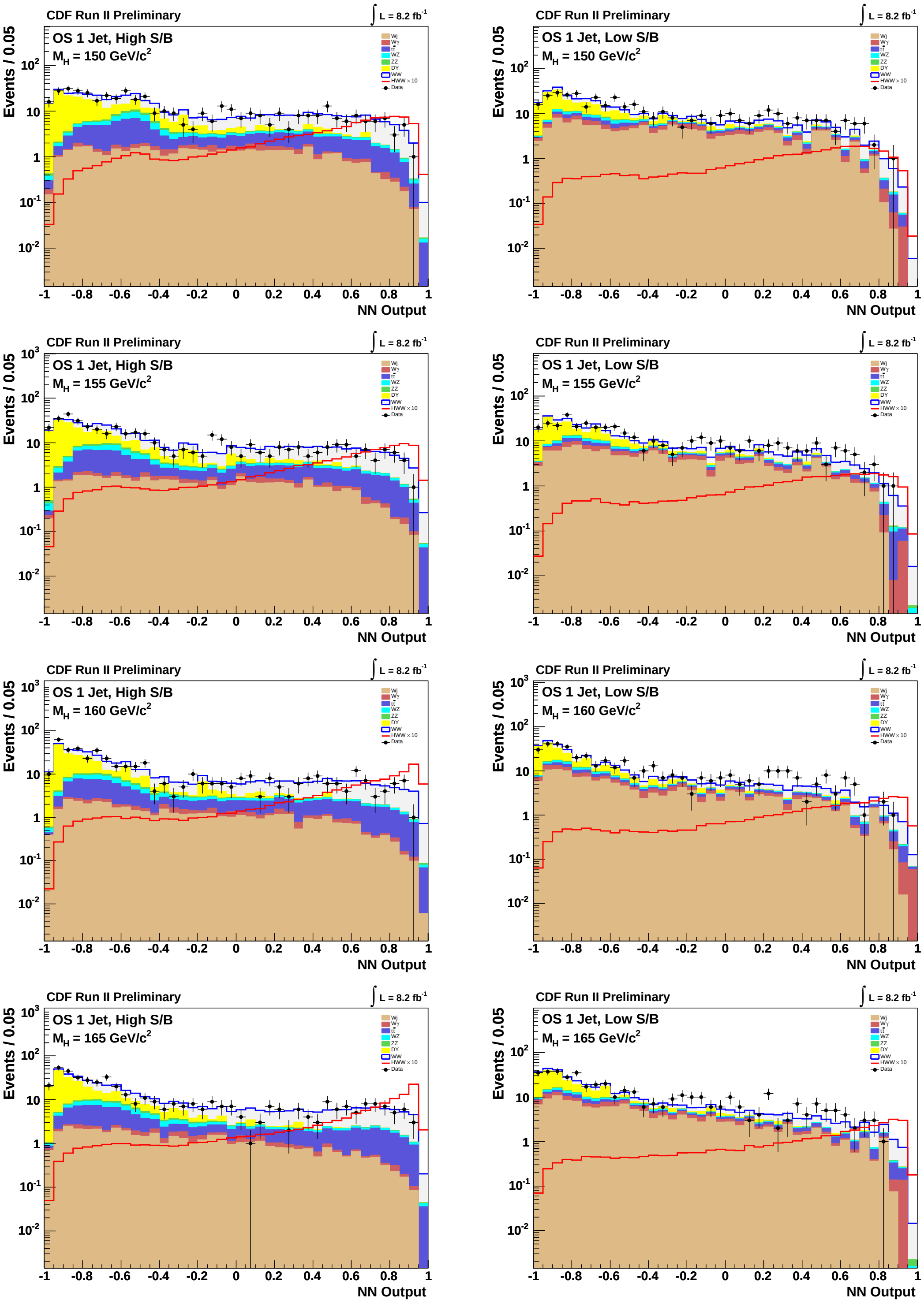

Figure 44: 1J Neural Network output templates for several Higgs masses. On the left for High S/B events and on the right for Low S/B. From the top to bottom: 150 GeV, 155 GeV, 160 GeV, and 165 GeV.

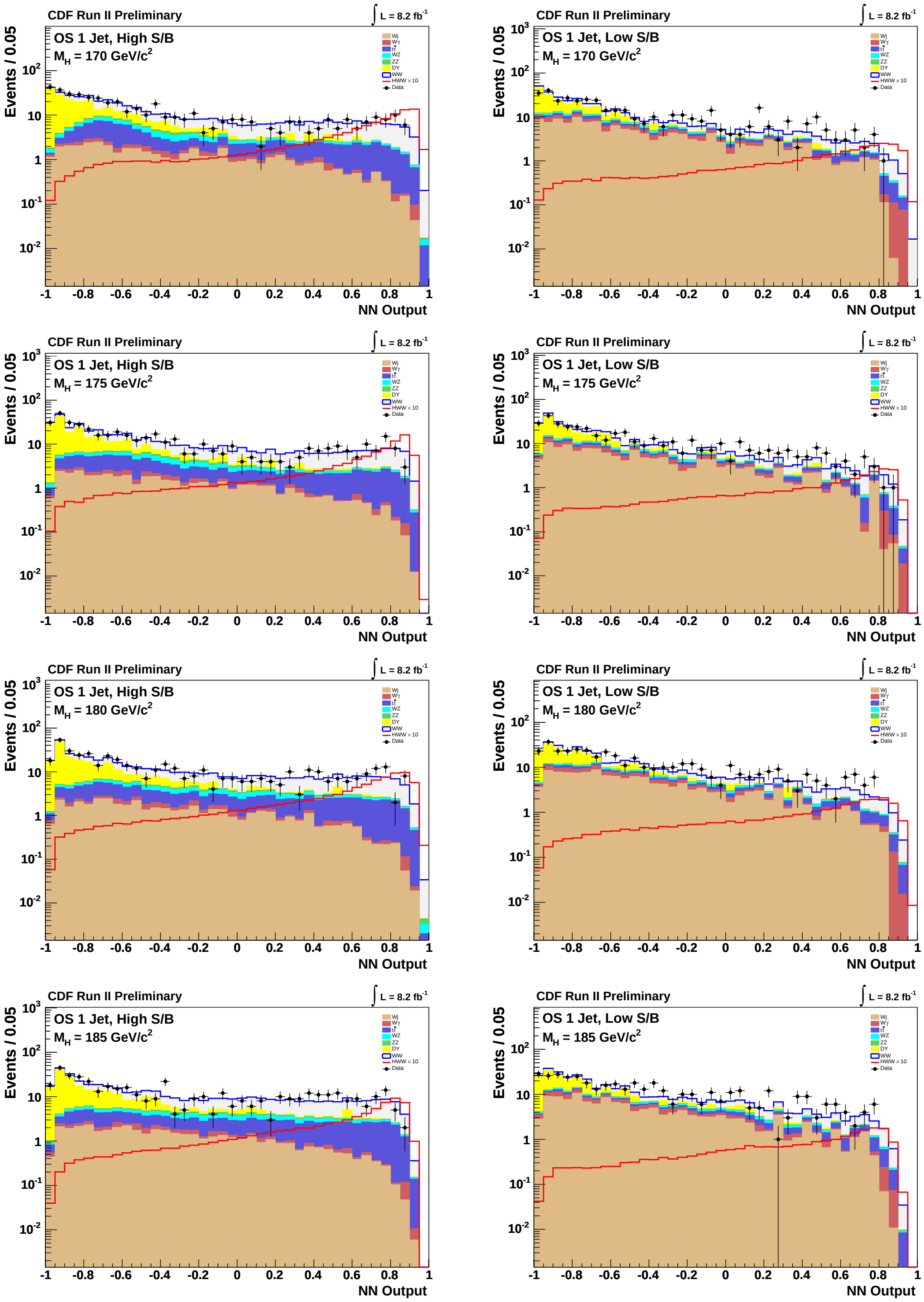

Figure 45: 1J Neural Network output templates for several Higgs masses. On the left for High S/B events and on the right for Low S/B. From the top to bottom: 170 GeV, 175 GeV, 180 GeV, 185 GeV.

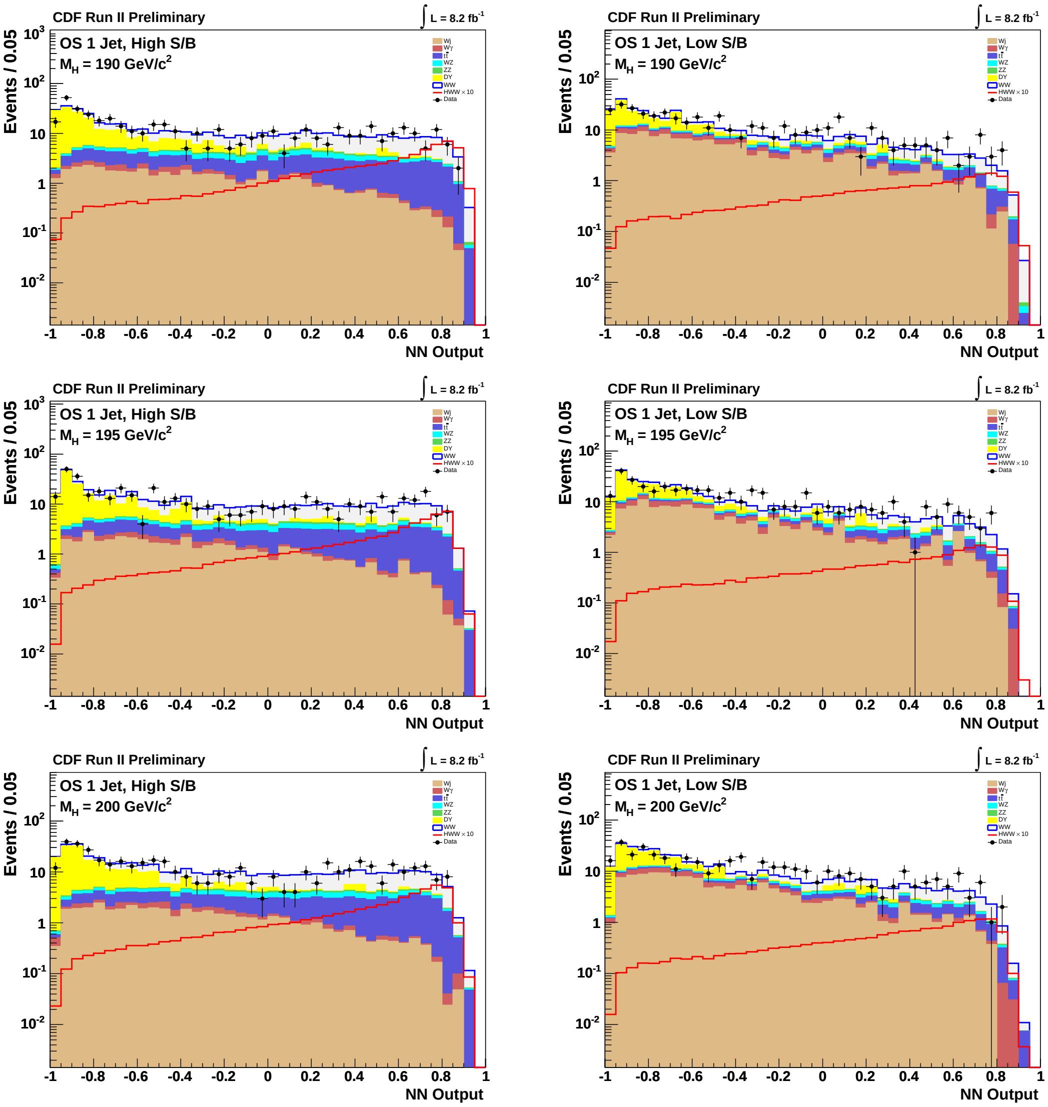

Figure 46: 1J Neural Network output templates for several Higgs masses. On the left for High S/B events and on the right for Low S/B. From the top to bottom: 190 GeV, 195 GeV, and 200 GeV.

Uncertainty Source	WW	WZ	ZZ	$t\bar{t}$	DY	$W\gamma$	W+jet
Cross Section							
Total	*6.0%*	*6.0%*	*6.0%*	10.0%			
Acceptance							
Scale (jets)	-4.0%						
PDF Model (jets)	4.7%						
Higher-order Diagrams		*10.0%*	*10.0%*	10.0%		10.0%	
Jet Energy Scale	*-5.5%*	*-1.0%*	*-4.3%*	*-13.0%*	*-6.5%*	*-9.5%*	
Missing E_T Modeling					20.0%		
$W\gamma$ Modeling						10.0%	
Jet Fake Rates							
(Low S/B)							23.0%
(High S/B)							28.0%
Luminosity	*7.3%*	*7.3%*	*7.3%*	*7.3%*	*7.3%*		

Table 49: Systematics table for 1J analysis background processes. Cross section systematics are correlated for the diboson processes (shown in italic font) but uncorrelated between all other processes. Scale (jets), PDF Model (jets), and Jet Energy Scale systematics are anticorrelated between the 0, 1, and 2+ jet bins, as these systematics cause events to fluctuate between jet bins.

Uncertainty Source	$gg \to H$	WH	ZH	VBF
Cross Section				
Scale	23.5%			
PDF Model	17.3%			
Total		*5.0%*	*5.0%*	10.0%
Acceptance				
Scale (leptons)	2.2%			
Scale (jets)	-1.9%			
PDF Model (leptons)	3.6%			
PDF Model (jets)	-6.3%			
EWK Higher-order Diagrams		*10.0%*	*10.0%*	*10.0%*
Jet Energy Scale	*-4.0%*	*-8.5%*	*-7.0%*	*-6.5%*
Luminosity	*7.3%*	*7.3%*	*7.3%*	*7.3%*

Table 50: Systematics table for 1J analysis signal processes. Cross section systematics are uncorrelated between the signal processes. Higher-order diagrams for the VH and VBF processes, shown in italic font, are correlated among each other but uncorrelated from background processes. The Scale (jets) and PDF Model (jets) systematics for $gg \to H$ are anticorrelated between the 0, 1, and 2+ jet bins, as these systematics cause events to fluctuate between jet bins.

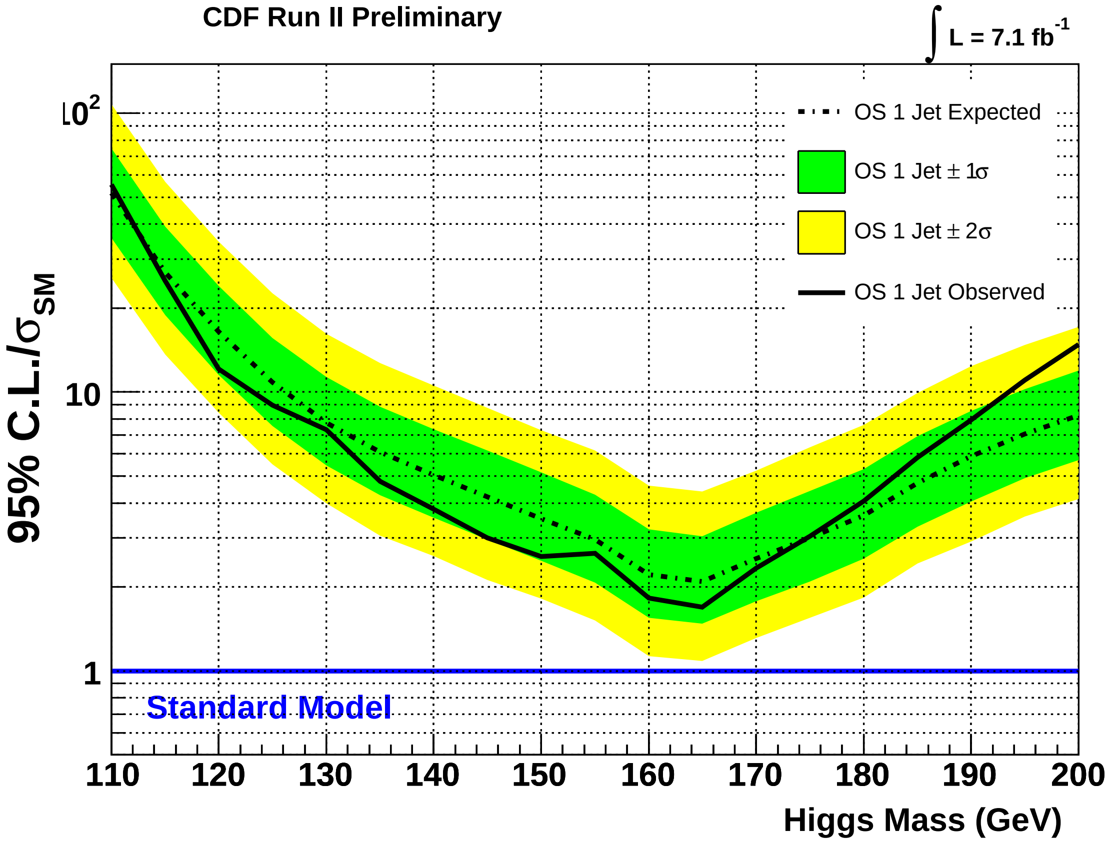

OS 1 Jet	110	115	120	125	130	135	140	145	150	155	160	165	170	175	180	185	190	195	200
$-2\sigma/\sigma_{SM}$	25.67	13.65	8.43	5.51	3.99	3.06	2.58	2.12	1.81	1.51	1.13	1.09	1.31	1.55	1.84	2.42	2.91	3.57	4.13
$-1\sigma/\sigma_{SM}$	35.71	18.85	11.51	7.57	5.46	4.27	3.54	2.96	2.48	2.08	1.55	1.48	1.78	2.09	2.53	3.30	4.05	4.91	5.70
Median/$\sigma_{\mathbf{SM}}$	**51.67**	**26.81**	**16.48**	**10.82**	**7.78**	**6.09**	**5.05**	**4.20**	**3.51**	**2.96**	**2.21**	**2.09**	**2.53**	**3.01**	**3.61**	**4.72**	**5.87**	**7.06**	**8.27**
$+1\sigma/\sigma_{SM}$	74.94	39.29	24.07	15.61	11.35	8.85	7.36	6.18	5.16	4.29	3.22	3.03	3.68	4.41	5.28	6.95	8.56	10.25	11.94
$+2\sigma/\sigma_{SM}$	107.90	56.74	34.71	22.66	16.16	12.72	10.56	8.80	7.29	6.16	4.62	4.40	5.23	6.35	7.63	9.94	12.37	14.73	17.14
Observed/$\sigma_{\mathbf{SM}}$	**55.48**	**25.00**	**12.12**	**8.97**	**7.32**	**4.78**	**3.81**	**2.99**	**2.57**	**2.64**	**1.83**	**1.69**	**2.34**	**3.04**	**4.06**	**5.84**	**7.94**	**11.04**	**14.85**

Figure 47: $H \to WW$ sensitivity normalized to NNLL σ_{SM} calculation from the combination of the High S/B and Low S/B channels in the 1J region. In this region we consider potential signal contributions from gluon fusion, vector boson fusion, and associated production with either a W or Z boson.

10 Opposite-sign Dilepton Signal Region with 2+ Jets

The event selection for events with two or more jets in the final state (2J) is nearly identical to that for events with zero or one jets. We require two or more jets with $E_{\mathrm{T}} > 15$ GeV and $|\eta| < 2.5$ using Level 5 jet corrections.

The dominant background in this region is from $t\bar{t}$ production where both top quarks decay via $t \to Wb \to \ell\nu b$. Our requirement of two jets in the final state is satisfied by the presence of the two b-quarks in the final state. In order to reduce the $t\bar{t}$ background, we additionally reject events that contain one or more b-tagged jets. For the b-tag, we use the tight SecVtx information in Stntuple [33]. Since we are apply b-tagging to our $t\bar{t}$ background model, we need to use the standard Data/MC efficiency scale factor correction for b-tagging which we take to be 0.94 ± 0.03. There are no real b-jets in the other sources of background, but we expect to occasionally mistag one of these jets as a b-jet. The mistag matrix for tight SecVtx requirements for the first 2.2 fb^{-1} of data is given in [34] and shows that the rate of mistags is very low. Because our other background sources are small contributions and the mistag rate is also very small, we expect the effect of mistags to be negligible and therefore do not attempt to apply any corrections to our models for these effects. There are two additional scale factors applied to the $t\bar{t}$ sample: one of 0.968 to account for generating the sample with a top quark mass of 175 GeV, and another of 1.023 due to not requiring events to be in the silicon good run list. These scale factors and their contributions to the uncertainty are described in Section 7.3. Even after rejecting events that contain b-tags, $t\bar{t}$ production accounts for more than 50% of the total background in the 2J region.

The background expectation and observed yield for the opposite-sign dilepton signal region for events containing two or more reconstructed jets with $E_T > 15$ GeV are shown in Table 51. The numbers in this table correspond to event totals prior to the removal of events containing b-tags. The expected and observed kinematic distributions for these events are shown in Figures 48-50. We stack the backgrounds on top of each other, and then for comparison we overlay the contribution from a 160 GeV/c^2 Higgs boson with yields scaled up by a factor of 10. In addition, we calculate a confidence level for data versus background expectations on each plot. The confidence levels shown are for Poisson fluctuations and the KS test.

10.1 $t\bar{t}$ Control Region

Events with at least one b-tagged jet are removed from the signal region and examined as a $t\bar{t}$ control region. Without considering systematic uncertainties on the other background contributions, the 208 observed events give a rough measurement of the $t\bar{t}$ cross-section as 7.2 pb with a systematic uncertainty of about 10%. This is consistent with the theoretical prediction of 7.04 pb and with previous Tevatron measurements. Plots of various kinematic variables shown in Figure 51 show good agreement between the MC prediction

Category	WW	WZ	ZZ	$t\bar{t}$	DY	$W\gamma$	W+jets	Total	Data
TCE TCE	0.0	0.0	0.0	0.0	0.0	0.0	0.0	0.0	0.0
TCE LBE	0.0	0.0	0.0	0.0	0.0	0.0	0.0	0.0	0.0
TCE PHX	0.0	0.0	0.0	0.0	0.0	0.0	0.0	0.0	0.0
TCE PLBE	0.0	0.0	0.0	0.0	0.0	0.0	0.0	0.0	0.0
LBE LBE	0.0	0.0	0.0	0.0	0.0	0.0	0.0	0.0	0.0
LBE PHX	0.0	0.0	0.0	0.0	0.0	0.0	0.0	0.0	0.0
LBE PLBE	0.0	0.0	0.0	0.0	0.0	0.0	0.0	0.0	0.0
PHX PHX	0.5	0.2	0.1	2.9	1.2	0.2	2.2	7.3	9.0
PHX PLBE	0.2	0.1	0.0	1.1	1.1	0.3	1.0	3.7	3.0
PLBE PLBE	0.0	0.0	0.0	0.1	0.0	0.0	0.1	0.3	1.0
TCEni TCEni	4.1	1.3	0.7	49.7	11.0	0.2	1.2	68.1	53.0
TCEni LBEni	1.5	0.6	0.3	21.2	10.1	0.3	1.8	35.8	24.0
TCEni PHXni	0.0	0.0	0.0	0.0	0.0	0.0	0.0	0.0	0.0
TCEni PLBEni	0.0	0.0	0.0	0.0	0.0	0.0	0.0	0.0	0.0
LBEni LBEni	0.2	0.1	0.0	2.4	0.0	0.1	0.4	3.2	3.0
LBEni PHXni	0.0	0.0	0.0	0.0	0.0	0.0	0.0	0.0	0.0
LBEni PLBEni	0.0	0.0	0.0	0.0	0.0	0.0	0.0	0.0	0.0
PHXni PHXni	0.0	0.0	0.0	0.0	0.0	0.0	0.0	0.0	0.0
PHXni PLBEni	0.0	0.0	0.0	0.0	0.0	0.0	0.0	0.0	0.0
PLBEni PLBEni	0.0	0.0	0.0	0.0	0.0	0.0	0.0	0.0	0.0
TCEni PHX	2.7	1.1	0.4	24.1	10.4	1.2	4.3	44.3	31.0
TCEni PLBE	0.5	0.2	0.1	4.7	2.9	0.3	1.2	9.8	10.0
LBEni PHX	0.5	0.2	0.1	5.1	0.6	0.3	1.5	8.4	12.0
LBEni PLBE	0.1	0.0	0.0	1.1	0.0	0.0	0.4	1.7	9.0
TCE CMUP	0.0	0.0	0.0	0.0	0.0	0.0	0.0	0.0	0.0
TCE CMU	0.0	0.0	0.0	0.0	0.0	0.0	0.0	0.0	0.0
TCE CMP	0.0	0.0	0.0	0.0	0.0	0.0	0.0	0.0	0.0
TCE CMX	0.0	0.0	0.0	0.0	0.0	0.0	0.0	0.0	0.0
TCE CMXMsKs	0.0	0.0	0.0	0.0	0.0	0.0	0.0	0.0	0.0
TCE BMU	0.0	0.0	0.0	0.0	0.0	0.0	0.0	0.0	0.0
TCE CMIOCES	0.0	0.0	0.0	0.0	0.0	0.0	0.0	0.0	0.0
TCE CMIOPES	0.0	0.0	0.0	0.0	0.0	0.0	0.0	0.0	0.0
LBE CMUP	0.0	0.0	0.0	0.0	0.0	0.0	0.0	0.0	0.0
LBE CMU	0.0	0.0	0.0	0.0	0.0	0.0	0.0	0.0	0.0
LBE CMP	0.0	0.0	0.0	0.0	0.0	0.0	0.0	0.0	0.0
LBE CMX	0.0	0.0	0.0	0.0	0.0	0.0	0.0	0.0	0.0
LBE CMXMsKs	0.0	0.0	0.0	0.0	0.0	0.0	0.0	0.0	0.0
LBE BMU	0.0	0.0	0.0	0.0	0.0	0.0	0.0	0.0	0.0
LBE CMIOCES	0.0	0.0	0.0	0.0	0.0	0.0	0.0	0.0	0.0
LBE CMIOPES	0.0	0.0	0.0	0.0	0.0	0.0	0.0	0.0	0.0
PHX CMUP	0.0	0.0	0.0	0.0	0.0	0.0	0.0	0.0	0.0
PHX CMU	0.0	0.0	0.0	0.0	0.0	0.0	0.0	0.0	0.0
PHX CMP	0.0	0.0	0.0	0.0	0.0	0.0	0.0	0.0	0.0
PHX CMX	0.0	0.0	0.0	0.0	0.0	0.0	0.0	0.0	0.0
PHX CMXMsKs	0.0	0.0	0.0	0.0	0.0	0.0	0.0	0.0	0.0
PHX BMU	0.2	0.0	0.0	1.1	0.1	0.1	0.1	1.6	4.0
PHX CMIOCES	0.0	0.0	0.0	0.0	0.0	0.0	0.0	0.0	0.0
PHX CMIOPES	0.3	0.0	0.0	1.8	2.1	0.1	2.0	6.3	4.0
PLBE CMUP	0.0	0.0	0.0	0.0	0.0	0.0	0.0	0.0	0.0
PLBE CMU	0.0	0.0	0.0	0.0	0.0	0.0	0.0	0.0	0.0
PLBE CMP	0.0	0.0	0.0	0.0	0.0	0.0	0.0	0.0	0.0
PLBE CMX	0.0	0.0	0.0	0.0	0.0	0.0	0.0	0.0	0.0

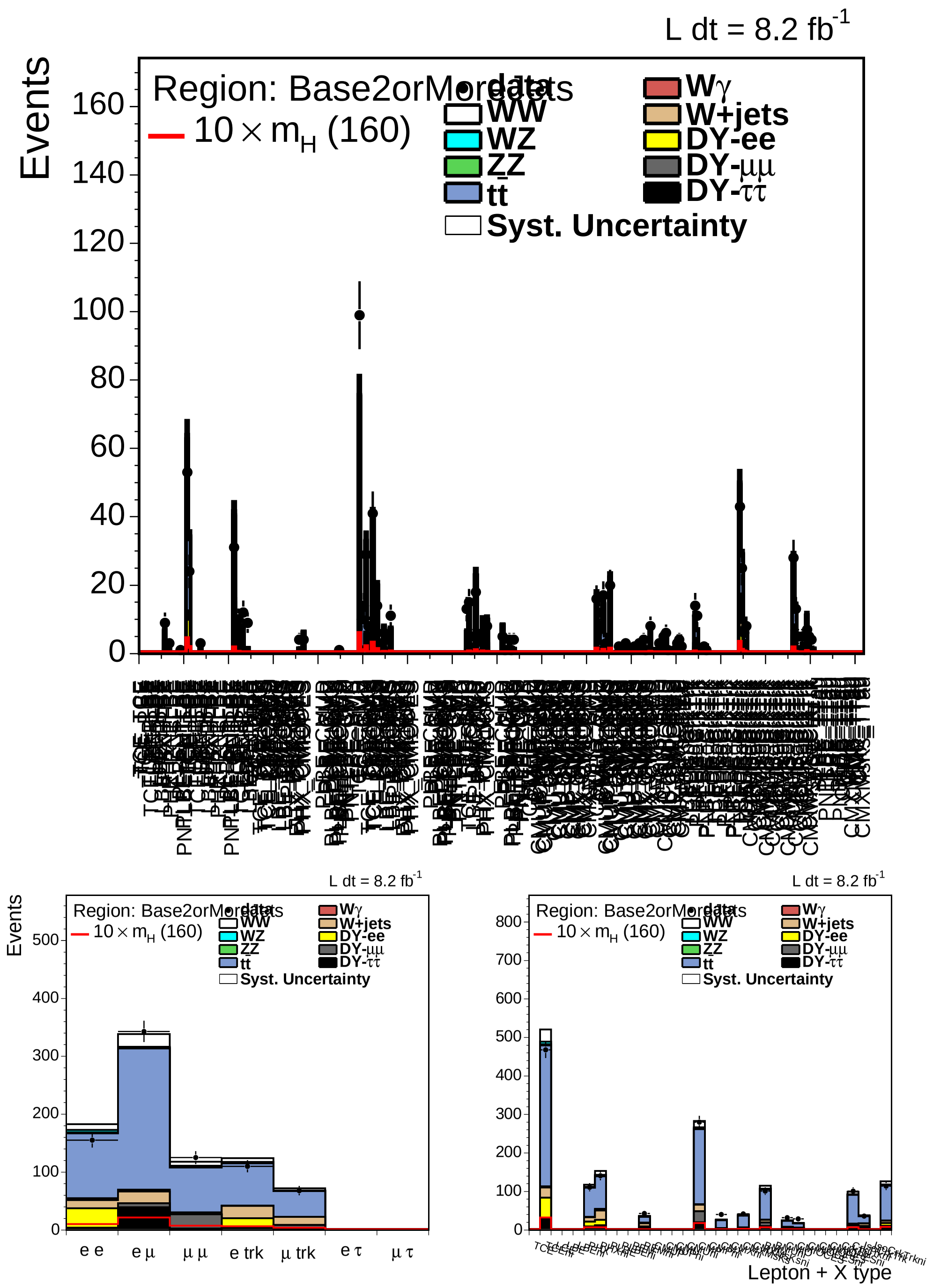

Figure 48: Signal and background in the opposite-sign signal region for events containing two or more reconstructed jets with $E_T > 15$ GeV (prior to removal of events containing a b-tagged jet).

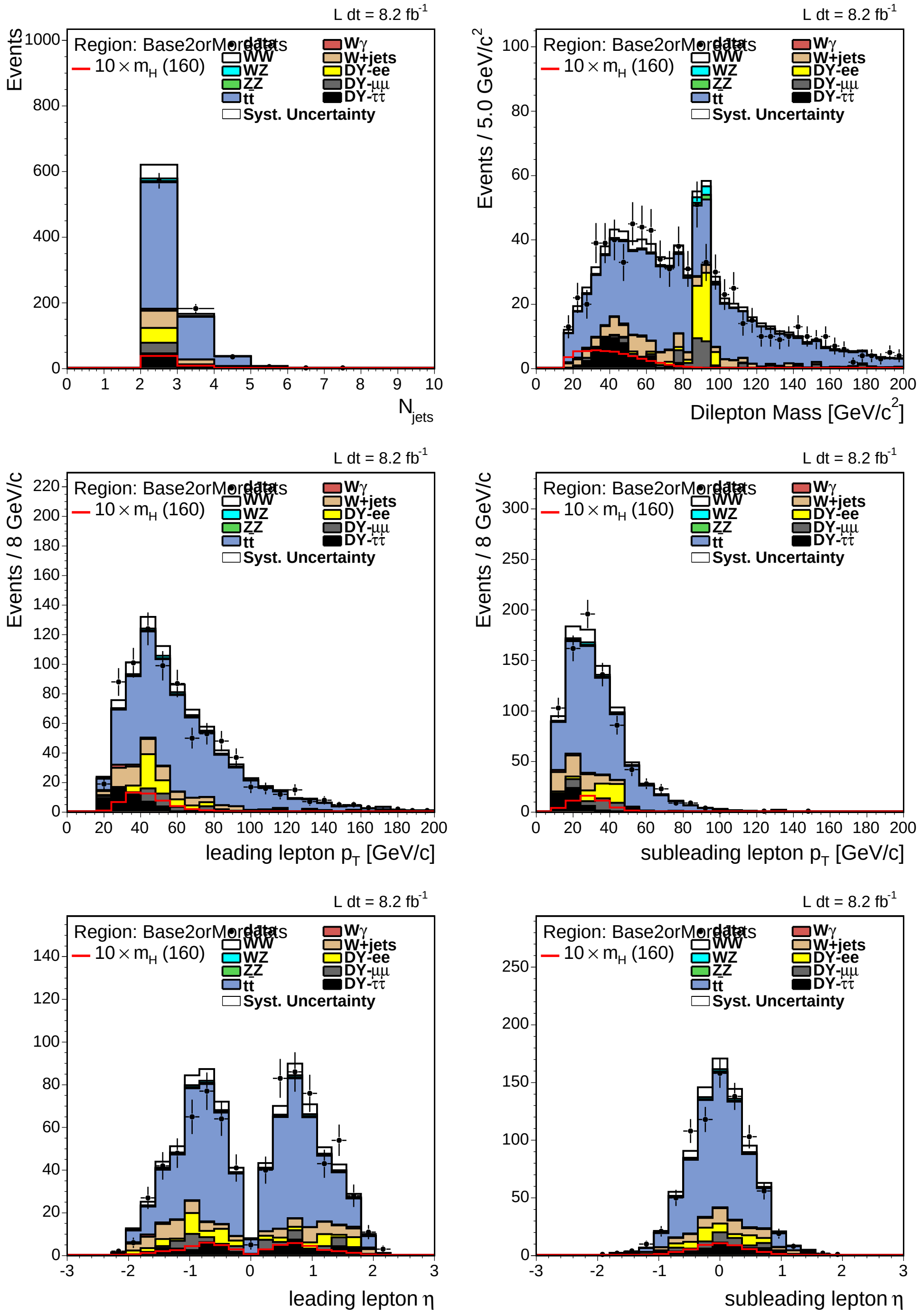

Figure 49: Signal and background in the opposite-sign signal region for events containing two or more reconstructed jets with $E_T > 15$ GeV (prior to removal of events containing a b-tagged jet).

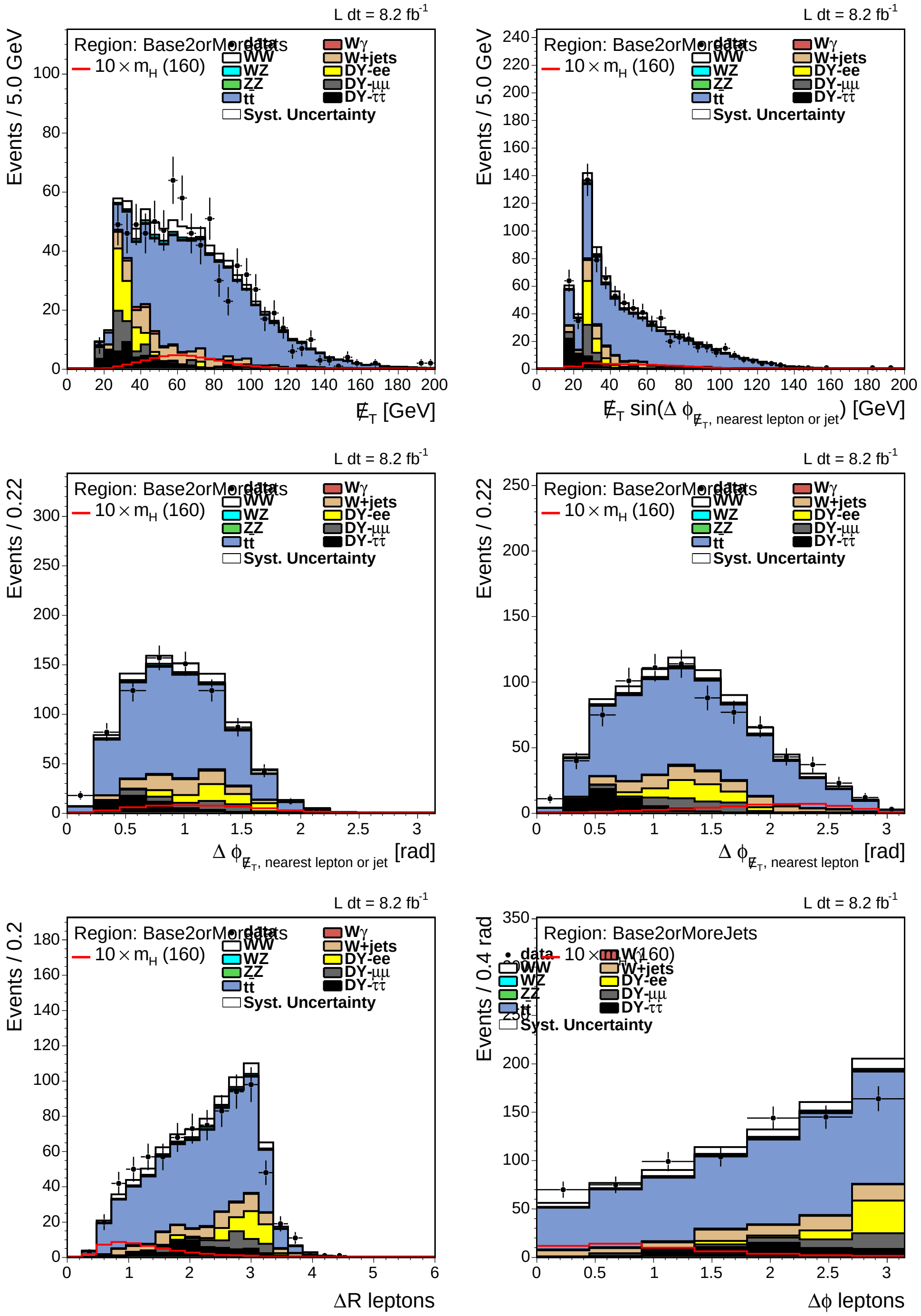

Figure 50: Signal and background in the opposite-sign signal region for events containing two or more reconstructed jets with $E_T > 15$ GeV (prior to removal of events containing a b-tagged jet).

Variable	Meaning
	2J neural networks
dRLeptons	ΔR between the leptons
dPhiLeptons	$\Delta\phi$ between the leptons
dPhiLepSumMet	$\Delta\phi$ between vector sum of first and second lepton momenta and $\not\!\!E_T$
sumJetPt	Vector sum of first and second jet p_{T}
Lep1Et	Transverse energy E_{T} of the first lepton
Lep2Et	Transverse energy E_{T} of the second lepton
Ht	Transverse mass H_{T} (scalar sum of lepton E_{T}'s, jet E_{T}'s, and $\not\!\!E_T$)
Mll	Dilepton invariant mass M_{ll}

Table 52: Summary of inputs to 2J neural networks.

and the distributions in data.

10.2 Analysis of Opposite-Sign 2+ Jet Events

As in the case of 1J events, we do not attempt to calculate Matrix Elements for 2J events. Instead, we rely solely on a neural network (NN) to discriminate signal from background using kinematic variables as inputs to the NN. We do not use jet angular variables, as they are not reliably reproduced by Pythia. Also, we find that using jet angular variables in the NN does not significantly improve the sensitivity. Optimization and training of the neural network are done in the same manner as for the 0J case described in Section 8. For the 2J region our neural network uses 8 inputs, 10 hidden nodes and 1 output node. The input variables used for the 2J NN are shown in Table 52. The observed distributions of each 2J neural network input parameter compared with the distributions predicted by our background model are shown in Figure 52. Here, events containing a b-tagged jet have been removed in both the observed and predicted distributions. For reference, we also include a hypothetical signal component for a Higgs boson with $m_H = 160$ GeV/c^2.

Templates are created for each neural network and used for calculating 95% CL limits with the MCLimit program [32]. Due to the low statistics in the 2J region, we do not divide events into High S/B and Low S/B categories as is done for the 0J and 1J regions. Output templates for the trained 2J neural network are shown in Figures 53 through 55.

In the 2J region we also consider potential signal contributions from all four Higgs production processes that contribute significantly at high masses (gluon fusion ($gg \to H \to WW \to ll\nu\nu$),Vector Boson Fusion (VBF), and associated production VH ($q\bar{q} \to ZH \to ZWW$ and $q\bar{q} \to WH \to WWW$). The additional processes contribute significantly to the event regions with one or more jets and incorporating their contributions is fairly straight-forward since we do not attempt to use neural network inputs based on Matrix Element calculations in these regions. We evaluate the number of events expected from each production process as a function of the mass of the Higgs. These numbers are

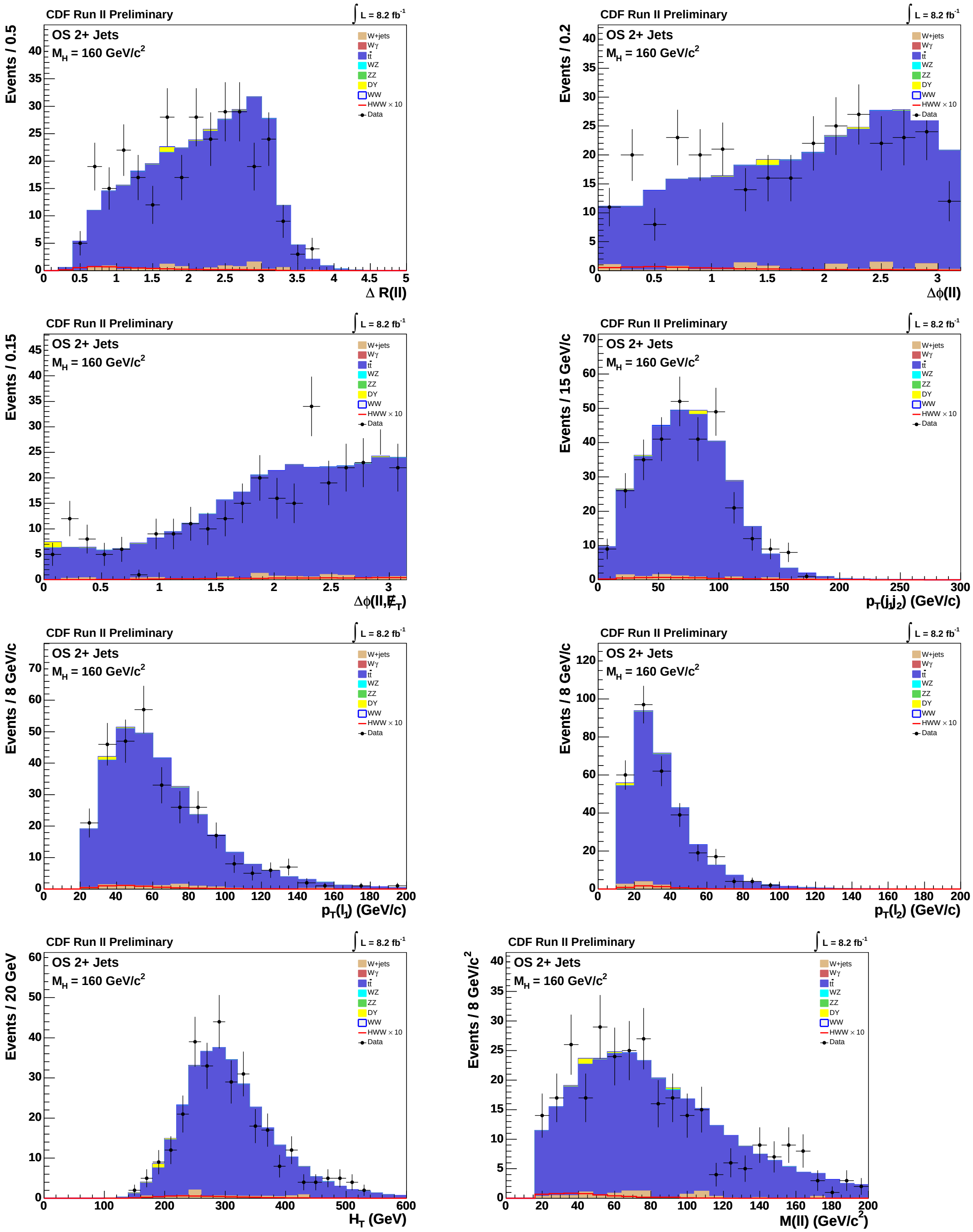

Figure 51: Control region for $t\bar{t}$, events with two or more jets in which at least one jet is tagged as originating from a b-quark (signal for $M_H = 160$ GeV/c^2).

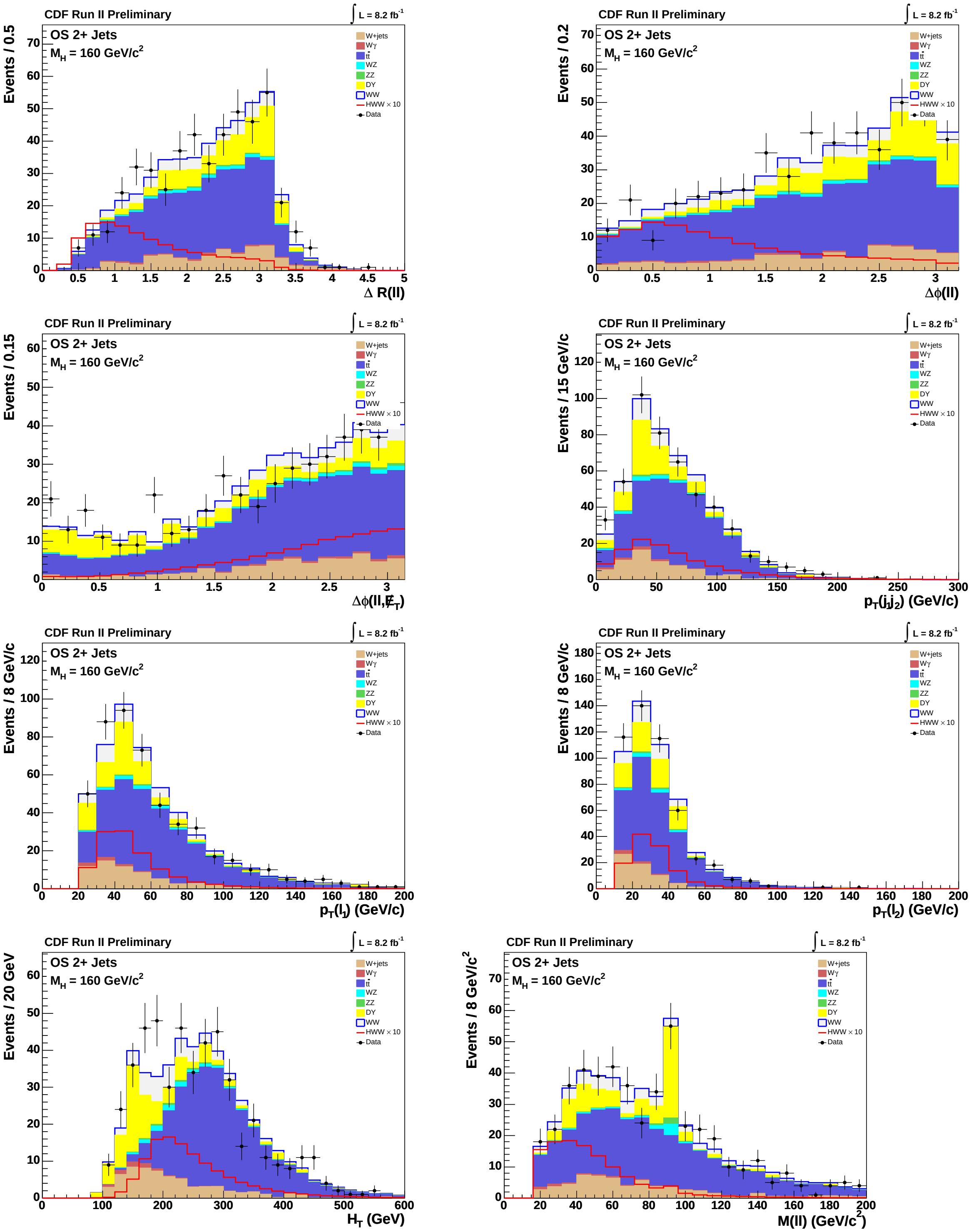

Figure 52: Neural Network input variables for 2J NN (signal for $M_H = 160$ GeV/c^2).

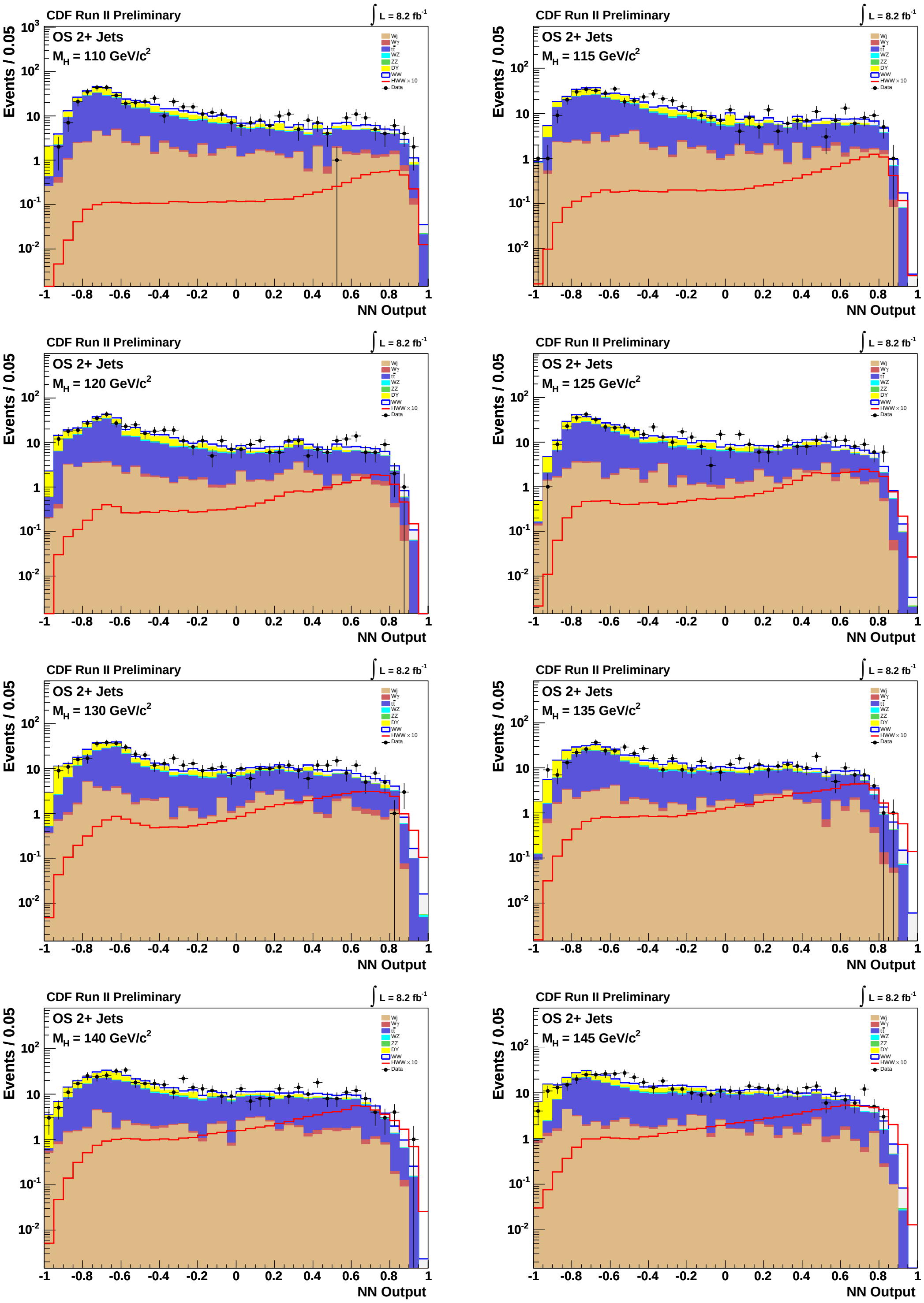

Figure 53: 2J Neural Network output templates for several Higgs masses. From the top left to bottom right: 110 GeV, 115 GeV, 120 GeV, 125 GeV, 130 GeV, 135 GeV, 140 GeV, and 145 GeV.

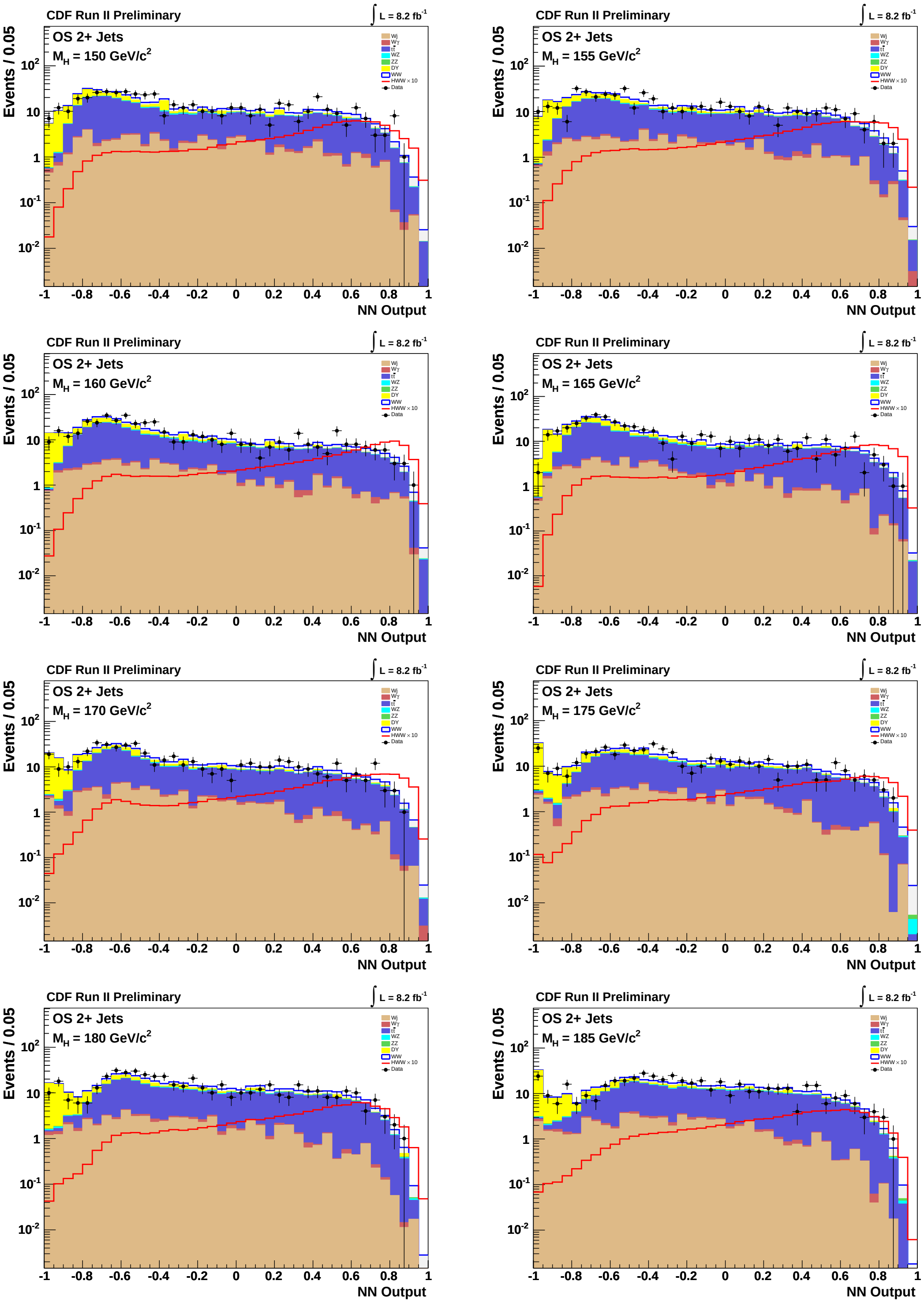

Figure 54: 2J Neural Network output templates for several Higgs masses. From the top left to bottom right : 150 GeV, 155 GeV, 160 GeV, 165 GeV, 170 GeV, 175 GeV, 180 GeV, and 185 GeV.

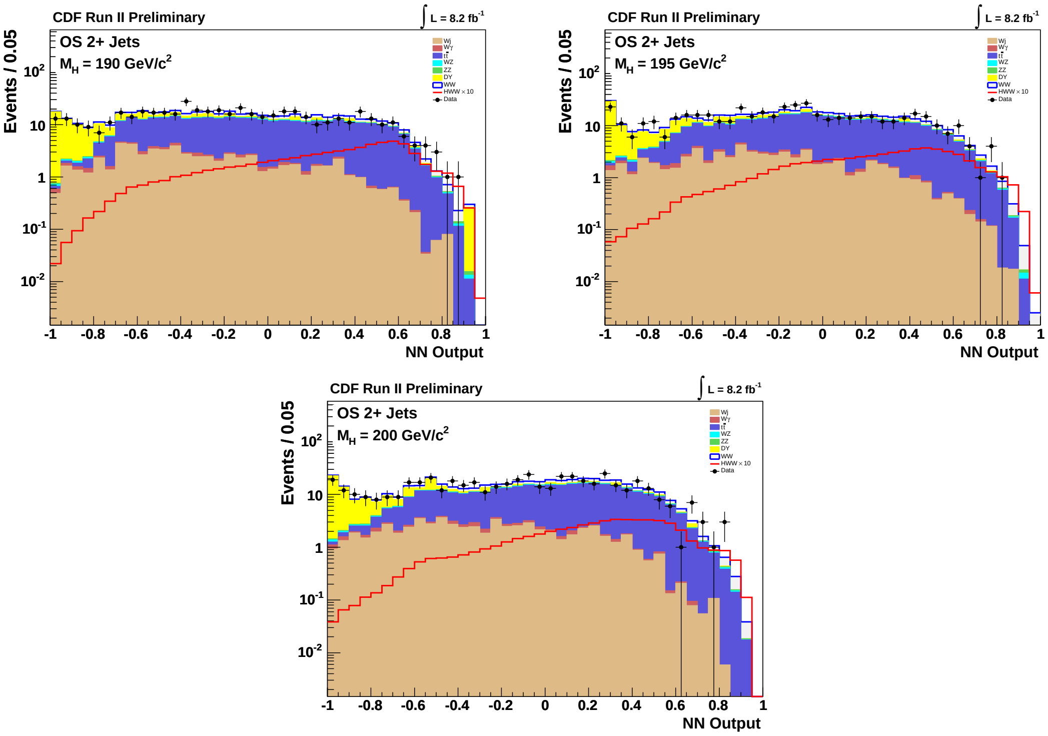

Figure 55: 2J Neural Network output templates for several Higgs masses. From the top left to bottom right : 190 GeV, 195 GeV, and 200 GeV.

Mass (GeV/c^2)	gg→H	WH	ZH	VBF
110	0.1 (0.089/0.016)	0.2 (0.17/0.033)	0.097 (0.081/0.016)	0.054 (0.047/0.0072)
115	0.21 (0.18/0.031)	0.36 (0.3/0.06)	0.17 (0.15/0.03)	0.11 (0.091/0.015)
120	0.32 (0.26/0.053)	0.6 (0.5/0.099)	0.29 (0.24/0.048)	0.18 (0.16/0.026)
125	0.52 (0.43/0.09)	0.9 (0.75/0.15)	0.43 (0.36/0.073)	0.3 (0.25/0.043)
130	0.78 (0.65/0.13)	1.2 (1/0.2)	0.59 (0.49/0.1)	0.44 (0.37/0.062)
135	1.1 (0.89/0.17)	1.5 (1.3/0.26)	0.76 (0.63/0.13)	0.59 (0.5/0.087)
140	1.4 (1.1/0.23)	1.8 (1.5/0.3)	0.9 (0.75/0.15)	0.73 (0.63/0.11)
145	1.7 (1.4/0.27)	2.1 (1.7/0.35)	1 (0.86/0.17)	0.89 (0.76/0.13)
150	1.9 (1.6/0.32)	2.3 (1.9/0.38)	1.1 (0.94/0.2)	1 (0.88/0.15)
155	2.2 (1.8/0.36)	2.4 (2/0.4)	1.2 (1/0.21)	1.2 (1/0.17)
160	2.5 (2.1/0.41)	2.6 (2.2/0.42)	1.3 (1.1/0.22)	1.3 (1.1/0.19)
165	2.6 (2.2/0.42)	2.5 (2.1/0.41)	1.3 (1.1/0.2)	1.4 (1.2/0.19)
170	2.5 (2.1/0.41)	2.3 (1.9/0.37)	1.2 (1/0.19)	1.3 (1.1/0.19)
175	2.3 (1.9/0.38)	2.1 (1.8/0.35)	1.1 (0.92/0.19)	1.2 (1.1/0.19)
180	2.1 (1.8/0.35)	1.9 (1.6/0.32)	0.99 (0.82/0.17)	1.1 (0.97/0.17)
185	1.8 (1.5/0.3)	1.6 (1.3/0.27)	0.84 (0.7/0.14)	0.99 (0.84/0.15)
190	1.6 (1.3/0.27)	1.4 (1.1/0.22)	0.71 (0.59/0.12)	0.87 (0.73/0.14)
195	1.4 (1.2/0.25)	1.2 (0.99/0.2)	0.63 (0.53/0.11)	0.78 (0.66/0.12)
200	1.3 (1.1/0.22)	1.1 (0.89/0.18)	0.57 (0.47/0.096)	0.71 (0.6/0.11)

Table 53: Expected Higgs Signal yields as a function of the Higgs boson mass in the 2J region for each of the contributing production processes.

shown in Table 53.

In calculating the final limits, we take into account systematic uncertainties on both the signal and background models we use to train our neural networks. Systematic uncertainties for the 2J region are summarized in Tables 54 and 55. Figure 56 shows the expected (based on 10000 pseudo-experiments) and observed limits obtained from the 2J region.

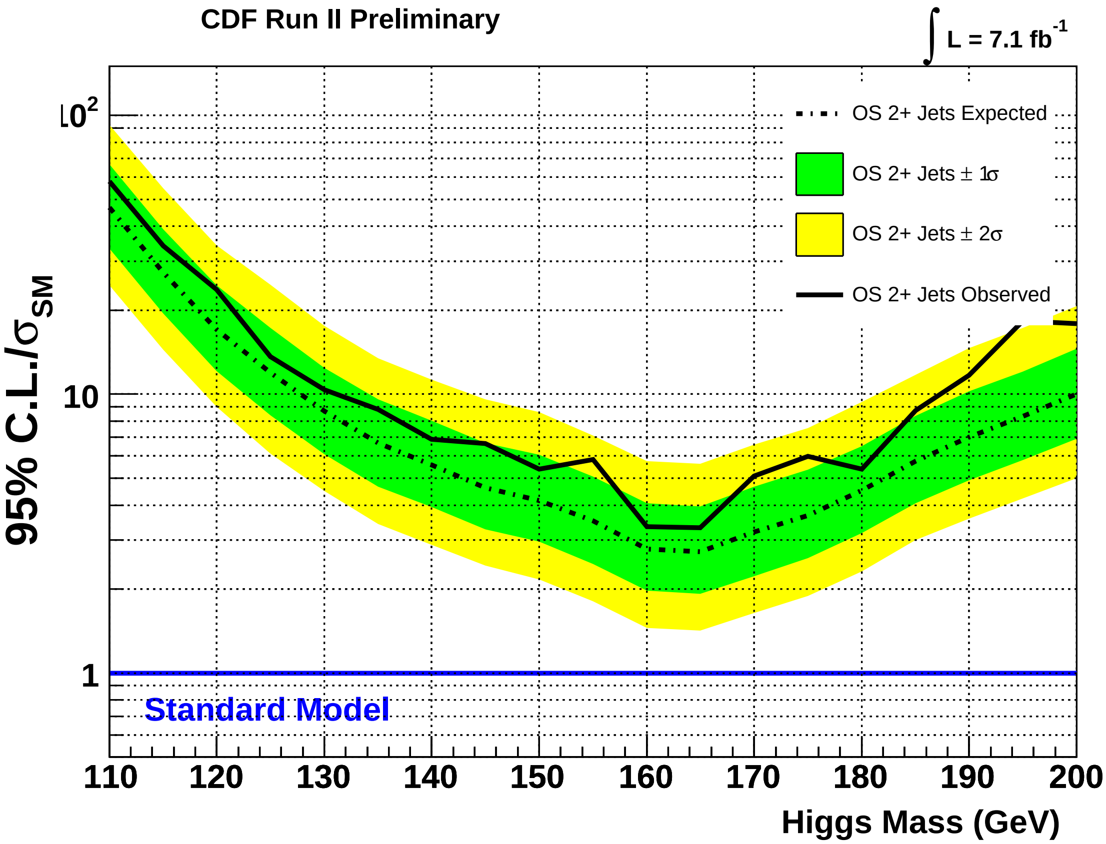

OS 2+ Jets	110	115	120	125	130	135	140	145	150	155	160	165	170	175	180	185	190	195	200
$-2\sigma/\sigma_{SM}$	24.64	14.42	9.02	6.12	4.49	3.43	2.88	2.42	2.17	1.81	1.45	1.42	1.64	1.89	2.31	2.99	3.57	4.23	4.99
$-1\sigma/\sigma_{SM}$	33.35	19.51	12.12	8.39	6.09	4.66	3.93	3.28	2.95	2.46	1.98	1.92	2.23	2.58	3.18	4.06	4.91	5.80	6.92
Median/σ_{SM}	**46.81**	**27.35**	**17.08**	**11.94**	**8.70**	**6.69**	**5.58**	**4.61**	**4.16**	**3.52**	**2.78**	**2.72**	**3.20**	**3.67**	**4.52**	**5.74**	**7.01**	**8.32**	**10.02**
$+1\sigma/\sigma_{SM}$	66.87	38.97	24.63	17.30	12.43	9.61	8.03	6.69	6.06	5.06	4.06	3.96	4.66	5.37	6.52	8.37	10.23	12.05	14.55
$+2\sigma/\sigma_{SM}$	92.62	54.81	34.26	24.67	17.63	13.44	11.30	9.60	8.63	7.11	5.75	5.62	6.60	7.57	9.40	11.76	14.65	17.26	20.68
Observed/σ_{SM}	**58.05**	**33.99**	**23.75**	**13.66**	**10.39**	**8.80**	**6.90**	**6.65**	**5.38**	**5.82**	**3.35**	**3.32**	**5.08**	**5.97**	**5.38**	**8.73**	**11.68**	**18.31**	**17.90**

Figure 56: $H \rightarrow WW$ sensitivity normalized to NNLL σ_{SM} calculation in the 2J region. In this region we consider potential signal contributions from gluon fusion, vector boson fusion, and associated production with either a W or Z boson.

Uncertainty Source	WW	WZ	ZZ	$t\bar{t}$	DY	$W\gamma$	W+jet
Cross Section							
Total	*6.0%*	*6.0%*	*6.0%*	10.0%			
Acceptance							
Scale (jets)	-8.2%						
PDF Model (jets)	4.2%						
Higher-order Diagrams		*10.0%*	*10.0%*	10.0%		10.0%	
Jet Energy Scale	*-14.8%*	*-12.9%*	*-12.1%*	*-1.7%*	*-29.2%*	*-22.0%*	
Missing E_T Modeling					25.5%		
$W\gamma$ Modeling						10.0%	
b-tag Veto				3.2%			
Jet Fake Rates							28.0%
Luminosity	*7.3%*	*7.3%*	*7.3%*	*7.3%*	*7.3%*		

Table 54: Systematics table for 2J region background processes. Cross section systematics are correlated for the diboson processes (shown in italic font) but uncorrelated between all other processes. Scale (jets), PDF Model (jets), and Jet Energy Scale systematics are anticorrelated between the 0, 1, and 2+ jet bins, as these systematics cause events to fluctuate between jet bins.

Uncertainty Source	$gg \to H$	WH	ZH	VBF
Cross Section				
Scale	67.5%			
PDF Model	29.7%			
Total		*5.0%*	*5.0%*	10.0%
Acceptance				
Scale (leptons)	3.1%			
Scale (jets)	-6.8%			
PDF Model (leptons)	4.8%			
PDF Model (jets)	-12.3%			
EWK Higher-order Diagrams		*10.0%*	*10.0%*	*10.0%*
Jet Energy Scale	*-17.0%*	*-4.0%*	*-2.3%*	*-4.0%*
Luminosity	*7.3%*	*7.3%*	*7.3%*	*7.3%*

Table 55: Systematics table for 2J region signal processes. Cross section systematics are uncorrelated between the signal processes. Higher-order diagrams for the VH and VBF processes, shown in italic font, are correlated among each other but uncorrelated from background processes. The Scale (jets) and PDF Model (jets) systematics for $gg \to H$ are anticorrelated between the 0, 1, and 2+ jet bins, as these systematics cause events to fluctuate between jet bins.

11 Low $M_{\ell\ell}$ Analysis

The three opposite-sign searches previously described all require a dilepton mass $M_{\ell\ell} > 16$ GeV/c^2. However, due the spin correlation in Higgs decay which causes the leptons to be close together (small ΔR), there is potentially a large amount of signal in the region with low $M_{\ell\ell}$. Due to the kinematic constraints imposed on events with $M_{\ell\ell} < 16$ GeV/c^2, we look at these events as a separate search channel.

11.1 Event Selection

For this search channel, the selection requirements are identical to those in the opposite-sign dilepton signal region with zero jets except that the $M_{\ell\ell}$ requirement is reversed to become $M_{\ell\ell} < 16$ GeV/c^2. Also, in this region we accept events with both zero and one jets, but reject those with two or more jets. Additionally, events containing leptons with energies above 400 GeV are rejected.

Modeling of the backgrounds is done using the Monte Carlo samples described in Section 5. For this region only, we use the low $M_{\ell\ell}$ Drell-Yan samples. This has little effect on the signal region; the high $\not{E}_{T spec}$ requirement removes most low-mass DY events. Using these samples does improve modeling in the low-$\not{E}_{T spec}$ control region described below. The dominant background in the signal region and the control regions is from $W\gamma$, in which one real lepton comes from the decay of the W and the other is a radiated photon which either converts to an e^-e^+ pair or is misidentified as an electron if a random track can be associated with the energy deposited in the calorimeter. The other main background is from W+jet events, although this contribution is much smaller, accounting for ~10% of the expected background in the signal and control regions even after correcting for the non-triggerable fake rates shown in Tables 27 and 28. The WW background is much reduced, but due to the kinematic restrictions, the WW that remains looks very similar to the $H \rightarrow WW$ signal. An important part of this search is the fact that the dominant background, $W\gamma$, can be measured in a control region as shown below.

11.2 Low $M_{\ell\ell}$ Control Regions

Two extremely powerful control regions are used for this part of the analysis. For $W\gamma$ events, the charge of the lepton reconstructed from conversion events is arbitrary. Thus, the $W\gamma$ background looks the same kinematically for opposite-sign and same-sign dilepton events. This suggests that using same-sign events as a control region would provide an excellent measure of the $W\gamma$ background, and this indeed turns out to be the case.

The second control region addresses the concern of unmodelled backgrounds. For low values of $M_{\ell\ell}$ there may be a contribution from backgrounds considered negligible in the other regions, such as low-mass Drell-Yan or resonant and nonresonant b-quark decays (J/Ψ, Υ). It is shown in Section 11.2.2 that such backgrounds do appear when the $\not{E}_{T spec}$

requirement is reversed, and in Section 11.2.3 this control region is used to estimate the possible contribution of unmodelled backgrounds to the search region.

11.2.1 Low $M_{\ell\ell}$ Same-Sign Control Region

The low $M_{\ell\ell}$ same-sign control region is selected with the same requirements as the low $M_{\ell\ell}$ signal region, except that the leptons have the same charge instead of opposite charge. The predicted contributions of each background are shown in Table 56. As expected, the $W \to \ell\gamma$ events dominate the sample, contributing 87% while fakes contribute another 11%. The remaining backgrounds contribute a negligible amount to events in this region, and there are no expected Higgs boson events. There are also no events arising in the $\mu\mu$ channel. The $W \to e\gamma$ channel has contributions in the ee channel where a conversion electron has paired with the electron from the W, but not the $e\mu$ channel since there is no source of conversion muons. The crack tracks show a contribution since they are sometimes electrons. For the $W \to \mu\gamma$ channel, one sees no contribution from ee but the $e\mu$ channel dominates since a conversion electron from the photon pairs with the muon from the W decay.

We use this control region to determine a normalization scale factor for the $W\gamma$ background. First we subtract the non-$W\gamma$ contributions from the number of observed data events. With 91 same-sign events measured in the data, subtracting the total predicted number of non-$W\gamma$ events (13.9) gives 77.1 events remaining for the $W\gamma$ contribution. The error on the subtraction is dominated by the systematic uncertainty on the number of W+jet events, which is 18.7%. Since there are 11.4 fake events predicted, the error on the subtraction is ± 2.1 events. The statistical error is $\sqrt{N}$, where N is the number of events remaining after subtraction, or ± 8.7 events. Adding these two uncertainties in quadrature gives a total error on the number of $W\gamma$ of 9.0 events. The number of predicted $W\gamma$ events is 89.1. Thus the correction is $77.1/89.1 = 0.87$ with an error of $9.0/89.1 = 0.10$, or 10%. This $W\gamma$ scale factor is applied to the $W\gamma$ prediction in all search channels of this analysis. Figures 57 through 59 show the excellent agreement in this control region after applying the scale factor.

Category	WW	WZ	ZZ	$t\bar{t}$	DY	$W\gamma$	W+jets	Total	Data
TCE TCE	0.0	0.0	0.0	0.0	0.0	0.0	0.0	0.0	0.0
TCE LBE	0.0	0.0	0.0	0.0	0.0	0.0	0.0	0.0	0.0
TCE PHX	0.0	0.0	0.0	0.0	0.0	0.0	0.0	0.0	0.0
TCE PLBE	0.0	0.0	0.0	0.0	0.0	0.0	0.0	0.0	0.0
LBE LBE	0.0	0.0	0.0	0.0	0.0	0.0	0.0	0.0	0.0
LBE PHX	0.0	0.0	0.0	0.0	0.0	0.0	0.0	0.0	0.0
LBE PLBE	0.0	0.0	0.0	0.0	0.0	0.0	0.0	0.0	0.0
PHX PHX	0.1	0.0	0.0	0.0	0.0	17.0	2.9	20.0	19.0
PHX PLBE	0.0	0.0	0.0	0.0	0.0	9.4	2.1	11.5	10.0
PLBE PLBE	0.0	0.0	0.0	0.0	0.0	1.4	0.4	1.8	5.0
TCEni TCEni	0.0	0.1	0.0	0.0	1.4	21.0	0.6	23.2	33.0
TCEni LBEni	0.0	0.0	0.0	0.0	0.0	11.2	1.1	12.4	15.0
TCEni PHXni	0.0	0.0	0.0	0.0	0.0	0.0	0.0	0.0	0.0
TCEni PLBEni	0.0	0.0	0.0	0.0	0.0	0.0	0.0	0.0	0.0
LBEni LBEni	0.0	0.0	0.0	0.0	0.0	3.0	0.4	3.4	4.0
LBEni PHXni	0.0	0.0	0.0	0.0	0.0	0.0	0.0	0.0	0.0
LBEni PLBEni	0.0	0.0	0.0	0.0	0.0	0.0	0.0	0.0	0.0
PHXni PHXni	0.0	0.0	0.0	0.0	0.0	0.0	0.0	0.0	0.0
PHXni PLBEni	0.0	0.0	0.0	0.0	0.0	0.0	0.0	0.0	0.0
PLBEni PLBEni	0.0	0.0	0.0	0.0	0.0	0.0	0.0	0.0	0.0
TCEni PHX	0.0	0.0	0.0	0.0	0.1	6.7	0.5	7.3	18.0
TCEni PLBE	0.0	0.0	0.0	0.0	0.0	1.9	0.1	2.0	3.0
LBEni PHX	0.0	0.0	0.0	0.0	0.0	2.0	0.7	2.6	5.0
LBEni PLBE	0.0	0.0	0.0	0.0	0.0	0.6	0.2	0.8	2.0
TCE CMUP	0.0	0.0	0.0	0.0	0.0	0.0	0.0	0.0	0.0
TCE CMU	0.0	0.0	0.0	0.0	0.0	0.0	0.0	0.0	0.0
TCE CMP	0.0	0.0	0.0	0.0	0.0	0.0	0.0	0.0	0.0
TCE CMX	0.0	0.0	0.0	0.0	0.0	0.0	0.0	0.0	0.0
TCE CMXMsKs	0.0	0.0	0.0	0.0	0.0	0.0	0.0	0.0	0.0
TCE BMU	0.0	0.0	0.0	0.0	0.0	0.0	0.0	0.0	0.0
TCE CMIOCES	0.0	0.0	0.0	0.0	0.0	0.0	0.0	0.0	0.0
TCE CMIOPES	0.0	0.0	0.0	0.0	0.0	0.0	0.0	0.0	0.0
LBE CMUP	0.0	0.0	0.0	0.0	0.0	0.0	0.0	0.0	0.0
LBE CMU	0.0	0.0	0.0	0.0	0.0	0.0	0.0	0.0	0.0
LBE CMP	0.0	0.0	0.0	0.0	0.0	0.0	0.0	0.0	0.0
LBE CMX	0.0	0.0	0.0	0.0	0.0	0.0	0.0	0.0	0.0
LBE CMXMsKs	0.0	0.0	0.0	0.0	0.0	0.0	0.0	0.0	0.0
LBE BMU	0.0	0.0	0.0	0.0	0.0	0.0	0.0	0.0	0.0
LBE CMIOCES	0.0	0.0	0.0	0.0	0.0	0.0	0.0	0.0	0.0
LBE CMIOPES	0.0	0.0	0.0	0.0	0.0	0.0	0.0	0.0	0.0
PHX CMUP	0.0	0.0	0.0	0.0	0.0	0.0	0.0	0.0	0.0
PHX CMU	0.0	0.0	0.0	0.0	0.0	0.0	0.0	0.0	0.0
PHX CMP	0.0	0.0	0.0	0.0	0.0	0.0	0.0	0.0	0.0
PHX CMX	0.0	0.0	0.0	0.0	0.0	0.0	0.0	0.0	0.0
PHX CMXMsKs	0.0	0.0	0.0	0.0	0.0	0.0	0.0	0.0	0.0
PHX BMU	0.0	0.0	0.0	0.0	0.1	0.8	0.0	0.9	1.0
PHX CMIOCES	0.0	0.0	0.0	0.0	0.0	0.0	0.0	0.0	0.0
PHX CMIOPES	0.0	0.0	0.0	0.0	0.2	1.8	0.7	2.7	3.0
PLBE CMUP	0.0	0.0	0.0	0.0	0.0	0.0	0.0	0.0	0.0
PLBE CMU	0.0	0.0	0.0	0.0	0.0	0.0	0.0	0.0	0.0
PLBE CMP	0.0	0.0	0.0	0.0	0.0	0.0	0.0	0.0	0.0
PLBE CMX	0.0	0.0	0.0	0.0	0.0	0.0	0.0	0.0	0.0

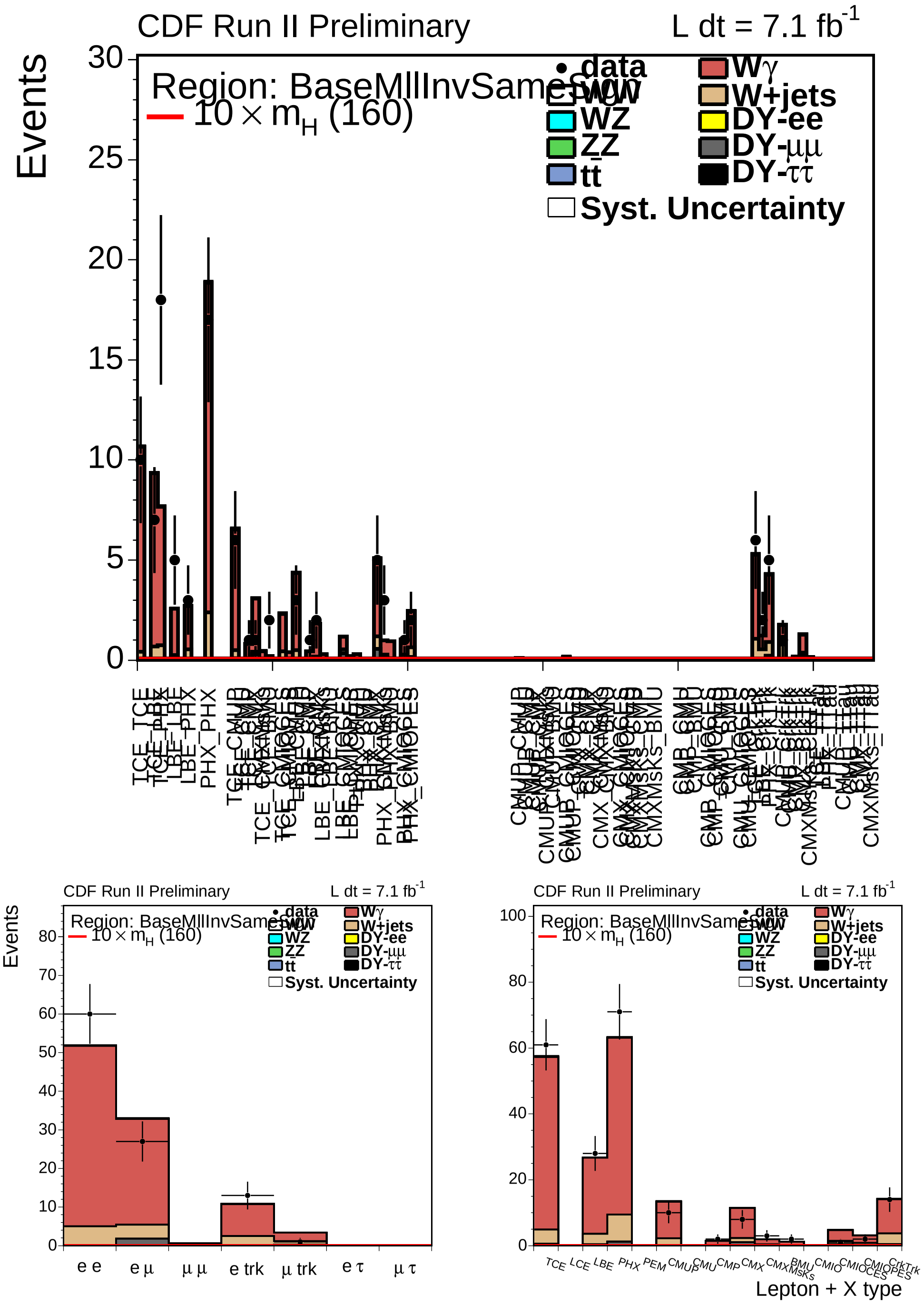

Figure 57: Signal and background in the low $M_{\ell\ell}$ same-sign dilepton control region, after the $W\gamma$ correction.

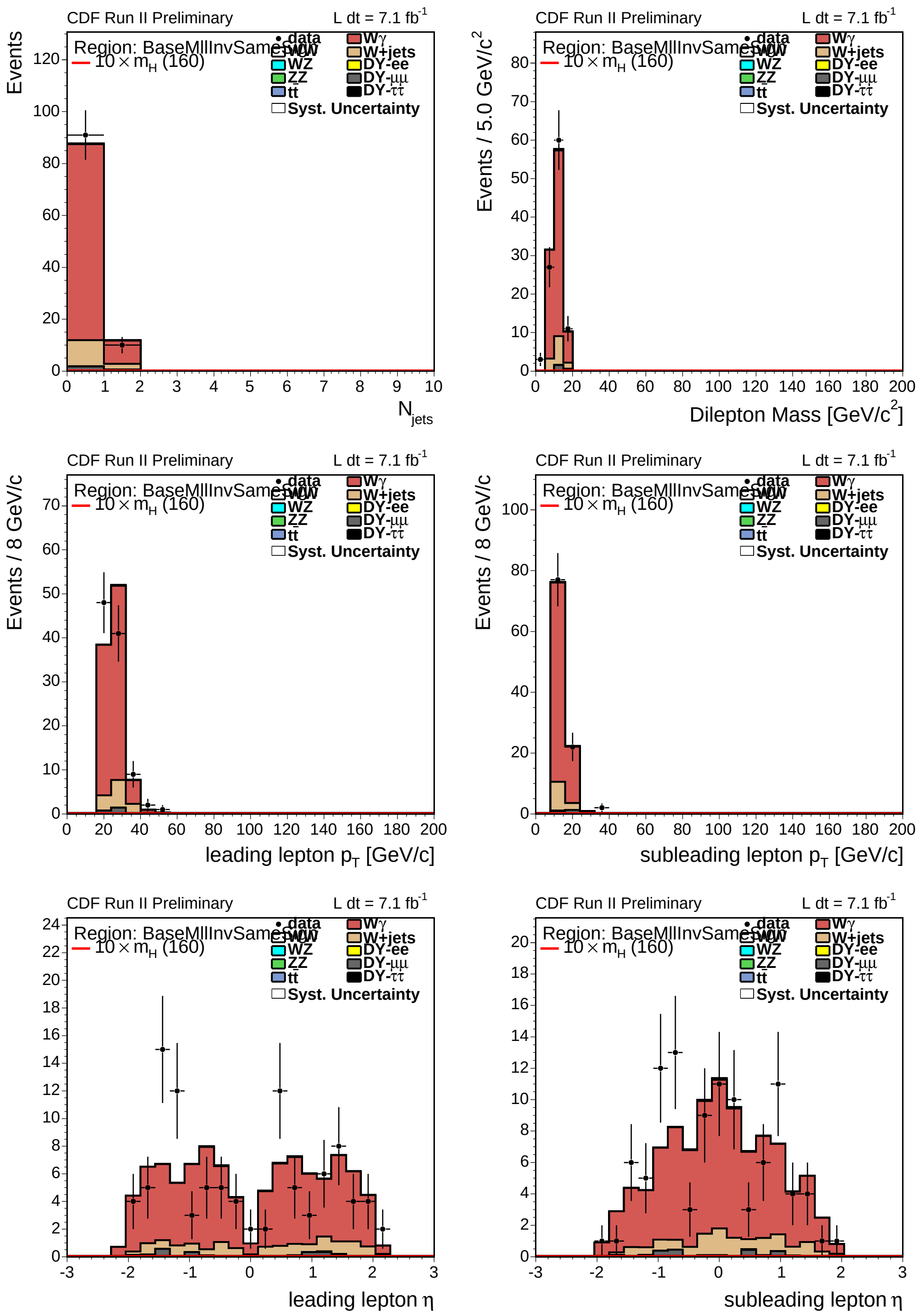

Figure 58: Signal and background in the low $M_{\ell\ell}$ same-sign dilepton control region, after the $W\gamma$ correction.

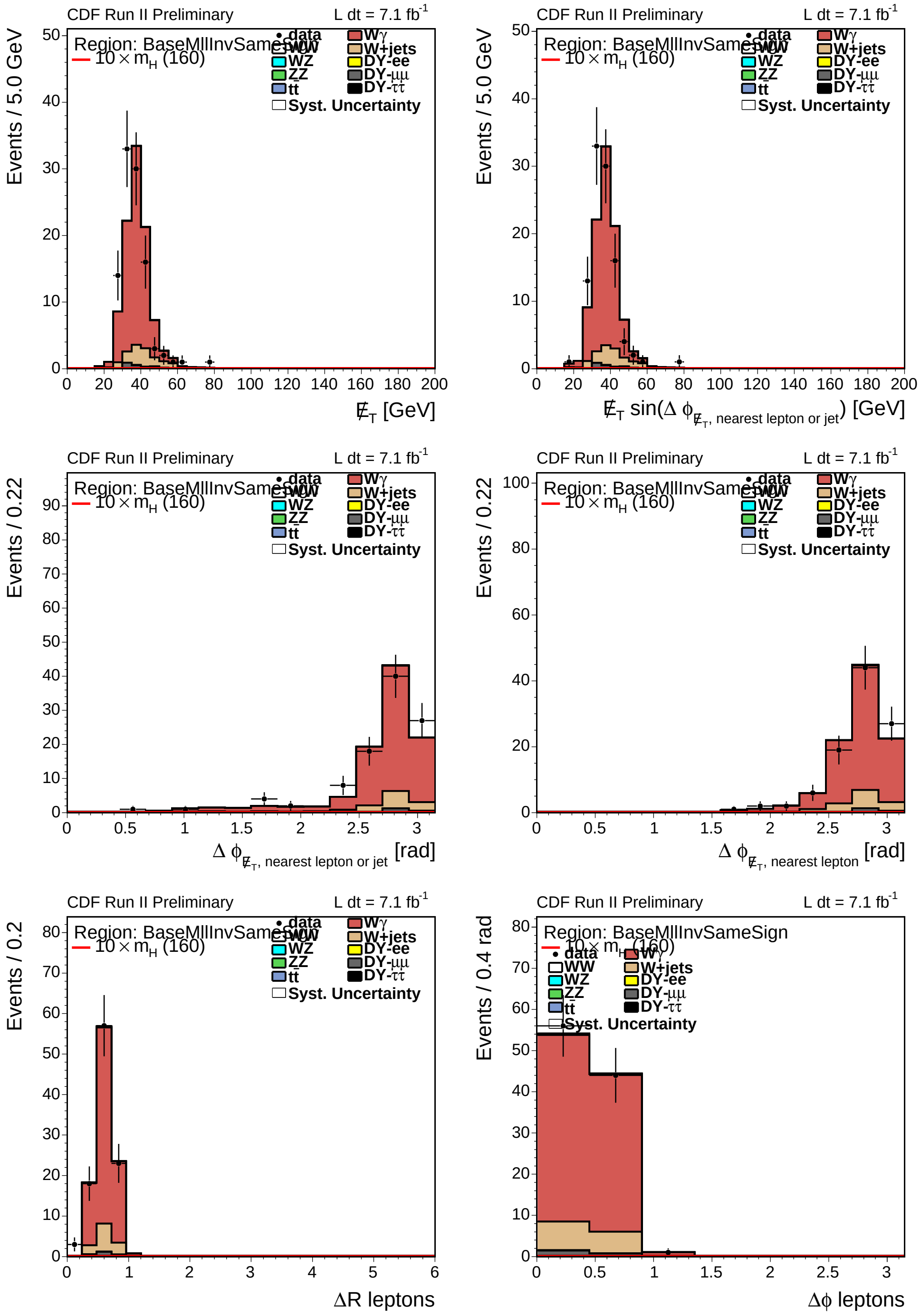

Figure 59: Signal and background in the low $M_{\ell\ell}$ same-sign dilepton control region, after the $W\gamma$ correction.

11.2.2 Low $M_{\ell\ell}$ Low $\not\!\!E_{Tspec}$ Control Region

A second orthogonal region provides a control of backgrounds that are more difficult to model. The low $M_{\ell\ell}$ region potentially has low-mass Drell-Yan as an important background in addition to contamination from J/Ψ or Υ resonances. For the portion of the Drell-Yan and dilepton resonances that are unmodelled, the characteristics are obtained from the data in this control region.

The low $M_{\ell\ell}$ low $\not\!\!E_{Tspec}$ control region is selected with the same requirements as the low $M_{\ell\ell}$ signal region, except that the $\not\!\!E_{Tspec}$ requirement has been reversed. In this region we require $\not\!\!E_{Tspec} < 15$ GeV for $e\mu$ candidates and $\not\!\!E_{Tspec} < 25$ GeV for all other candidates. The predicted contributions of each background are shown in Table 57. Events in this control region are compared to the MC prediction in Figure 60. We see a large excess in data over the prediction, which has $W\gamma$ and W+jets as the dominant contributions. The data populating this region are primarily same-flavor dilepton events, with no contribution from $e\mu$ candidates. One would expect to see mixed flavor events if the background were due to sequential b decays.

The most likely source of the unmodelled background is thus low mass Drell-Yan events, which are being removed by the $\not\!\!E_{Tspec}$ cut in the signal region. The Drell-Yan computation was done in two pieces, one with the CKIN parameter that specifies the propagator mass to be above 20 GeV/c^2 and the other, referred to as the Drell-Yan low mass sample, with the parameter set to be between 10 and 20 GeV/c^2. The Drell-Yan prediction in this control region comes almost entirely from the low mass samples. This suggests that ideally an even lower cut should be used and that the upsilon resonance region should be modelled in order to account for all the currently unmodelled background. For the analysis at hand, the control region is used to estimate the unmodelled background contribution and its potential signal-like behaviour as shown in Section 11.2.3.

11.2.3 Unmodelled background rates

The amount of the unmodelled background that may remain in the signal region is estimated by extrapolating the $\not\!\!E_{Tspec}$ distribution from below the $\not\!\!E_{Tspec}$ cut to the region above. This check was performed on 4.8 fb^{-1} of data [2], and is reproduced here.

To investigate this possible contamination, the $\not\!\!E_{Tspec}$ spectrum is examined in the signal region before and after the $\not\!\!E_{Tspec}$ cut is applied. This is shown in Figure 60. It can be seen that the agreement after the $\not\!\!E_{Tspec}$ cut is significantly better than before the cut is applied. The $\not\!\!E_{Tspec}$ cut was also released for the same-sign control region as shown in Figure 60. There is a significantly smaller contribution from unmodelled backgrounds in the same-sign sample.

The $\not\!\!E_{Tspec}$ distribution in the signal region was fit to an exponential in the region $0 \leq \not\!\!E_{Tspec} \leq 25$ GeV. The resulting fit is shown in Figure 61. The fit was repeated with the known background subtracted from the data and this is also shown. The fit was extrapolated (as indicated by the red part of the curve) to the signal region, $\not\!\!E_{Tspec} > 25$

Category	WW	WZ	ZZ	$t\bar{t}$	DY	$W\gamma$	W+jets	Total	Data
TCE TCE	0.0	0.0	0.0	0.0	0.0	0.0	0.0	0.0	0.0
TCE LBE	0.0	0.0	0.0	0.0	0.0	0.0	0.0	0.0	0.0
TCE PHX	0.0	0.0	0.0	0.0	0.0	0.0	0.0	0.0	0.0
TCE PLBE	0.0	0.0	0.0	0.0	0.0	0.0	0.0	0.0	0.0
LBE LBE	0.0	0.0	0.0	0.0	0.0	0.0	0.0	0.0	0.0
LBE PHX	0.0	0.0	0.0	0.0	0.0	0.0	0.0	0.0	0.0
LBE PLBE	0.0	0.0	0.0	0.0	0.0	0.0	0.0	0.0	0.0
PHX PHX	0.0	0.0	0.0	0.0	0.2	0.9	2.1	3.2	7.0
PHX PLBE	0.0	0.0	0.0	0.0	0.0	0.5	0.4	0.9	2.0
PLBE PLBE	-0.0	0.0	0.0	0.0	0.0	0.1	0.0	0.1	1.0
TCEni TCEni	0.1	0.0	0.0	0.0	0.0	1.2	1.0	2.5	84.0
TCEni LBEni	0.0	0.0	0.0	0.0	0.1	0.7	1.8	2.6	36.0
TCEni PHXni	0.0	0.0	0.0	0.0	0.0	0.0	0.0	0.0	0.0
TCEni PLBEni	0.0	0.0	0.0	0.0	0.0	0.0	0.0	0.0	0.0
LBEni LBEni	0.0	0.0	0.0	0.0	0.0	0.4	0.5	0.8	9.0
LBEni PHXni	0.0	0.0	0.0	0.0	0.0	0.0	0.0	0.0	0.0
LBEni PLBEni	0.0	0.0	0.0	0.0	0.0	0.0	0.0	0.0	0.0
PHXni PHXni	0.0	0.0	0.0	0.0	0.0	0.0	0.0	0.0	0.0
PHXni PLBEni	0.0	0.0	0.0	0.0	0.0	0.0	0.0	0.0	0.0
PLBEni PLBEni	0.0	0.0	0.0	0.0	0.0	0.0	0.0	0.0	0.0
TCEni PHX	0.0	0.0	0.0	0.0	0.0	0.4	1.8	2.2	4.0
TCEni PLBE	0.0	0.0	0.0	0.0	0.0	0.1	0.1	0.2	3.0
LBEni PHX	0.0	0.0	0.0	0.0	0.0	0.1	0.1	0.2	4.0
LBEni PLBE	0.0	0.0	0.0	0.0	0.0	0.0	0.0	0.0	0.0
TCE CMUP	0.0	0.0	0.0	0.0	0.0	0.0	0.0	0.0	0.0
TCE CMU	0.0	0.0	0.0	0.0	0.0	0.0	0.0	0.0	0.0
TCE CMP	0.0	0.0	0.0	0.0	0.0	0.0	0.0	0.0	0.0
TCE CMX	0.0	0.0	0.0	0.0	0.0	0.0	0.0	0.0	0.0
TCE CMXMsKs	0.0	0.0	0.0	0.0	0.0	0.0	0.0	0.0	0.0
TCE BMU	0.0	0.0	0.0	0.0	0.0	0.0	0.0	0.0	0.0
TCE CMIOCES	0.0	0.0	0.0	0.0	0.0	0.0	0.0	0.0	0.0
TCE CMIOPES	0.0	0.0	0.0	0.0	0.0	0.0	0.0	0.0	0.0
LBE CMUP	0.0	0.0	0.0	0.0	0.0	0.0	0.0	0.0	0.0
LBE CMU	0.0	0.0	0.0	0.0	0.0	0.0	0.0	0.0	0.0
LBE CMP	0.0	0.0	0.0	0.0	0.0	0.0	0.0	0.0	0.0
LBE CMX	0.0	0.0	0.0	0.0	0.0	0.0	0.0	0.0	0.0
LBE CMXMsKs	0.0	0.0	0.0	0.0	0.0	0.0	0.0	0.0	0.0
LBE BMU	0.0	0.0	0.0	0.0	0.0	0.0	0.0	0.0	0.0
LBE CMIOCES	0.0	0.0	0.0	0.0	0.0	0.0	0.0	0.0	0.0
LBE CMIOPES	0.0	0.0	0.0	0.0	0.0	0.0	0.0	0.0	0.0
PHX CMUP	0.0	0.0	0.0	0.0	0.0	0.0	0.0	0.0	0.0
PHX CMU	0.0	0.0	0.0	0.0	0.0	0.0	0.0	0.0	0.0
PHX CMP	0.0	0.0	0.0	0.0	0.0	0.0	0.0	0.0	0.0
PHX CMX	0.0	0.0	0.0	0.0	0.0	0.0	0.0	0.0	0.0
PHX CMXMsKs	0.0	0.0	0.0	0.0	0.0	0.0	0.0	0.0	0.0
PHX BMU	0.0	0.0	0.0	0.0	0.0	0.0	0.0	0.0	0.0
PHX CMIOCES	0.0	0.0	0.0	0.0	0.0	0.0	0.0	0.0	0.0
PHX CMIOPES	0.0	0.0	0.0	0.0	0.0	0.0	0.0	0.0	0.0
PLBE CMUP	0.0	0.0	0.0	0.0	0.0	0.0	0.0	0.0	0.0
PLBE CMU	0.0	0.0	0.0	0.0	0.0	0.0	0.0	0.0	0.0
PLBE CMP	0.0	0.0	0.0	0.0	0.0	0.0	0.0	0.0	0.0
PLBE CMX	0.0	0.0	0.0	0.0	0.0	0.0	0.0	0.0	0.0

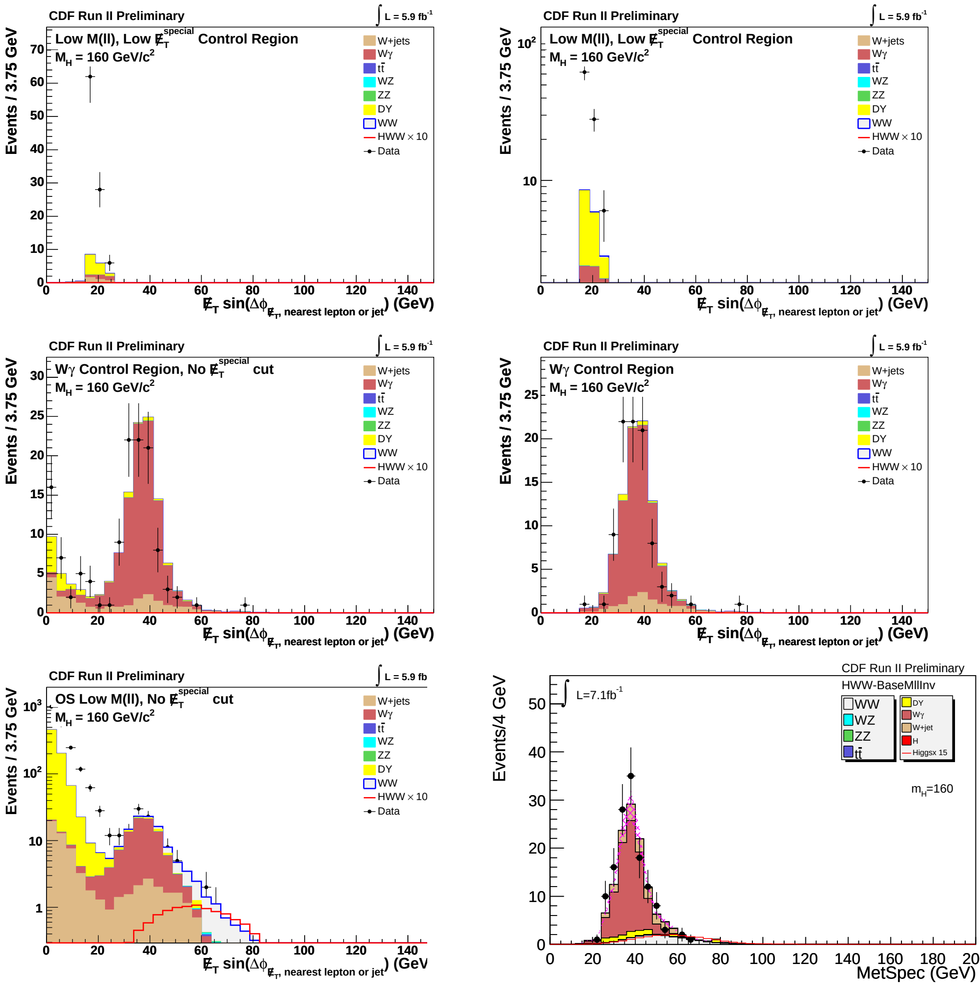

Figure 60: $\not{E}_{Tspec}$ distribution in the low-$M_{\ell\ell}$ low-$\not{E}_{Tspec}$ control region for data and Monte Carlo on a linear (top left) and logarithmic (top right) scale. $\not{E}_{Tspec}$ distribution in the low-$M_{\ell\ell}$ same-sign control region for data and Monte Carlo without (middle left) and with (middle right) the $\not{E}_{Tspec}$ cuts. $\not{E}_{Tspec}$ distribution in the low-$M_{\ell\ell}$ signal region for data and Monte Carlo without (bottom left) and with (bottom right) the $\not{E}_{Tspec}$ cuts.

$\not\!\!E_{Tspec}$ Fit Range (GeV)	Events with $\not\!\!E_{Tspec} > 25$ GeV/c^2	
	No Bkg Sub (Events)	Bkg Sub (Events)
0-15	32	49
10-25	22	18
5-20	21	25
5-15	21	31

Table 58: Variation of computation of the nonmodelled background yield with fit range in $\not\!\!E_{Tspec}$.

GeV. The data for this region are shown in Figure 61 both without and with the known background subtracted. The fitted function was evaluated at each bin center and summed to obtain the number of events in the signal region. An estimate of 19 events is obtained. The exercise was repeated for three other ranges of $\not\!\!E_{Tspec}$. The variation in the results is summarized in Table 58 and from this we obtain an error on the estimate of 5 events based on half the maximum variation.

The low-$\not\!\!E_{Tspec}$ control sample is used to estimate the dynamics of the background. The shape of the neural network distribution for the unmodelled background is extracted from this control region, which is defined by events having a $\not\!\!E_{Tspec}$ value in a band just below the $\not\!\!E_{Tspec}$ cut. It is shown in Fig. 69 that the unmodelled events populate low values of the neural net score distribution based on a neural net trained on Monte Carlo events passing the signal selection.

11.3 Low $M_{\ell\ell}$ Event Selection

The background expectation and observed yield for the $M_{\ell\ell} < 16$ GeV/c^2 opposite-sign dilepton signal region are shown in Table 59. The expected and observed kinematic distributions for these events are shown in Figures 62-64. We stack the backgrounds on top of each other, and then for comparison we overlay the contribution from a 160 GeV/c^2 Higgs boson with yields scaled up by a factor of 10. In addition, we calculate a confidence level for data versus background expectations on each plot. The confidence levels shown are for Poisson fluctuations and the KS test. The dominance of the $W\gamma$ events is very striking. The WW background is significantly smaller in this sample as is the W+jets. The rest of the backgrounds are negligible. The number of data events is consistent with the total background.

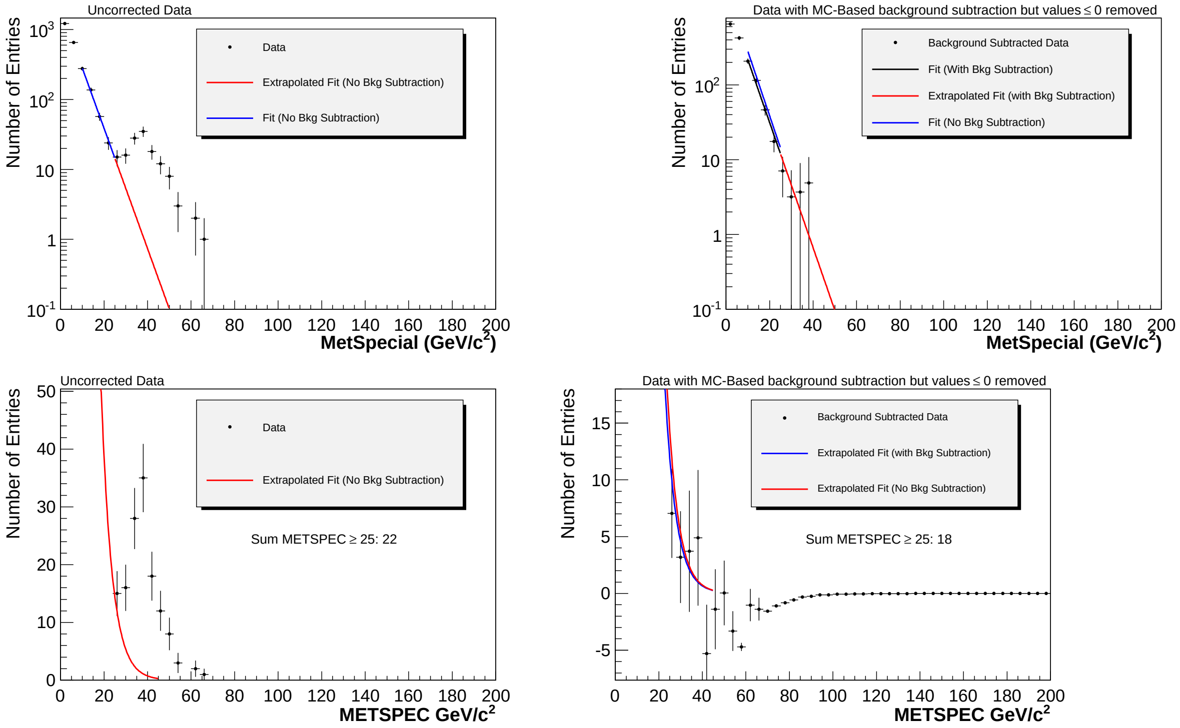

Figure 61: Fits to the $\not\!\!E_{Tspec}$ distribution in the low $M_{\ell\ell}$ signal region after removing the $\not\!\!E_{Tspec}$ cut. The fitted region corresponds to $10 \leq \not\!\!E_{Tspec} \leq 25$ GeV. The extrapolation of the curve into the signal region is indicated in red. The data used for the graphs on the left have no subtraction of known backgrounds while those on the right do have a background subtraction. The graphs on the top show the fit on a log scale over the entire $\not\!\!E_{Tspec}$ region. The graphs on the bottom show only data having $\not\!\!E_{Tspec} > 25$ GeV/c^2. Negative bins are set to zero in order to make the plot on a logarithmic scale.

Category	WW	WZ	ZZ	$t\bar{t}$	DY	$W\gamma$	W+jets	Total	Data
TCE TCE	0.0	0.0	0.0	0.0	0.0	0.0	0.0	0.0	0.0
TCE LBE	0.0	0.0	0.0	0.0	0.0	0.0	0.0	0.0	0.0
TCE PHX	0.0	0.0	0.0	0.0	0.0	0.0	0.0	0.0	0.0
TCE PLBE	0.0	0.0	0.0	0.0	0.0	0.0	0.0	0.0	0.0
LBE LBE	0.0	0.0	0.0	0.0	0.0	0.0	0.0	0.0	0.0
LBE PHX	0.0	0.0	0.0	0.0	0.0	0.0	0.0	0.0	0.0
LBE PLBE	0.0	0.0	0.0	0.0	0.0	0.0	0.0	0.0	0.0
PHX PHX	0.3	0.0	0.0	0.0	0.0	16.6	2.4	19.3	21.0
PHX PLBE	0.2	0.0	0.0	0.0	0.0	10.0	1.8	12.0	10.0
PLBE PLBE	0.0	0.0	0.0	0.0	0.0	1.5	0.3	1.9	4.0
TCEni TCEni	4.4	0.1	0.0	0.2	1.2	22.7	1.4	30.1	47.0
TCEni LBEni	1.2	0.0	0.0	0.1	0.1	11.3	2.6	15.3	18.0
TCEni PHXni	0.0	0.0	0.0	0.0	0.0	0.0	0.0	0.0	0.0
TCEni PLBEni	0.0	0.0	0.0	0.0	0.0	0.0	0.0	0.0	0.0
LBEni LBEni	0.2	0.0	0.0	0.0	0.0	1.8	0.9	2.9	8.0
LBEni PHXni	0.0	0.0	0.0	0.0	0.0	0.0	0.0	0.0	0.0
LBEni PLBEni	0.0	0.0	0.0	0.0	0.0	0.0	0.0	0.0	0.0
PHXni PHXni	0.0	0.0	0.0	0.0	0.0	0.0	0.0	0.0	0.0
PHXni PLBEni	0.0	0.0	0.0	0.0	0.0	0.0	0.0	0.0	0.0
PLBEni PLBEni	0.0	0.0	0.0	0.0	0.0	0.0	0.0	0.0	0.0
TCEni PHX	0.3	0.0	0.0	0.0	0.0	6.5	1.3	8.1	14.0
TCEni PLBE	0.1	0.0	0.0	0.0	0.0	1.9	0.3	2.4	1.0
LBEni PHX	0.1	0.0	0.0	0.0	0.0	2.4	0.8	3.3	3.0
LBEni PLBE	0.0	0.0	0.0	0.0	0.0	0.5	0.2	0.7	0.0
TCE CMUP	0.0	0.0	0.0	0.0	0.0	0.0	0.0	0.0	0.0
TCE CMU	0.0	0.0	0.0	0.0	0.0	0.0	0.0	0.0	0.0
TCE CMP	0.0	0.0	0.0	0.0	0.0	0.0	0.0	0.0	0.0
TCE CMX	0.0	0.0	0.0	0.0	0.0	0.0	0.0	0.0	0.0
TCE CMXMsKs	0.0	0.0	0.0	0.0	0.0	0.0	0.0	0.0	0.0
TCE BMU	0.0	0.0	0.0	0.0	0.0	0.0	0.0	0.0	0.0
TCE CMIOCES	0.0	0.0	0.0	0.0	0.0	0.0	0.0	0.0	0.0
TCE CMIOPES	0.0	0.0	0.0	0.0	0.0	0.0	0.0	0.0	0.0
LBE CMUP	0.0	0.0	0.0	0.0	0.0	0.0	0.0	0.0	0.0
LBE CMU	0.0	0.0	0.0	0.0	0.0	0.0	0.0	0.0	0.0
LBE CMP	0.0	0.0	0.0	0.0	0.0	0.0	0.0	0.0	0.0
LBE CMX	0.0	0.0	0.0	0.0	0.0	0.0	0.0	0.0	0.0
LBE CMXMsKs	0.0	0.0	0.0	0.0	0.0	0.0	0.0	0.0	0.0
LBE BMU	0.0	0.0	0.0	0.0	0.0	0.0	0.0	0.0	0.0
LBE CMIOCES	0.0	0.0	0.0	0.0	0.0	0.0	0.0	0.0	0.0
LBE CMIOPES	0.0	0.0	0.0	0.0	0.0	0.0	0.0	0.0	0.0
PHX CMUP	0.0	0.0	0.0	0.0	0.0	0.0	0.0	0.0	0.0
PHX CMU	0.0	0.0	0.0	0.0	0.0	0.0	0.0	0.0	0.0
PHX CMP	0.0	0.0	0.0	0.0	0.0	0.0	0.0	0.0	0.0
PHX CMX	0.0	0.0	0.0	0.0	0.0	0.0	0.0	0.0	0.0
PHX CMXMsKs	0.0	0.0	0.0	0.0	0.0	0.0	0.0	0.0	0.0
PHX BMU	0.1	0.0	0.0	0.0	0.1	0.8	0.0	1.0	4.0
PHX CMIOCES	0.0	0.0	0.0	0.0	0.0	0.0	0.0	0.0	0.0
PHX CMIOPES	0.1	0.0	0.0	0.0	0.4	2.0	0.4	2.8	2.0
PLBE CMUP	0.0	0.0	0.0	0.0	0.0	0.0	0.0	0.0	0.0
PLBE CMU	0.0	0.0	0.0	0.0	0.0	0.0	0.0	0.0	0.0
PLBE CMP	0.0	0.0	0.0	0.0	0.0	0.0	0.0	0.0	0.0
PLBE CMX	0.0	0.0	0.0	0.0	0.0	0.0	0.0	0.0	0.0

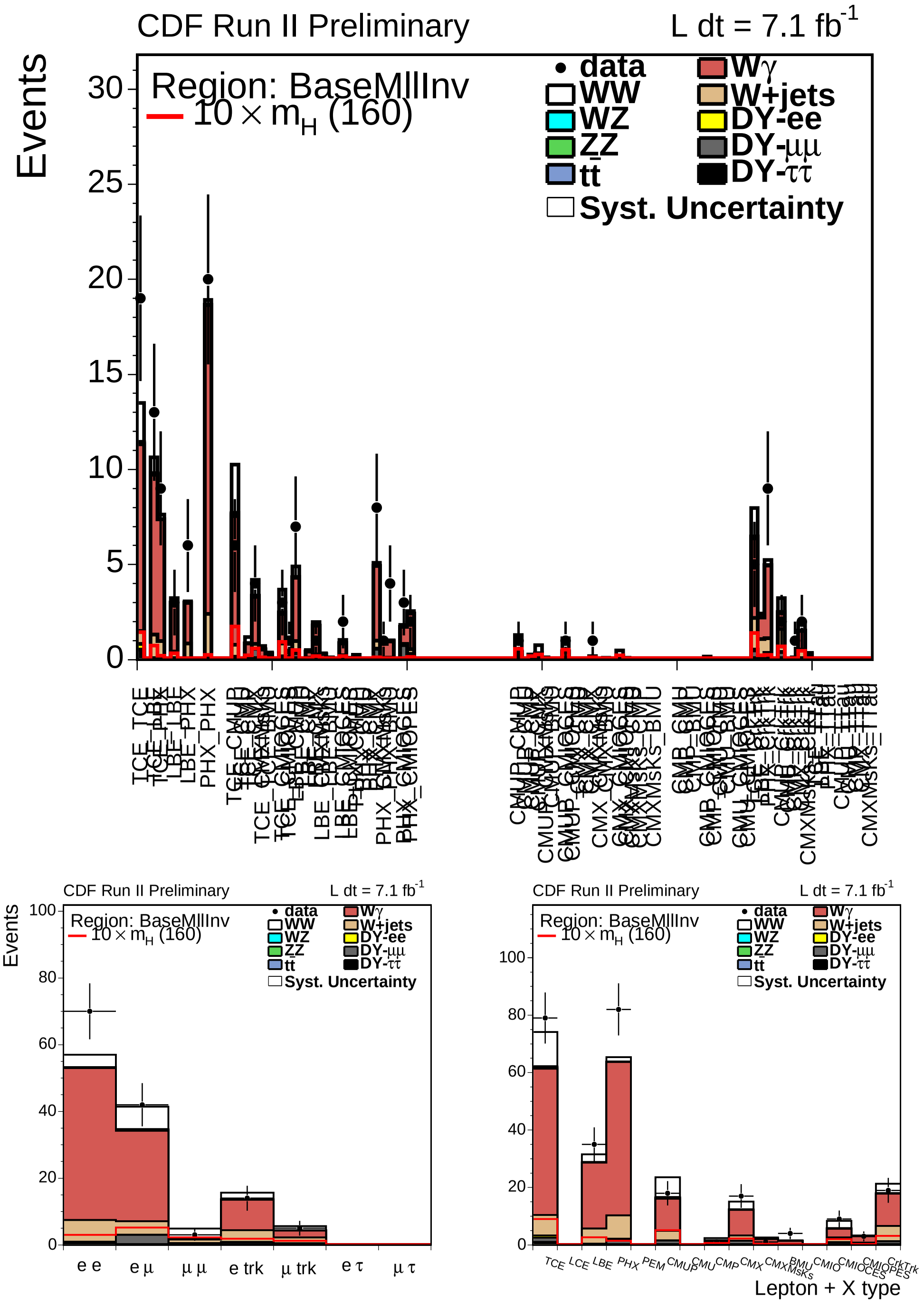

Figure 62: Signal and background in the low $M_{\ell\ell}$ same-sign dilepton control region.

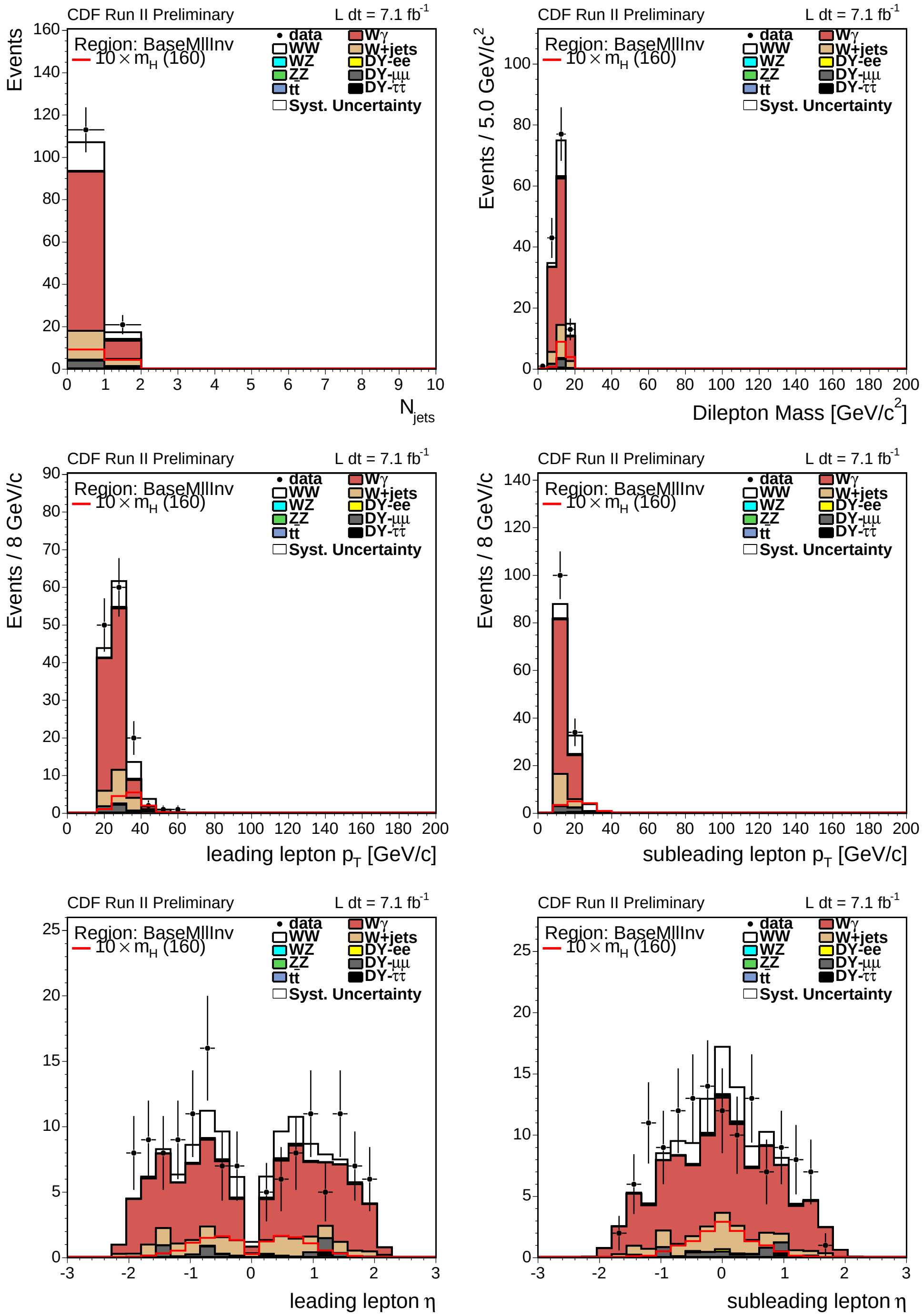

Figure 63: Signal and background in the low $M_{\ell\ell}$ same-sign dilepton control region.

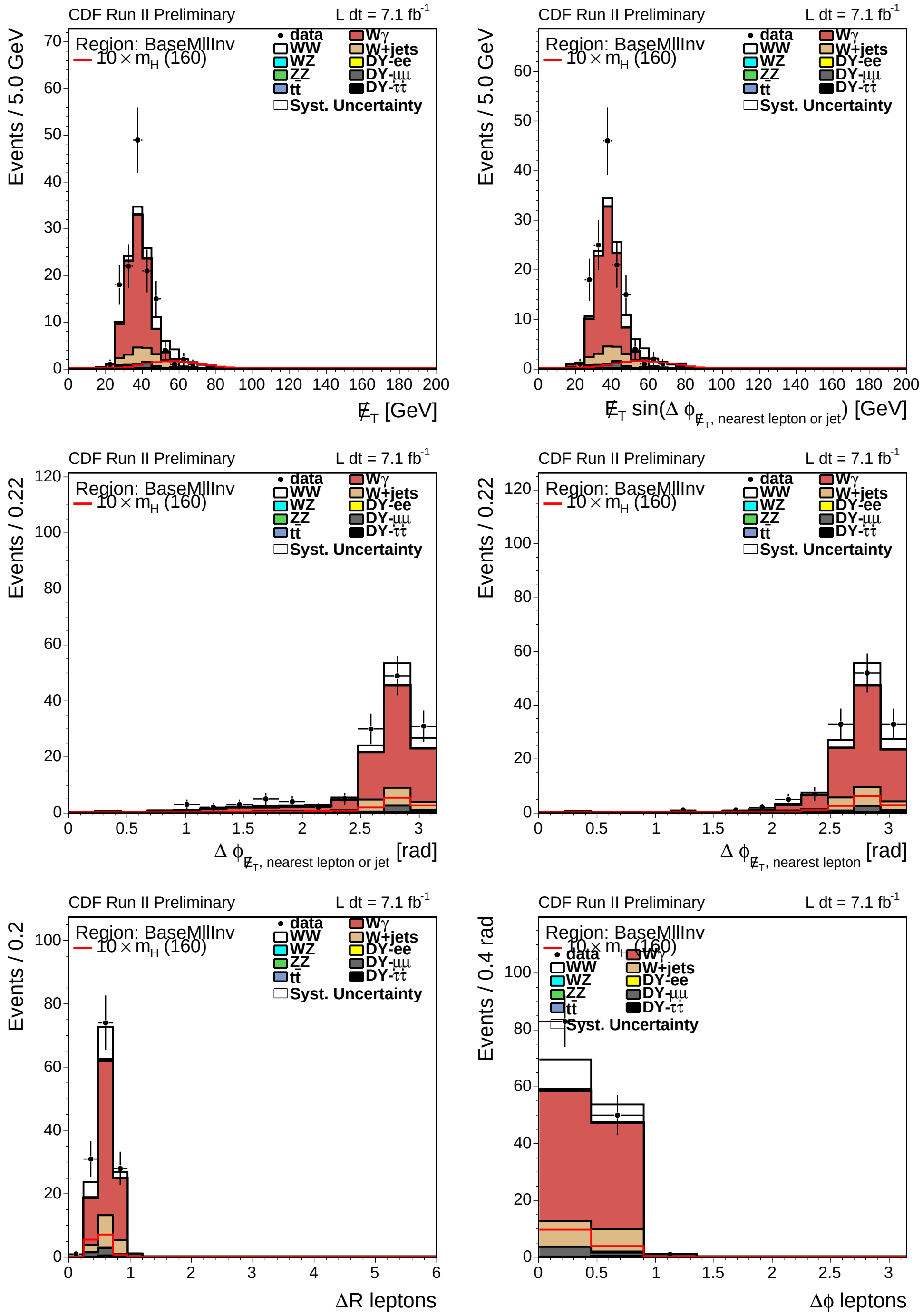

Figure 64: Signal and background in the low $M_{\ell\ell}$ same-sign dilepton control region.

Variable	Meaning
LepBPt	Lower-energy lepton p_T
LepAPt	Higher-energy lepton p_T
lep1_E	Higher-energy lepton energy
lep2_E	Lower-energy lepton energy
addEt	Scalar sum of the E_T of leptons and $\not\!\!E_T$
dPhiLepVSumMet	Azimuthal angle between the $\not\!\!E_T$ and the vector sum of the Lepton p_T
MetSigLeptonJets	$\not\!\!E_T$ significance with sum of energy over leptons and jets
MetSpec	$\not\!\!E_{Tspec} = \not\!\!E_T$ if $\Delta\phi$ ($\vec{\not\!\!E}_T$, l or j) $> \frac{\pi}{2}$ $\not\!\!E_{Tspec} = \not\!\!E_T$ $\sin(\Delta\phi$ ($\vec{\not\!\!E}_T$, l or j)) if $\Delta\phi$ ($\vec{\not\!\!E}_T$, l or j) $< \frac{\pi}{2}$
dRLeptons	Lepton separation in $\sqrt{(\Delta\eta)^2 + (\Delta\phi)^2}$
Ht	Scalar sum of the E_T of leptons and jets and the $\not\!\!E_T$
VSumJetLeptonsPt	Magnitude of the vector sum of p_T of the leptons and jet(s)
SumEtLeptonsJets	Scalar sum of the leptons and jet E_T
dPhiLeptons	Azimuthal angle between leptons

Table 60: Variables used in the neural network training listed in order of the importance as determined by the neural network for a Higgs of mass 160 GeV.

11.4 Analysis of Low $M_{\ell\ell}$ Opposite-Sign events

In this channel we rely on a neural network (NN) to discriminate signal from background using kinematic variables as inputs to the NN. Optimization and training of the neural network are done in the same manner as for the 0J case described in Section 8. For this channel, TMVA was used as a cross check and gives similar results. The 13 input variables are listed in Table 60. The observed distributions of each neural network input parameter compared with the distributions predicted by our background model are shown in Figure 65. For reference, we also include a hypothetical signal component for a Higgs boson with $m_H = 160$ GeV/c^2. It can be seen that the shape of the $W\gamma$ background is the same as that in the same-sign control region. Also, the WW and Higgs are distinguished from the $W\gamma$ background but have similar shapes, which results in a poor signal-to-background limit. Further training specifically against the WW background to exploit its differences from the signal could yield a better significance.

Templates are created for each neural network and used for calculating 95% CL limits with the MCLimit program [32]. Due to the low statistics in the low $M_{\ell\ell}$ region, we do not divide events into High S/B and Low S/B categories as is done for the other OS regions. Output templates for the trained neural network are shown in Figures 66-68.

As a check, the distribution of NN scores for events in the two control region are shown in Figure 69. The neural net is that trained in the signal region for $m_H = 160$ GeV/c^2.

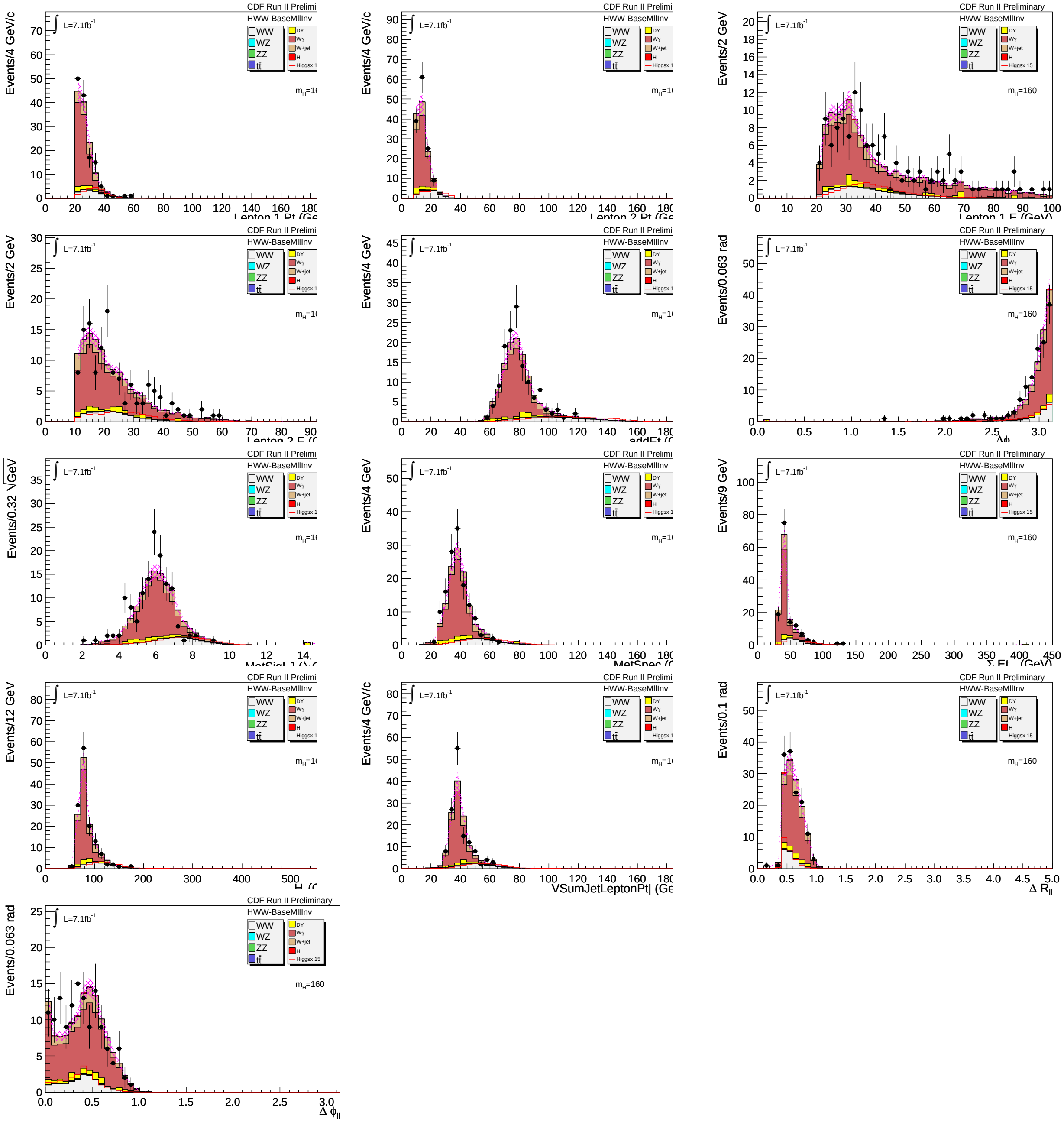

Figure 65: Neural network input variables for the signal region of opposite-sign low invariant mass dilepton events with zero or one jets in the final state. The Higgs boson signal is shown for a Higgs of mass $m_H = 160$ GeV/c^2 for the $gg \rightarrow H$ production mode.

Mass (GeV/c^2)	gg→H	WH	ZH	VBF
110	0.22	-	-	-
115	0.36	-	-	-
120	0.53	-	-	-
125	0.71	-	-	-
130	0.86	-	-	-
135	0.99	-	-	-
140	1.1	-	-	-
145	1.1	-	-	-
150	1.1	-	-	-
155	1.1	-	-	-
160	1.2	-	-	-
165	1	-	-	-
170	0.83	-	-	-
175	0.67	-	-	-
180	0.51	-	-	-
185	0.38	-	-	-
190	0.28	-	-	-
195	0.22	-	-	-
200	0.17	-	-	-

Table 61: Expected Higgs Signal yields as a function of the Higgs boson mass in the low $M_{\ell\ell}$ region for the $gg \to H$ production process.

The same-sign control region and its background are well-modelled, while the unmodelled events in the low-$\not{E}_{Tspec}$ control region are consistent with being background events.

The most significant signal contributions in the low $M_{\ell\ell}$ region are from $gg \to H$ production. Other production modes (associated production and vector boson fusion) contribute little and are not considered in this analysis. We evaluate the number of events expected from each production process as a function of the mass of the Higgs. These numbers are shown in Table 61.

In calculating the final limits, we take into account systematic uncertainties on both the signal and background models we use to train our neural networks. Since the low $M_{\ell\ell}$ sample is dominated by zero-jet events, the systematic uncertainties are derived from those in the opposite-sign zero jet region with the following modifications specific to this analysis. The systematic uncertainties are given in Table 62.

First, the uncertainty in the $W\gamma$ estimate is dominated by the statistics with a tiny correction for the subtraction of fakes in the same-sign control region as described in Section 11.2.1.

Second, the rate of events in the unmodelled background has been computed in Sec-

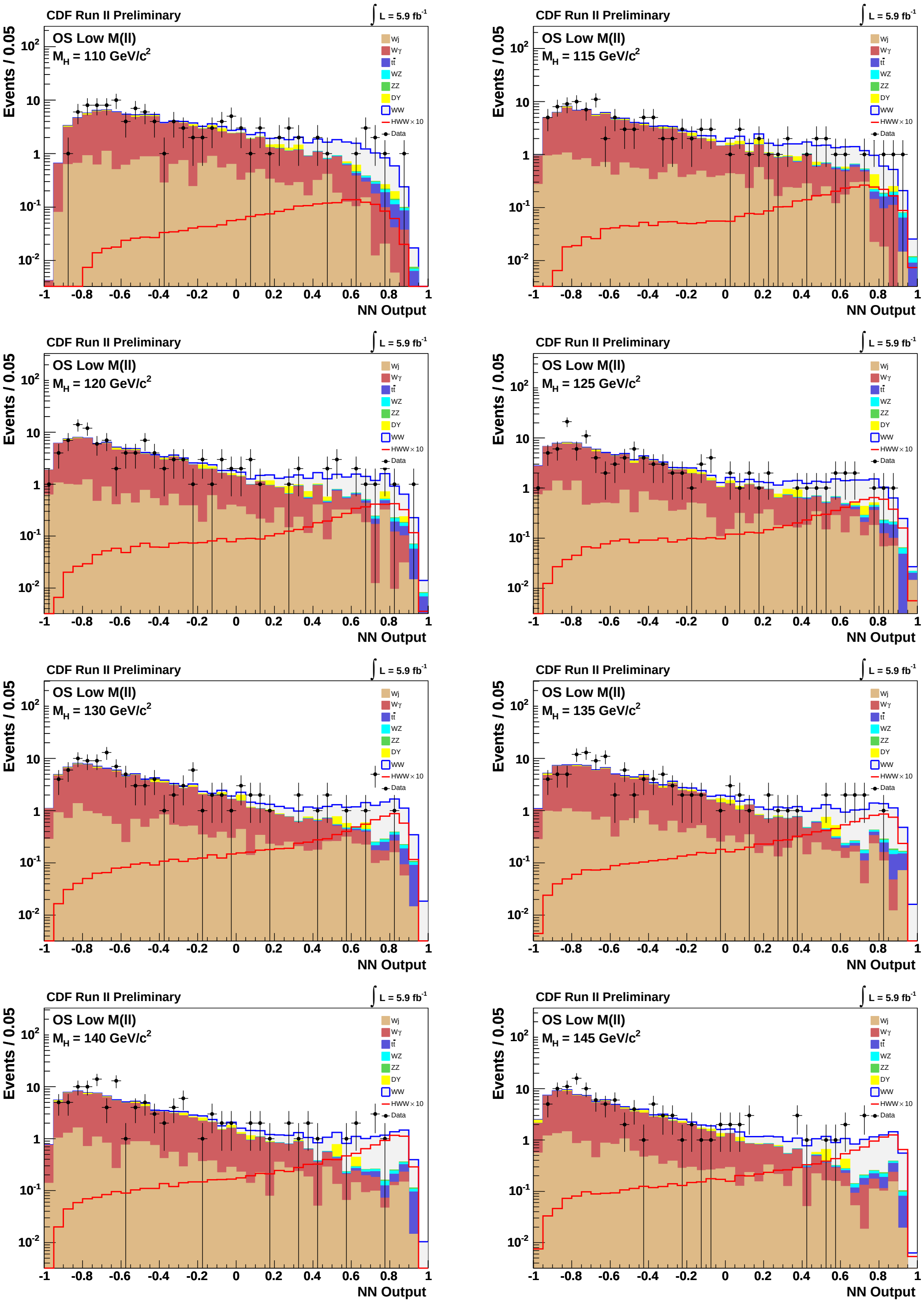

Figure 66: Low M_{ll} Neural Network output templates for several Higgs masses. From the top left to bottom right: 110 GeV, 115 GeV, 120 GeV, 125 GeV, 130 GeV, 135 GeV, 140 GeV, and 145 GeV.

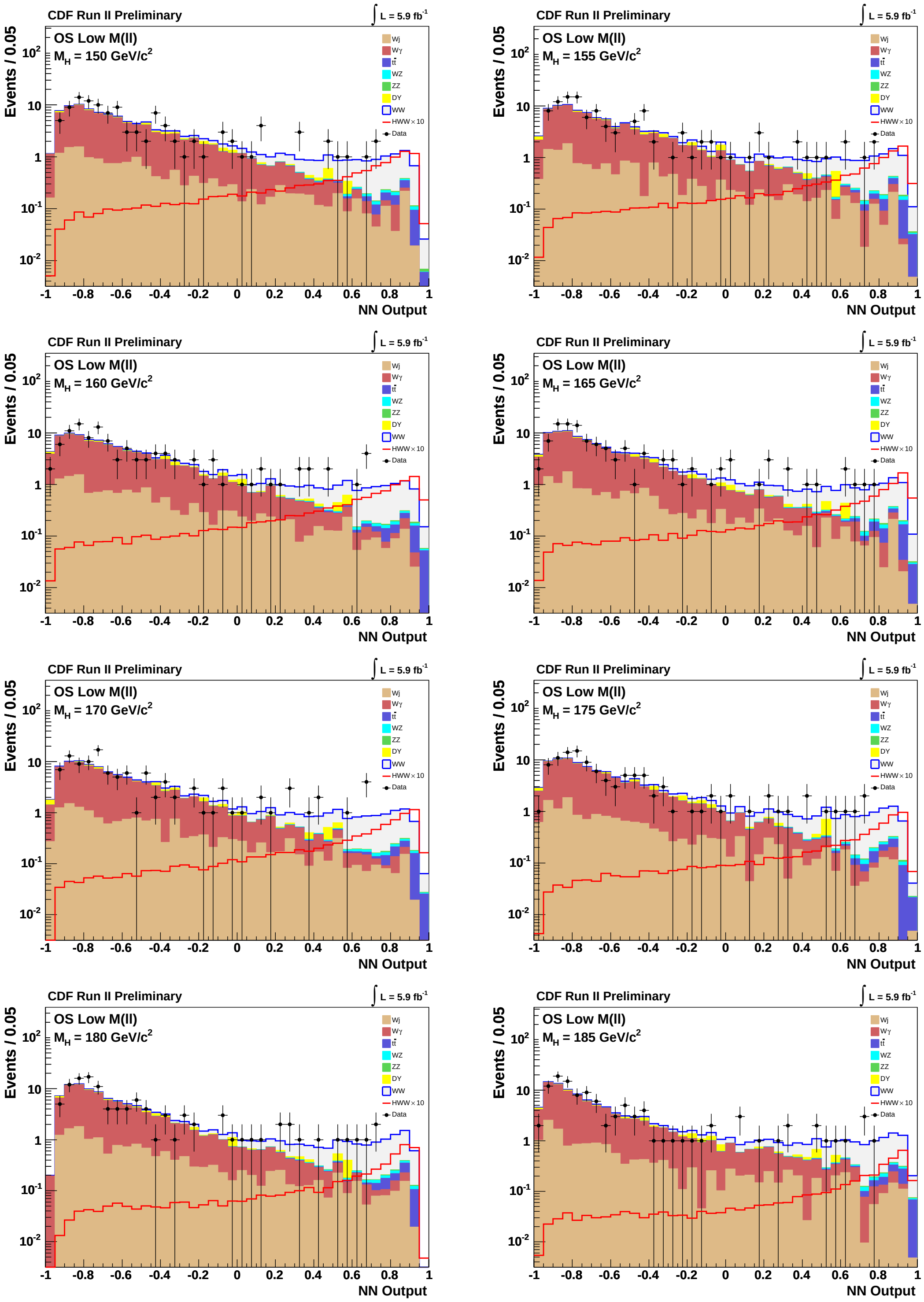

Figure 67: Low M_{ll} Neural Network output templates for several Higgs masses. From the top left to bottom right : 150 GeV, 155 GeV, 160 GeV, 165 GeV, 170 GeV, 175 GeV, 180 GeV, and 185 GeV.

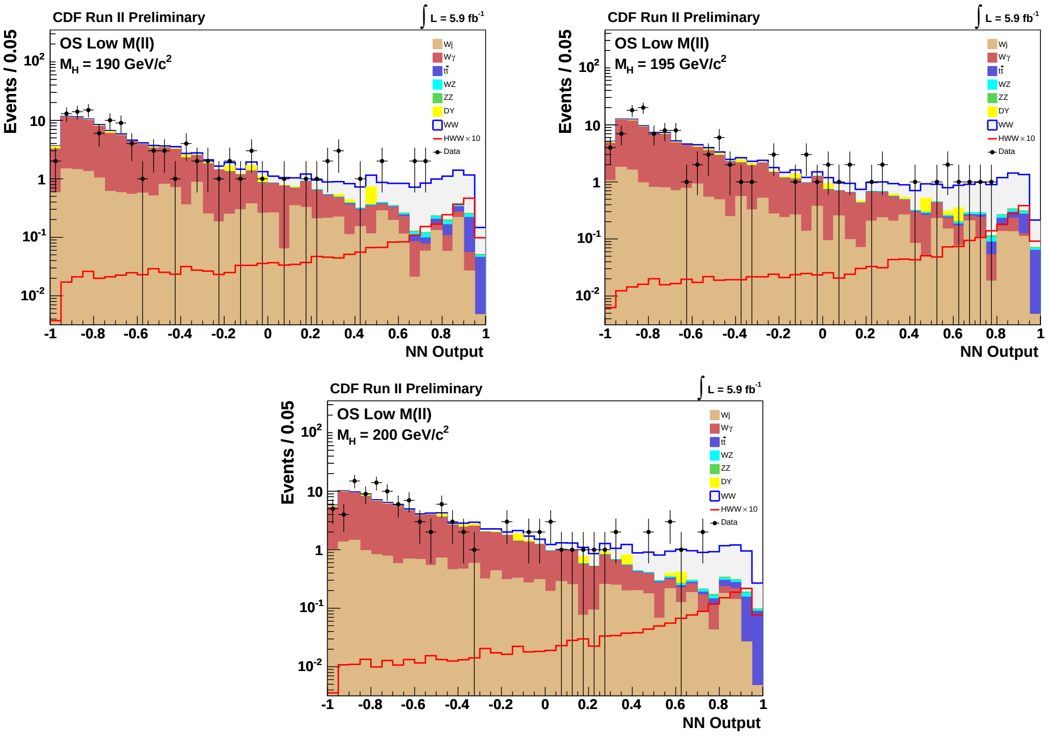

Figure 68: Low M_{ll} Neural Network output templates for several Higgs masses. From the top left to bottom right : 190 GeV, 195 GeV, and 200 GeV.

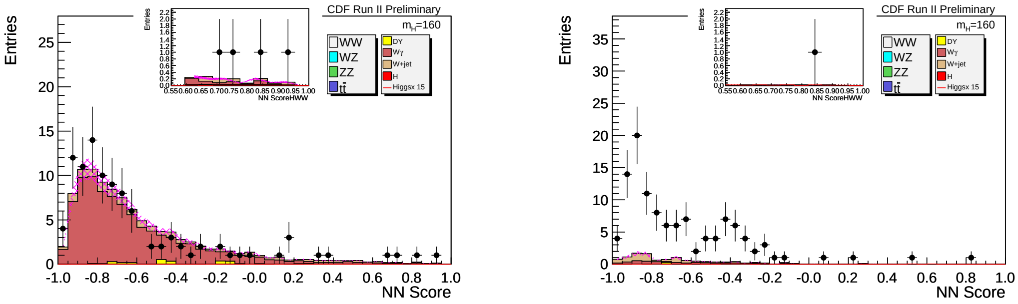

Figure 69: Neural network output templates for $m_H = 160$ GeV/c^2 for the two low $M_{\ell\ell}$ control regions: same-sign on the left and low $\not{E}_{Tspec}$ on the right.

Uncertainty Source	WW	WZ	ZZ	$t\bar{t}$	DY	$W\gamma$	W+jet(s)	$gg \rightarrow H$	WH
Cross Section									
Scale								12.0%	
PDF Model								10.5%	
Total	*6.0%*	*6.0%*	*6.0%*	7.0%	5.0%				5.0%
Acceptance									
Scale (jets)	*-0.4%*								
PDF Model (leptons)								*1.0%*	*1.0%*
PDF Model (jets)	*1.6%*							2.1%	2.1%
Higher-order Diagrams		10.0%	10.0%	10.0%	10.0%				
Jet Energy Scale	*1.0%*	*2.3%*	*2.0%*	*12.9%*	*6.4%*	*1.3%*		*2.4%*	*10.5%*
Conversion Modeling						10.0%			
Jet Fake Rates							18.4%		
Lepton ID Efficiencies	*3.8%*	*3.8%*	*3.8%*	*3.8%*	*3.8%*			*3.8%*	*3.8%*
Trigger Efficiencies	*2.0%*	*2.0%*	*2.0%*	*2.0%*	*2.0%*			*2.0%*	*2.0%*
Luminosity	*5.9%*	*5.9%*	*5.9%*	*5.9%*	*5.9%*			*5.9%*	*5.9%*

Table 62: Systematics table for low M_{ll} analysis background and signal (only $gg \rightarrow H$ production is considered) processes. Cross section systematics are correlated for the diboson processes (shown in italic font) but uncorrelated between all other processes. The DY Met modeling systematic (shown in boldface font) is uncorrelated between channels.

tion 11.2.3 and the shape of the unmodelled neural network distribution is computed using events in the low $\not{E}_{Tspec}$ control region as shown in Figure 69. This shape has a similar distribution to that for $W\gamma$ and since it falls at predominantly low values of neural net score is not expected to impact the fit to the signal region. This has been tested by changing the scale factor on $W\gamma$ from 0.92 to 1.116 to account for the potential additional 19 ± 5 events (27% of events in $W\gamma$) coming from the unmodelled background. At the same time the systematic uncertainty was increased from 11% to 17% to account for the uncertainty in the modelled background rate. No impact was seen on the limits from these changes, and no further treatment of the background is considered.

Figure 70 shows the expected (based on 10000 pseudo-experiments) and observed limits obtained from the low $M_{\ell\ell}$ region. Excellent separation of the $W\gamma$ background is seen and the Higgs is pushed with reasonable separation from the WW as well.

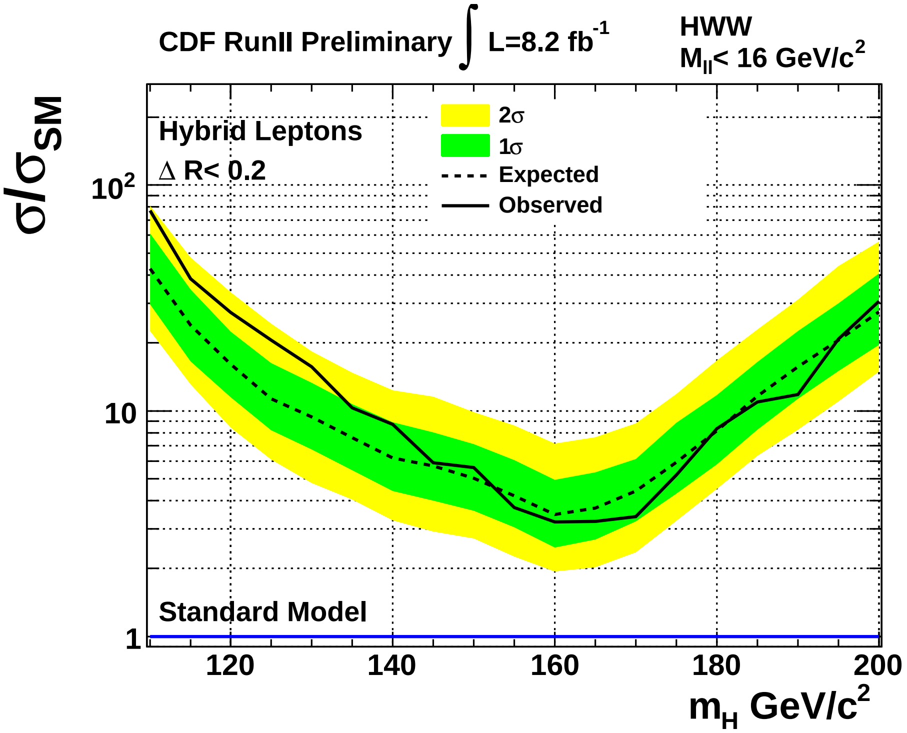

Low M(ll)	110	115	120	125	130	135	140	145	150	155	160	165	170	175	180	185	190	195	200
-2σ	22.59	13.09	8.43	6.09	4.79	4.04	3.26	2.92	2.72	2.25	1.94	2.03	2.36	3.25	4.52	6.33	8.26	11.02	14.91
-1σ	29.58	16.59	11.47	8.19	6.76	5.46	4.43	4.00	3.61	3.05	2.48	2.69	3.24	4.29	5.81	8.27	11.29	15.02	19.64
Median	**42.72**	**23.94**	**16.11**	**11.31**	**9.38**	**7.60**	**6.20**	**5.71**	**5.04**	**4.20**	**3.47**	**3.70**	**4.42**	**5.93**	**8.16**	**11.63**	**15.65**	**20.63**	**27.51**
$+1\sigma$	60.98	34.59	22.45	16.26	13.31	10.71	8.88	8.05	7.12	6.04	4.96	5.33	6.13	8.84	11.77	16.48	22.53	30.01	40.73
$+2\sigma$	81.24	47.91	33.56	24.34	18.38	14.80	12.35	11.58	9.85	8.62	7.16	7.65	8.81	11.90	16.71	22.98	31.06	43.92	56.44
Observed	77.07	38.38	27.32	20.59	15.64	10.33	8.69	5.88	5.60	3.73	3.22	3.23	3.41	5.20	8.33	10.96	11.84	20.83	30.56

Figure 70: $H \rightarrow WW$ sensitivity normalized to NNLL σ_{SM} calculation in the low M_{ll} region. In this region we consider potential signal contributions from gluon fusion only.

12 Same-Sign Dilepton Signal Region with 1+ Jets

To gain extra sensitivity, we also search for Higgs signal in like-sign, or same-sign (SS), dileptons. These occur naturally in $ZH \to ZWW$ production, when the Z and one or both W bosons decay leptonically, and $WH \to WWW$ production, when the associated W and one or both W bosons from the Higgs decay leptonically.

12.1 Event Selection

The event selection for same sign dilepton events focues on eliminating background from fake and charge misidentified leptons. Because PHX and LBE electrons have a high rate of charge mismeasurement, we do not use PHX or LBE electrons in the SS analysis. All other lepton types are included. The WH and ZH events tend to have lower values of missing transverse energy because there are three neutrinos, and the leptons are not necessarily back-to-back. Because Drell-Yan contributes to the same-sign region only when a lepton charge is misidentified, it is not as large a background source in the same-sign region as in the opposite-sign. Therefore we remove all $\not\!\!E_T$ and $\not\!\!E_{\mathrm{T}}^{\mathrm{spec}}$ requirements. To reduce the number of fake leptons in the sample, we increase the p_{T} requirement for the second lepton from 10 GeV/c to 20 Gev/c. To reduce the W+jets and $W\gamma$ contributions, we only use events with one or more jets with $E_{\mathrm{T}} > 15$ GeV and $|\eta| < 2.5$ at L5 correction. Same sign events with zero jets are used as a control sample, as described in Section 12.2.

After all selection cuts, W+jets accounts for about 50% of the background in the same-sign channel. Drell-Yan contributes about 25% of the total background. Smaller background contributions come from WW, WZ, ZZ, $W\gamma$, and $t\bar{t}$ processes. To estimate the backgrounds, we use the same MC samples as used in the opposite-sign HWW analysis. The W+jets contribution is measured from data, as described in Section 5.3.

The primary background to the SS analysis is W+jets; thus, it is important to accurately predict the number of W+jets events. The W+jets contribution measured from data must be corrected for non-triggerable fakes as described in Section 5.3. Due to the low statistics in the same-sign regions, it is difficult to measure the non-triggerable fake contributions directly from these regions. Instead, we use the regions with all SS event selections applied, except with opposite-sign leptons instead of same-sign. Because there is no $\not\!\!E_T$ cut, this region has considerable statistics, primarily due to Drell-Yan events. The non-triggerable fake rates measured in the opposite-sign regions are then applied to the SS W+jets predictions. The rates, shown in Tables 27 and 28, cause the total number of W+jets events to increase by about 20% in both SS events with 0 jets and SS events with one or more jets.

The background expectation and observed yield for same-sign events with one or more jet are shown in Table 63. The expected and observed kinematic distributions for these events are shown in Figures 71-73. We stack the backgrounds on top of each other, and then for comparison we overlay the contribution from a 160 GeV/c^2 Higgs boson with yields scaled up by a factor of 10. In addition, we calculate a confidence level for data versus background expectations on each plot. The confidence levels shown are for Poisson fluctuations and the KS test.

12.2 Same-Sign Control Region

The primary background in the same-sign signal region is fakes. The best non-overlapping control region to study the agreement of the fakes prediction is in the region of same-sign dileptons with zero jets. Table 64 and Figures 74 through 76 show the agreement between data and the fakes prediction. Although there is an excess of predicted events over observed events in data, the agreement is well within one standard deviation of the W+jets uncertainty. Agreement between kinematic variables in MC and data is good.

Category	WW	WZ	ZZ	$t\bar{t}$	DY	$W\gamma$	W+jets	Total	Data
TCE TCE	0.0	0.0	0.0	0.0	0.0	0.0	0.0	0.0	0.0
TCE LBE	0.0	0.0	0.0	0.0	0.0	0.0	0.0	0.0	0.0
TCE PHX	0.0	0.0	0.0	0.0	0.0	0.0	0.0	0.0	0.0
TCE PLBE	0.0	0.0	0.0	0.0	0.0	0.0	0.0	0.0	0.0
LBE LBE	0.0	0.0	0.0	0.0	0.0	0.0	0.0	0.0	0.0
LBE PHX	0.0	0.0	0.0	0.0	0.0	0.0	0.0	0.0	0.0
LBE PLBE	0.0	0.0	0.0	0.0	0.0	0.0	0.0	0.0	0.0
PHX PHX	0.0	0.0	0.0	0.0	0.0	0.0	0.0	0.0	0.0
PHX PLBE	0.0	0.0	0.0	0.0	0.0	0.0	0.0	0.0	0.0
PLBE PLBE	0.0	0.0	0.0	0.0	0.0	0.0	0.0	0.0	0.0
TCEni TCEni	0.0	2.4	0.4	0.1	12.1	1.2	6.4	22.7	29.0
TCEni LBEni	0.0	0.0	0.0	0.0	0.0	0.0	0.0	0.0	0.0
TCEni PHXni	0.0	0.0	0.0	0.0	0.0	0.0	0.0	0.0	0.0
TCEni PLBEni	0.0	0.0	0.0	0.0	0.0	0.0	0.0	0.0	0.0
LBEni LBEni	0.0	0.0	0.0	0.0	0.0	0.0	0.0	0.0	0.0
LBEni PHXni	0.0	0.0	0.0	0.0	0.0	0.0	0.0	0.0	0.0
LBEni PLBEni	0.0	0.0	0.0	0.0	0.0	0.0	0.0	0.0	0.0
PHXni PHXni	0.0	0.0	0.0	0.0	0.0	0.0	0.0	0.0	0.0
PHXni PLBEni	0.0	0.0	0.0	0.0	0.0	0.0	0.0	0.0	0.0
PLBEni PLBEni	0.0	0.0	0.0	0.0	0.0	0.0	0.0	0.0	0.0
TCEni PHX	0.0	0.0	0.0	0.0	0.0	0.0	0.0	0.0	0.0
TCEni PLBE	0.0	0.0	0.0	0.0	0.0	0.0	0.0	0.0	0.0
LBEni PHX	0.0	0.0	0.0	0.0	0.0	0.0	0.0	0.0	0.0
LBEni PLBE	0.0	0.0	0.0	0.0	0.0	0.0	0.0	0.0	0.0
TCE CMUP	0.0	0.0	0.0	0.0	0.0	0.0	0.0	0.0	0.0
TCE CMU	0.0	0.0	0.0	0.0	0.0	0.0	0.0	0.0	0.0
TCE CMP	0.0	0.0	0.0	0.0	0.0	0.0	0.0	0.0	0.0
TCE CMX	0.0	0.0	0.0	0.0	0.0	0.0	0.0	0.0	0.0
TCE CMXMsKs	0.0	0.0	0.0	0.0	0.0	0.0	0.0	0.0	0.0
TCE BMU	0.0	0.0	0.0	0.0	0.0	0.0	0.0	0.0	0.0
TCE CMIOCES	0.0	0.0	0.0	0.0	0.0	0.0	0.0	0.0	0.0
TCE CMIOPES	0.0	0.0	0.0	0.0	0.0	0.0	0.0	0.0	0.0
LBE CMUP	0.0	0.0	0.0	0.0	0.0	0.0	0.0	0.0	0.0
LBE CMU	0.0	0.0	0.0	0.0	0.0	0.0	0.0	0.0	0.0
LBE CMP	0.0	0.0	0.0	0.0	0.0	0.0	0.0	0.0	0.0
LBE CMX	0.0	0.0	0.0	0.0	0.0	0.0	0.0	0.0	0.0
LBE CMXMsKs	0.0	0.0	0.0	0.0	0.0	0.0	0.0	0.0	0.0
LBE BMU	0.0	0.0	0.0	0.0	0.0	0.0	0.0	0.0	0.0
LBE CMIOCES	0.0	0.0	0.0	0.0	0.0	0.0	0.0	0.0	0.0
LBE CMIOPES	0.0	0.0	0.0	0.0	0.0	0.0	0.0	0.0	0.0
PHX CMUP	0.0	0.0	0.0	0.0	0.0	0.0	0.0	0.0	0.0
PHX CMU	0.0	0.0	0.0	0.0	0.0	0.0	0.0	0.0	0.0
PHX CMP	0.0	0.0	0.0	0.0	0.0	0.0	0.0	0.0	0.0
PHX CMX	0.0	0.0	0.0	0.0	0.0	0.0	0.0	0.0	0.0
PHX CMXMsKs	0.0	0.0	0.0	0.0	0.0	0.0	0.0	0.0	0.0
PHX BMU	0.0	0.0	0.0	0.0	0.0	0.0	0.0	0.0	0.0
PHX CMIOCES	0.0	0.0	0.0	0.0	0.0	0.0	0.0	0.0	0.0
PHX CMIOPES	0.0	0.0	0.0	0.0	0.0	0.0	0.0	0.0	0.0
PLBE CMUP	0.0	0.0	0.0	0.0	0.0	0.0	0.0	0.0	0.0
PLBE CMU	0.0	0.0	0.0	0.0	0.0	0.0	0.0	0.0	0.0
PLBE CMP	0.0	0.0	0.0	0.0	0.0	0.0	0.0	0.0	0.0
PLBE CMX	0.0	0.0	0.0	0.0	0.0	0.0	0.0	0.0	0.0
PLBE CMXMsKs	0.0	0.0	0.0	0.0	0.0	0.0	0.0	0.0	0.0
PLBE BMU	0.0	0.0	0.0	0.0	0.0	0.0	0.0	0.0	0.0
PLBE CMIOCES	0.0	0.0	0.0	0.0	0.0	0.0	0.0	0.0	0.0
PLBE CMIOPES	0.0	0.0	0.0	0.0	0.0	0.0	0.0	0.0	0.0
TCEni CMUPni	0.0	1.9	0.4	0.0	0.5	0.6	4.3	7.8	9.0
TCEni CMUni	0.0	0.0	0.0	0.0	0.0	0.0	0.0	0.0	0.0
TCEni CMPni	0.0	0.3	0.1	0.0	0.0	0.0	0.7	1.1	3.0

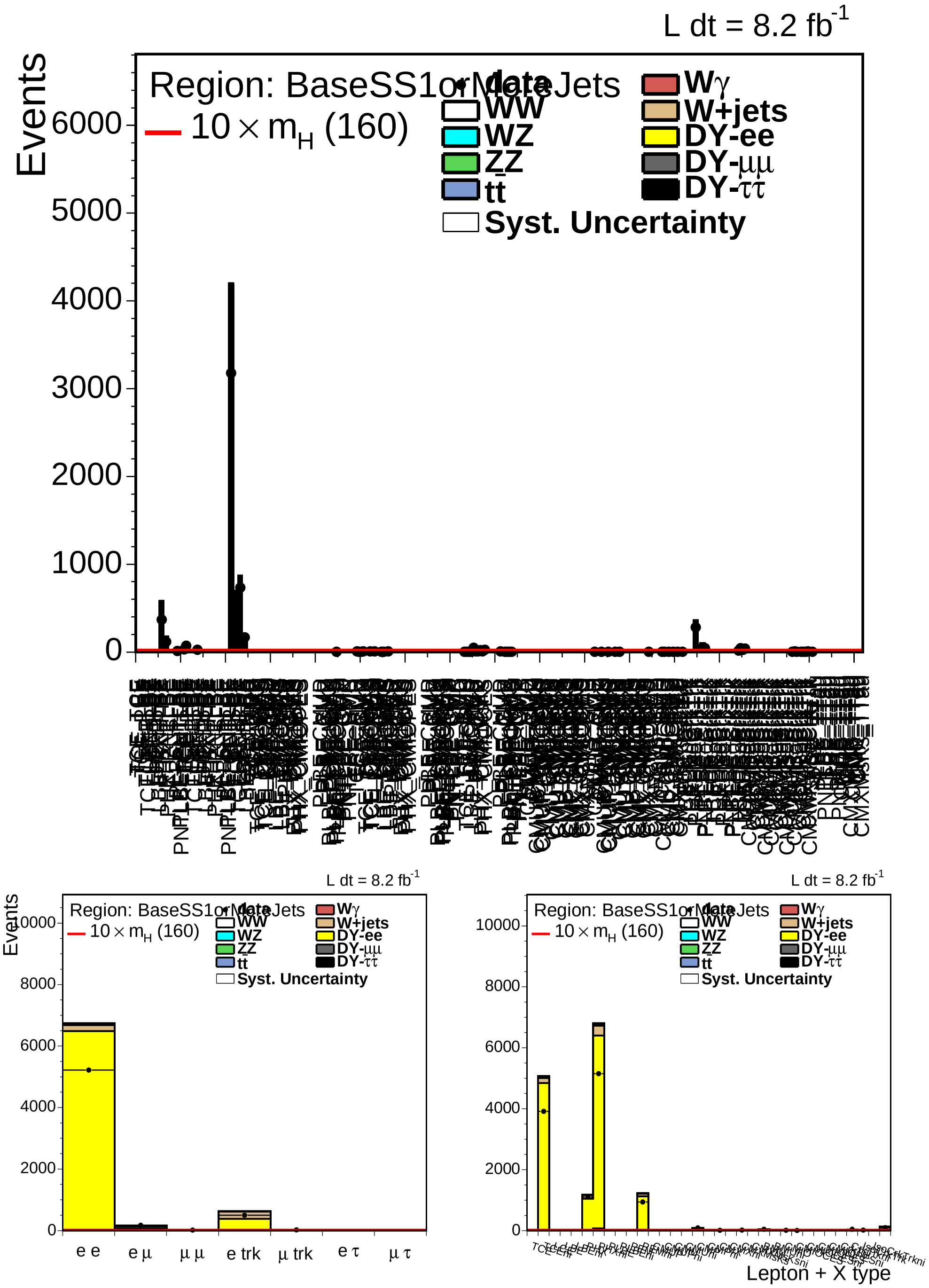

Figure 71: Same-Sign dilepton 1+ jet signal region.

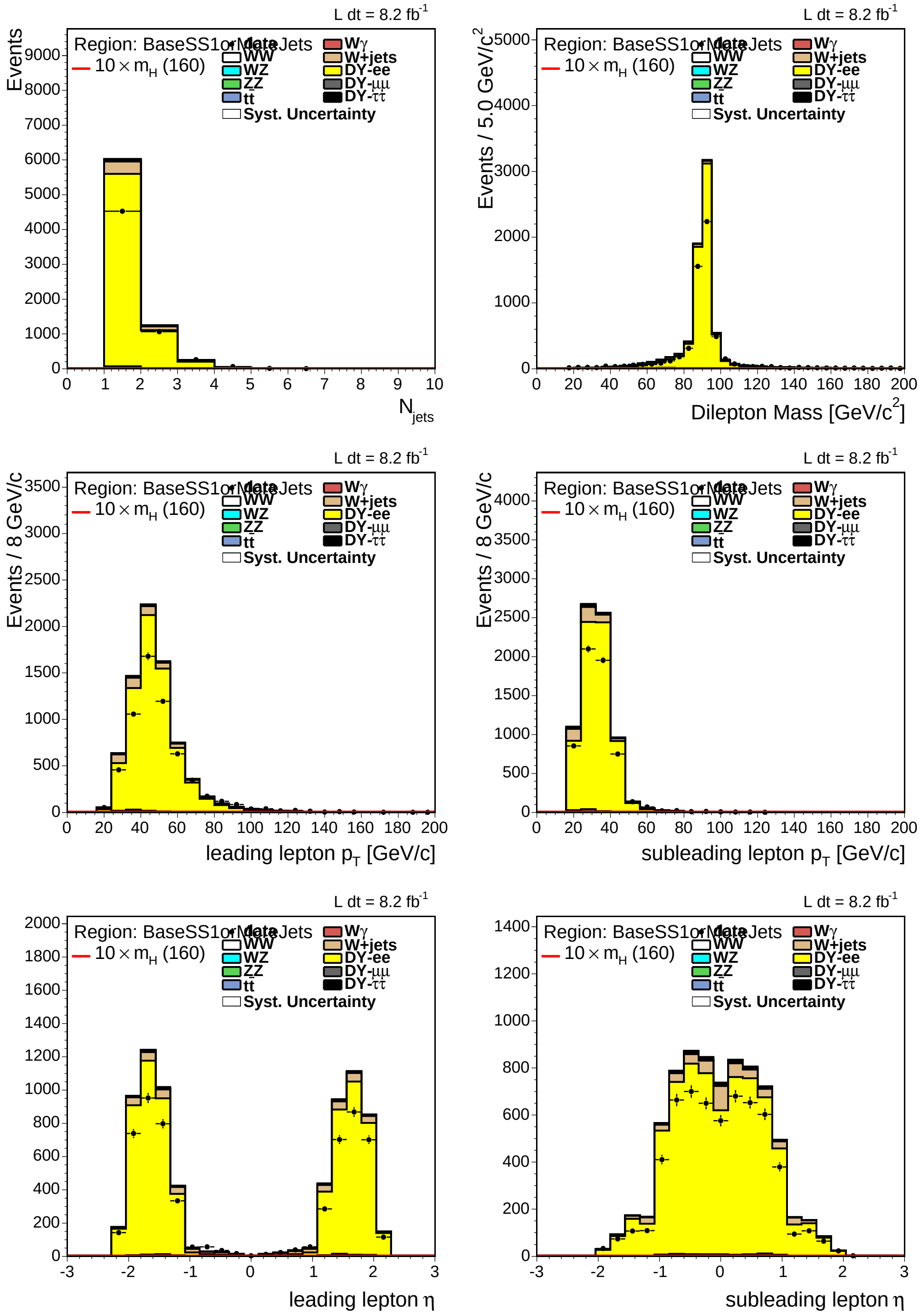

Figure 72: Same-Sign dilepton 1+ jet signal region.

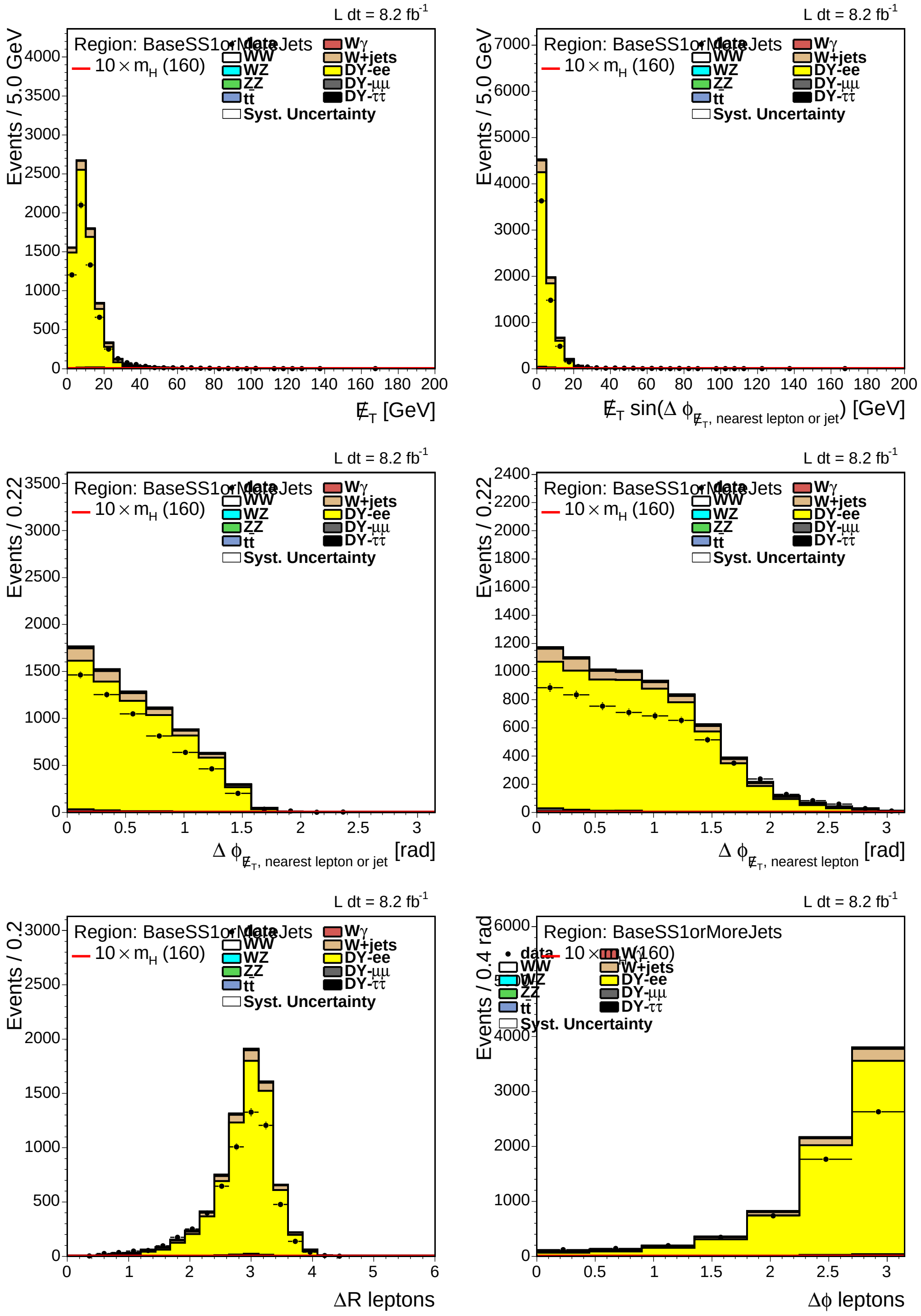

Figure 73: Same-Sign dilepton 1+ jet signal region.

Category	WW	WZ	ZZ	$t\bar{t}$	DY	$W\gamma$	W+jets	Total	Data
TCE TCE	0.0	0.0	0.0	0.0	0.0	0.0	0.0	0.0	0.0
TCE LBE	0.0	0.0	0.0	0.0	0.0	0.0	0.0	0.0	0.0
TCE PHX	0.0	0.0	0.0	0.0	0.0	0.0	0.0	0.0	0.0
TCE PLBE	0.0	0.0	0.0	0.0	0.0	0.0	0.0	0.0	0.0
LBE LBE	0.0	0.0	0.0	0.0	0.0	0.0	0.0	0.0	0.0
LBE PHX	0.0	0.0	0.0	0.0	0.0	0.0	0.0	0.0	0.0
LBE PLBE	0.0	0.0	0.0	0.0	0.0	0.0	0.0	0.0	0.0
PHX PHX	0.0	0.0	0.0	0.0	0.0	0.0	0.0	0.0	0.0
PHX PLBE	0.0	0.0	0.0	0.0	0.0	0.0	0.0	0.0	0.0
PLBE PLBE	0.0	0.0	0.0	0.0	0.0	0.0	0.0	0.0	0.0
TCEni TCEni	0.0	0.6	0.0	0.0	24.4	3.0	10.4	38.3	52.0
TCEni LBEni	0.0	0.0	0.0	0.0	0.0	0.0	0.0	0.0	0.0
TCEni PHXni	0.0	0.0	0.0	0.0	0.0	0.0	0.0	0.0	0.0
TCEni PLBEni	0.0	0.0	0.0	0.0	0.0	0.0	0.0	0.0	0.0
LBEni LBEni	0.0	0.0	0.0	0.0	0.0	0.0	0.0	0.0	0.0
LBEni PHXni	0.0	0.0	0.0	0.0	0.0	0.0	0.0	0.0	0.0
LBEni PLBEni	0.0	0.0	0.0	0.0	0.0	0.0	0.0	0.0	0.0
PHXni PHXni	0.0	0.0	0.0	0.0	0.0	0.0	0.0	0.0	0.0
PHXni PLBEni	0.0	0.0	0.0	0.0	0.0	0.0	0.0	0.0	0.0
PLBEni PLBEni	0.0	0.0	0.0	0.0	0.0	0.0	0.0	0.0	0.0
TCEni PHX	0.0	0.0	0.0	0.0	0.0	0.0	0.0	0.0	0.0
TCEni PLBE	0.0	0.0	0.0	0.0	0.0	0.0	0.0	0.0	0.0
LBEni PHX	0.0	0.0	0.0	0.0	0.0	0.0	0.0	0.0	0.0
LBEni PLBE	0.0	0.0	0.0	0.0	0.0	0.0	0.0	0.0	0.0
TCE CMUP	0.0	0.0	0.0	0.0	0.0	0.0	0.0	0.0	0.0
TCE CMU	0.0	0.0	0.0	0.0	0.0	0.0	0.0	0.0	0.0
TCE CMP	0.0	0.0	0.0	0.0	0.0	0.0	0.0	0.0	0.0
TCE CMX	0.0	0.0	0.0	0.0	0.0	0.0	0.0	0.0	0.0
TCE CMXMsKs	0.0	0.0	0.0	0.0	0.0	0.0	0.0	0.0	0.0
TCE BMU	0.0	0.0	0.0	0.0	0.0	0.0	0.0	0.0	0.0
TCE CMIOCES	0.0	0.0	0.0	0.0	0.0	0.0	0.0	0.0	0.0
TCE CMIOPES	0.0	0.0	0.0	0.0	0.0	0.0	0.0	0.0	0.0
LBE CMUP	0.0	0.0	0.0	0.0	0.0	0.0	0.0	0.0	0.0
LBE CMU	0.0	0.0	0.0	0.0	0.0	0.0	0.0	0.0	0.0
LBE CMP	0.0	0.0	0.0	0.0	0.0	0.0	0.0	0.0	0.0
LBE CMX	0.0	0.0	0.0	0.0	0.0	0.0	0.0	0.0	0.0
LBE CMXMsKs	0.0	0.0	0.0	0.0	0.0	0.0	0.0	0.0	0.0
LBE BMU	0.0	0.0	0.0	0.0	0.0	0.0	0.0	0.0	0.0
LBE CMIOCES	0.0	0.0	0.0	0.0	0.0	0.0	0.0	0.0	0.0
LBE CMIOPES	0.0	0.0	0.0	0.0	0.0	0.0	0.0	0.0	0.0
PHX CMUP	0.0	0.0	0.0	0.0	0.0	0.0	0.0	0.0	0.0
PHX CMU	0.0	0.0	0.0	0.0	0.0	0.0	0.0	0.0	0.0
PHX CMP	0.0	0.0	0.0	0.0	0.0	0.0	0.0	0.0	0.0
PHX CMX	0.0	0.0	0.0	0.0	0.0	0.0	0.0	0.0	0.0
PHX CMXMsKs	0.0	0.0	0.0	0.0	0.0	0.0	0.0	0.0	0.0
PHX BMU	0.0	0.0	0.0	0.0	0.0	0.0	0.0	0.0	0.0
PHX CMIOCES	0.0	0.0	0.0	0.0	0.0	0.0	0.0	0.0	0.0
PHX CMIOPES	0.0	0.0	0.0	0.0	0.0	0.0	0.0	0.0	0.0
PLBE CMUP	0.0	0.0	0.0	0.0	0.0	0.0	0.0	0.0	0.0
PLBE CMU	0.0	0.0	0.0	0.0	0.0	0.0	0.0	0.0	0.0
PLBE CMP	0.0	0.0	0.0	0.0	0.0	0.0	0.0	0.0	0.0
PLBE CMX	0.0	0.0	0.0	0.0	0.0	0.0	0.0	0.0	0.0
PLBE CMXMsKs	0.0	0.0	0.0	0.0	0.0	0.0	0.0	0.0	0.0
PLBE BMU	0.0	0.0	0.0	0.0	0.0	0.0	0.0	0.0	0.0
PLBE CMIOCES	0.0	0.0	0.0	0.0	0.0	0.0	0.0	0.0	0.0
PLBE CMIOPES	0.0	0.0	0.0	0.0	0.0	0.0	0.0	0.0	0.0
TCEni CMUPni	0.0	1.5	0.1	0.0	2.6	2.2	7.0	13.5	9.0
TCEni CMUni	0.0	0.0	0.0	0.0	0.0	0.0	0.0	0.0	0.0
TCEni CMPni	0.0	0.2	0.0	0.0	1.3	0.4	1.2	3.1	2.0

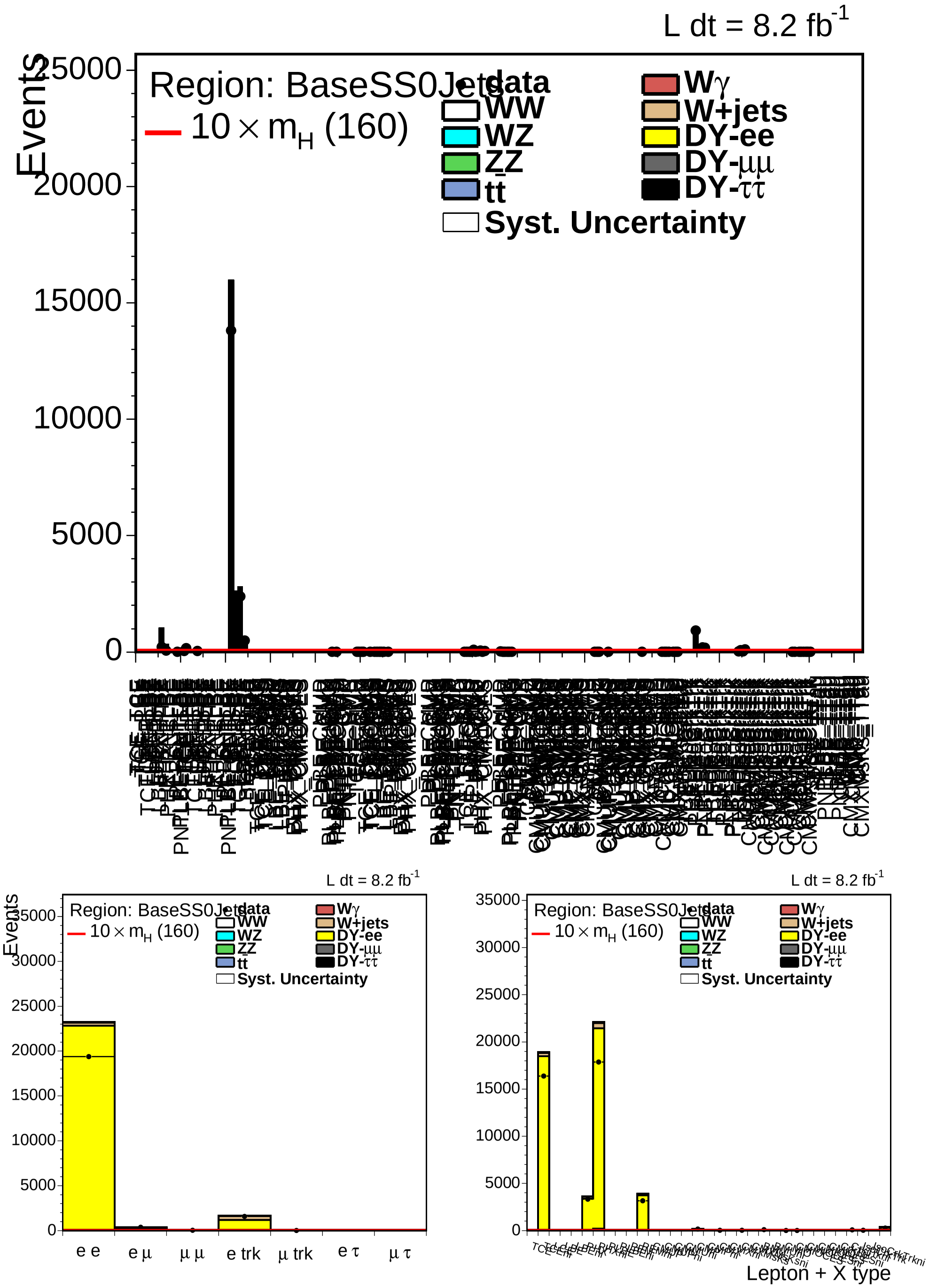

Figure 74: Same-Sign dilepton 0 jet control region.

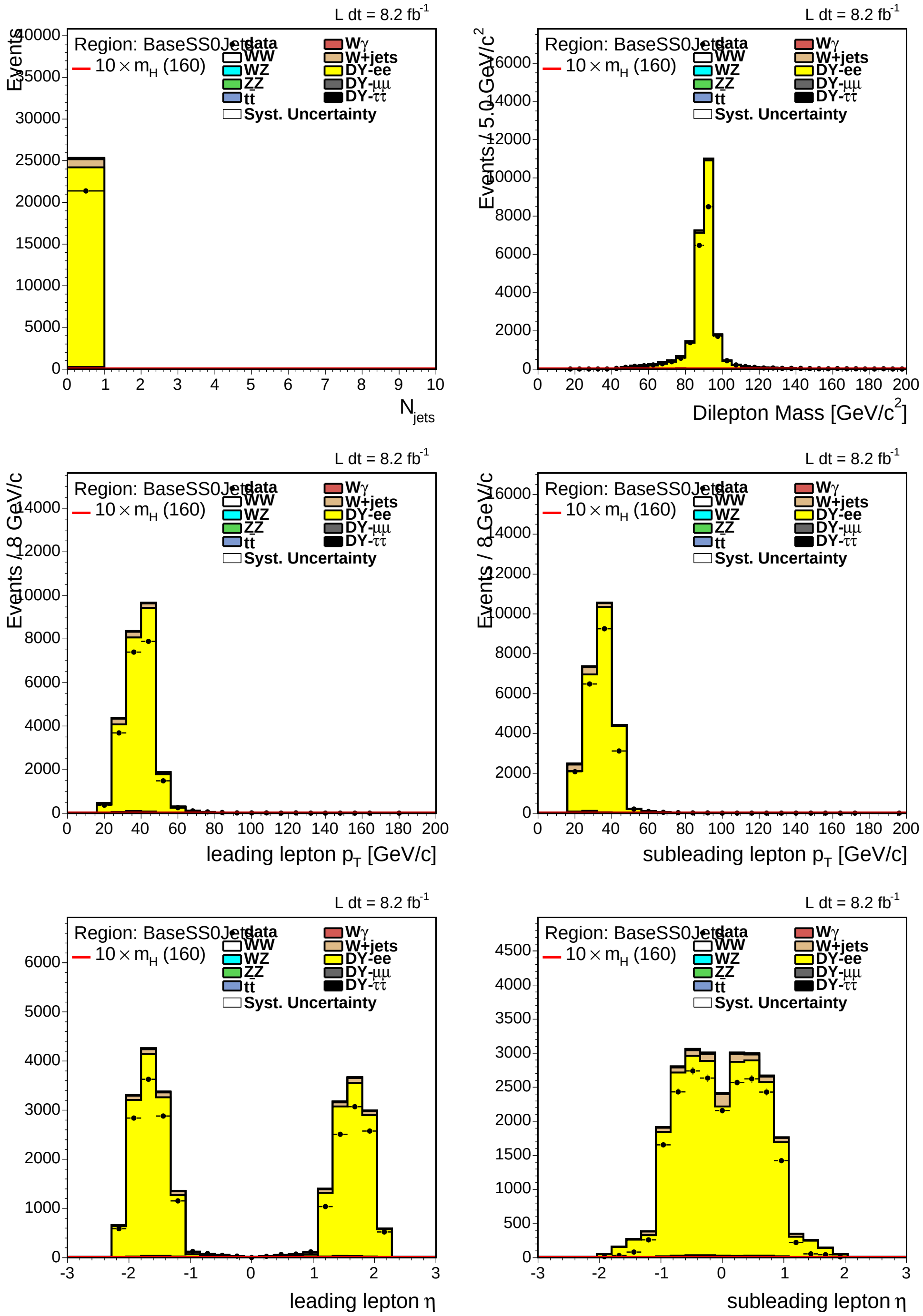

Figure 75: Same-Sign dilepton 0 jet control region.

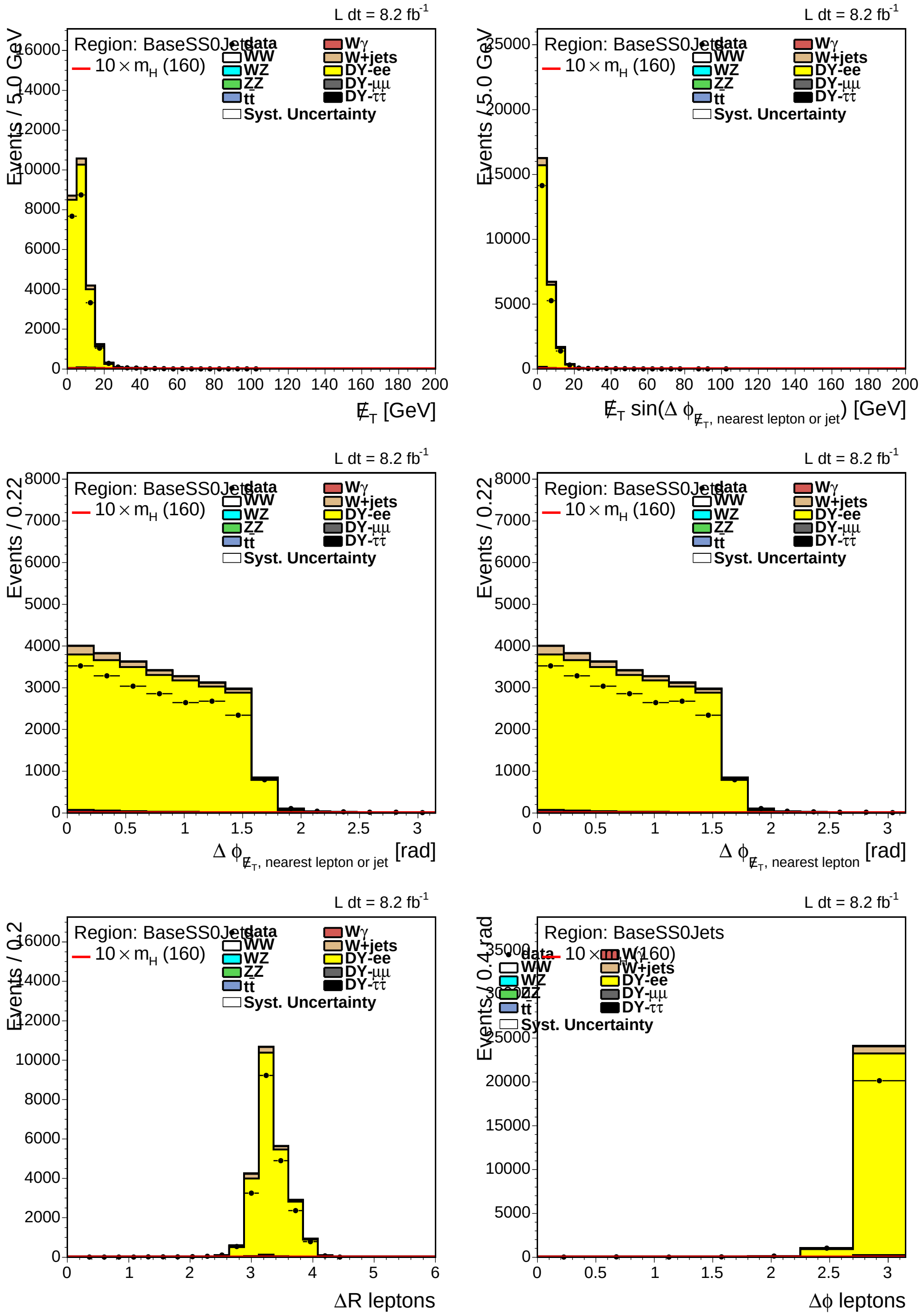

Figure 76: Same-Sign dilepton 0 jet control region.

Variable	Meaning
Njets	Number of jets
MetSig	$\not\!\!E_T$ significance ($\not\!\!E_T/\sqrt{\Sigma E_{\mathrm{T}}}$)
Ht	Transverse mass H_{T}
MetSpec	${\not\!\!E_T}^{\mathrm{spec}}$
dimass	Dilepton mass M_{ll}
jet1Et	E_{T} of leading jet
lep2Pt	p_{T} of subleading lepton
LepJetSumEt	ΣE_T of leptons and jets
MetLepSumEt	Sum of leptons' p_T and $\not\!\!E_T$
MetDelPhi	$\Delta\phi$ between $\not\!\!E_T$and nearest lepton or jet

Table 65: Kinematic neural network inputs for the same-sign analysis. Variables are listed in order of decreasing significance to the NN for a Higgs mass of 160. Plots of the input variables are shown in Fig. 77.

12.3 Analysis of Same-Sign 1+ Jet Events

We do not attempt to calculate Matrix Elements for SS events. Instead, we rely solely on a neural network (NN) to discriminate signal from background using kinematic variables as inputs to the NN. Optimization and training of the neural network are done in the same manner as for the 0J case described in Section 8. For this update, the NN inputs for the SS region were optimized. This was done primarily because the discrete variable N_{jets} was seen as a potentially strong discriminant; the Higgs signal is stronger in same-sign dilepton events with two or more jets. To avoid the low statistics of higher jet multiplicity bins, events with three or more jets were all assigned to $N_{\mathrm{jets}} = 3$. During the optimization, N_{jets} was found to be the most significant discriminating variable for $m_H = 160$. The new SS NN uses 10 input variables (compared to 13 in the previous version), and the expected sensitivity improves by ∼8% compared to using the previous training.

The input variables used for the updated SS NN are shown in Table 65. The observed distributions of each SS neural network input parameter compared with the distributions predicted by our background model are shown in Figure 77. For reference, we also include a hypothetical signal component for a Higgs boson with $m_H = 160$ GeV/c^2.

Templates are created for each neural network and used for calculating 95% CL limits with the MCLimit program [32]. Due to the low statistics in the SS region and the fact that we exclude PHX electrons, we do not divide events into High S/B and Low S/B categories as is done for the OS regions. Output templates for the trained SS neural network are shown in Figures 78 and 79.

The most significant signal contributions in the SS region are from associated production VH ($q\bar{q} \to ZH \to ZWW$ and $q\bar{q} \to WH \to WWW$). The gluon fusion ($gg \to H \to WW \to ll\nu\nu$) and Vector Boson Fusion (VBF) production methods con-

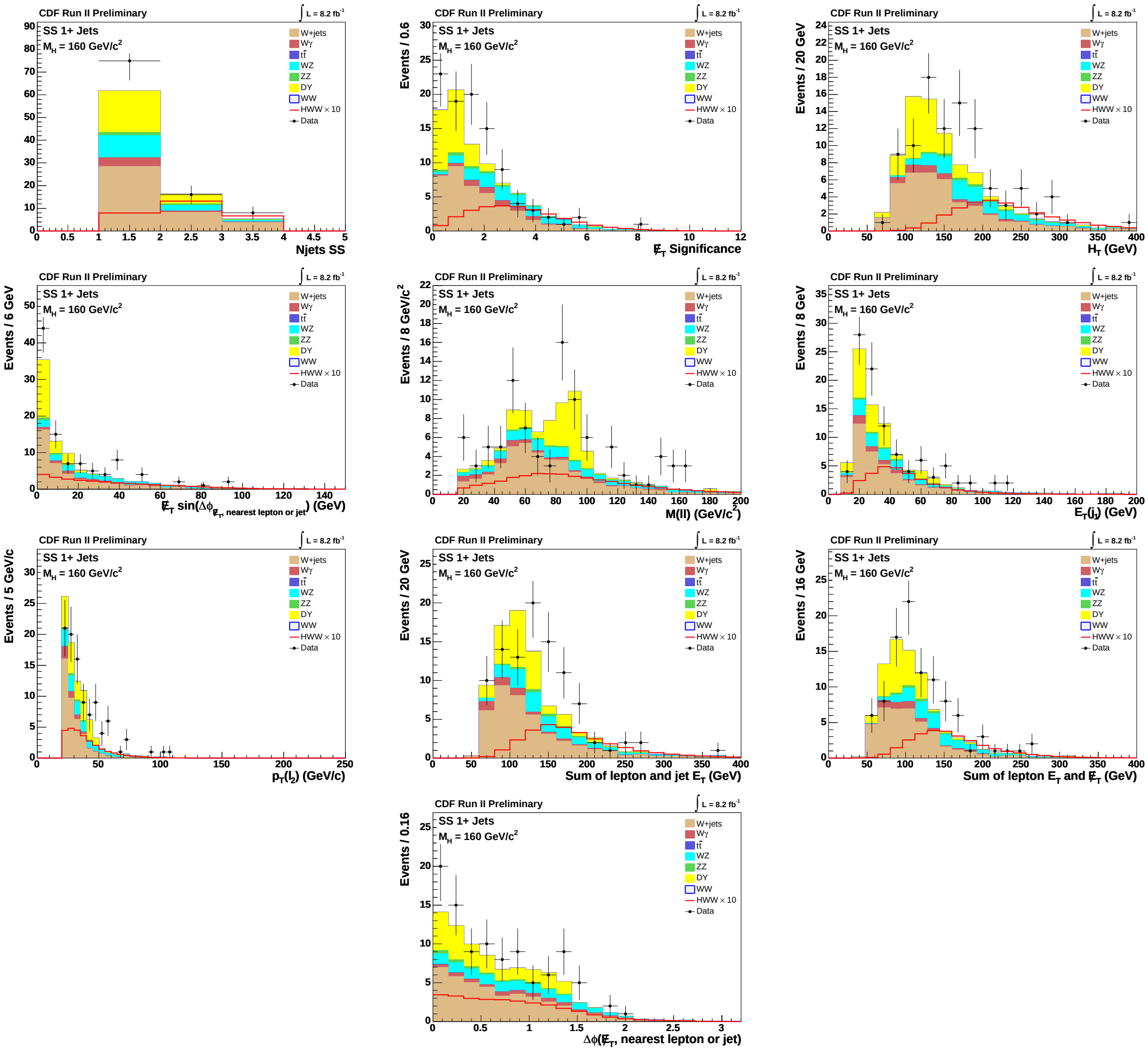

Figure 77: Neural Network input variables for SS NN (signal for $M_H = 160$ GeV/c^2).

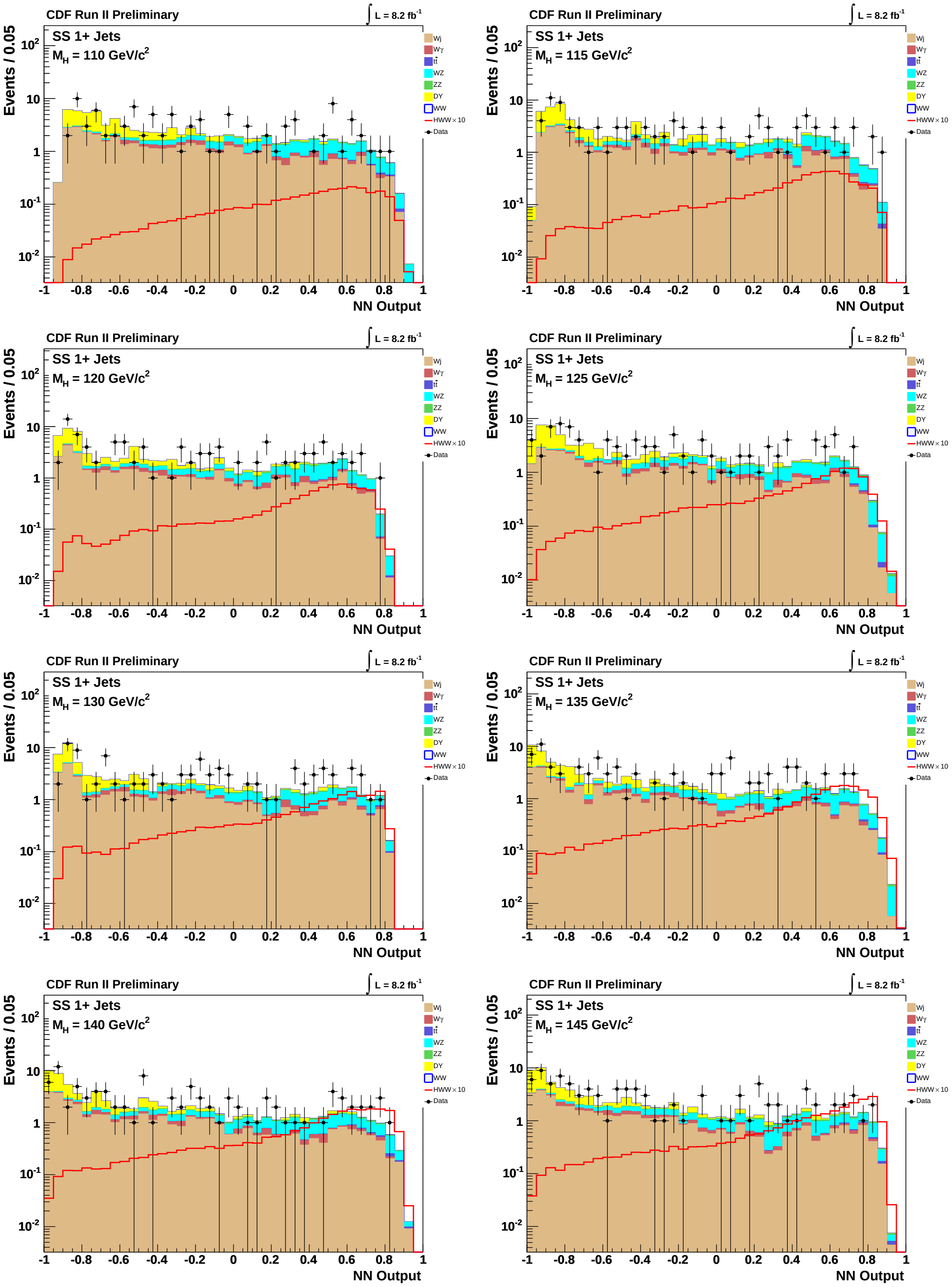

Figure 78: SS Neural Network output templates for several Higgs masses. From the top left to bottom right: 110 GeV, 115 GeV, 120 GeV, 125 GeV, 130 GeV, 135 GeV, 140 GeV, and 145 GeV.

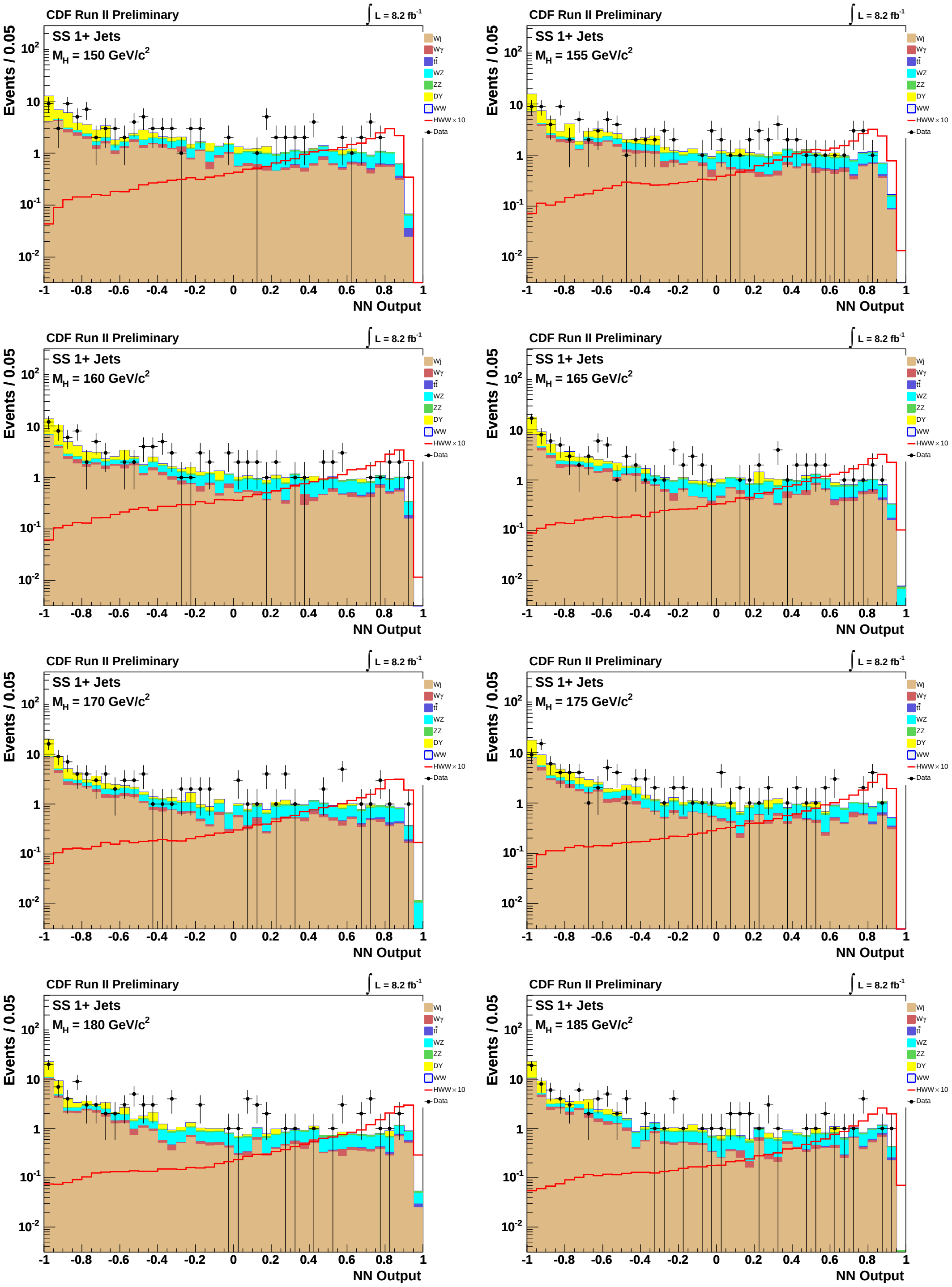

Figure 79: SS Neural Network output templates for several Higgs masses. From the top left to bottom right : 150 GeV, 155 GeV, 160 GeV, 165 GeV, 170 GeV, 175 GeV, 180 GeV, and 185 GeV.

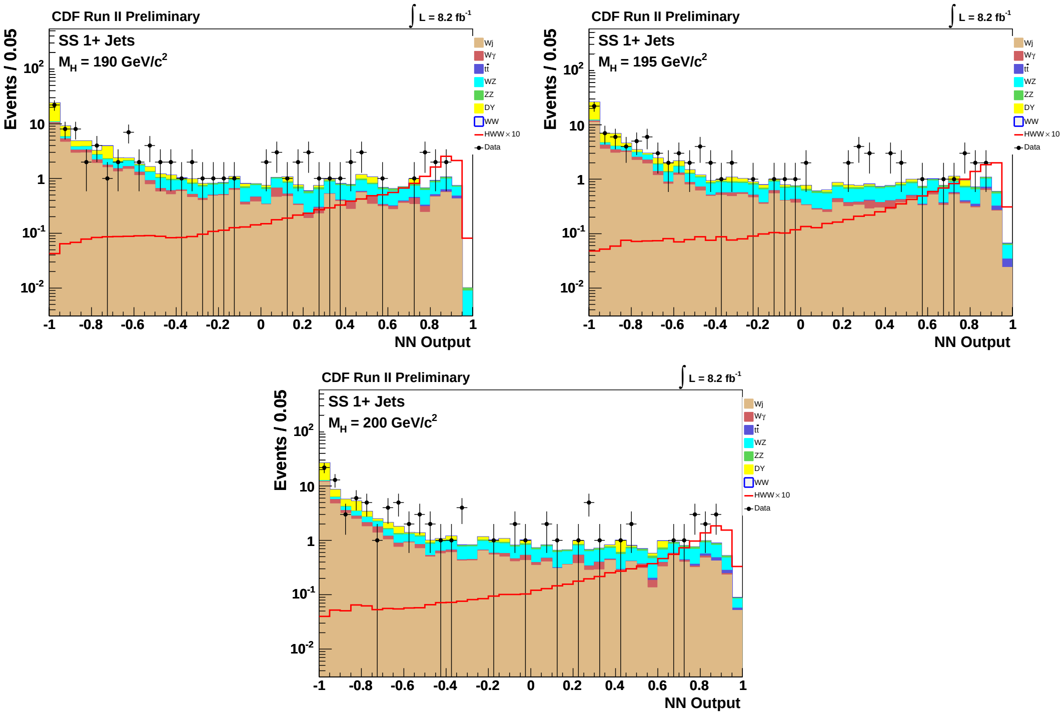

Figure 80: SS Neural Network output templates for several Higgs masses. From the top left to bottom right : 190 GeV, 195 GeV, and 200 GeV.

Mass (GeV/c^2)	gg→H	WH	ZH	VBF
110	-	0.21	0.033	-
115	-	0.35	0.057	-
120	-	0.56	0.088	-
125	-	0.82	0.13	-
130	-	1.1	0.17	-
135	-	1.3	0.2	-
140	-	1.5	0.23	-
145	-	1.7	0.26	-
150	-	1.8	0.28	-
155	-	1.9	0.29	-
160	-	1.9	0.29	-
165	-	1.8	0.28	-
170	-	1.7	0.26	-
175	-	1.6	0.24	-
180	-	1.4	0.22	-
185	-	1.2	0.18	-
190	-	1	0.16	-
195	-	0.89	0.14	-
200	-	0.8	0.12	-

Table 66: Expected Higgs Signal yields as a function of the Higgs boson mass in the SS region for each of the contributing production processes.

tribute only when the charge of a lepton is misidentified. Consequently, we only consider WH and ZH production in the SS analysis. We evaluate the number of events expected from each production process as a function of the mass of the Higgs. These numbers are shown in Table 66.

In calculating the final limits, we take into account systematic uncertainties on both the signal and background models we use to train our neural networks. Systematic uncertainties for the SS region are summarized in Table 67. Figure 81 shows the expected (based on 10000 pseudo-experiments) and observed limits obtained from the SS region.

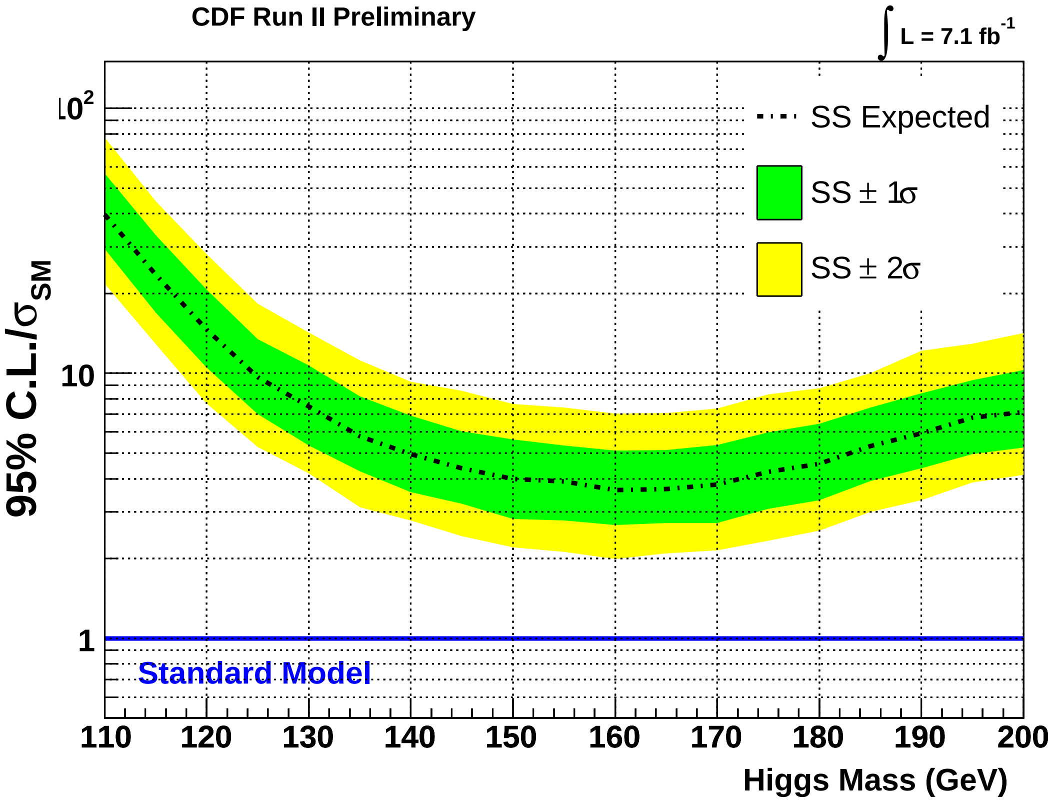

SS	110	115	120	125	130	135	140	145	150	155	160	165	170	175	180	185	190	195	200
$-2\sigma/\sigma_{SM}$	21.75	12.85	7.70	5.28	4.19	3.12	2.78	2.42	2.20	2.12	1.99	2.09	2.15	2.33	2.55	3.00	3.33	3.86	4.13
$-1\sigma/\sigma_{SM}$	29.44	16.90	10.53	7.00	5.34	4.26	3.56	3.22	2.82	2.78	2.68	2.73	2.72	3.07	3.31	3.92	4.38	4.95	5.25
Median/σ_{SM}	**39.65**	**23.56**	**14.63**	**9.66**	**7.50**	**5.79**	**4.95**	**4.38**	**4.00**	**3.91**	**3.63**	**3.65**	**3.80**	**4.24**	**4.56**	**5.32**	**5.93**	**6.80**	**7.13**
$+1\sigma/\sigma_{SM}$	56.70	33.12	20.73	13.46	10.68	8.17	6.93	6.03	5.64	5.34	5.11	5.12	5.36	5.98	6.45	7.43	8.41	9.42	10.27
$+2\sigma/\sigma_{SM}$	77.49	44.60	28.19	18.33	14.22	11.18	9.30	8.59	7.67	7.42	7.06	7.06	7.37	8.34	8.80	10.01	12.18	12.95	14.21
Observed/σ_{SM}	**88.42**	**53.61**	**32.31**	**20.10**	**16.05**	**11.70**	**10.34**	**8.67**	**7.63**	**8.06**	**7.04**	**6.10**	**7.39**	**9.23**	**9.24**	**10.57**	**12.20**	**13.64**	**15.23**

Figure 81: Expected and observed sensitivity for $H \rightarrow WW$ events with two same-sign leptons in the final state. In this region we consider potential signal contributions from associated production with either a W or Z boson.

Uncertainty Source	WW	WZ	ZZ	$t\bar{t}$	DY	$W\gamma$	W+jet	WH	ZH
Cross Section									
Total	*6.0%*	*6.0%*	*6.0%*	10.0%	5.0%			**5.0%**	**5.0%**
Acceptance									
Scale (jets)	-6.1%								
PDF Model (jets)	5.7%								
Higher-order Diagrams		*10.0%*	*10.0%*	10.0%	10.0%	10.0%		**10.0%**	**10.0%**
Jet Energy Scale	*-14.0%*	*-3.9%*	*-2.8%*	*-0.6%*	*-9.3%*	*-7.6%*		*-1.0%*	*-0.7%*
$W\gamma$ Modeling						10.0%			
Jet Fake Rates							39.1%		
Charge Mismeasurement Rate	*19.0%*			*19.0%*	*19.0%*				
Luminosity	*7.3%*	*7.3%*	*7.3%*	*7.3%*	*7.3%*			*7.3%*	*7.3%*

Table 67: Systematics table for SS region signal and background processes. Cross section systematics are correlated for the diboson processes (shown in italic font) but uncorrelated between all other processes. Higher-order diagrams for the VH, shown in boldface font, are correlated among each other but uncorrelated from background processes.

13 Event Summary and Signatures of the WH and ZH Trilepton Analyses

13.1 Trilepton Signal Regions Defined

The trilepton analysis focuses virtually entirely on the two associated production channels because there are three vector bosons that allow for decays to more than two leptons, whereas the gluon fusion and vector boson fusion signals do not contribute a real third lepton. Monte Carlo signal simulation does indicate that gluon fusion and vector-boson fusion have negligible contribution to the three-lepton bin. Thus, we are left with two signals to study: a $WH \rightarrow WWW \rightarrow l\nu, l\nu, l\nu$ signal and a $ZH \rightarrow ZWW \rightarrow ll, l\nu, \text{jet(s)}$ signal. With two signals we naturally define two new trilepton signal regions attempting to isolate each, ameliorating the effort to discriminate each from background based on their unique characteristics.

Consider the three leptons as ordered by their transverse momentum (p_T) for muons or transverse energy (E_T) for electrons such that the highest p_T (E_T) lepton is the 1^{st} and the lowest p_T (E_T) lepton is the 3^{rd}. We filter trilepton events into *InZPeak1Jets* and *InZPeak2orMoreJets* categories if any of the three possible dilepton pairings (that is, pairing the 1^{st} lepton with the 2^{nd} lepton; the 1^{st} lepton with the 3^{rd} lepton; or the 2^{nd} lepton with the 3^{rd} lepton) has an invariant mass value that falls within a ± 15 GeV window of the Z-boson mass at 91 GeV, have opposite signs, and have same flavor. These *InZPeak1Jets* and *InZPeak2orMoreJets* regions are chosen to isolate the ZH signal process. The rest of the trileptons events are directed toward the *NoZPeak* region, which focuses on the WH signal process.

Additionally, the WH analysis has a missing energy cut of $\not{E}_T > 20$ GeV. This cut drastically reduces the $Z\gamma$ background contribution and also provides a WH control region in $10.0 < \not{E}_T < 20.0$ GeV. Because the $WH \rightarrow WWW \rightarrow l\nu l\nu l\nu$ event topology has three $W \rightarrow l\nu$ decays, the missing energy is relatively large and a negligible amount of signal is lost from moving the $\not{E}_T$ cut up to 20.0 GeV from 10.0 GeV.

The $\not{E}_T$ distribution for the $ZH \rightarrow ZWW$ trilepton events is somewhat lower than that of the WH analysis because it produces fewer neutrinos ($WWW \rightarrow l\nu, l\nu, l\nu$ has three neutrinos while $ZWW \rightarrow ll, l\nu, jet$ has only one), so defining a control region by a higher $\not{E}_T$ cut is less appropriate. The ZH analysis also has somewhat larger backgrounds than the WH region and is topologically similar to the most significant background, WZ. However, for a $ZH \rightarrow ZWW$ event to produce a three-lepton signature we either have one of the W-leptons decaying hadronically or–less frequently–we have a $ZH \rightarrow ZWW \rightarrow llll$ physics event that loses one of it's leptons to an area of the detector that is incapable of reconstructing a track (detector holes or too far forward in pseudorapidity, for example) but is still recorded by the calorimeter system. Therefore, ZH trilepton events inherently have a higher number of jets than the backgrounds and very little signal in the NJet$= 0$ bin. By the event topology, one of the Higgs-W-bosons decays hadronically, so two jets are expected. This characteristic of the ZH trilepton signal allows us to create a control region for the ZH analysis in the NJet= 0 bin with very little signal loss, and so NJet= 0 events are not included in the ZH analysis.

Observe in table 13.2 that $\sim 77\%$ of the signal in the *NoZPeak* region is WH, while $\sim 96\%$ of the signal in the *InZPeak* region is ZH. We will see in section 17 how this division allows us to focus on the unique characteristic of each signal for discrimination from the background in the NeuroBayes neural net treatment.

Summarily, the signal regions are defined as:

1. WH Analysis:
   - Z-Peak is removed ($m_{ll} \notin [76.0, 106.0]$ GeV)
   - $\not{E}_T > 20.0$ GeV
   - Any number of jets
2. ZH, NJet=1 Analysis:
   - Z-Peak is selected ($m_{ll} \in [76.0, 106.0]$ GeV)
   - $\not{E}_T > 10.0$ GeV
   - Number of jets = 1
3. ZH, NJet≥2 Analysis:
   - Z-Peak is selected ($m_{ll} \in [76.0, 106.0]$ GeV)
   - $\not{E}_T > 10.0$ GeV
   - Number of jets ≥ 2

13.2 Backgrounds

All regions of this trilepton analysis have five background categories considered: WZ, ZZ, $Z\gamma$ (replacing Drell-Yan), Fakes (data-based WW and Z+jets), and $t\bar{t}$. Each is summarized in table 13.2 along with the predicted signal for a $m_H = 165$ GeV Standard Model Higgs boson and the data.

CDF Run II Prebless $\int \mathcal{L} = 7.1$ fb^{-1}

($m_H = 165$ GeV/c^2)	**WH**	**ZH 1-Jet**	**ZH $\geq$ 2-Jet**
WZ	$6.29 \pm 0.89_{\text{syst}}$	$10.1 \pm 1.42_{\text{syst}}$	$2.70 \pm 0.38_{\text{syst}}$
ZZ	$1.53 \pm 0.22_{\text{syst}}$	$4.70 \pm 0.66_{\text{syst}}$	$1.57 \pm 0.22_{\text{syst}}$
$Z\gamma$	$3.71 \pm 0.73_{\text{syst}}$	$4.89 \pm 0.96_{\text{syst}}$	$1.59 \pm 0.31_{\text{syst}}$
Fakes (WW,Z+Jets)	$3.32 \pm 0.82_{\text{syst}}$	$6.28 \pm 1.62_{\text{syst}}$	$2.89 \pm 0.73_{\text{syst}}$
$t\bar{t}$	$0.36 \pm 0.12_{\text{syst}}$	$0.07 \pm 0.02_{\text{syst}}$	$0.07 \pm 0.02_{\text{syst}}$
Total Background	$15.2 \pm 1.70_{\text{syst}}$	$26.0 \pm 2.98_{\text{syst}}$	$8.82 \pm 1.05_{\text{syst}}$
WH	$0.72 \pm 0.10_{\text{syst}}$	$0.03 \pm 0.005_{\text{syst}}$	$0.01 \pm 0.001_{\text{syst}}$
ZH	$0.19 \pm 0.03_{\text{syst}}$	$0.24 \pm 0.03_{\text{syst}}$	$0.58 \pm 0.08_{\text{syst}}$
Total Signal	$0.91 \pm 0.12_{\text{syst}}$	$0.27 \pm 0.04_{\text{syst}}$	$0.59 \pm 0.08_{\text{syst}}$
Data	11	28	16

High Mass

13.2.1 Heavy Dibosons: WZ, ZZ

The WZ and ZZ diboson contributions provide three physical leptons, with WZ being the dominant background in both trilepton signal regions. Both samples are Pythia-based, where the W is allowed to decay inclusively and the Z is forced to decay leptonically (electron, muon, or tau pairs)[1].

13.2.2 $Z\gamma$

The $Z\gamma$ background in the trilepton analyses replaces the Drell Yan contribution of the dilepton analyses and is created by the Bauer generator. The third lepton from a Drell Yan process is acquired when either an initial or final state radiated photon undergoes a "conversion" (the photon interacts with detector apparatus to become an $e\bar{e}$ pair) and showers in the calorimeter for the third lepton signature. As such, the $Z\gamma$ is the restriction of Drell Yan to those events which do radiate a photon for the purpose of working with a larger statistical sample.

13.2.3 Fakes(WW, Z+Jets)

In the dilepton analysis, the Fakes category is measured from single high p_T lepton data (rather than MC) and assumed to have a predominantly Z+jets event topology, where the two leptons are from the Z-boson.

13.2.4 $t\bar{t}$

The $t\bar{t}$ process is the smallest background, but arguably the most complex. This process decays to a pair of b-jets accompanied by a W bosons. For the case of trileptons, we consider the situation of the two W's decaying leptonically. The third lepton signature is then due to one of the b-jets, which is supposed to produce a lepton candidate with higher probability than a light jet, but this rate is not precisely known.

Because of this, we cannot ignore the possible contribution of $t\bar{t}$ in our Fakes background category where the lepton decayed from the b-jet is the fake lepton (denominator object). However, any $t\bar{t}$ that might be included in the high p_T lepton data of the Fakes background is then scaled down by a fake rate determined for a sample of jets assumed to be mostly light–hence, the $t\bar{t}$ contribution to the Fakes background is scaled down further than it should be since its jets are only the heavy b-jets.

The standard MC $t\bar{t}$ ntuple used by the $H \rightarrow WW$ group requires reconstructed leptons to pass a matching criteria to either a generator-level lepton or photon (for the case of photon conversion). For our purposes in the trilepton analysis, we are interested in a third lepton whose signature is the result of those b-jets, so we have our own MC $t\bar{t}$ sample that allows matching to b-jets as well as leptons and photons. The MC $t\bar{t}$ sample accounts for such events that result in three fully identified leptons, as opposed to the 2 leptons+1 fake lepton signature of the Fakes background.

Lastly, there is inevitably some overlap between the $t\bar{t}$ that occurs implicitly in the Fakes data-based background and the MC sample. By measuring the difference between the 3-lepton bin of the default $t\bar{t}$ sample (lepton match only to generator-level leptons or photons) with another $t\bar{t}$ sample allowing matching to b-jets as well, we take half the percentage difference to be the systematic error accounting for overlap.

14 Neural Net

The trilepton $H \to WW$ analyses rely on the NeuroBayes neural network package to discriminate signal from background; we do not attempt the Matrix Element method in this study. We use 14 input variables for the WH analysis, and 16 for the ZH (1 jet) analysis, and 18 for the ZH (≥ 2) analyis. The neural net results can be seen in figures 82, 83, 84, 85, 86, 87.

Recall that the standard model Higgs boson is postulated as a scalar particle and so decays to two W-bosons having $+1$ and -1 spin, respectively. Leptonic W-boson decays have a $V - A$ distribution, so one of the W bosons decays to a lepton projected forward along its momentum vector while the other decays its lepton backwards along its momentum vector. If the two Higgs-W-bosons decay close to back-to-back in the experimental rest frame–which is not a terrible assumption for a high mass Higgs–then the two decayed leptons will tend to have a relatively close proximity. Indeed, we find that this is the case for WH events since both Higgs-W-bosons must decay leptonically. Also, $\not{E}_T$ is an excellent discriminating variable for WH events since three leptonic decays of W's implies at least three neutrinos carrying away undetected energy.

Other variables that are excellent for discriminating ZH in the trilepton case are $\not{E}_T$ (ZH may have fewer neutrinos that WH, but the distribution still tends to be higher than the backgrounds), Lead Jet E_T (jets from vector bosons tend to have higher energy than other sources of jets), and ΔR between the W-lepton and the leading jet (that is, between the decay products of the two Higgs-W-bosons).

- $\not{E}_T$: The missing transverse energy of the signal is high because of the neutrinos decaying from W-bosons.
- NJet: The ZH signal tends to have two jets while the background tend to have zero jets (except for $t\bar{t}$).
- ΔR b/w Opp. Sign Close Leptons: With three leptons there are three possible pairings of leptons. Events with all three leptons having the same sign are rejected from this analysis, so every event has two possible pairings of opposite-signed leptons. Of those two pairings, this variable is the ΔR value of the pairing with lower ΔR value.
- H_T: Sum of the transverse energies of all three leptons, the $\not{E}_T$, and all jets. Basically, this is a sum of all transverse energy produced in the event.
- Invariant mass of opposite-signed leptons closest in ϕ: This is a partial reconstruction of the WH Higgs boson mass with the energy of the neutrinos left out. Since there are two neutrinos inherent to this decay, we cannot know how much energy each individually had. Also, if such neutrinos have momentum vectors with magnitudes in opposite directions, those values would cancel out, so using the sum of these two leptons with the $\not{E}_T$ would be inappropriate.

- $\Delta\phi$(Lep2,$\not\!\!E_T$): The magnitude of the difference in ϕ between the 2nd lepton by p_T and the $\not\!\!E_T$.

- Inv. Mass(Lep3,$\not\!\!E_T$,Jets): Invariant mass of the vector sum of the 3rd lepton, $\not\!\!E_T$, and Jets.

- m_T(Leptons,$\not\!\!E_T$,Jets): Transverse mass of the vector sum of all three leptons, $\not\!\!E_T$, and all jets.

- p_T of the 2nd lepton by p_T: The signals tend to produce pairs of leptons with similar momenta, so the second lepton by p_T trends higher for signals than backgrounds.

- ΔR Opp. Sign Far Leptons: With three leptons there are three possible pairings of leptons. Events with all three leptons having the same sign are rejected from this analysis, so every event has two possible pairings of opposite-signed leptons. Of those two pairings, this variable is the ΔR value of the pairing with higher ΔR value.

- m_T Trilepton Mass: Transverse mass of the vector sum of the three leptons.

- m_T (Lep3, $\not\!\!E_T$): Transverse mass of the vector sum of the 3rd lepton and the $\not\!\!E_T$.

- Inv. Mass(Lep1,Lep2,$\not\!\!E_T$): Invariant mass of the vector sum of the 1st lepton, 2nd lepton, and $\not\!\!E_T$.

- Lead Jet E_T: Transverse energy of the leading jet. The ZH analysis tends to have high energy jets since they come from a W that comes from the Higgs boson.

- ΔR(W-Lep, Lead Jet): The *InZPeak* region is defined by having one lepton paring (opposite signed, same flavor) near the Z boson mass. Denote the one other lepton not in this pairing as the W-lepton. This variable is then the ΔR between the W-lepton and the leading jet, both descending from the Higgs.

- Dimass(W-Lep,$\not\!\!E_T$): The ZH analysis regions are defined by having one lepton paring (opposite signed, same flavor) near the Z-boson mass. Denote the one other lepton not in this pairing as the W-lepton. This variable is then the invariant mass of the vector sum of the W-lepton and the $\not\!\!E_T$.

- m_T(W-Lep,$\not\!\!E_T$): Transverse mass of the vector sum of the W-lepton and the $\not\!\!E_T$.

- $\Delta\phi$(Leptons,$\not\!\!E_T$): $\Delta\phi$ between the vector sum of the three leptons and the $\not\!\!E_T$.

- The invariant mass of the vector sum of the three leptons.

- m_T Jets: Transverse mass of the vector sum of all jets.

- $\Delta\phi$(Z-Leptons,W-Lepton): ΔR between the vector sum of the two leptons identified as the Z-leptons, and the other lepton.
- Lepton Type Combination: Identified lepton flavor combination, eee, $ee\mu$, $e\mu\mu$, etc.
- Invariant mass of the leading two jets.
- ΔR between the leading two jets.
- ZH Higgs mass: Invariant mass of the leading two jets and the W-lepton.

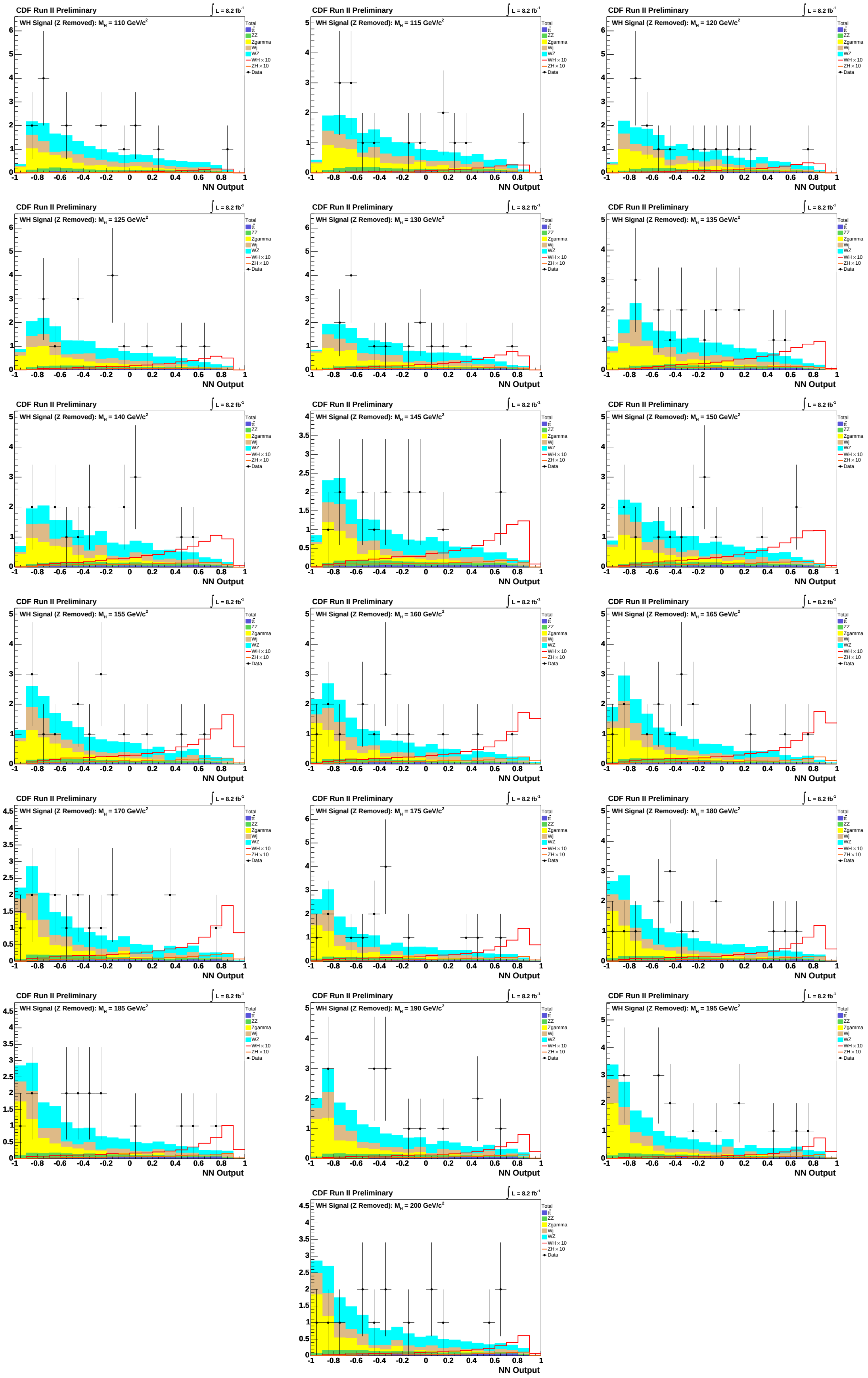

Figure 82: Trilepton WH NeuroBayes Neural Network output (linear scale)

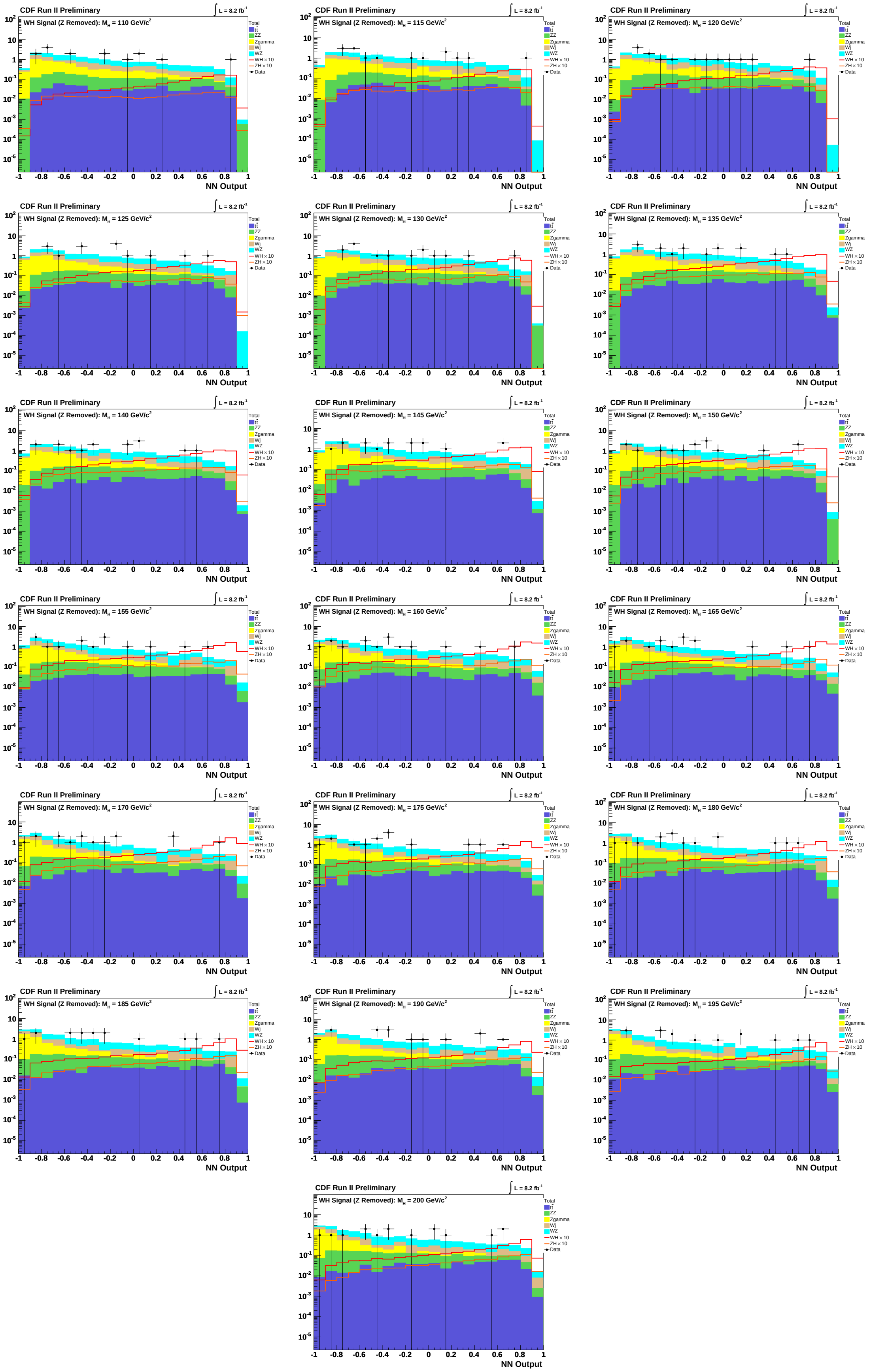

Figure 83: Trilepton WH NeuroBayes Neural Network output (logarithmic scale)

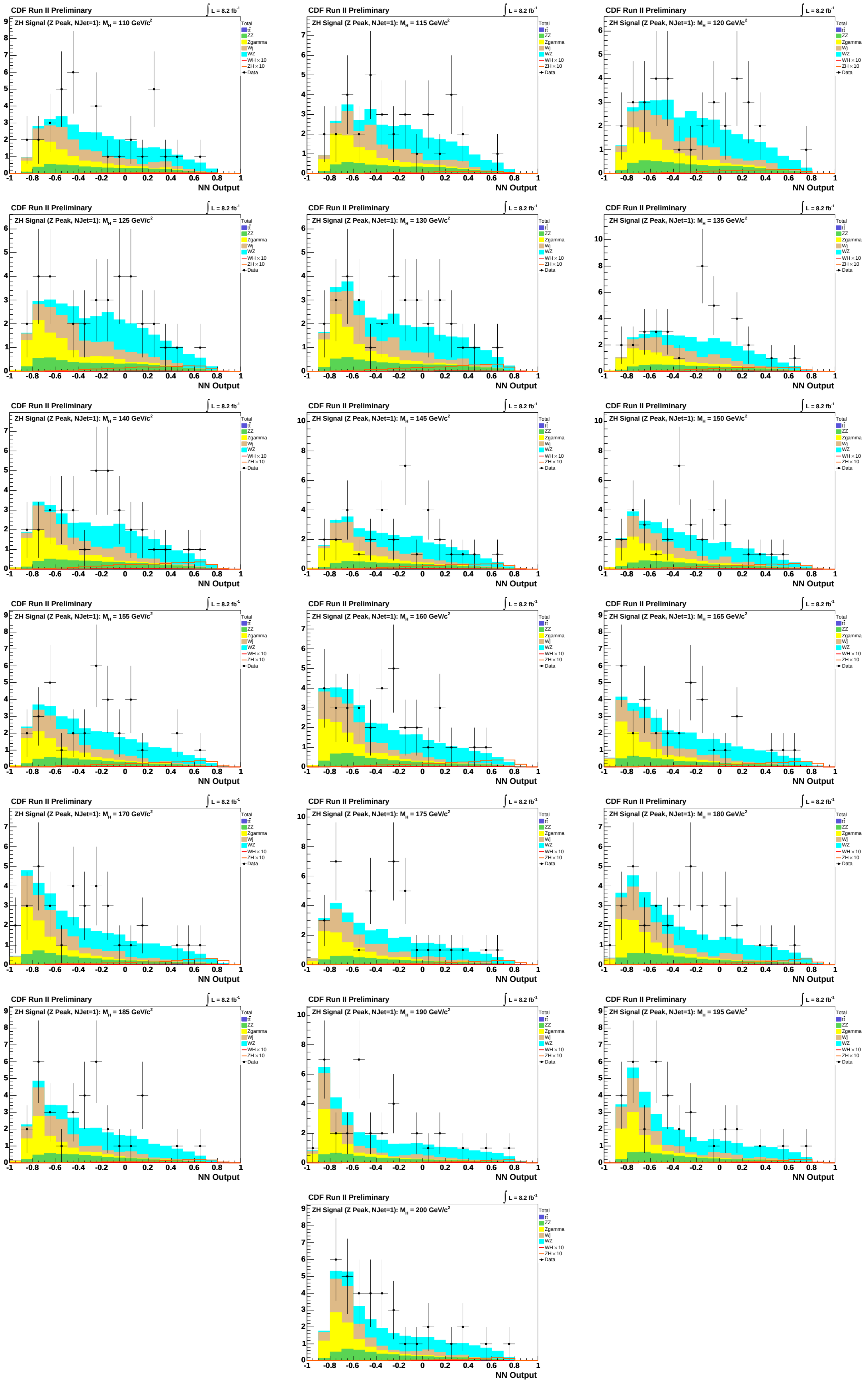

Figure 84: Trilepton ZH (1 jet) NeuroBayes Neural Network output (linear scale)

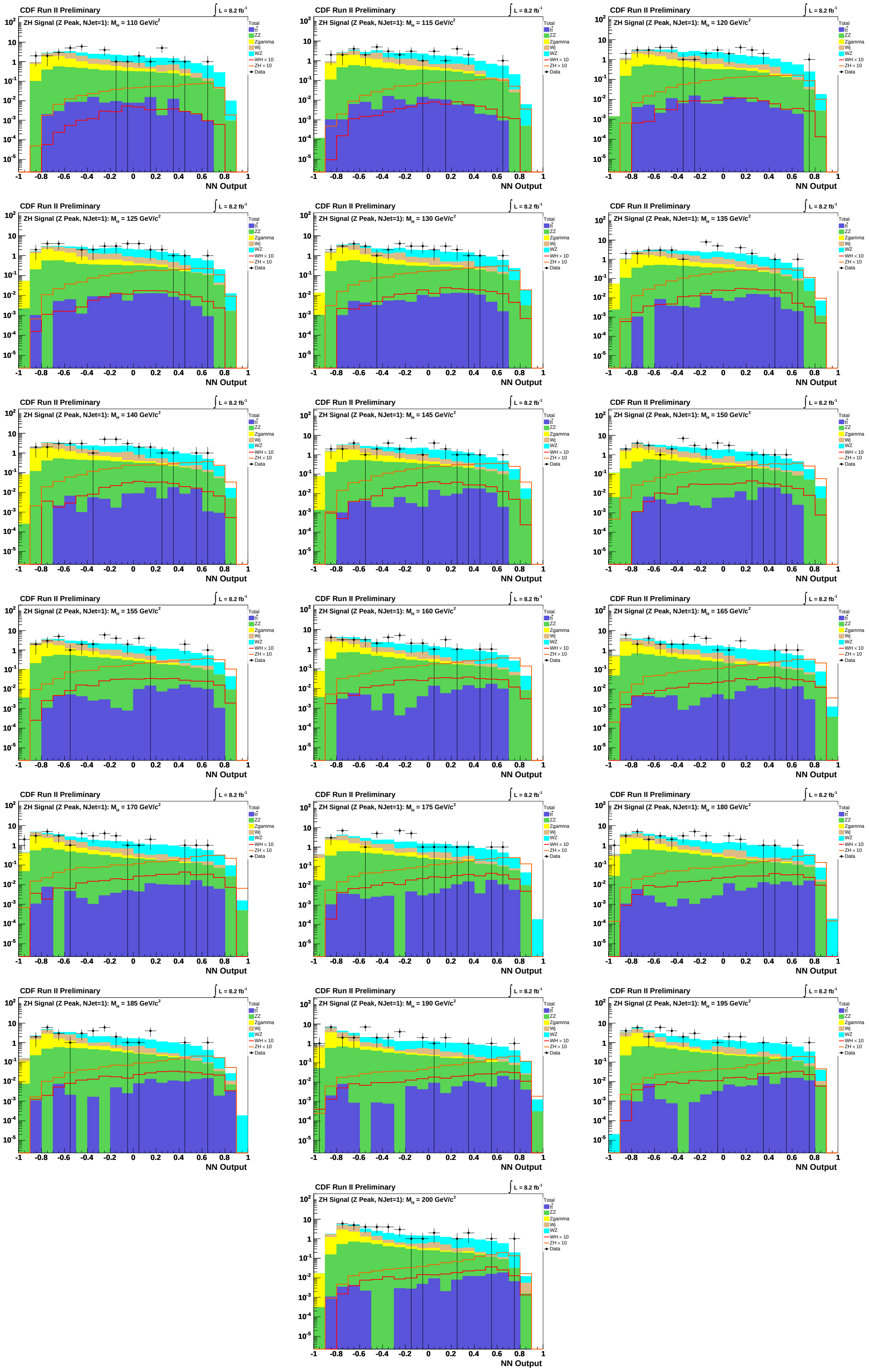

Figure 85: Trilepton ZH (1 jet) NeuroBayes Neural Network output (logarithmic scale)

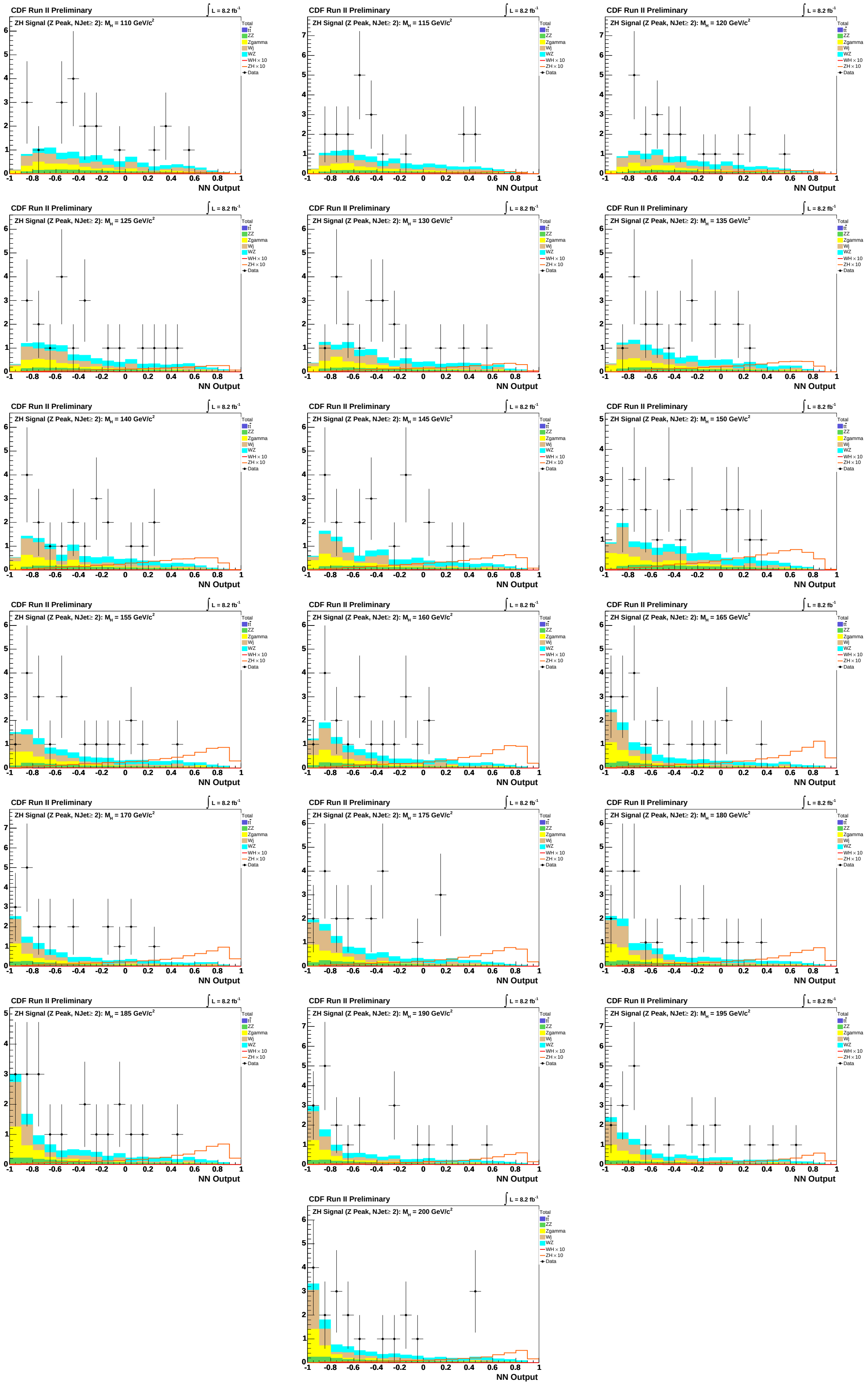

Figure 86: Trilepton ZH (≥ 2 jets) NeuroBayes Neural Network output (linear scale)

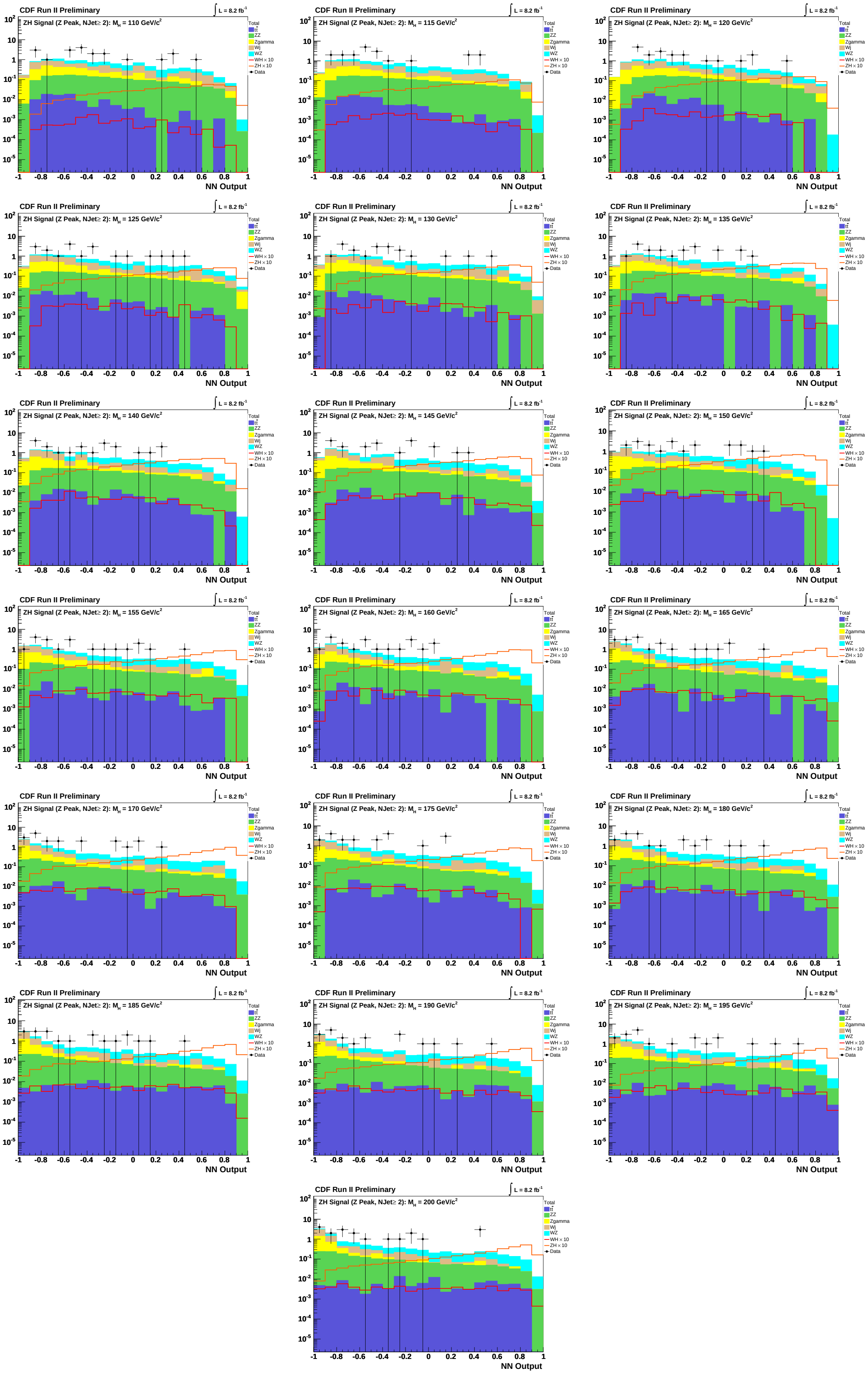

Figure 87: Trilepton ZH ($\geq$ 2 jets) NeuroBayes Neural Network output (logarithmic scale)

15 Control Regions

The modeling of basic kinematic properties and the discriminating variables in the Monte Carlo simulation is tested by comparing the distributions of these variables in the final selected data. Ideally, the modeling of these variables is further tested by creating orthogonal "control regions" which are enhanced in specific major backgrounds and contain minimum possible signal contribution.

The control regions we choose for both the WH and ZH trilepton analyses contain minimal signal (see table 15) so cutting them out of the analyses drastically cuts down the background to discriminate against in addition to providing a verification of modeling.

CDF Run II Prebless $\int \mathcal{L} = 7.1$ fb^{-1}

($m_H = 165$ GeV/c^2)	**WH Control**	**ZH Control**
WZ	0.71 ± 0.10_{syst}	44.5 ± 8.61_{syst}
ZZ	0.70 ± 0.10_{syst}	4.99 ± 0.77_{syst}
$Z\gamma$	27.3 ± 5.44_{syst}	11.79 ± 2.49_{syst}
Fakes (WW,Z+Jets)	6.84 ± 1.70_{syst}	13.5 ± 4.05_{syst}
$t\bar{t}$	0.02 ± 0.005_{syst}	0.009 ± 0.003_{syst}
Total Background	35.6 ± 5.74_{syst}	74.8 ± 11.4_{syst}
WH	0.03 ± 0.004_{syst}	0.12 ± 0.02_{syst}
ZH	0.01 ± 0.002_{syst}	0.09 ± 0.01_{syst}
Total Signal	0.04 ± 0.006_{syst}	0.20 ± 0.03_{syst}
Data	35	78

High Mass

They are:

- WH Analysis Control Region: $10.0 < \not\!\!E_T < 20.0$
- ZH Analysis Control Region: Number of Jets= 0

The topology of WH associated production in the trilepton channel also contains at least three neutrinos (more if $W \to \tau\nu_\tau \to l_{e,\mu}\nu_{e,\mu}\nu_\tau$ decays are involved), resulting in high missing energy values. The low $\not\!\!E_T$ region is a natural choice for a control region in the WH analysis since it contains negligible signal contribution and is enriched in $Z\gamma$ and Fakes backgrounds. Also including a $\not\!\!E_T > 20$ cut for the WH signal region substantially enhances the signal to background ratio in the final signal region.

Similarly, the topology of ZH associated production lends to a preference for at least one or two jets since one of the two Higgs-W-bosons decays hadronically. Only $\sim 12\%$ of the trilepton ZH signal is present in the NJet= 0 bin, but much of it's most dominant background, WZ, is. Thus, the NJet= 0 bin is a natural choice for the control region of the ZH trilepton analysis. Unfortunately, there are several nefarious difficulties that arise from this choice that must be discussed. First, three of the discriminating variables chosen in the neural network treatment discussed in section 17 are undefined when NJet= 0 (though can be powerful discriminators among those events that do have at least one jet, serving as yet another argument for this choice of control region) and NJet must be excluded as a discriminating variable as well since the control region allows it only one possible value by definition (a variable cannot be used to discriminate background from signal when both background and signal must have identical values for that variable). The neural network result for the control region of ZH has the following removed from the list of discriminating variables:

- NJet
- E_T of the leading jet
- ΔR between the W-lepton and the leading jet. Denote the two leptons with dilepton invariant mass $\in [81.0, 101.0]$ GeV (the definition of the *InZPeak* region for the ZH analysis) as the Z-leptons, then the other lepton is denoted the W-lepton.
- Transverse mass of the vector sum of all jets

While this choice of control region poses challenges, we are rewarded with both a cut that excludes a large portion of the backgrounds with minimal signal loss and with three powerful discriminating variables that would be ill-defined otherwise.

We provide here the neural net score for the discriminating variables in the WH and ZH trilepton analyses control regions. The MC models the data well.

16 Systematic Errors

The systematic uncertainties used are summarized in table 68. Most values used are standard to all $H \to WW$ analyses, but since $Z\gamma$ is a new background in this analysis–and a couple other reasons–there are several new systematics particular to this analysis.

- *$Z\gamma$ (and $W\gamma$) Scaling*: Note that the $W\gamma$ background is already scaled down by 17% in other $H \to WW$ analyses due to known mismodelling of photon conversions. We are using the same scale factor for the $Z\gamma$ contribution since the same photon conversion affect is assumed, as such we use the same systematic error associated with this scale factor. Also, we keep this systematic error correlated between the $Z\gamma$ of the trilepton analyses and $W\gamma$ of the dilepton analyses because of the common origin.
- *$Z\gamma$ Higher Order Diagrams*: We have for $W\gamma$ in the dilepton analysis the $W\gamma$ *higher order diagrams* systematic, which accounts for poor MC modeling beyond leading order. Likewise, we assume the same error of 11% for a new $Z\gamma$ *higher order diagrams* systematic since both are modelled by the Bauer MC generator.

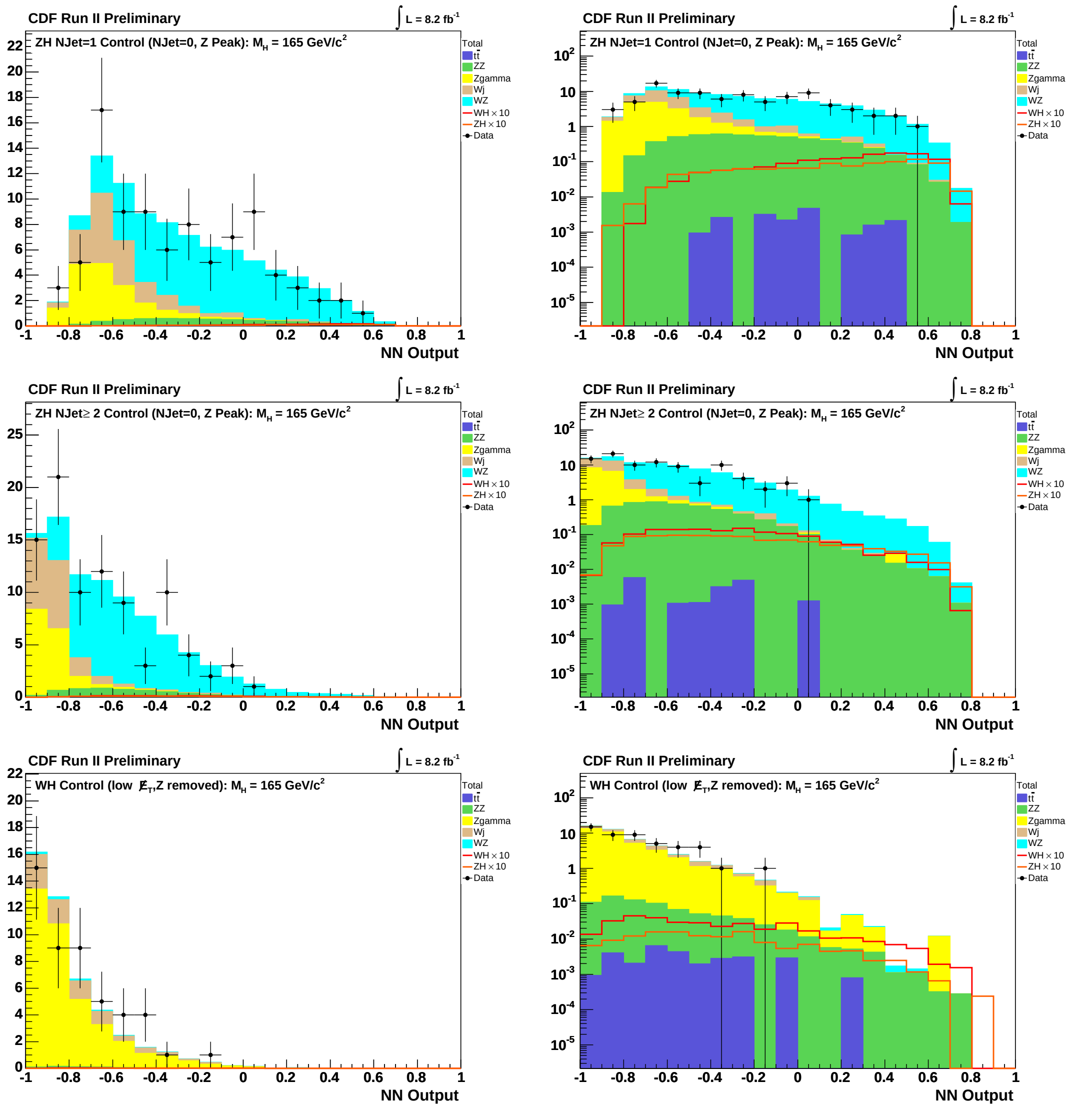

Figure 88: WH Control Region (10.0 GeV < $\not{E}_T$ < 20.0 GeV) and ZH Control Region (NJet= 0) neural net results against samples trained on signal regions.

Systematic Uncertainty	WZ	ZZ	$Z\gamma$	$t\bar{t}$	Fakes	WH	ZH
Diboson Higher Order Diagrams	0.100	0.100					
$t\bar{t}$ Higher Order Diagrams				0.100			
Higgs Higher Order Diagrams						0.100	0.100
PDF Model	0.027	0.027		0.021		0.012	0.009
Lepton ID Efficiencies	0.020	0.020		0.020		0.020	0.020
Trigger Efficiences	0.021	0.021		0.020		0.021	0.021
Light Jet Fake Rates					0.300		
b-Jet Fake Rate*				0.23			
Luminosity	0.059	0.059		0.059		0.059	0.059
MC Run Dependence			0.050*				
Jet Energy Scale	0.098*[a]	0.053*[a]	0.086*[a]			0.084*[a]	0.011*[a]
$Z\gamma$ Higher Order Diagrams*			0.110*				
$W\gamma$ Scaling			0.110*				
σ_{Diboson}	0.060	0.060					
$\sigma_{t\bar{t}}$				0.100			
σ_{VH}						0.050	0.050
$\sigma_{\text{Z}\gamma}$*			0.050*				

Table 68: Systematic Uncertainties: Standard values for systematics used in other $H \rightarrow WW$ analyses are used wherever applicable.

[a] Only for the ZH analysis (*trilep-InZPeak* region) because the NJet= 0 bin is removed from the signal region and made a control region.
* New to trilepton analysis, not in dilepton analysis.

- *b-Jet Fake Rate*: Although $t\bar{t}$ is a small contribution to the background for these high m_H standard model Higgs boson in the trilepton case, we do have to account for the peculiar situation that our 3$^{\text{rd}}$ lepton is faked from a b-jet and the rate at which a b-jet fakes a lepton–as opposed to a light jet–is not well-known. Further, as a background with two real leptons and one faked, we cannot ignore the possible coverage of $t\bar{t}$ in the data-based Fakes category. We know that the fake rates used in the Fakes category is based on jet samples populated mostly with light jets and presume that b-jets in particular are more likely than light jets to produce a signature that could fake a lepton. Hence, whatever $t\bar{t}$ contribution that exists in the Fakes category is scaled down by the light jet dominated fake rate, meaning it is scaled down too far. To make up for the difference we use an MC $t\bar{t}$ sample that allows reconstructed leptons to match to generator-level leptons, photons, or b-jets (typically, for these reconstructed MC leptons to be considered fully "found" they must pass a matching criterion to a generator-level lepton or photon only). Now, of course, we have the problem of possible double-counting of $t\bar{t}$ between the

MC and what implicit $t\bar{t}$ contribution populates the Fakes category. To account for the double-counting possibility, we assign a systematic error defined to be one half the percentage difference between the MC $t\bar{t}$ sample that allows leptons to match to generator-level leptons, photons, and b-jets; and the MC $t\bar{t}$ sample that allows such matching to generator-level leptons and photons only. The systematic errors adopted are:

  - WH Analysis (*trilep-NoZPeak region*): 0.223
  - ZH Analysis (*trilep-InZPeak region*): 0.231

- *MC Run Dependence*: The $Z\gamma$ stntuples used cover only periods $0-11$, so we assign the customary MC run dependence systematics for such samples. This is determined by comparing a WW sample with partial run dependence (periods $0-7$) with a fully run-dependent WW sample.

- *Lepton, Trigger ID, Luminosity, Parton Distribution Function Model*: Finally, note that we do not use systematic errors for the lepton, trigger ID, luminosity, and PDF model efficiencies because of the scale factor derived from the $W\gamma$ control region in the dilepton analysis. Since we're measuring the $W\gamma$ normalization directly from data, that systematic should cover these effects. However, to be conservative–especially since we measure the scale factor in a control region with selection cuts that differ from our various signal regions–we keep the systematic uncertainties on the MC that are not related to normalization (higher-order kinematic effects, MC jet modelling).

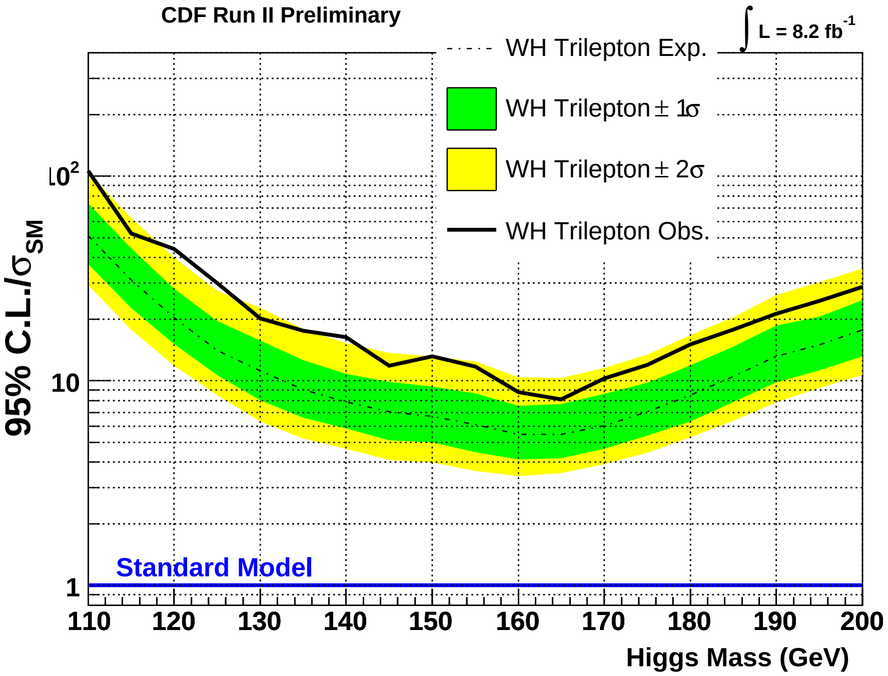

Figure 89: WH Region Limits

17 Results

The results of this trilepton analysis present a significant contribution to the $H \to WW$ combined result. In the 165 GeV bin, the WH analysis expected limits are set at 6.6 times the expected standard model limit; the ZH (1 jet) analysis is set at 29.4 times the expected standard model limit; the ZH (≥ 2 jets) analysis expected limits are set at 8.8 times the expected Standard Model limit; and the combined trilepton analysis is set at 4.4 times the expected standard model limit.

The limit calculations presented were computed with `HWWLimit` version of `MCLimit`. Expected limits for the ZH, WH, and combined trileptons were calculated in each case with 1,000 iterations of 10,000 pseudoexperiments (1000 iterations of 1000 pseudoexperiments performed 10 times), while 500,000 iterations of 1 pseudoexperiment were performed for the observed results–as is standard.

Limits	110	115	120	125	130	135	140	145	150	155
$+2\sigma/\sigma_{\mathrm{SM}}$										
$+1\sigma/\sigma_{\mathrm{SM}}$										
Median/$\sigma_{\mathbf{SM}}$	**65.2**	**37.4**	**24.7**	**17.0**	**13.2**	**10.7**	**9.4**	**8.3**	**8.0**	**7.2**
$-1\sigma/\sigma_{\mathrm{SM}}$										
$-2\sigma/\sigma_{\mathrm{SM}}$										
Observed/$\sigma_{\mathbf{SM}}$	**48.2**	**28.9**	**20.7**	**13.5**	**11.2**	**10.0**	**8.4**	**7.3**	**7.3**	**7.3**
Limits	160	165	170	175	180	185	190	195	200	
$+2\sigma/\sigma_{\mathrm{SM}}$										
$+1\sigma/\sigma_{\mathrm{SM}}$										
Median/$\sigma_{\mathbf{SM}}$	**6.4**	**6.6**	**7.5**	**8.3**	**9.8**	**12.3**	**14.8**	**16.8**	**19.4**	
$-1\sigma/\sigma_{\mathrm{SM}}$										
$-2\sigma/\sigma_{\mathrm{SM}}$										
Observed/$\sigma_{\mathbf{SM}}$	**6.6**	**6.1**	**7.5**	**8.8**	**11.1**	**12.9**	**17.6**	**18.9**	**21.1**	

Table 69: WH trilepton analysis limits for 7.1fb^{-1}.

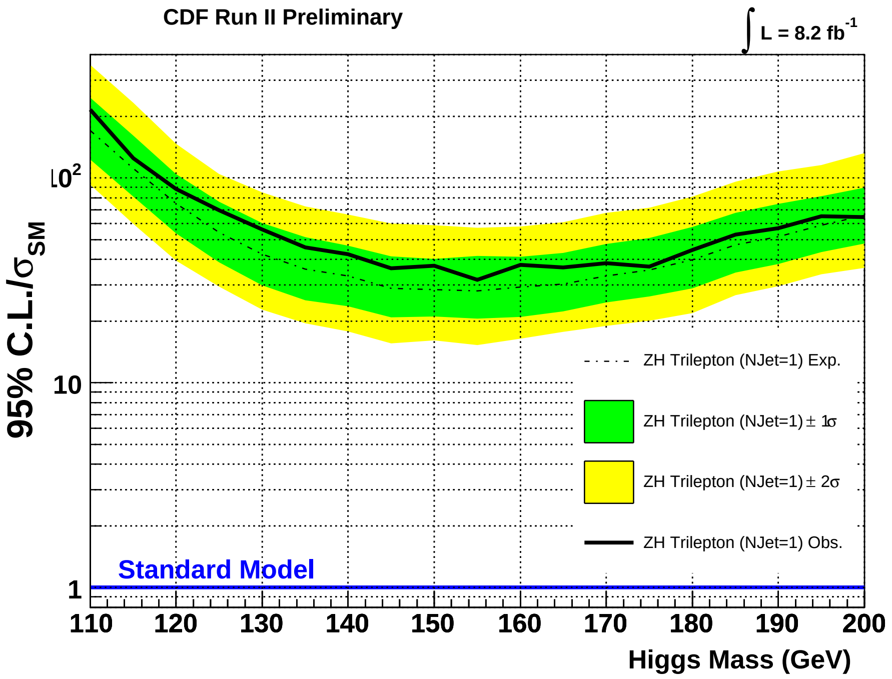

Figure 90: Trilepton *InZPeak* Region Limits

Limits	110	115	120	125	130	135	140	145	150	155
$+2\sigma/\sigma_{\mathrm{SM}}$ $+1\sigma/\sigma_{\mathrm{SM}}$ **Median**$/\sigma_{\mathrm{SM}}$ $-1\sigma/\sigma_{\mathrm{SM}}$ $-2\sigma/\sigma_{\mathrm{SM}}$	**176**	**109**	**71.7**	**53.0**	**41.0**	**35.7**	**31.5**	**29.3**	**28.1**	**27.3**
Observed$/\sigma_{\mathrm{SM}}$	**180**	**114**	**80.9**	**56.2**	**48.8**	**41.8**	**35.4**	**32.2**	**29.0**	**28.1**
Limits	160	165	170	175	180	185	190	195	200	
$+2\sigma/\sigma_{\mathrm{SM}}$ $+1\sigma/\sigma_{\mathrm{SM}}$ **Median**$/\sigma_{\mathrm{SM}}$ $-1\sigma/\sigma_{\mathrm{SM}}$ $-2\sigma/\sigma_{\mathrm{SM}}$	**27.3**	**29.4**	**32.0**	**35.1**	**38.2**	**47.0**	**52.5**	**59.4**	**66.2**	
Observed$/\sigma_{\mathrm{SM}}$	**28.6**	**29.9**	**30.9**	**31.3**	**37.8**	**40.2**	**43.6**	**47.2**	**55.7**	

Table 70: ZH (1 jet) trilepton analysis limits for 7.1fb^{-1}.

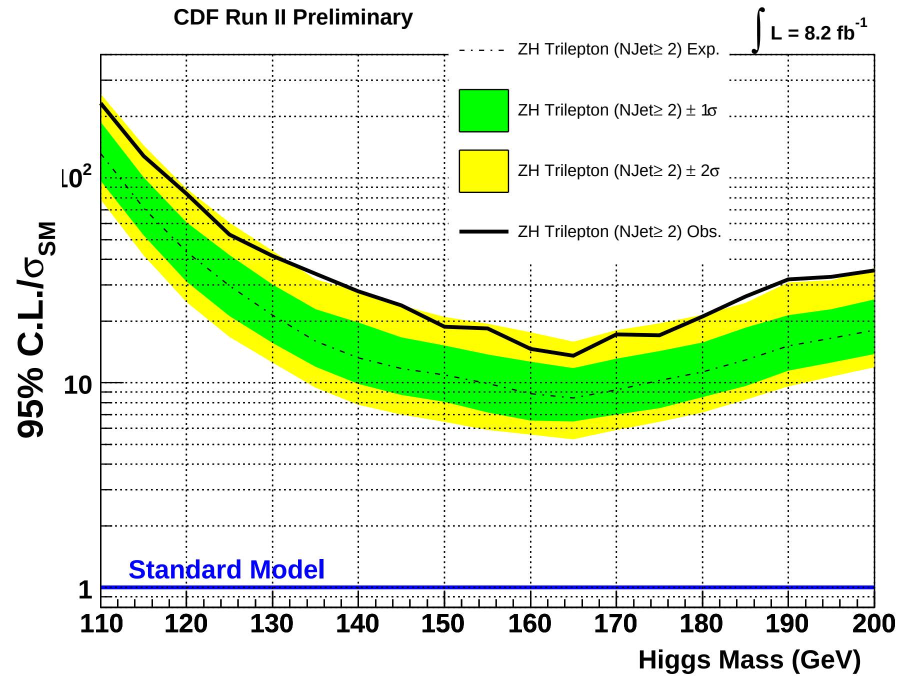

Figure 91: Trilepton *InZPeak* Region Limits

Limits	110	115	120	125	130	135	140	145	150	155
$+2\sigma/\sigma_{\mathrm{SM}}$ $+1\sigma/\sigma_{\mathrm{SM}}$ **Median**$/\sigma_{\mathrm{SM}}$ $-1\sigma/\sigma_{\mathrm{SM}}$ $-2\sigma/\sigma_{\mathrm{SM}}$	**144**	**79.3**	**46.1**	**30.7**	**22.5**	**17.3**	**14.3**	**12.4**	**11.1**	**10.0**
Observed$/\sigma_{\mathrm{SM}}$	**185**	**114**	**76.4**	**50.2**	**34.3**	**31.7**	**24.2**	**20.5**	**16.9**	**14.0**
Limits	160	165	170	175	180	185	190	195	200	
$+2\sigma/\sigma_{\mathrm{SM}}$ $+1\sigma/\sigma_{\mathrm{SM}}$ **Median**$/\sigma_{\mathrm{SM}}$ $-1\sigma/\sigma_{\mathrm{SM}}$ $-2\sigma/\sigma_{\mathrm{SM}}$	**9.1**	**8.8**	**9.7**	**10.3**	**11.3**	**13.7**	**15.8**	**17.4**	**19.0**	
Observed$/\sigma_{\mathrm{SM}}$	**12.0**	**10.8**	**14.2**	**16.8**	**17.1**	**21.8**	**23.8**	**29.4**	**35.8**	

Table 71: ZH (≥ 2 jets) trilepton analysis limits for 7.1fb^{-1}.

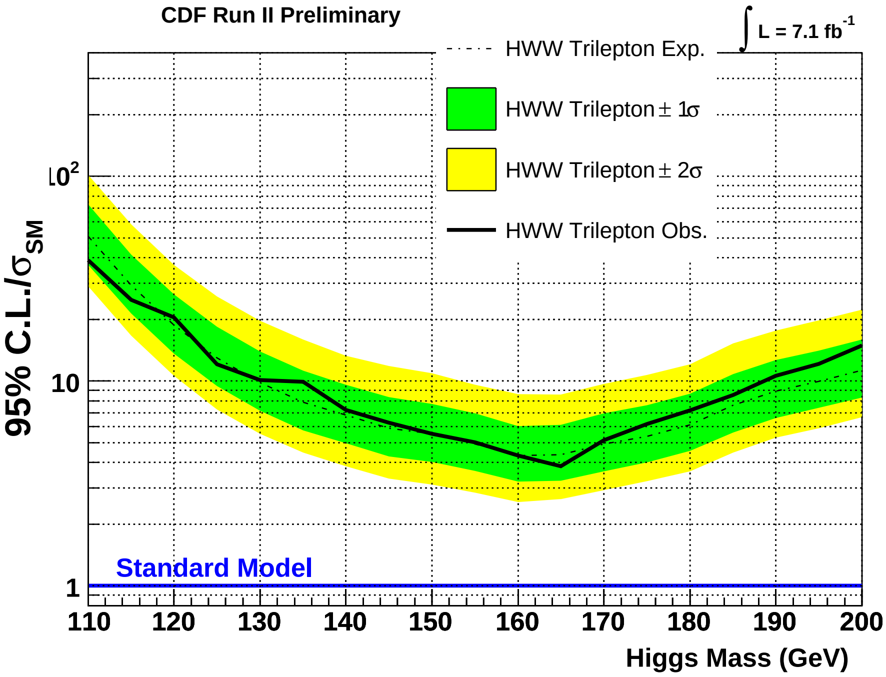

Figure 92: Trilepton Combined Limits

18 Combination of All High-Mass Search Channels

Because we separate events into High S/B and Low S/B categories in the 0J and 1J regions, there are a total of six opposite-sign channels (including opposite-sign events with low dilepton mass). Each channel has its own unique background composition and signal to background ratio, and therefore will contribute different relative sensitivities to the overall cross section limit. As previously mentioned, in the 2J region, we choose to consider all events as a single channel, primarily to maintain sufficient statistics for some of the Monte-Carlo based templates as well as the W+jets (Fakes) templates which lack statistics for the higher jet multiplicities.

Incorporating the same-sign and trilepton regions leaves us with a total of ten channels from which we produce our combined limits. As in the case of 2 or more-jets region, events in the same-sign channel are grouped as a single channel, primarily to maintain sufficient statistics for some of the Monte-Carlo based templates as well as the $W+$ jets (Fakes) templates which lack statistics for the higher jet multiplicities. In addition, dilepton categories including a PHX electron are removed in the same-sign, and most categories treated as Low S/B in the 0-jet and 1-jet regions contain at least one PHX electron. The sensitivity in the same-sign region comes almost entirely from associated production channels (WH, ZH).

We also now incorporate channels where one lepton is a hadronically decaying τ lepton [35, 36]. These channels use the same data samples and e, μ reconstruction as the channels outlined in this note. Events with $e\tau$ and $\mu\tau$ are considered separately, adding two more channels to give a total of twelve channels from which we produce our combined limits.

Limits	110	115	120	125	130	135	140	145	150	155
$+2\sigma/\sigma_{\mathrm{SM}}$ $+1\sigma/\sigma_{\mathrm{SM}}$ **Median**$/\sigma_{\mathbf{SM}}$ $-1\sigma/\sigma_{\mathrm{SM}}$ $-2\sigma/\sigma_{\mathrm{SM}}$	**50.9**	**29.3**	**18.7**	**13.0**	**9.8**	**7.9**	**6.8**	**5.9**	**5.5**	**4.9**
Observed$/\sigma_{\mathbf{SM}}$	**38.9**	**24.9**	**20.5**	**12.1**	**10.1**	**9.9**	**7.2**	**6.3**	**5.5**	**5.0**
Limits	160	165	170	175	180	185	190	195	200	
$+2\sigma/\sigma_{\mathrm{SM}}$ $+1\sigma/\sigma_{\mathrm{SM}}$ **Median**$/\sigma_{\mathbf{SM}}$ $-1\sigma/\sigma_{\mathrm{SM}}$ $-2\sigma/\sigma_{\mathrm{SM}}$	**4.3**	**4.9**	**5.4**	**6.1**	**6.1**	**7.6**	**8.9**	**10.0**	**11.3**	
Observed$/\sigma_{\mathbf{SM}}$	**4.3**	**3.8**	**5.2**	**6.2**	**7.2**	**8.6**	**10.6**	**12.1**	**14.9**	

Table 72: Combined trilepton analysis limits for 7.1fb^{-1}.

As is the case in each of the individual regions, we use Tom Junk's MCLimit [32] to produce a combined limit from all channels. We have opted to set our own statistical errors on each bin and use the CSM_GAUSSIAN_BINERR option in MCLimit. The bin errors are nothing more then the typical statistical errors calculated by ROOT's Sumw2. The current limits from the combination of all twelve channels are not yet ready, and this note will be updated as soon as the combination is available.

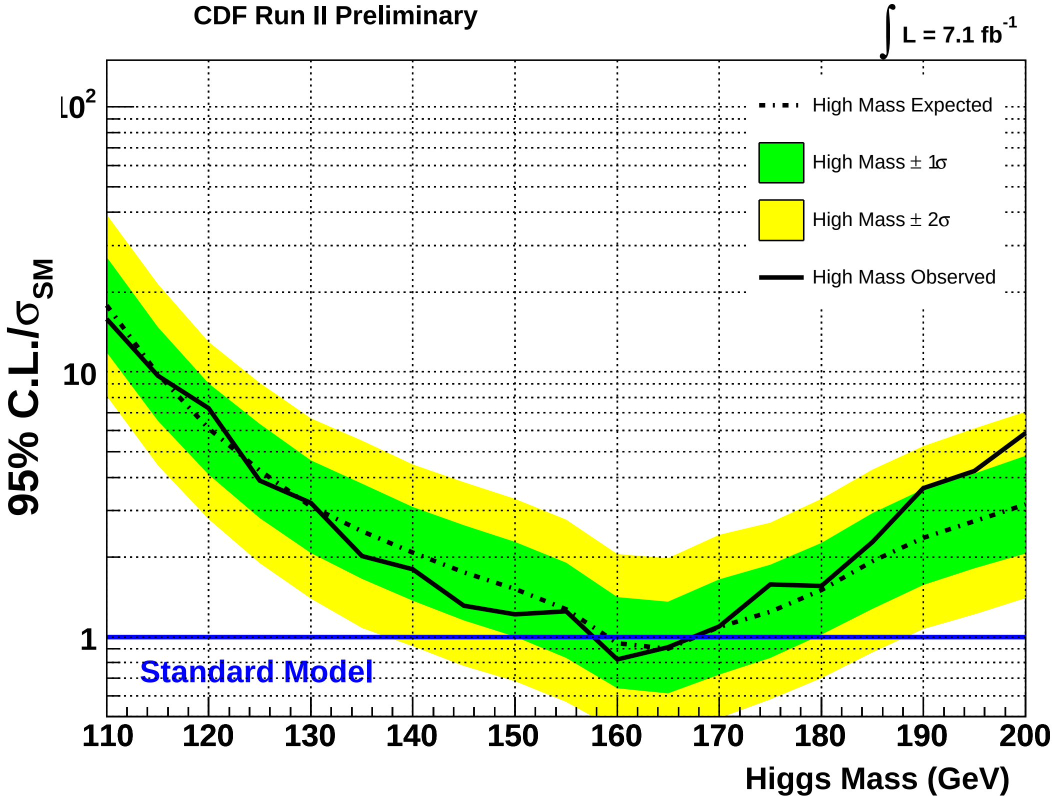

High Mass	110	115	120	125	130	135	140	145	150	155	160	165	170	175	180	185	190	195	200
$-2\sigma/\sigma_{SM}$	8.10	4.44	2.78	1.90	1.39	1.08	0.92	0.77	0.68	0.57	0.45	0.43	0.49	0.58	0.70	0.87	1.07	1.22	1.40
$-1\sigma/\sigma_{SM}$	11.83	6.52	4.09	2.81	2.07	1.65	1.37	1.15	1.00	0.83	0.64	0.61	0.72	0.83	1.02	1.28	1.57	1.81	2.07
Median/σ_{SM}	**17.80**	**9.82**	**6.11**	**4.25**	**3.10**	**2.51**	**2.08**	**1.75**	**1.51**	**1.27**	**0.95**	**0.90**	**1.09**	**1.24**	**1.50**	**1.93**	**2.37**	**2.73**	**3.16**
$+1\sigma/\sigma_{SM}$	27.05	14.74	9.04	6.36	4.64	3.78	3.09	2.64	2.28	1.90	1.41	1.36	1.65	1.87	2.26	2.93	3.60	4.14	4.82
$+2\sigma/\sigma_{SM}$	39.25	21.41	13.01	9.08	6.69	5.50	4.48	3.84	3.32	2.77	2.06	1.98	2.43	2.70	3.31	4.29	5.25	6.11	7.08
Observed/σ_{SM}	**15.84**	**9.67**	**7.29**	**3.88**	**3.20**	**2.02**	**1.80**	**1.31**	**1.22**	**1.25**	**0.82**	**0.92**	**1.09**	**1.58**	**1.55**	**2.29**	**3.64**	**4.24**	**5.87**

Figure 93: $H \rightarrow WW$ sensitivity normalized to NNLL σ_{SM} calculation for combination of all ten channels (0-jet High S/B, 0-jet Low S/B, 1-jet High S/B, 1-jet Low S/B, 2 or more-jets, low-M_{ll}, same-sign, WH trilepton, ZH 1-jet trilepton, and ZH 2+ jets trilepton).

References

[1] D. Benjamin, D. Hidas, M. Kruse, M. Casarsa, E. James, S. Jindariani, B. Rutherford, R. Lysak, A. Robson, R. St. Denis, et al., *Updated search for h to ww production using 4.8 fb-1* (2009), CDF/ANAL/EXOTIC/CDFR/9863.

[2] D. Benjamin, D. Hidas, M. Kruse, M. Casarsa, E. James, S. Jindariani, B. Rutherford, R. Lysak, A. Robson, R. St. Denis, et al., *Search for higgs to ww production in the low mll region using 4.8 fb-1* (2009), CDF/ANAL/EXOTIC/CDFR/9864.

[3] D. Benjamin, M. Kruse, S. Oh, G. Yu, M. Casarsa, E. James, S. Jindariani, T. Junk, R. Lysak, M. d'Errico, et al., *Search for h to ww production using 5.9 fb-1* (2010), CDF/PHYS/EXOTIC/CDFR/10086.

[4] D. Benjamin, D. Hidas, M. Kruse, E. James, S. Jindariani, B. Rutherford, R. Lysak, J. Nett, A. Robson, R. St. Denis, et al., *Search for vh $\rightarrow$ vww sm higgs production in the trilepton signature* (2009), CDF/PHYS/EXOTIC/CDFR/10020.

[5] D. Benjamin, D. Hidas, M. Kruse, E. James, S. Jindariani, B. Rutherford, R. Lysak, A. Robson, R. St. Denis, P. Bussey, et al., *Updated search for h to ww production using 3.6 fb-1* (2009), CDF/PHYS/EXOTIC/CDFR/9697.

[6] T. Rodriguez and E. Lipeles, *Measurement of the standard model zz cross-section in the final state zz $\rightarrow \ell\ell\ell\ell$* (2011), CDF/DOC/ELECTROWEAK/GROUP/10480.

[7] E. Lipeles, M. Neubauer, S.-C. Hsu, and F. Wurthwein, *Lepton id for multilepton diboson analyses* (2007), CDF/PHYS/ELECTROWEAK/CDFR/8538.

[8] *Cdf data processing status*, *http://www-cdf.fnal.gov/tiki/tiki-index.php?page=ProductionFarm.DataProcessing*.

[9] U. Baur and E. L. Berger, Phys. Rev. **D47**, 4889 (1993).

[10] D. Benjamin, A. Goshaw, M. Kirby, B. Heinemann, H. Hayward, and N. Tanimoto, *Measurement of the wgamma and zgamma production cross sections using 200/pb of run 2 data* (2003), CDF/PHYS/ELECTROWEAK/CDFR/6601.

[11] A. Nagano, J. Deng, A. Goshaw, B. Heinemann, and T. Phillips, *Measurement of the wgamma to e nu gamma cross sections using 1/fb of cdf data* (2007), CDF/ANAL/ELECTROWEAK/CDFR/8756.

[12] J. Deng, M. Goncharov, A. Goshaw, and T. Phillips, *Measurement of z-gamma production in ppbar collisions at sqrt(s) = 1.96 tev* (2009), CDF/PUB/ELECTROWEAK/CDFR/9904.

[13] D. de Florian and M. Grazzini, Phys. Lett. B **674**, 291 (2009), `0901.2427 [hep-ph]`.

[14] S.-O. Moch, *Private communications*, http://tevnphwg.fnal.gov/protected/minutes/ttxs_mstw2008.p

[15] J. Campbell and K. Ellis, MCFM - *monte carlo for femtobarn processes* (2005), http://mcfm.fnal.gov/.

[16] J. M. Campbell and R. K. Ellis, Phys. Rev. **D60**, 113006 (1999), `hep-ph/9905386`.

[17] U. Baur, T. Han, and J. Ohnemus, Phys. Rev. **D57**, 2823 (1998).

[18] *See the* TEV4LHC *working group webpage*, http://maltoni.home.cern.ch/maltoni/TeV4LHC/SM.html

[19] C. Anastasiou, K. Melnikov, and F. Petriello, Nucl. Phys. **B724**, 197 (2005), `hep-ph/0501130`.

[20] S. Catani and M. Grazzini, Phys. Rev. Lett. **98**, 222002 (2007), `hep-ph/0703012`.

[21] M. Grazzini, JHEP **0802**, 043 (2008), `0801.3232 [hep-ph]`.

[22] HNNLO *program is publically available at*, http://theory.fi.infn.it/grazzini/codes.html.

[23] S. Catani, D. de Florian, M. Grazzini, and P. Nason, JHEP **0307**, 028 (2003), `hep-ph/0306211`.

[24] C. Anastasiou, G. Dissertori, M. Grazzini, F. Stoeckli, and B. R. Webber (2009), `0905.3529 [hep-ph]`.

[25] A. D. Martin, W. J. Stirling, R. S. Thorne, and G. Watt (2009), `0901.0002 [hep-ph]`.

[26] S. Moch and A. Vogt, Phys. Lett. B **631**, 48 (2005), `hep-ph/0508265`.

[27] F. Petriello, *Talk from* CDF *week june 16-20, 2008, with comparisons between* N^{3}LO *and* FEHIP*, day 3 in webtalks*, http://www-cdf.fnal.gov/internal/WebTalks/Archive/0806/080618_collaboration_meeting_day_3/01_080618_collaboration_meeting_day_3_Frank_Petriello_1_roser_Fermi2008.pdf.

[28] A. D. Martin, W. J. Stirling, R. S. Thorne, and G. Watt, Eur. Phys. J. **C64**, 653 (2009), `0905.3531`.

[29] G. Bozzi, S. Catani, D. de Florian, and M. Grazzini, Phys. Lett. **B564**, 65 (2003), `hep-ph/0302104`.

[30] G. Bozzi, S. Catani, D. de Florian, and M. Grazzini, Nucl. Phys. **B737**, 73 (2006), `hep-ph/0508068`.

[31] M. Feindt, Technical Report IEKP-KA/01-1 (2001).

[32] T. Junk, *Sensitivity, exclusion and discovery with small signals, large backgrounds, and large systematics* (2006), CDF/DOC/STATISTICS/PUBLIC/8128.

[33] C. Rott, H. Bachacou, K. Hoffman, A. Dominguez, W. Yao, D. Glenzinski, D. Bortoletto, and M. Shochet, *Secvtx optimization for the 2003 winter conferences* (2002), CDF/DOC/SEC VTX/CDFR/6242.

[34] J. Freeman, T. Junk, E. Palencia, and S. Grinstein, *Secvtx mistag matrices for 2.2 fb*$^{-1}$ *of data up to p13* (2008), CDF/DOC/SEC VTX/CDFR/9280.

[35] A. Canepa, M. Casarsa, D. Benjamin, D. Hidas, M. Kruse, S. Oh, G. Yu, E. James, S. Jindariani, B. Rutherford, et al., *Search for h to ww production in the e-tau and mu-tau final states using 5.9 fb-1* (2010), CDF/PHYS/EXOTIC/CDFR/10087.

[36] M. Bauce, S. Behari, D. Benjamin, P. Bussey, A. Canepa, B. Carls, C. S, M. Casarsa, M. D'Errico, M. Herndon, et al., *Search for h to ww production in the e-tau and mu-tau final states using 7.1 fb-1* (2011), CDF/PHYS/EXOTIC/CDFR/10392.

A Scale factors used in Ntp processing

This section summarizes the scale factors we apply in our our analysis at the level of Ntuple processing. It is meant mainly for our internal purposes.

We apply the following set of the scale factors in this version ("v18") of analysis:

- $W\gamma$ **normalization scaling** – **0.87** scale factor is applied to the $W\gamma$ samples. This scale factor is determined from the low-$M_{\ell\ell}$ same-sign control region as described in Section 11.2.1.

- $t\bar{t}$ **b-tag and anti-btag scale factor** We apply anti-btag scale factor of **1.087** on $t\bar{t}$ events in OS 2+ Jets signal region. Accordingly, we apply b-tag scale factor of **0.94** on events in $t\bar{t}$ control region.

- $t\bar{t}$ **Silicon/No-Silicon good run list scale factor** – we apply a scale factor which accounts for the difference in b-tagging efficiency between the Silicon and No-Silicon GRL.
  - for anti-b-tagged region (signal region): **1.020**
  - for b-tagged region ($t\bar{t}$ control region): **0.972**